Investigations of weak and dilute magnetic behaviour in organic and inorganic systems

Sean R. Giblin

Investigations of Weak and Dilute Magnetic Behaviour in Organic and Inorganic Systems

Sean R. Giblin

A thesis submitted in partial fulfilment
of the requirements for the degree of
Doctor of Philosophy

Department of Physics
University of Durham
June 2005

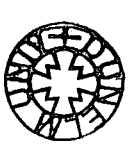

Investigations of Weak and Dilute Magnetic Behaviour in Organic and Inorganic Systems

Sean R Giblin

Abstract Muon spin relaxation is an ideal tool with which to study dilute magnetic systems, coupled with tailored bulk magnetic susceptibility measurements it is possible to examine previously unobserved magnetic exchange interactions. Investigations into non-stoichiometric $LaCoO_3$ reveals evidence of magnetic excitons in transition metal oxides for the first time. Moreover, data is presented that supports the concept of the defect driven excitons interacting with the stoichiometric $LaCoO_3$ which is known to undergo a thermally driven spin state transition. The data suggest the occurrence of more than one possible magnetic interaction of the excitons. Hole doped $La_{1-x}Sr_xCoO_3$ is of interest as it is known to be magnetically and electronically phase separated; by a direct analogy with magnetic excitons it is suggested that the Sr rich ferromagnetic clusters interact with the pure $LaCoO_3$ below the metal insulator transition ($x = 0.18$). It is suggested that it is this interaction observed for the first time that enables the rich phase diagram of $La_{1-x}Sr_xCoO_3$.

The persistent photoconductivity effect on the spin glass transition in the dilute magnetic semiconductor $Cd_{0.85}Mn_{0.15}Te$:In has been investigated using low temperature magnetic susceptibility measurements and for the first time muon spectroscopy. Muon measurements on an Al doped sample clearly show the spin glass transition, however the presence of the DX centre, which causes PPC when doping with In donors, perturbs the muon response. Particular attention is paid to possibility of the DX centre trapping muonium and preventing the detection of the spin glass transition. PPC does not induce a change in the muon response, however continuous illumination of the sample allows the observation of the spin glass transition, suggesting the presence of multiple DX centres, moreover the centre is found to be diamagnetic.

The search for magnetic ordering at room temperature in an organic material has generally neglected polymers. PANiCNQ combines a fully conjugated nitrogen containing backbone with molecular charge transfer side groups. This combination gives rise to a stable polymer with a high density of localised spins, which are expected to give rise to coupling. Magnetic measurements suggest that the polymer is ferri- or ferro- magnetic with a Curie temperature of over 350 K, and a maximum saturation magnetization of 0.1 $JT^{-1}kg^{-1}$. Magnetic force microscopy images support this picture of room temperature magnetic order by providing evidence for domain wall formation and motion.

Declaration

I confirm that no part of the material offered has previously been submitted by myself for a degree in this or any other University. Where material has been generated through joint work, the work of others has been indicated.

Sean R Giblin
Durham, June 2005

Acknowledgements

I would like to take this opportunity to thank all those who have helped me through my PhD. Specifically I would like to thank my supervisor Dr. Ian Terry for his support, enthusiasm and ideas, all of which have been required in abundance to enable this thesis to be completed. I would also like to thank Prof. M. R. Pennington and Prof. R. Abram who in their role as departmental heads have provided the facilities and resources I have required.

The experimental support provided by the staff of the physics department has ensured the building and maintenance of the equipment has been significantly easier. In particular I would like to thank J. Dobson for his organisational skills, small box and his willingness to assist in the insertion and removal of the probe.

I would also like to thank my friends which have made this last few years a pleasure, in no particular order; Matt Killeya, Paul Griffin, Nick Parker, Anna Shaw, Little Tom, Pickles, Rob Fielding, Jim and Sarah, Beki Langford, Pete Man, Louise Speake, Adam van Wotsit and Taz Clarke, without whom insanity would have arrived long ago.

Finally I would like to thank my parents and Ciaran, who have helped me in ways to numerous to mention.

Acronyms and Abbreviations

A list of acronyms and abbreviations used throughout this thesis is presented.

A = Asymmetry.
a = Field Distribution.
ac = Alternating Current.
AF = AntiFerromagnetic.
AFM = Atomic Force Microscope.
APD = Air Products Design.
B = Backward.
BMP = Bound Magnetic Polaron.
C = Curie Constant.
CT = Charge Transfer.
CMR = Colossal MagnetoResistance.
D = Down.
dc = Direct Current.
DFT = Density Functional Theory.
DMS = Dilute Magnetic Semiconductor.
E = Energy.
EDAX = Energy Dispersive X-Ray Analysis.
ESR = Electron Spin Resonance.
F = Forward.
FC = Field Cooled.
Fm = Ferromagnetic.
FTIR = Fast Fourier Transform Infrared Spectroscopy.
H = Heisenberg Hamiltonian.
HS = High Spin.
I = Current.
ICPMS = Inductively Coupled Mass Spectroscopy.
IMT = Insulator Metal Transition.
IS = Intermediate Spin.
IVC = Inner Vacuum Can.
J = Exchange Integral.
JJ = Josephson Junction.
JT = Jahn Teller.
KT = Kubo Toyabe.

LDA + U = Local Density Approximation + Hubbard Energy.
LEM = Low Energy Muon.
LF = Longitudinal Field.
LS = Low Spin.
M = Magnetisation.
MIT = Metal Insulator Transition.
MFM = Magnetic Force Microscope.
NMBO = Non-Bonding Molecular Orbits.
OI = Oxford Instruments.
$P(H)$ = Probability of Field Distribution.
$P(T)$ = Effective Moment.
PID = Power, Integral and Derivative.
PPC = Persistent PhotoConductivity.
ppm = Parts Per Million.
PSI = Paul Scherrer Institut.
QD = Quantum Design.
R = Resistance.
RF = Radio Frequency.
S = Spin.
SG = Spin Glass.
SQUID = Superconducting QUantum Interference Device.
T = Tesla.
T_C = Curie Temperature.
T_g = Spin Glass Transition Temperature.
TM = Muon Trigger.
T_N = Néel Temperature.
T_{irr} = Irreversibility Temperature.
TF = Transverse Field.
U = Up.
uv = Ultra Violet.
V = Voltage.
v = Vacancy.
VI = Voltage Current.
VSM = Vibrating Sample Magnetometer.
ZF = Zero Field.
ZFC = Zero Field Cooled.

$B_J(x)$ = Brillouin Function.
E_a = Activation Energy.
$G_z(t)$ = Muon Spin Relaxation Function.
k_B = Boltzmann Constant.
χ = Susceptibility.
Δ = Field Distribution.
γ_μ = Gyromagnetic Ratio.
$\sigma_z(t)$ = Spin Polarisation.

ξ = Localisation Energy.
ρ = Resistivity.
μ = Magnetic Moment.
μ_B = Bohr Magneton.
μSR = Muon Spin Rotation/Relaxation/Resonance.
θ = Curie Weiss Temperature.
υ = Fluctuation Rate.
ϕ = Magnetic Flux.

Contents

List of Figures

List of Tables

Chapter 1

Introduction

This chapter will outline the structure of the thesis and briefly discuss the content of each chapter. This thesis consists of work performed in the search for novel magnetic behaviour; as such three different magnetic systems are investigated, each with their own individual magnetic properties. Therefore each results chapter outlines the motivation behind each project before the results are reported, all of which are linked by the goal to further the basic understanding of magnetism.

Oxide materials have enjoyed a renaissance since the discovery of high temperature superconductivity in LaBaCuO crystals. Much work has concentrated upon manganites as they have produced properties such as high temperature superconductivity, Colossal MagnetoResistance (CMR) and co-incident metal-insulator transitions[1, 2, 3]. The rich phase diagram of the manganites is partially due to the complexity of the materials, therefore work has also been performed on the less complex cobaltites, particularly in the search for magneto-electronic phase separated materials[4]. $LaCoO_3$ is of particular interest in this study because it has a diamagnetic ground state upon cooling, making it an ideal material in which to study the effects of defect driven magnetic interactions, such as magnetic excitons (due to oxygen vacancies) which have been predicted but never previously observed. Understanding the interactions of the excitons may help to explain the behaviour of the ferromagnetic clusters observed when the parent material is doped with Sr ions. $La_{1-x}Sr_xCoO_3$ has a

rich magnetic phase diagram (CMR, glassy behaviour and magneto-electronic phase separation), however the local magnetic interactions are not well understood. Understanding of the local interactions may be relevant not only to cobaltites but also to oxide materials in general.

Semiconductors in the form of dilute and concentrated systems have stimulated research for many decades. Of particular interest is the work performed on dilute magnetic semiconductors, a wide area encompassing many different materials. For example, one of the first ferromagnetic dilute magnetic semiconductor was PbSnMnTe[5], a II-VI material, but recently work has concentrated upon III-V materials as they have been shown to have higher Curie temperatures[6]. $Cd_{1-x}Mn_xTe$:In is of interest as its carrier concentration can be persistently increased when at low temperatures upon application of sub-bandgap radiation. Currently work is also being performed on dilute magnetic semiconductors to explore the idea of carrier induced ferromagnetism[7]. It is the nature of the electron trap, the so-called DX^- centre that is of interest in this study, the magnetic ground state of which has never been probed directly. This study will investigate the DX^- centre with muon spectroscopy, the muon being sensitive to the DX^- centre because of the large Coulomb attraction. It is generally though that all DX^- centres contribute to the conductivity after excitation, however this work will attempt to demonstrate that not all centres are excited, and as such will be of particular interest to those studying the carrier induced insulator to metal transition.

Investigations into magnetic properties have primarily concentrated on materials containing metallic elements, due to their natural abundance and their ease of processing. However this does not preclude the possibility of spins being coupled on an organic material. Indeed the radical formation required to obtain spins on organic molecules is essential to modern chemistry, the difficulty has arisen in stabilising the radicals. Over the past century chemical processes have been improved so that spin coupled materials now exist, however the magnetic ordering temperatures have been capped well below 50 K[8]. The material developed for this project, PANiCNQ has a high density of spin bearing radicals together with unique stability in air, that allows for magnetic coupling[9] at

room temperature.

1.1 Layout of Chapters

Chapter 2 introduces some basic generic magnetism relevant to the remainder of the thesis, this will include a brief summary of defect induced magnetism. This is followed by a theoretical introduction to muon spin relaxation, demonstrating the suitability of this tool to investigate dilute magnetic materials.

Chapter 3 details the experimental procedures required to fulfill this thesis, as well as reporting on any sample preparation techniques that were required. The design and calibration of the equipment used to perform magnetic characterisation measurements is discussed.

Chapter 4 presents the results of both magnetic and electrical data on $LaCoO_3$, the principles of defect induced magnetism specific to this oxide material are discussed. The interpretation of the data presented infers the presence of magnetic excitons in $LaCoO_3$ and the subsequent magnetic interactions are discussed in detail.

Chapter 5 presents work performed upon $La_{1-x}Sr_xCoO_3$, in an attempt to measure the local magnetic interactions of a phase separated material. Moreover the Sr rich magnetic clusters present upon doping at low x compositions, signify behaviour similar to the magnetic excitons observed in chapter 4. The importance of the Sr ion upon the spin states of the surrounding Co ions is also discussed in depth.

Chapter 6 investigates the magnetic properties of the dilute magnetic semiconductors $Cd_{0.85}Mn_{0.15}Te$:In and $Cd_{0.86}Mn_{0.14}Te$:Al, with muon spectroscopy. The local magnetic interactions of the doping induced, DX^- centre are measured for the first time. Illuminating $Cd_{0.85}Mn_{0.15}Te$:In with infra-red radiation detects the local magnetic properties of the centres, demonstrating the centres are in fact diamagnetic.

Chapter 7 discusses the initial characterisation of an organic material (PANiCNQ) which indicates magnetic ordering at room temperature. The possible mechanisms of exchange in organic materials are discussed and the subsequent characterisation reported. Several experiments conclude that the observed behaviour cannot be a consequence of transition metal impurities.

In chapter 8 conclusions are drawn on each results chapter and highlight the important conclusions discovered. Any subsequent work required to further clarify the work presented is also briefly discussed.

1.2 Publication List

The work in this thesis has been partially covered in the following publications.

• Observation of Magnetic Excitons in $LaCoO_3$, S. R. Giblin, I. Terry, S. J. Clark, T. Prokscha, D. Prabhakaran, A. T. Boothroyd, J. Wu and C. Leighton, Europhys. Lett **70**, 667 (2005)

• Probing the Magnetic Ground State of the DX^- Centre in $Cd_{1-x}Mn_xTe$:In Using Muon Spin Relaxation, S. R. Giblin, I. Terry, D. E. Read, A. D. Hillier and P. Becla, *submitted* Phys. Rev. B

• Room Temperature Magnetic Order in an Organic Magnet Derived From Polyaniline, Naveed A. Zaidi, S. R. Giblin, I. Terry and A. P. Monkman, Polymer **45**, 5683 (2004)

References

[1] M. Imada, A. Fujimori and Y. Tokura, Rev. Mod. Phys **70**, 1039 (1998)

[2] Y. Tokura and Y. Tomioka, J. Magn. Magn. Mater **200**, 1 (1999)

[3] J. M. D. Coey, M . Viret and S. von Molnár, Adv. Phys. **48**, 167 (1999)

[4] P. L. Kuhns, M. J. R. Hoch, W. G. Moulton, A. P. Reyes, J. Wu, and C. Leighton, Phys. Rev. Lett **91**, 127202 (2003)

[5] T. Story, R. R. Galazka, R. B. Frankel and P. A. Wolff, Phys. Rev. Lett **56**, 777 (1986)

[6] H. Ohno, Science **281**, 951 (1998)

[7] H. Munekata, T. Abe, S. Koshihara, A. Oiwa, M. Hirasawa, S. Katsumoto, Y. Iye, C. Urano, and H. Takagi, J. Appl. Phys **81**, 4862 (1997)

[8] J. A. Crayston, J. N. Devine and J. C. Walton, Tetrahedron **56**, 7829 (2000)

[9] H. C. Longuet-Higgins. J. Chem. Phys **18**, 265 (1950)

Chapter 2

Introduction to Magnetic Behaviour

This chapter will present theoretical ideas and any relevant corresponding experimental results. As the scope of this work is rather broad this chapter will concentrate upon the general physical principles relevant to the materials investigated. Along with a general introduction to magnetism an in-depth discussion will describe dilute magnetic properties and the sensitivity of muon spin relaxation/resonance (μSR) to the various magnetic properties identified. The desired effect of this theoretical discussion is simply to enable interpretation of the work in later chapters and is not presented as a comprehensive review of magnetism.

2.1 Principles of Magnetism

This section will outline the classification of magnetic materials by their physical properties, a more detailed treatment can be found in many standard university textbooks[1, 2, 3]. The "types" of magnetism discussed in this section are diamagnetism, paramagnetism, ferromagnetism, antiferromagnetism and frustrated magnetism, which are all applicable to the materials of interest. Magnetism can result because of rotating electric currents or by a contribution from the spin vectors of electrons. The resulting magnetic properties are generally

summarised by the magnetic susceptibility (χ) which is defined by,

$$\chi = \frac{M}{H} = \frac{\mu_0 M}{B} \tag{2.1}$$

where M is the magnetisation, defined as the magnetic moment per unit volume, H is the magnetic field strength, B is the flux density and μ_0 is the permeability of free space. To avoid confusion this thesis will use standard SI units throughout.

2.1.1 Diamagnetism

Diamagnetism is inherent to all materials, it can be easily visualised when considering an atom with its electronic shell complete, there will be no lone electrons and therefore zero spin. However, the electron orbit will be susceptible to an applied magnetic field and obeys Lenzs' law which states, "the magnetic flux produced by the acceleration of an orbital electron is always negative to the change in internal field". The magnetic properties can be derived from a semiclassical approach, whereby the application of a field creates a magnetic moment (μ) opposing the change in field via a circulating electron current which has a magnitude $\mu = IA$, where I is the electric current and A is the area of electron orbit, The resulting susceptibility is a net contribution from all the electrons present in the material to give,

$$\chi_{Dia} = -\frac{\mu_0 N Z e^2}{6m} \left\langle r^2 \right\rangle \tag{2.2}$$

where N is the number of atoms per unit mass, Z is the number of electrons, e and m are the charge and mass of the electron respectively. The electron mean square radius, $\langle r^2 \rangle$ can only be calculated from quantum mechanical theory. A typical value of dimensionless volume susceptibility is 10^{-5}, as the discussion progresses this value will be seen to be small compared to the positive contribution from the valence electron susceptibility. A plot of M against H will yield a linear (with a negative slope) behaviour that is generally temperature independent.

2.1.2 Paramagnetism

Paramagnetism is a positive contribution to the magnetic susceptibility and is associated with materials that contain magnetic ions (lone electrons), moreover the ions can be thought of as widely spaced so that there is no appreciable interaction between them. The magnetic moments will respond to the direction of the applied magnetic field, the initial classical result yields a susceptibility of the form,

$$\chi = \frac{NM^2}{3kT} \tag{2.3}$$

where T is the temperature, k the Boltzmann constant and M the magnetisation (magnetic moment per unit volume), demonstrating that the susceptibility is inversely proportional to the temperature, this is the Curie law.

However this classical behaviour must be modified by quantum mechanics, whereby not all orientations of spin can be accomplished, only discrete orientations can be achieved, so called quantisation. Therefore the moment (μ) of a magnetic ion in free space can be given by,

$$\mu = \gamma\hbar J = -g\mu_B J \tag{2.4}$$

where γ is the gyromagnetic ratio, which is the ratio of the magnetic moment to angular momentum, μ_B is the Bohr magneton and g the Landé factor. J is the total angular momentum of the electron which is a summation of the spin (S) and orbital angular momentum (L), $J = L + S$. The resulting magnetic ground state of the magnetic ion can be determined by applying Hund's rules. By applying Boltzmann statistics and assuming that the angular momentum J has quantised levels, where the $2J+1$ energy levels are equally spaced it is possible to write down the average magnetization in a magnetic field by,

$$\begin{aligned} M &= Ng\mu_B \frac{\sum_{-J}^{J} J \exp\left(\frac{g\mu_B HJ}{kT}\right)}{\sum_{-J}^{J} \exp\left(\frac{g\mu_B HJ}{kT}\right)} \\ M &= Ng\mu_B \left(\frac{2J+1}{2J} \coth \frac{2J+1}{2J}\alpha - \frac{1}{2J} \coth \frac{\alpha}{2J}\right) \\ M &= Ng\mu_B B_J(\alpha) \end{aligned} \tag{2.5}$$

where $\alpha = gJ\mu_B H/kT$ and $B_J(\alpha)$ is the famous Brillouin function. Therefore the paramagnetic susceptibility can be obtained after simplifying the Brillouin

function to $B_J(\alpha) = \frac{J+1}{3J}\alpha$, the paramagnetic susceptibility can then be given by,

$$\chi = \frac{\mu_0 N J(J+1) g^2 \mu_B^2}{3kT} = \frac{C}{T} \tag{2.6}$$

where C is the Curie constant. This is only valid for small magnetic fields, in large fields saturating behaviour occurs due to the full Brillouin function. The classical limit can be derived by taking into account the effective number of Bohr magnetons. A typical value of the dimensionless susceptibility is 10^{-3}, a positive slope is normally measured.

2.1.3 Ferromagnetism and Antiferromagnetism

The magnetic ions highlighted thus far neglected any magnetic interaction, which may result in a net magnetic moment in zero applied field. Assuming a mean field theory, where each spin can align neighbouring ones, a spontaneous magnetic order can be achieved below a certain temperature known as the Curie Temperature (T_c). It has been shown that equation 2.6, when taking into account the mean field theory becomes,

$$\chi = \frac{C}{T - T_c} \tag{2.7}$$

This is known as the Curie-Weiss law; below T_c the moments upon the magnetic ions in the matrix align spontaneously, the actual interaction between the ions is quantum mechanical in nature and will be discussed in depth in section 2.2.

The spontaneous magnetisation can be imagined to be on a repeating sublattice, where the moments align themselves, as this could be the lowest energy state. However, another similar situation can be envisaged where neighbouring spins have a lower energy state if they lie antiparallel to one another. So called antiferromagnetism occurs below the Néel temperature (T_N), in which case the susceptibility can be written in the form,

$$\chi = \frac{C}{T + \theta} \tag{2.8}$$

where normally θ is close to T_N. However the ratio $\frac{\theta}{T_N}$ can increase to over 5 when next nearest neighbour interactions are included in the calculation.

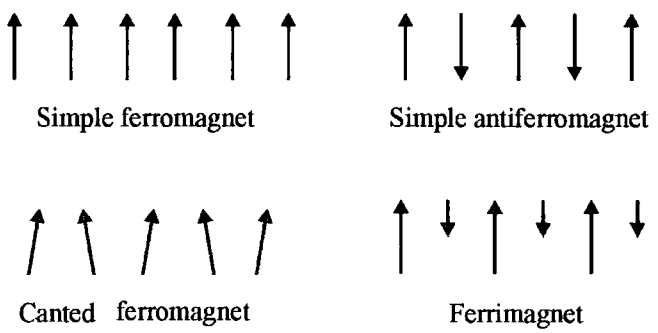

Figure 2.1: Some of the possible ordered arrangement of valence electron spins. From [1].

The bulk crystal alignments outlined are not unique, indeed there are other possible mechanisms that result in bulk magnetic order over the entire crystal. Fig. 2.1 demonstrates some of the possible ordered arrangements of the electron spins. As well as ferromagnetism and antiferromagnetism, two other simple forms of bulk order are demonstrated. Ferrimagnetism is observed when the spins on an alternating sublattice have different magnitudes and canted ferromagnetism, which has a net spin. However on an atomic level the spins point in different directions.

2.2 Magnetic Exchange

Comparison of the various exchange energies that drive possible magnetic interactions relevant to this particular study are given, specifically the mechanisms demonstrated are based on quantum mechanics, and as such will have to obey Hund's rules and the Pauli exclusion principle. Ferromagnetic and antiferromagnetic behaviour can be modeled as a result of two electrons with overlapping wavefunctions; therefore when considering a many electron system it is possible to describe the exchange interaction for the entire ordered system, using the Heisenberg exchange Hamiltonian,

$$H = -\sum_{i,j} J_{ij} S_i \cdot S_j \tag{2.9}$$

where S represents the spin of the electrons and J_{ij} is the nearest neighbour exchange integral. This is known as direct exchange and is a result of the direct Coulomb interactions between two electrons that obey the Pauli exclusion

principle. If $J_{ij} > 0$ then the interaction is ferromagnetic whilst if negative the exchange becomes antiferromagnetic.

The nature of exchange specific for each material investigated will be discussed in the appropriate results chapter. However a brief discussion of generic exchange mechanisms applicable to the materials investigated is required. If magnetic ions are connected by non-magnetic ions the direct exchange mechanism is very weak. However, the interstitial ions can mediate exchange, one specific example concerns the interaction between two magnetic Mn ions mediated through a O^{2-} ion in MnO, the first antiferromagnet discovered. The following exchange was termed superexchange following the initial work in the middle of the twentieth century[4, 5]. The mechanism can be most easily envisaged by considering Fig. 2.2 which shows the overlap of the oxygen $2p$ orbital with adjacent Mn ions.

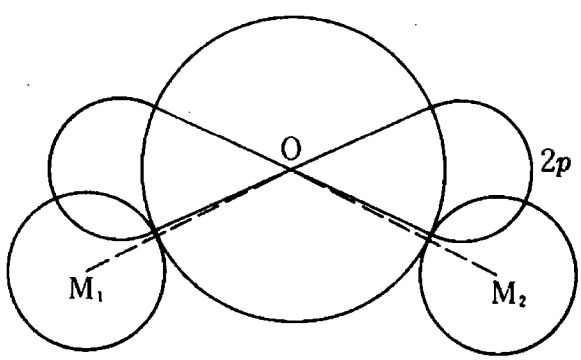

Figure 2.2: The p orbit of the O overlaps the Mn ions, mediating exchange via the oxygen ion, so-called superexchange. From [2].

The exchange relies upon the interaction of the electrons in the orbitals and obeys the Pauli principle, no two electrons can occupy the same state. In a Mn^{2+} ion there are five d electrons, if one Mn ion accepts one electron from the oxygen p orbital the remaining electron in the O ion must have an opposite spin. Any exchange between the unoccupied Mn orbital and the O $2p$ orbital will result in the transfer of an electron with opposite spin, leading to antiferromagnetic exchange between the two Mn ions. The interaction is strongest

when the Mn-O-Mn bond is maximised, deviation from this angle can result in ferromagnetic interactions between the magnetic ions when the bond angle is at 90^0. However this exchange is much weaker. This mechanism simply requires partially filled d levels for exchange to occur. Subsequently Goodenough and Kanamori proposed a set of semi-empirical rules[6] to calculate the exchange of transition metal ions. The general rules are well obeyed; experimental deviation from the expected behaviour is generally dependent upon strained bond angles.

The situation can be somewhat more complicated in some Perovskite compounds. The presence of magnetic ions with different valence states, for consistency Mn^{3+} and Mn^{4+} ions are considered in the material $La_{1-x}Ca_xMnO_3$, will alter the exchange mechanism. From superexchange rules it is expected, assuming a 180^0 Mn-O-Mn bond angle that the material is antiferromagnetic, however the material is actually ferromagnetic[7]. This exchange mechanism can be described by the double exchange mechanism[8], where conduction is mediated by the d band which can therefore mediate the spin of the electrons from one Mn site to the other through the ferromagnetic exchange mechanism. If there are competing exchange interactions from site to site the magnetic properties of the materials can become very complicated.

2.3 Frustrated Magnetic Systems

The discussion thus far has concentrated upon materials where the bulk is magnetically ordered, however, clearly identified already is the concept of multiple exchange mechanisms acting upon a magnetic ion. When this situation is combined with a "random" distribution of magnetic elements there may be magnetic frustration. This particular discussion will limit itself to the so called canonical spin glasses, in particular CuMn. If magnetic ions (Mn) are antiferromagnetically coupled in a non-magnetic matrix (Cu ions) it is easy to assume that bulk magnetic order will result after significant homogenous doping leading to magnetic percolation. However if randomly distributed throughout the matrix some magnetic ions may cluster. This behaviour may directly lead to the situation shown in Fig. 2.3, here the exchange mechanism is antiferromagnetic and the moments are arranged in an equilateral triangle formation. If the top two

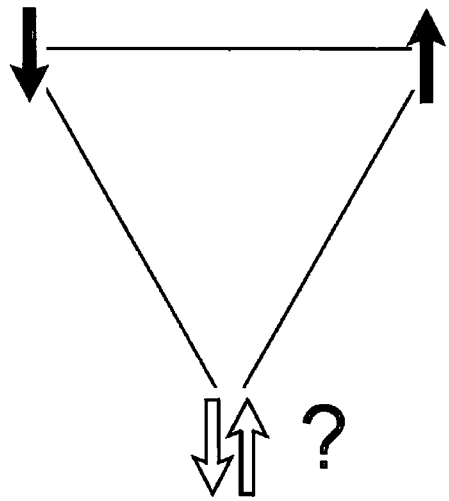

Figure 2.3: Magnetic frustration in an antiferromagnetic material.

moments are considered momentarily the ground state energy is satisfied, i.e. it is at the lowest energy (antiferromagnetically coupled), however the third moment is in somewhat of a quandary. It can only satisfy an antiferromagnetic interaction with one of the two moments, leading to magnetic frustration.

The moments identified in Fig. 2.3 will fluctuate above the spin glass freezing temperature T_g; however below it the moments will freeze into place. The direction of the frozen moments will be dependent upon the cooling protocol as field cooled and zero field cooled measurements will diverge at the transition, allowing magnetic susceptibility measurements to obtain T_g. However the application of a small measuring field can smear out the transition, the temperature dependence of the inverse magnetic susceptibility is shown in Fig. 2.4, for increasing compositions of Mn. The measurement was performed in an applied field of 0.6 T, a simple Curie-Weiss law, equation 2.7 cannot fit the data at low temperature as the transition is broadened because of the large measuring field.

It has been shown that a more accurate fit to the data in Fig. 2.4 can be obtained by substituting into equation 2.7 an effective moment ($p(T)$) of the form,

$$p(T) = \frac{N\mu_B^2}{3k}\left[\frac{d\chi^{-1}}{dT}\right]^{-0.5} \tag{2.10}$$

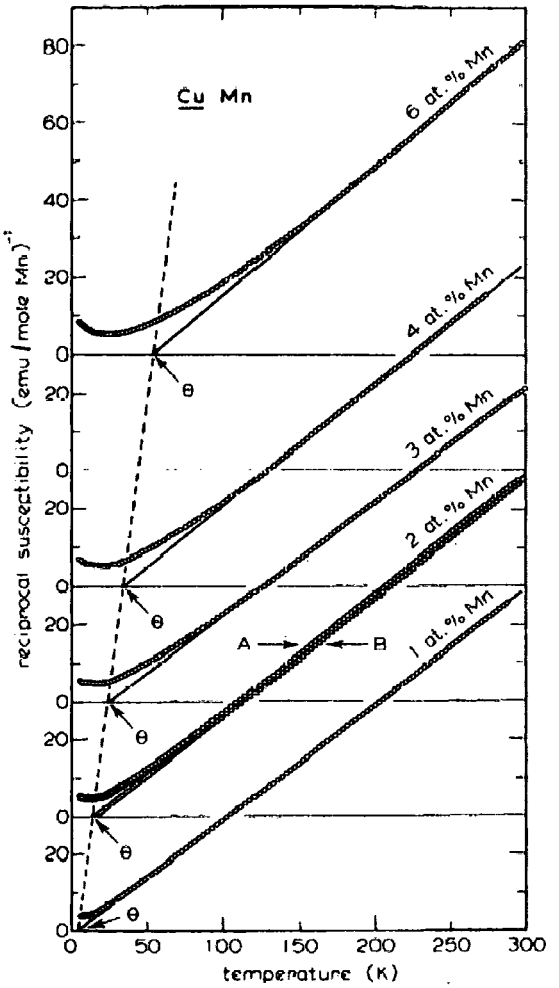

Figure 2.4: The temperature dependent inverse susceptibility of various compositions of CuMn. The dashed line is a fit to the data using a standard Curie-Weiss Law. From [9].

Subsequently, it has been found that the effective magnetic moment per Mn ion is constant throughout the compositional range[9], indicating that clusters are beginning to form in the material. It is essential to note that clustering in a canonical spin glass is occurring at even the lowest composition, the deviation from Curie-Weiss behaviour is always seen above T_g.

The smearing of the transition region leaves two distinct possibilities to measure T_g accurately, either use a very small measuring field in a dc type experiment,

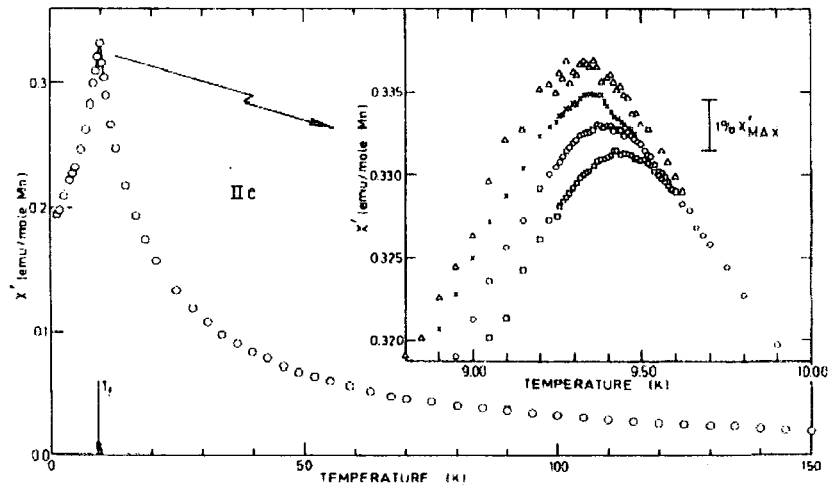

Figure 2.5: The temperature dependence of the real part of the susceptibility for CuMn. The inset shows the frequency dependence of the transition, square = 1.33 kHz, o = 234 HZ, x = 10.4 Hz and $\triangle$ = 2.6 Hz. From [10].

or perform ac susceptibility measurements. Ac susceptibility is very useful, although not always possible to measure for weak magnetic systems, it allows a direct comparison of the real (χ') and imaginary (χ'') part of the susceptibility, or the dispersion and absorption. The temperature dependence of the zero field χ' for CuMn (1 %) is shown in Fig. 2.5, T_g is easily observed, however it is the frequency dependence of the peak that is of most interest; this is shown in the inset of Fig. 2.5. The frequency dependence is inherent to canonical spin glasses as it occurs at such low frequencies, the transition temperature is lowered when decreasing the measuring frequency from 1.33 kHz to 26 Hz, for this particular sample[10].

Crucially as the spin glass transition is approached there is a peak in χ'', i.e. the spins are being decoupled from the lattice, therefore there is an absorption peak. Although canonical systems are not considered in this particular study a working knowledge of their properties is required in the interpretation of the work presented. Specifically a glass type transition is different from a superparamagnetic type transition as there are inter ion/cluster interactions in frustrated systems. Superparamagnetism is a specific form of magnetism where the interactions are governed by a stronger thermal agitation, which allows a

coherent rotation of all the spins present above a blocking temperature, the material appears paramagnetic. Below the blocking temperature ferromagnetic behaviour is observed, however unlike ferromagnetism the behaviour of the susceptibility is cooling field dependent.

The glass transitions discussed so far have considered only interactions between low density concentration magnetic ions, however if enough magnetic ions are doped into a non-magnetic host clustering of the ions may occur. This will have a profound effect on the magnetism as these clusters will freeze with a random orientation of the moment in a manner akin to spin glass freezing. Large ferromagnetic moments will occur, but the behaviour of the cluster systems are difficult to model because of the complicated interactions between the clusters.

2.4 Defect Induced Magnetism

The magnetic behaviour described in previous sections has concentrated upon properties induced by magnetic ions, however there are scenarios where local perturbations due to defects can have a profound effect upon the bulk system. Specifically two such magnetic phenomena will be described here, so called magnetic polarons and the relatively new concept of magnetic excitons. This review is not exhaustive and as such will concentrate upon the physical phenomena associated with defect induced magnetism.

In its simplest form the existence of a bound magnetic polaron can be understood in terms of an simple antiferromagnetic semiconductor doped with electron donors. A localised carrier may orientate a small region of the antiferromagnetic matrix in its effective Bohr radius, if its energy can be lowered. Many researchers have used a simple theoretical argument to base their calculations on ([14] and references there-in) a potential well with a depth E and width 2ξ is considered, where ξ is the localisation radius. By its very nature a magnetic polaron will deepen the well to $E + \Delta E$, consequently there is a reduction of the width of the well by $2\xi - \Delta\xi$ leading to a reduction in the localisation length, i.e the state is more bound. A schematic of this particular

scenario is shown in Fig. 2.6 where a charge carrier becomes trapped creating a region of ferromagnetic order within an antiferromagnetic matrix. As a result of the local polarisation of the spins within the wavefunction of the donor electron, the energy is reduced and the electron becomes self-trapped, a so-called bound state.

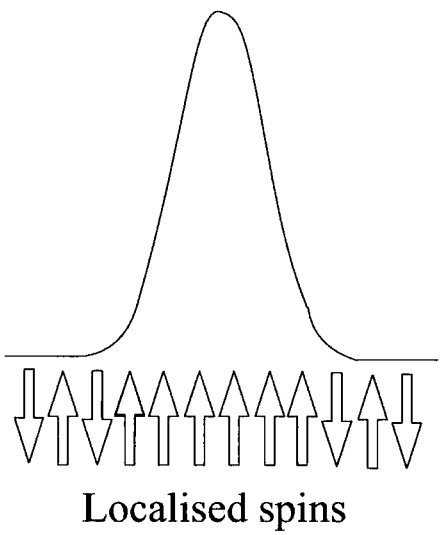

Figure 2.6: Sketch of a self trapped magnetic polaron, the antiferromagnetic matrix is interspersed with a ferromagnetic regions due to a hypothetical self trapped charge carrier. The arrows represent the spin direction and the line is the wavefunction of the trapped elctron.

Some of the most convincing evidence of the existence of bound magnetic polarons has come from transport measurements upon $Gd_{3-x}v_xS_4$[11], where v represents a vacancy. At low temperatures the material shows negative magnetoresistance where, as the field increases, the resistivity decreases. This is attributed to the destructive effect of the magnetic field which will eventually align the spins of the matrix with that of the polaron. Moreover magnetic field sweeps at low temperatures demonstrate the polarons as a high susceptibility species, and as such they appear as a parasitic component to the undoped material.

Previous work has indicated that bound magnetic polarons exist in CdMnTe

and other dilute magnetic semiconductors, when doped with donors or acceptors. At sufficiently low temperatures the donor electron (acceptor hole) will polarise the spin of the Mn ions within the Bohr radius of the donor electron (acceptor hole), creating a polaron as the $s-d$ ($p-d$) exchange dominates over the thermal fluctuations of the magnetic ions. Fig. 2.7A shows the schematic representation of the polaron forming in paramagnetic matrix. The physical properties of the magnetic polaron have been well documented both theoretically[12] and experimentally[13] in dilute magnetic semiconductors.

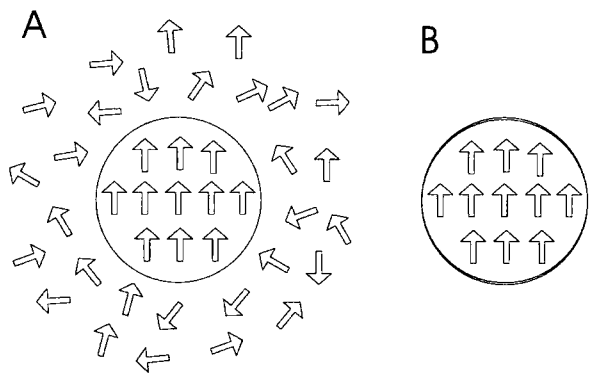

Figure 2.7: Sketch A shows a donor bound electron (acceptor bound hole) aligning the spins of magnetic ions to form a polaron in a paramagnetic matrix. Sketch B shows that an exciton is formed by a donor bound electron (acceptor bound hole) by inducing a magnetic moment in surrounding ions, the surrounding matrix is diamagnetic.

A subtle variation of a magnetic polaron is a so called magnetic exciton, which is inherently different from a magnetic polaron in the fact that it does not need a magnetic ion matrix to polarise. Specifically magnetic exciton formation has been proposed for $LaCoO_3$[14]. As the Co ions undergo a thermally induced low spin to high spin transition, at low temperatures the material is diamagnetic. However if an extra electron/hole is present in the system this will excite the surrounding Co ions into a magnetic state, this is shown schematically in Fig. 2.7B where there are no magnetic ions surrounding the exciton. Unlike polarons, magnetic excitons cannot be destroyed by the application of a magnetic field and in theory should be easily measurable (excitons will not show the magnetoresitive response of polarons). For the case of $LaCoO_3$ electrons can

be induced by oxygen vacancies. No experimental evidence of the existence of magnetic excitons has yet been interpreted but, like polarons, it is expected that they will have a profound influence on the electrical and magnetic properties of materials if present.

2.5 Muon Relaxation in Magnetic Materials

There are several fine reviews covering the relaxation of muons in various different physical states[15, 16]. This section will briefly consider the case of muon relaxation in magnetic materials; specifically it will discuss the effect of the muon position on the possible relaxation in dilute magnetic systems. The inherent difficulty with interpretation of muon spectroscopy data is that the exact behaviour of a muon in the material is difficult to obtain. Specifically an implanted muon can hop, capture an electron forming a muonium and have different implantation sites throughout the material. As a spin 1/2 particle, a muon is extremely sensitive to any local magnetic field. Due to parity violation at the point of decay the spin direction of the muon is conserved. As such the muon position is essential to understand the data collected. Fig. 2.8 shows a schematic of muon implantation in a canonical spin glass with two different implantation sites, any fluctuation in the moments will change the modulation of the decay depending upon the position of the muon (star) with respect to the magnetic ions.

There are two possible plausible solutions, specific to the kind of magnetism expected where there is a large density of valence electrons which contribute to the net moment of the system. The field distribution can be either described by a gaussian or a lorentzian distribution, the consequences of which will now be discussed in detail.

The experimental set up will be described in detail in chapter 3. If no field is applied and the local fields are static then the muon will Larmor precess about the component of local field that is perpendicular to the muon spin direction, giving rise to a discrete local muon precession frequency about each inequivalent

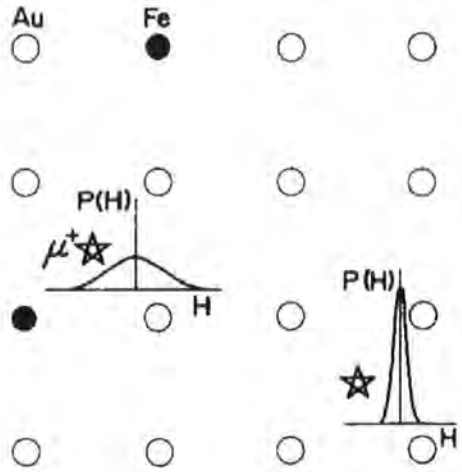

Figure 2.8: Muon distribution in a dilute magnetic material, typical of a canonical spin glass. From [17].

site. Therefore the spin polarisation ($\sigma_z(t)$) can be described by,

$$\sigma_Z(t) = \cos^2\theta + \sin^2\theta\cos(\gamma_\mu|H|t) \tag{2.11}$$

where θ denotes the angle between the initial muon spin direction (z) and the average static internal field (H), t represents time and γ_μ is the muon gyromagnetic ratio.

To obtain the spin relaxation function $G_z(t)$ the spin polarisation must be averaged over the local field distribution ($P(H)$). By definition, a gaussian relaxation of the local fields around the muon can be expected when the implanted muon is surrounded by static moments in a random direction; with the local field having a continuous distribution, such a situation can easily be envisaged with nuclear dipole fields. The internal field distribution of a gaussian can be well explained by,

$$P^G(|H|) = 4\pi|H|^2\left(\frac{\gamma_\mu}{\Delta\sqrt{2\pi}}\right)^3\exp\left(\frac{-\gamma_\mu^2|H|^2}{2\Delta^2}\right) \tag{2.12}$$

where Δ represents the field distribution. When combined with the spin polarisation it has be shown that the spin relaxation function can be written in the

form,

$$G_z(t) = \frac{1}{3} + \frac{2}{3}(1 - \Delta^2 t^2) \exp\left(-\frac{\Delta^2 t^2}{2}\right). \tag{2.13}$$

This is the famous Kubo-Toyabe (KT) function[18]. The first term shows that the signal will recover back to one third of its original value because in a random field distribution the muons will not precess along the polarisation of the incoming muons. Fig 2.9 demonstrates the zero field spectra at room temperature of MnSi, this was the first measurement of the KT relaxation, moreover the application of a longitudinal field, i.e. along the incoming muon spin direction, results in a decoupling of the relaxation rate as the spin direction of the material is forced along z direction. For early times or slow relaxation

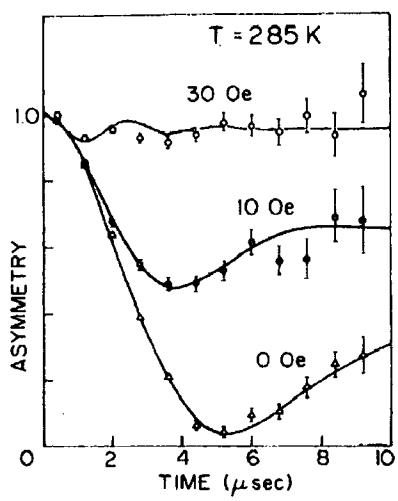

Figure 2.9: Longitudinal relaxation of MnSi showing the KT function, when a field is applied parallel to the incoming muon polarisation the relaxation will decouple. From [19].

the KT relaxation can be simplified down using a simple Taylor expansion to give,

$$\begin{aligned} G^G_{KT}(t) &= \tfrac{1}{3} + \tfrac{2}{3}(1 - \Delta^2 t^2)\left(1 - \tfrac{\Delta^2 t^2}{2} + \tfrac{\Delta^4 t^4}{8}\right) \\ &\approx 1 - \Delta^2 t^2 + \tfrac{5\Delta^4 t^4}{12} \\ &\approx \exp(-\Delta^2 t^2) \end{aligned} \tag{2.14}$$

This is a standard form of a typical gaussian relaxation that can be used to fit the data if the full relaxation occurs out of the muon time window.

The case for a KT relaxation is conclusive only for static randomly distributed magnetic moments around the muon implantation site. However another case can be envisaged where the moments have a different distribution. It has been shown that the behaviour of a frozen magnetic glass can be described by a lorentzian distribution of the form,

$$P^L(|H|) = 4|H|^2 \frac{\gamma_\mu^3}{\pi} \frac{a}{(a^2 + \gamma_\mu^2 |H|^2)^2} \tag{2.15}$$

where a represents the field distribution. Combining with the spin polarisation will reveal the so called lorentzian Kubo-Toyabe of the form,

$$G_z^L(t) = \frac{1}{3} + \frac{2}{3}(1 - at)\exp(-at) \tag{2.16}$$

The lorentzian KT will have a shallower dip than the standard KT because there is a wider range of $|H|$ leading to faster damping. This kind of relaxation is prevalent in frustrated magnetic systems below T_g. For slow relaxations or quick times this can be expanded to produce the a "standard exponential" relaxation of the form,

$$\begin{aligned} G_{KT}^L(t) &= \tfrac{1}{2} + \tfrac{2}{3}(1 - at)\left(1 - at + \tfrac{a^2t^2}{2}\right) \\ &\approx 1 - \tfrac{4at}{3} + a^2t^2 \\ &\approx \exp\left(-\tfrac{4at}{3}\right) \\ &\approx \exp(-\lambda t) \end{aligned} \tag{2.17}$$

where $\lambda = \frac{4a}{3}$.

The previous discussions have concentrated upon static fields. However in systems such as spin glasses there will be local fluctuations of the local fields. To describe the effect of the local field fluctuations it is necessary to take into account the strong collision approximation. After a time (t) a local field changes its direction with a probability distribution of the form $\rho(t) \propto \exp(-\nu t)$, where ν is the local fluctuation rate. After the collision the probability distribution has no information about its previous behaviour. When considering a gaussian distribution as identified in equation 2.12, it has been shown that the relaxation function can be written in the form[20, 21];

$$\begin{aligned} G_z^G(t, \upsilon) = \exp(-\upsilon t) \Big[& g_z(t) + \upsilon \int_0^t g_z(t_1) g_z(t - t_1) dt_1 \\ & + \upsilon_2 \int_0^t \int_0^{t_2} g_z(t_1) g_z(t_2 - t_1) g_z(t - t_2) dt_1 dt_2 + \ldots \Big] \end{aligned} \tag{2.18}$$

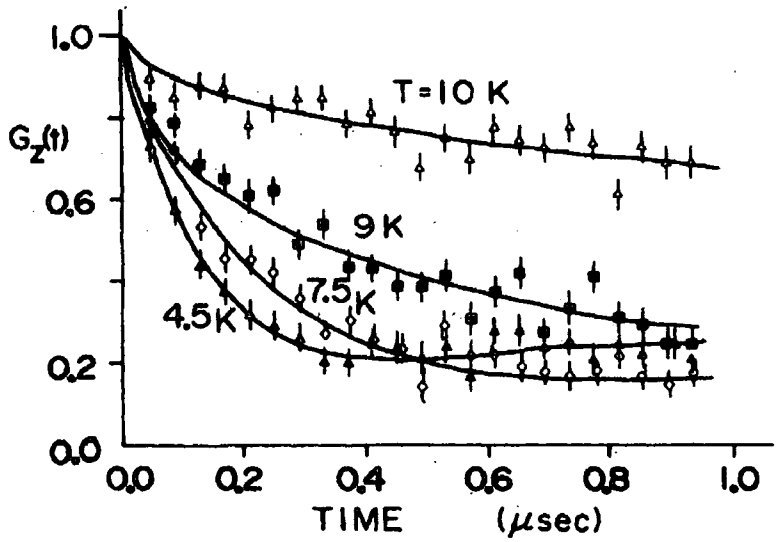

Figure 2.10: The zero field μSR spectra of the canonical spin glass AuFe (Fe at 1 %, $T_g = 9.1$ K). From[17].

where $g_z(t)$ represents the static relaxation function. The relaxation will stop once all the muons have decayed but until that point there may be numerous "collisions". Obviously it is possible to replace the gaussian relaxation with the lorentzian relaxation to obtain the relaxation function, however this will exhibit no change in the initial decay rate for very fast fluctuations, $\nu/a \gg 1$, i.e. the envelope function described in equation 2.18 becomes the static function. However for a canonical spin glass the relaxation rate changes as a function of temperature around the freezing temperature (T_g), as can be seen in Fig. 2.10 which shows the zero field μSR spectra for the canonical spin glass AuFe around T_g. The initial relaxation rates decrease as the temperature is reduced even below T_g presumably due to the fast fluctuations of the Fe moments. This contradiction can be resolved when noticing that the muons can have different variable ranges of local fields, see Fig. 2.8. When the field at a muon site undergoes a dynamic fluctuation the field "after" is chosen from a variable range of random fields such that "sub-distribution" of fields gives a gaussian distribution P_j^G with a width Δ_j. Therefore the probability to find a site with such a field distribution will satisfy the equation,

$$P^L(H_i) = \int_0^\infty P^G(H_i\Delta_j)\rho(\Delta_j)d\Delta_j \tag{2.19}$$

In the narrowing limit, it has been shown[17] that the relaxation is of the form of a root exponential dependence,

$$G_z^L(t, a, v) = \exp(-\sqrt{4a^2 t/v}) \tag{2.20}$$

The natural logarithm of the relaxation function above T_g will follow a root exponential behaviour. This is very similar to the possibility of coexisting static and dynamic fields and is representative of canonical spin glasses. Any clustering of the moments that give rise to spin glass behaviour have yet to be modeled.

References

[1] C. Kittel, Introduction to Solid State Physics (seventh edition), Wiley, New York (1996)

[2] S. Chikazumi, Physics Of Ferromagnetism (second edition), Clarendon Press, Oxford (1997)

[3] K. Yosida, Theory of Magnetism, Springer, London (1998)

[4] H. A. Kramers, Physica **1**, 182 (1934)

[5] P. W. Anderson, Phys. Rev **79**, 350 (1950)

[6] J. B. Goodenough, Magnetism and the Chemcial Bond, Wiley, New York (1963)

[7] G. H. Jonker and J. H. van Saten, Physica **16**, 337 (1950)

[8] C. Zener, Phys. Rev **82**, 403 (1951)

[9] A. F. J. Morgownik and J. A. Mydosh, Phys. Rev. B **24**, 5277 (1981)

[10] C. A. M. Mulder, A. J. van Duyneveldt and J. A. Mydosh, Phys. Rev. B **23**, 1384 (1981)

[11] S. von Molnár, I. Terry, T. Penney and P. Becla, Physica B **197**, 151 (1994)

[12] T. Dietl and J. Spałek, Phys. Rev. B **28**, 1548 (1983)

[13] D. L. Peterson, D. U. Bartholomew, U. Debska, A. K. Ramdas, and S. Rodriguez, Phys. Rev. B **32**, 323 (1985)

[14] E.L. Nagaev and A.I. Podelshchikov, J. Phys.: Cond. Matt **8**, 5611 (1996)

[15] S. L. Lee, S. H. Kilcoyne and R. Cyminski, Muon Science, Institute of Physics, Bristol (1998)

[16] S. F. J. Cox, J. Phys. C: Solid State Phys, **20**, 3187 (1987)

[17] Y. Uemura, T. Yamazaki, D. R. Harshman, M.Senba and E. J. Ansaldo, Phys. Rev. B **31**, 546 (1985)

[18] R. Kubo and T. Toyabe, Magnetic Resonance and Relaxation, p 810, North Holland, Amsterdam (1967)

[19] R. S. Hayano, Y. J. Uemura, J. Imazato, N. Nishida, T. Yamazaki, H. Yasuoka and Y. Ishikawa, Phys. Rev. Lett **41**, 1743 (1978)

[20] D. E. MacLaughlin and H. Alloul, Phys. Rev. Lett **36**, 1158 (1976)

[21] Y. J. Uemura, R. S. Hayano, J. Imazato, N. Nishida and T. Yamazaki, Solid State Comms **31**, 731 (1979)

Chapter 3

Experimental Details

This chapter outlines the major experimental procedures used in this study. Specifically it will discuss techniques for both electrical and magnetic measurements along with any technical information required to demonstrate the performance of the equipment.

3.1 Electrical Measurements

Temperature dependent resistivity measurements were performed on a number of different samples, in the range 350 mK - 300 K. For the temperature range 350 mK - 10 K an Oxford Instruments (OI) helium-3 refrigerator was used; its operation will be discussed in section 3.2.5. Higher temperature measurements (T > 4.2K) were performed on three different systems, an APD closed cycle refrigerator (10 K - 270 K), an OI continuous flow cryostat (77 K - 300 K) and a simple probe involving direct immersion into liquid Helium (4.2 K - 300 K). In all systems operating above 4.2 K the temperature was accurately measured using RhFe thermometers.

3.1.1 Performing Electrical Measurements

Consideration should be paid to sample preparation and mounting. All samples were of a uniform thickness and it was found that gold wires could be contacted with indium (4 nines purity) onto a smooth surface. Surface preparation was

tailored to individual samples; oxide materials were simply polished down with a 0.5 μm cloth and diamond paste. Semiconducting (II - VI) materials were polished and then etched in a bromine - methanol solution to removed unwanted surface oxidation, rinsed in methanol and contacted as soon as the sample dried to prevent re-oxidation.

Copper is an effective material with which to fabricate sample holders within the temperature range. The sample holders were all screw threaded to the cold finger/main body of the cryostat and locked in place with a layer of indium to ensure good thermal contact. In all cases a thermometer was attached directly to the sample holder. The samples were mounted on a thin layer of Rizla paper to provide electrical insulation but reasonable thermal conduction, the Rizla paper was attached to the copper mount with a thin layer of GE varnish. Any additional strain caused by the different thermal contractions of the sample and the mount was kept to a minimum by attaching the sample to the Rizla paper via a thin layer of Si vacuum grease, which only solidifies at 10 K.

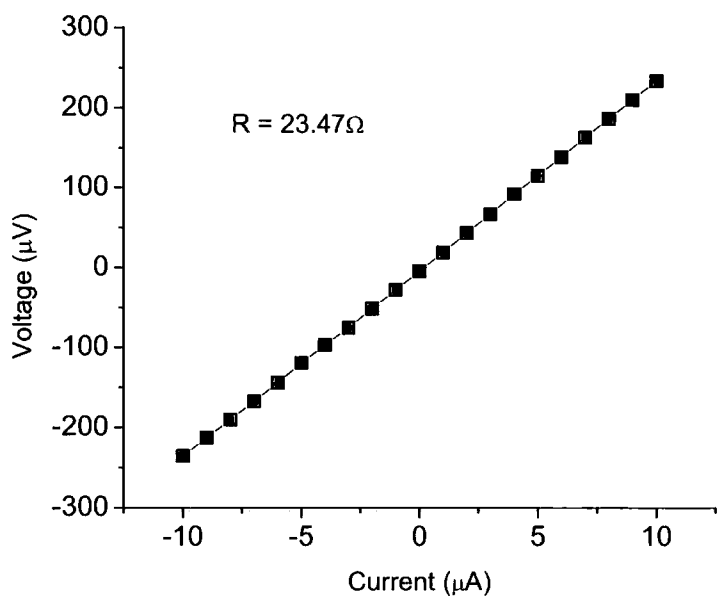

Figure 3.1: A VI plot showing good Ohmic behaviour. This particular sample of $La_{0.85}Sr_{0.15}CoO_3$ was measured at 14 K, the error bars are within the symbols.

Before resistivity measurements could be performed the samples were always tested for Ohmic behaviour, at the lowest temperature available for a given cryostat. A typical Voltage against Current (VI) curve is shown in Fig. 3.1, showing a linear response within the given current range. In all cases either a full VI curve was performed or the resistance was calculated after measurements were taken in both current directions for d.c electrical measurements. This was to ensure that any instrumental offsets, and thermal voltages across the sample were taken into account when calculating the true resistance. Resistivity measurements were performed with In contacts in the van der Pauw configuration[1], with current being injected via two of the contacts and the voltage measured between the two opposite configurations as shown in Fig. 3.2. If the contacts are Ohmic and on the edge of the sample, this technique can compute the resistivity regardless of shape, solong as it is of uniform thickness, t. Measurements have to made in both configurations shown in Fig. 3.2, the resistivity (ρ) can then be given by,

$$\rho = \frac{\pi t}{\ln 2}\left(\frac{R_A + R_B}{2}\right)\gamma\left(R_A/R_B\right) \tag{3.1}$$

where R_A and R_B are the resistances of two configurations and γ is a function dependent on the ratios between the two resistances. For an isotropic sample,

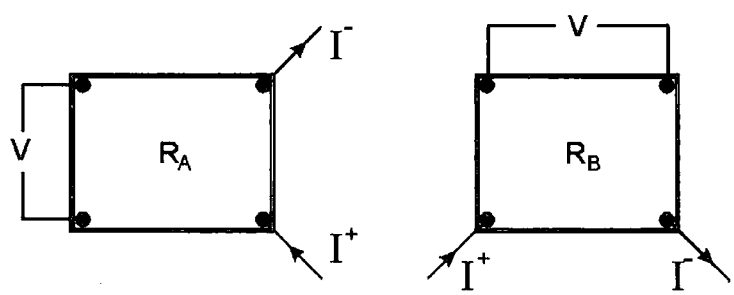

Figure 3.2: The van der Pauw technique; this diagram shows the perimeter current and voltage taps for the resistance configurations to calculate the resistivity.

with contacts in a perfect square configuration the ratio R_A/R_B is unity. However γ will quickly begin to deviate, falling to 0.7 when the ratio is 7. The importance of the temperature dependent resistance anisotropy will be commented upon in later chapters. The van der Pauw configuration can also be used to measure the Hall carrier density using the same 4 Ohmic contacts.

3.2 Magnetic Measurements

Magnetic field and temperature dependent experiments were an essential part of this study using both commercial and "home-built" equipment. A commercial Quantum Design (QD) MPMS XL Superconducting QUantum Interference Device (SQUID) system has been used for temperature dependent measurements (2 K - 340 K) in fields up to 5 T. This system is able to resolve a magnetic moment as small as 1 x 10^{-11} JT^{-1}[2]. In conjunction with standard characterisation measurements a home built SQUID system has been developed with an extended temperature range from 350 mK - 5 K; both systems are detailed below.

3.2.1 Basic Principles of a SQUID system

A direct analogy can be drawn to the interference of light waves and the operation of optical interferometers. Except in the case of a SQUID magnetometer, the interference of electron-wave processes is of concern. A SQUID system consists of a superconducting ring which is interrupted by one (rf SQUID) or two (dc SQUID) Josephson Junctions (JJ's). A JJ consists of a thin insulating barrier, in this case breaking super-conducting rings. The systems described all use superconductors with a low critical temperature (T_c) where the charge carriers are Cooper pairs that move coherently with the same wave function energy and phase. A SQUID utilises two unique properties of superconductors, namely magnetic flux quantisation and Josephson tunneling. Application of a magnetic flux to the SQUID causes an output that is a function of the magnetic flux threading the SQUID ring. In essence a SQUID is a very sensitive current to voltage convertor.

3.2.2 rf SQUID

rf systems are the base of most commercial magnetometers simply because the actual ring itself contains only one JJ and is thus easier to make. The magnetic flux (Φ) inside a SQUID loop acquires a discrete value such that, $\Phi = n\Phi_n$, where n is an integer and Φ_n being one flux quanta, $\Phi_n = h/2e = 2.07$ x 10^{-15}

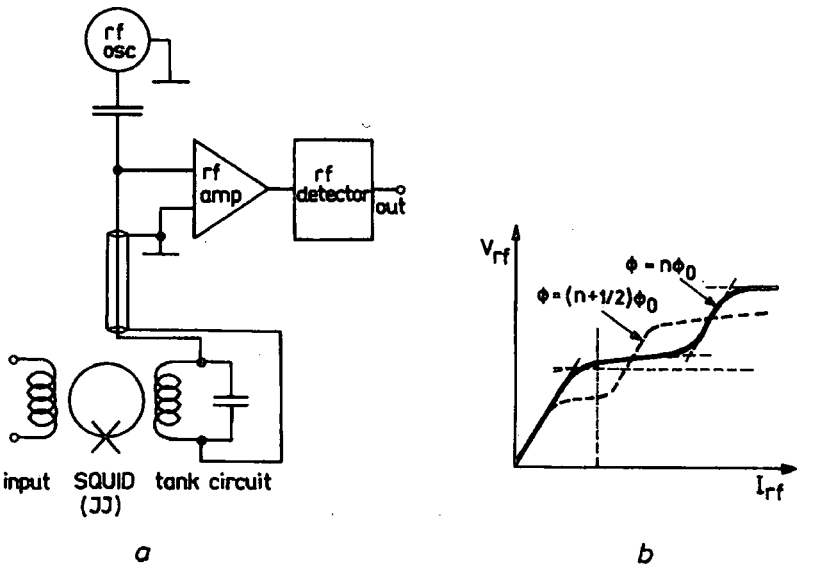

Figure 3.3: (a) LC circuit for obtaining rf SQUID characteristics. (b) The VI curve showing the response of the SQUID ring to an external field.

Wb. The JJ interrupts a flow of current around the ring which maintains a constant phase difference; the sensor will respond to any additional rf magnetic flux. The SQUID ring is coupled to the inductor of a resonant LC circuit, typically between 20 MHz and 5 GHz. A typical LC tank circuit is shown in Fig. 3.3a; the value of the output voltage V_{rf} is dependent on the input from a pickup coil (I_{rf}). Any variation of external magnetic flux causes a variation in phase of the current (I_{rf}) across the JJ. Any change in current is a non - linear function, the relative change in impedance can be registered by elements of the rf circuit. The V_{rf}-I_{rf} characteristics of a rf SQUID are shown in Fig. 3.3b; V_{rf} oscillates as a function of applied magnetic flux with a period Φ_n. Any change in the magnetic flux applied to the pick up coil can therefore give a proportional voltage change.

Due to the physically small size of the SQUID ring the relative change in external field is detected by a flux transformer consisting of superconducting pick up coils. The sensing coils are inductively coupled via a small coil to the SQUID ring. The pickup coils themselves are often gradiometrically wound. One coil would be very susceptible to any stray magnetic flux, therefore the most basic

usable configuration is a pair of counter-wound coils with the sample being placed in the centre of one coil. The design is such that uniform external fields will not affect the SQUID response. This is known as a first order gradiometer configuration. When detailed spatial derivatives are required (i.e. moving sample) a so called second order configuration is needed; in this scenario two small coils are wound either side of a large counter-wound coil, the number of turns in both directions being equal.

3.2.3 dc SQUID

A dc SQUID consists of two separate JJs connected in series, and operates with a constant current. In this scenario an a.c magnetic flux is applied across one junction with a frequency in the order of 100 kHz, having a peak to peak voltage of $\Phi_0/2$. The other junction is connected to a flux transformer; if the change in magnetic flux is equal to $n\Phi_0$ the modulation frequency remains constant. A change in flux induces a change in the peak to peak voltage of the modulation frequency. As in all SQUID's this response is again non - linear allowing a large variation in the change in total flux to be measured. The phase difference of the signal is dependent upon the sign of flux change. Although more difficult to fabricate, a dc SQUID is more sensitive than its rf equivalent primarily because the electronics simpler.

3.2.4 High Temperature SQUID Measurements

As mentioned previously, work was performed upon a QD SQUID magnetometer with an absolute sensitivity of 1 x 10^{-11} JT^{-1}. This level of sensitivity is somewhat difficult to regularly reproduce because it requires a uniform magnetic field measurement which is complicated by trapped flux present in superconducting magnets at low fields. The sample temperature is maintained using Helium as an exchange gas, after it passes through a resistive heater to enable a temperature range between 5 K and 340 K. A low temperature regime (2 K - 5 K) is possible, by pumping a small liquid Helium bath to reduce the vapour pressure. In all measurements performed the constant temperature option was utilised; before the magnetic response is recorded a thermometer

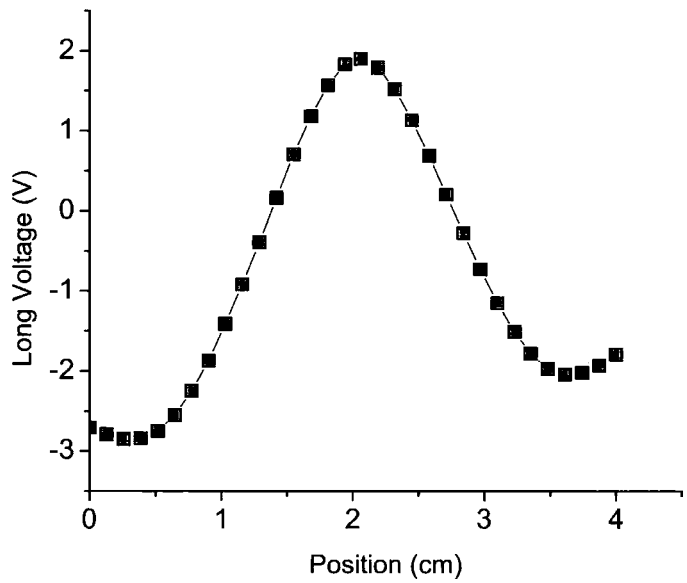

Figure 3.4: Plot showing the typical QD SQUID response as a magnetic moment is moved through the pickup coils. The sample is centred around 2 cm.

at the base of the sample chamber and one level with the sample must be in agreement, and this method gives a temperature stability ± 5 mK. The maximum sample length was 5 mm because the sample was moved over a distance of 40 mm through the second order gradiometer coils and measured repeatedly. Therefore a longer sample would induce a response from the compensating coils in the pickup coils. The absolute flux was measured through the SQUID ring at various points through the scan; a typical response of a magnetic moment through the coil set is shown in Fig 3.4. The sample is centred around 2 cm in this particular case. The tails of the response are not level because there is a small yet significant field gradient across the sample space. The absolute value of magnetic moment is then obtained by fitting the data with the spatial response of a magnetic moment.

When using the SQUID MPMS system there are several important experimental parameters to be taken into consideration. The field gradient across the sample, although small (0.01 % over 40 mm), will distort the results of samples with

a non-uniform magnetic moment. This however can be minimised depending upon the type of measurement performed. A "dc" measurement moves the sample but it stops for every measurement, hence measuring the absolute flux cutting the SQUID ring. The "reciprocating sample oscillation" constantly moves the sample during measurement, and hence any field gradient across a material that does not have a uniform magnetic response will cause a deviation from the ideal moment shape as in Fig. 3.4, and the moment calculation will be incorrect. The residual field cannot be reduced to below 0.1 mT as the magnet has no quench facility to get rid of any trapped flux. The final experimental consideration when performing measurements concerns the setting of magnetic field values. There is a "no overshoot" mode where the current in the magnet is reduced/increased to the desired value. (There is no Hall probe in the sample space and the field value is determined from a factory calibration of the current through the coil). There is also an "oscillate" mode which obtains a more accurate value of field; however the field oscillates around the set value to reduce the trapped flux. This method of setting fields for glassy/remnant materials, especially when setting the field to zero, will cause remnant behaviour in the sample and therefore affect the interpretation of the results. The above considerations must be taken into account when using this particular SQUID system.

3.2.5 A Low Temperature SQUID Magnetometer

The lowest temperature available at present upon a commercial system is $\sim$ 2 K. As the study involves looking at dilute magnetic systems, a SQUID magnetometer was designed and constructed to enable studies of exchange interactions as low as 350 mK. Two commercial systems were combined, an OI Heliox Probe sorption pumped ^{3}He refrigerator and a QD Model 5000 dc SQUID sensor fabricated from a thin film of niobium. A working version of the apparatus existed before this particular study commenced[3]. However modifications to improve the sensitivity and overall convenience were essential for this work.

As the operation of the Heliox probe is essential to the SQUID response, understanding the principles of operation is required. Fig. 3.5 shows the schematic of

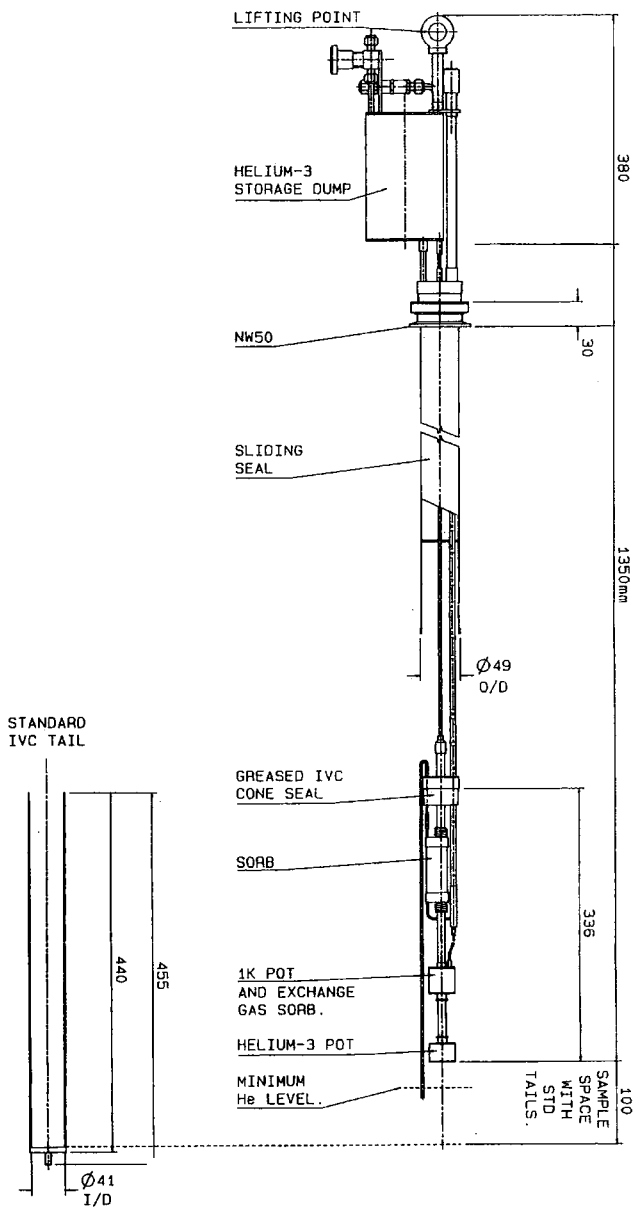

Figure 3.5: A schematic diagram of the Oxford Instruments He^3 Heliox cryostat, all dimensions are in mm.

the Heliox probe; cooling can be commenced once the vacuum can (IVC) has been sealed, evacuated and a small amount of ^{4}He gas introduced (10 cc). The system can be simply lowered into a dewar of liquid ^{4}He allowing quick cooling and if necessary a quick sample change. Once in the liquid the exchange gas in the IVC ensures efficient cooling of the sample holder to 10 K. This excess He gas is removed by an activated charcoal sorbtion pump located above the 1 K pot. Once the probe is in equilibrium with the dewar the 1 K pot is filled with liquid Helium via an evacuated pick-up tube submerged in the liquid. The gas pressure above the 1 K pot is reduced via the operation of a large (40 litres per second) rotary pump reducing the temperature of ^{4}He in the 1 K pot to $\sim$ 1.3 K. The sorb is kept at 45 K to expel the ^{3}He gas which begins to condense into the ^{3}He pot below 1.4 K. After condensation of all the ^{3}He gas the charcoal sorb is activated, reducing the vapour pressure of the gas, which creates a base temperature in the system of 350 mK once the experiment has been loaded onto the sample stage.

Base temperature stability with a minimum load onto the ^{3}He pot can be up to 36 hours. However it is the heating protocol which is of importance in this study, as the temperature dependent magnetic susceptibility is its prime concern. In the range 300 mK $<$ T $<$ 1.4 K, the sample temperature is controlled by altering the pumping speed of the ^{3}He sorbtion pump; in practice the sorb temperature is controlled. Above 1.4 K, temperature control is achieved by directly heating the ^{3}He pot with a resistive heater. For both situations the heaters are supposedly non-inductively wound. However any deviation from perfect counter-wound symmetry will result in a stray magnetic field in the IVC when a current is passed through the heater. With a SQUID sensor in the IVC any stray field will be measured; as the heater is controlled by standard PID controls this results in non-uniform oscillations of the background. This makes stable, sensitive magnetic measurements almost impossible for this experimental setup. Dynamic temperature sweeps were therefore performed from 350 mK - 5 K, although the maximum temperature was determined by the method of warming. Two separate methods of dynamic warming were devised so that over the entire temperature range the sample was in thermal equilibrium with the thermometer. The first involves pumping upon the 1 K pot with the

external rotary pump and the needle valve closed so no further liquid ^{4}He was picked up. This method gave good temperature equilibrium in the range 350 mK < T < 2.5 K. The second method requires simply sealing the 1 K pot at the top of the probe and then opening the needle valve of the pick-up tubes which are submerged in liquid. As the exhaust tube of the 1 K pot fills, the ^{4}He gas expands due to the temperature gradient up the probe and forces the liquid in the 1 K pot back into the dewar, giving good temperature equilibrium between 1 K - 5 K. The effect of these warming conditions on the SQUID performance will be given later in this section.

The SQUID detection ensemble was designed to fit in the bottom of an extended IVC; the schematic of the experiment is shown in Fig. 3.6. The SQUID ring is housed in a superconducting shield which is mounted in a copper block heat sunk into the IVC maintaining a constant temperature of 4.2 K via thermal conduction. An inductance matched flux transformer (1.9 μH)[5] in a first order gradiometer configuration made out of multi-core NbTi superconducting wire is wound upon a MACOR former. An inductance matched flux transformer linked to the input of the SQUID maximises the sensitivity[4]. Multi-core wire was chosen instead of single filament wire as it is more resistant to damage. The copper sample holder sits in the middle of the top pickup coil and is insulated from the SQUID assembly by a vacuum sleave. Around the pick-up coil is a copper wound electro-magnet capable of producing an external field of 0.03 T; copper was chosen as there is no chance of trapping any magnetic flux as frequently happens in a superconducting magnet. To prevent stray field penetration, the IVC is wrapped in a lead shield which is superconducting at 4.2 K, thus preventing fluctuations in the earth's field (mainly due to large moving metallic objects) from distorting the measurements. Mu-metal foil was wrapped around the lead to minimise the field inside the lead shield prior to it becoming superconducting. At 77 K it was found the field in the IVC was 10 μT, a factor of five lower than the earth's field. For all measurements performed this was the measuring field as hysteresis loops/high field susceptibility could not be performed due to a combination of a non-uniform field from the copper electromagnet and ambient electrical noise. The latter could be improved by housing the experiment in a screened room. Importantly the dewar was placed

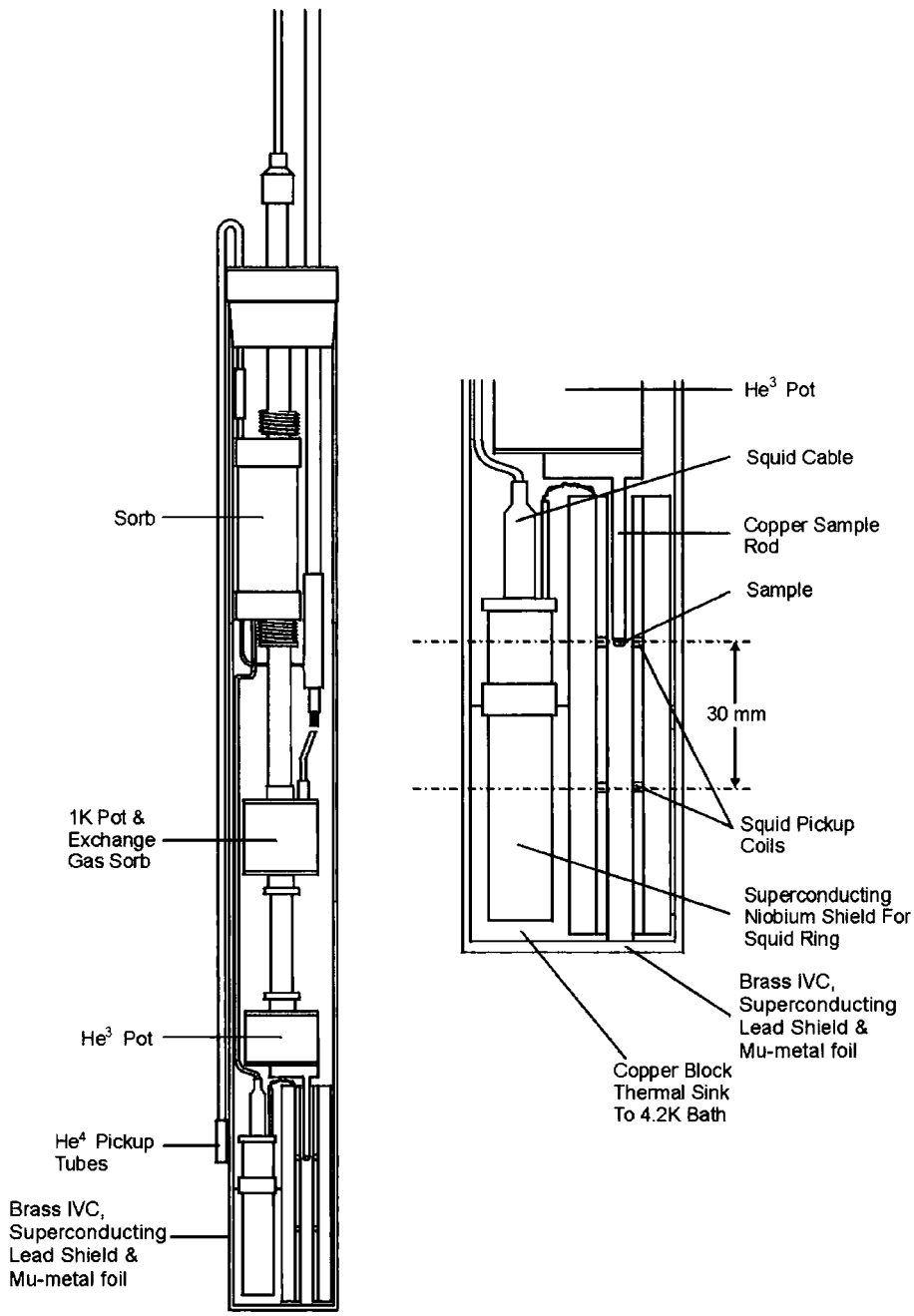

Figure 3.6: A schematic diagram of the low temperature Durham SQUID, the inset shows a magnification of the SQUID assembly. Reproduced from Read[3].

on an metallic plate sitting on high density rubber to damp out any vibrations through the floor. The entire system was grounded in series, in order to maintain a stable background over the time period of experiment. In many cases this was several hours.

3.2.6 Characterisation of the Durham, Low Temperature SQUID

The QD commercial magnetometer described in section 3.2.4 works by measuring the spatial dependence of the moving magnetic moment, whilst the Durham SQUID system does not move the sample and measures only the absolute flux cutting the SQUID ring. Careful placement of the sample in the flux transformer is essential to enable accurate temperature dependence of the change in magnetisation. The calibration of the SQUID is a rather complex and laborious task, the first step entails placing a magnetic dipole in the flux transformer. This dipole is a small copper electromagnet made from 0.15 mm diameter copper wire with 21 turns wrapped around the sample holder, when current is passed there will be a change in magnetisation. Fig. 3.7 shows the response of the Durham SQUID to changes in current through the magnetic dipole when the current is applied in both directions and stepped down uniformly in 10 steps from 1μA to 0.1 μA. This graph is of huge importance as it allows the change in moment of the sample to be accurately calculated. This graph can also be used to show the stability of the system. The recording of the graph took $\sim$ 10 mins, and it is clear from this that the background remains constant, i.e. when the current is switched off in the magnetic dipole the SQUID voltage returns to its previous value. The reproducibility of these data is essential to ensure accurate characterisation of samples.

The absolute sensitivity of the SQUID is not in terms of the absolute moment that can be detected but the smallest change in moment. This is an advantage over the commercial QD SQUID as small changes in moment upon a large magnetic background can be detected because the sample is not moved and only the change in absolute flux measured. The calibration of Fig. 3.7 is shown in Fig. 3.8, in this case the setting on the electronic amplifier is, sensitivity 50,

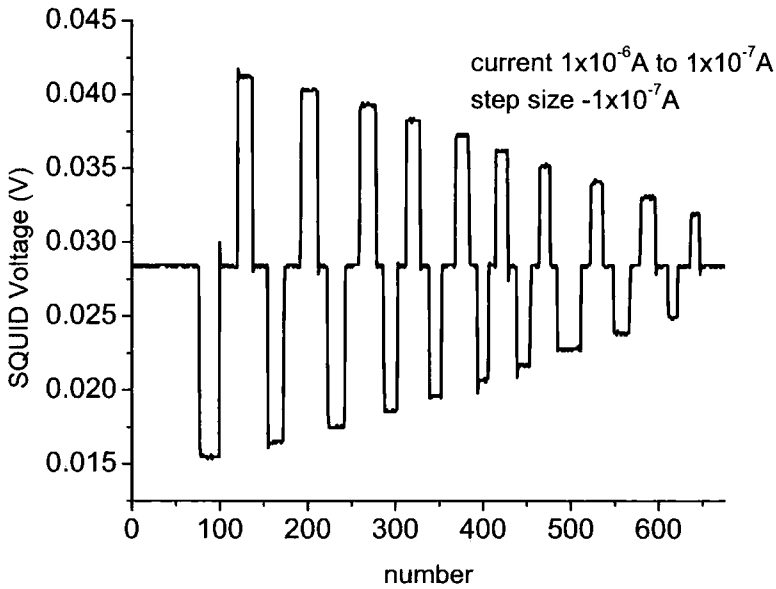

Figure 3.7: The response of the SQUID to a change in current of an electromagnet wrapped around the sample holder. The current was applied in both directions and stepped uniformly down in 10 steps from 1μA to 0.1 μA.

gain 5. The smallest change in moment detectable was 1 x 10^{-12} JT^{-1}, this is an order of magnitude more sensitive than the smallest moment detectable by the commercial QD system. To gain any useful information once the sample has been measured and the change in moment calculated, an absolute value of moment is required at one temperature. Therefore a temperature overlap region between the Durham SQUID and the QD system is essential, and as the QD system has a base temperature of 2 K the absolute moment can be measured.

The Durham SQUID was designed to measure dilute magnetic systems, and therefore the background needed to be well characterised and reproducible. Fig. 3.9, shows the temperature dependent background measurements for the two separate dynamic warming protocols identified in section 3.2.5, 300 mK < T < 2.5 K (low temperature configuration) and 1 K < T < 5 K (high temperature configuration). In both cases the experiment was cooled and measured in an external field of 10 μT along the axis of the SQUID; field cooled experiments (

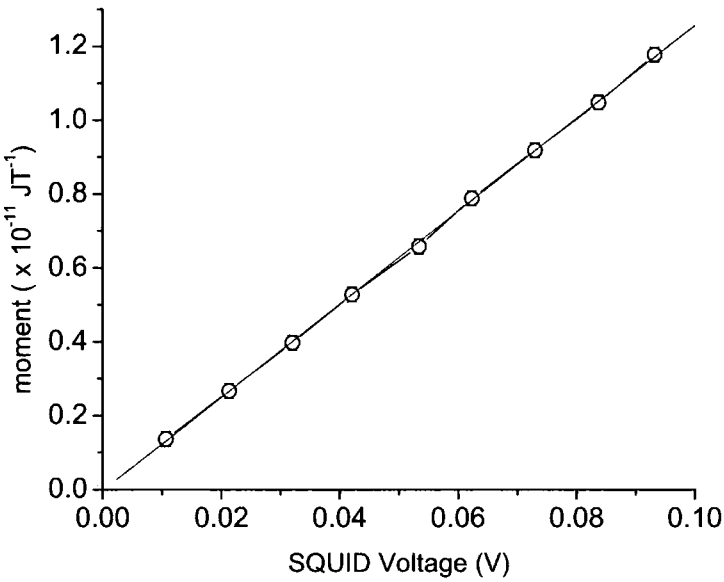

Figure 3.8: Calibration of the Durham SQUID system, the absolute magnetic moment against the change in the SQUID voltage. The response is linear as expected.

up to 0.03 T and then measured in 10 μT) are possible. However this has little effect upon the background and is reproducible. The temperature dependent background is very small, and when glassy systems were field cooled (FC) the sample signal was so strong the background effect was minimal. The graph does however demonstrate an insight into the sensitivity of the system as there is a difference in response depending upon how the system is warmed. The Heliox probe is not designed for sensitive magnetic measurements and there are materials with strongly temperature dependent magnetic responses on the probe. For example, the ^{3}He pot and the sample holder are close to lead-tin solder; this behaviour could explain the background response shown in Fig. 3.9. When comparing the two temperature configurations, the high temperature configuration has a relatively large temperature dependent background, and one plausible explanation for this is the method of warming. In this scenario the 1 K pot exhaust valve is sealed, meaning that any liquid ^{4}He that evaporates is trapped in the exhaust tube. The gas up the tube will have a large temperature gradient, and this will warm parts of the Heliox at the lower end along with

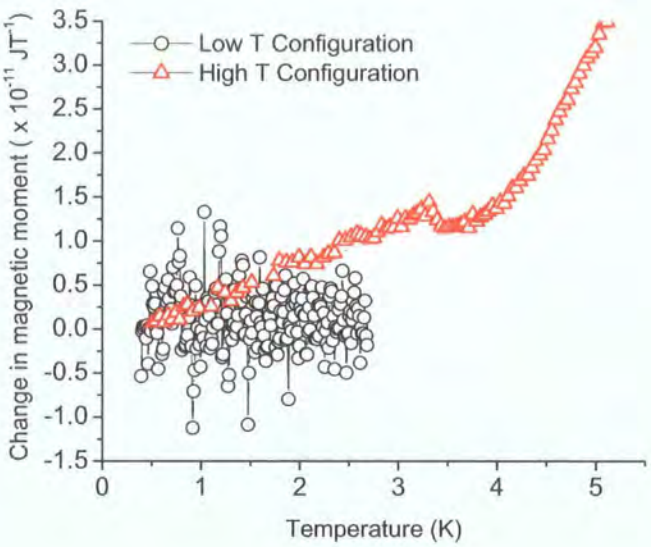

Figure 3.9: Temperature dependent change in the magnetic moment of the background for the temperature regions, 350 mK < T < 2.5 K (low temperature configuration) and 1 K < T < 5 K (high temperature configuration). The measuring field in both cases was 10 μT.

the ^{3}He pot. Therefore if any material undergos a magnetic phase transition because of artificially increasing the temperature of the main body of the Heliox due to the warm exhaust gas, this will be detected by the SQUID. In the low temperature configuration the temperature of the Heliox will be in equilibrium as any gas released by the 1 K pot is quickly removed by the large rotary pump attached to the exhaust. From Fig. 3.9 , it is clear that the change in moment is very small. There is however more noise in the low temperature configuration, this is simply because of the vibrational noise from the rotary pump. The bellows from the pump to the probe did consist of two 20 kg lead dampers. However not all the mechanical coupling could be removed, indicating the importance of isolating the entire system when performing measurements due to its sensitivity. Both mesophonics and grounding determine the base noise level of the Durham SQUID.

3.3 Muon Spin Spectroscopy

The response of the muons to specific magnetic environments has already been described in chapter 2, the basics of muon production and the operation of a basic muon spectrometer will now be discussed. A relatively new instrument known as a Low Energy Muon (LEM) spectrometer will also be discussed in depth, as this allows control of the implantation energy thus enabling depth dependent muon relaxations to be measured.

3.3.1 Muon Facilities

Muon production can only occur at large central facilities where energetic protons are produced by a high energy cyclotron. In this study two proton accelerators and their associated muon beamlines were used, the ISIS (the Egyptian God of light) facility in Oxford and the Paul Scherrer Institute (PSI) in Zurich, Switzerland. In both cases the basics of muon production are similar; a high energy beam of protons impact upon a graphite target producing pions. The pions (π^+) have a half-life of 26 ns and decay into muons (μ^+) which are then focused onto the sample with a combination of quadrapole magnets and electric lenses. There are, however, two distinct types of muon production, surface and decay channels. In the surface scenario the π^+ decays whilst still in the graphite target. The advantage of this type of beam is that it is easy to focus the muon beam, as the resultant muons have a much smaller distribution of energy. In a decay channel the π^+ decays in flight and as such the μ^+ beam has a higher momentum, so the implantation depth into the material is a little deeper. This can be an advantage when considering the effect of surface contributions. Decay channels also have the capability of producing μ^- although they are not required in this particular study. ISIS and PSI cyclotrons also work in a different way. ISIS produces a 50 Hz pulsed source whilst PSI is quasi-continuous. Therefore there are advantages for each facility, for example a pulsed source has a lower background and the time measurement domain can be increased by a factor of 3, whilst a continuous source has a higher frequency range in which to measure and is more susceptible to fast decays. The important properties of the respective muon beamlines between the different facilities used are highlighted in Table. 3.1. In both cases the muon decay is 100 % spin

Beamline properties	ISIS (pulsed beam)	PSI (continuous beam)
Muon production	Surface	Surface and decay
Range	110 mg/cm^2	150 mg/cm^2
Count rate	15 - 25 Mevent/hr	15 - 25 Mevent/hr
Field range	0 - 0.5 T	0 - 5 T
Frequency range	0.1 - 10 MHz	0.1 - 500 MHz
Time resolution	0.3 μs	$\leq$ 0.02 μs

Table 3.1: The beamline properties are identified for each particular muon source used in this study. Careful consideration is required when deciding where to do a particular experiment.

polarised ensuring the relaxation observed is still of great use and interest.

3.3.2 Detecting the Muon Decay

μSR relies upon the weak decay of the μ^+ with a half-life of 2.2 μs of the form,

$$\mu^+ \rightarrow e^+ + \upsilon_e + \overline{\upsilon}_\mu \tag{3.2}$$

where υ_e and $\overline{\upsilon}_\mu$ are the neutrino and anti-neutrino of the electron and muon respectively, e^+ is the positron. It is because of parity violation in the weak interaction that there is an asymmetric distribution of the positron with respect to the spin of the μ^+. To obtain information about the μ^+ spin at the point of decay, the positrons are simply counted. In a muon experiment plastic scintillators surround the sample space and are connected to a photomultiplier tube by a plastic light guide. The specific layout of the detectors are dependent upon the type of muon source identified in section 3.3.1, Fig. 3.10, shows the layout of the scintillators for a continuous beam (PSI). The detector arrangement consists of a forward (F), backward (B), up (U) and down (B) scintillator; this particular arrangement is suitable for LF, ZF, and TF measurements. A magnetic field (B) is applied perpendicular to the beam direction causing a larmor precession of the muons, which will causes positrons to be emitted in all directions. In a typical ZF/LF measurement only the forward and backward detectors will be useful. The results of a typical muon decay will be discussed in section 3.3.3.

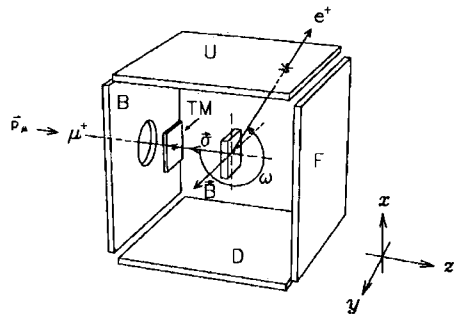

Figure 3.10: The scintillator arrangement for a continuous source the detectors are labeled, forward (F), backward (B), up (U) and down (B). Application of a magnetic field (B) perpendicular to the beam will cause muon precession. TM is the scintillator switch to start the timing of the muon decay[7].

Fig. 3.10, only has four detectors because it is a continuous source, in effect only one muon is in the sample at any time. The detection is triggered by an electronic switch (TM) that registers a μ^+ passing through it starting the clock, a decay is only counted so-long as another muon does not enter the sample. A pulsed source is different as all the muons arrive together in a 80 ns time window 50 times every second, this means more detectors are required so the multiple muon decays can be monitored. ISIS detectors typically consist of 32 scintillators arranged in 4 banks, 2 before and 2 after the sample space. The obvious advantage of this particular arrangement, on top of the reduced background, is that detectors can be removed from the analysis allowing smaller samples to be investigated as the solid angle of the muon beam is decreased.

3.3.3 How to Obtain Data From Muon Relaxation

μSR is only possible because muons have a half life of 2.2 μs. However the question of how the positron emission are turned into useful data remains. The data which are useful in this study is based upon the asymmetry ($a_0(t)$) spectrum, determined from the difference in detection rates between the F and

B detectors. The asymmetry can be defined by,

$$a_0(t) = \frac{N_B(t) - \alpha N_F(t)}{N_B(t) + \alpha N_F(t)} \tag{3.3}$$

where N represents the number of counts of the detector and α is an experimental parameter dependent upon detector efficiency and the position of the sample with respect to the detectors. α can easily be determined by obtaining a fit to transverse field data with no decay for a Ag sample. Ag has a vey small nuclear and electronic spin. α can be calculated from the asymmetry spectrum of Eq. 3.3, assuming oscillation around the time axis. Fig. 3.11a, shows the response over the lifetime of the experiment of one positron detector at a continuous source for a sample of $La_{0.85}Sr_{0.15}CoO_3$, in this case the forward detector in the presence of a transverse field of 0.01 T. The oscillations of the decay over time are clearly visible, which are due to the larmor precession of the muon. Fig. 3.11b, demonstrates the asymmetry spectrum due to both the forward and the backward detector as deduced from Eq. 3.3, for the same TF experiment, the oscillations are clearly visible. $a_0(t)$ is averaged aver all muon sites meaning any variation in the local magnetic field experienced by the muons will be detected. The muons may not process coherently, the larmor precession induced by an external field is technically a summation of the applied field and the internal field of the sample, explaining the sensitivity of muons to their local magnetic environment. Therefore a dephasing of the muons will occur manifesting itself as decay of the oscillatory function, in the asymmetry spectrum. Therefore a relaxation function ($G_z(t)$) is measured which can be neatly described by;

$$G_z(t) = A \exp - (\Delta t)^2 \tag{3.4}$$

where A represents the initial asymmetry, t is time, τ the half-life of the muon decay and Δ the depolarisation rate of the muons. Δ is proportional to the dephasing of the muons and therefore to the local magnetic environment. It is the study of Δ, already discussed in chapter 2, that is of great interest. The above discussion concentrates only upon TF experiments because the muon response is easier to envisage however μSR is unique in that it can be configured in the LF or ZF configuration, which is simply the zero field limit of the LF configuration. All muon data in this thesis was fitted with the Wimda program[6].

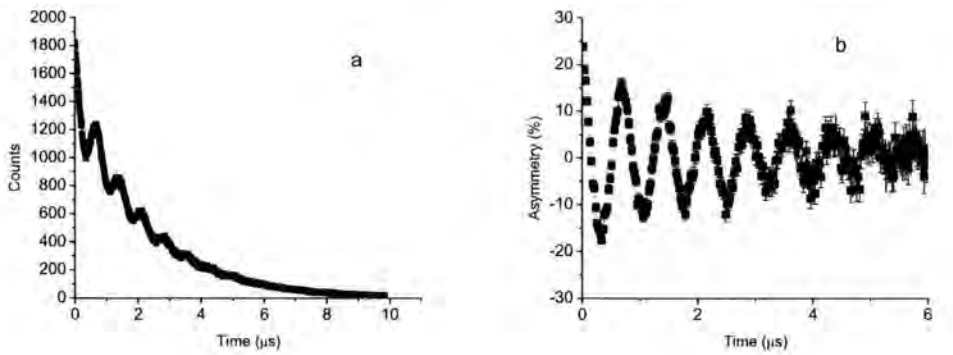

Figure 3.11: Time dependent positron detection for $La_{0.85}Sr_{0.15}CoO_3$. (a) The response of the forward detector to the muon decay in a TF experiment of 0.01 T. (b) A typical asymmetry spectrum denoted by equation 3.3 for the same TF as (a).

3.3.4 Low Energy Muon Spectroscopy

Due to the high momentum of the incoming muons from both surface and decay muon channels (Table. 3.1) μSR detects the bulk properties of materials. This can be a huge advantage as surface properties due to oxidation effects can generally be ignored, the muons having an implantation depth of 0.5 mm (in Al) and a spatial sensitivity of 2 nm. However thin film magnetism has stimulated much work over the past twenty years and μSR is an ideal probe to study the magnetic interactions. There are two possible methods to stop muons in thin films/surface regions, the first simply involves capping the sample with an appropriate layer of silver, as it has a very small valence and nuclear magnetic component but this method is slow and cumbersome. The second method involves slowing the momenta of the incoming muons with a moderator before reaching the sample space. This has the advantage of being able to tune the energy and thus vary the implantation depth. This is known as Low Energy Muon (LEM) spectroscopy.

A LEM beamline has been developed[8] at the PSI in Switzerland over the past ten years, a schematic of the schematic of the apparatus is shown in Fig. 3.12. The instrument is situated upon a surface muon channel with a muon energy at the apparatus entrance of $\sim$ 4 Mev. The first step is to slow the muons

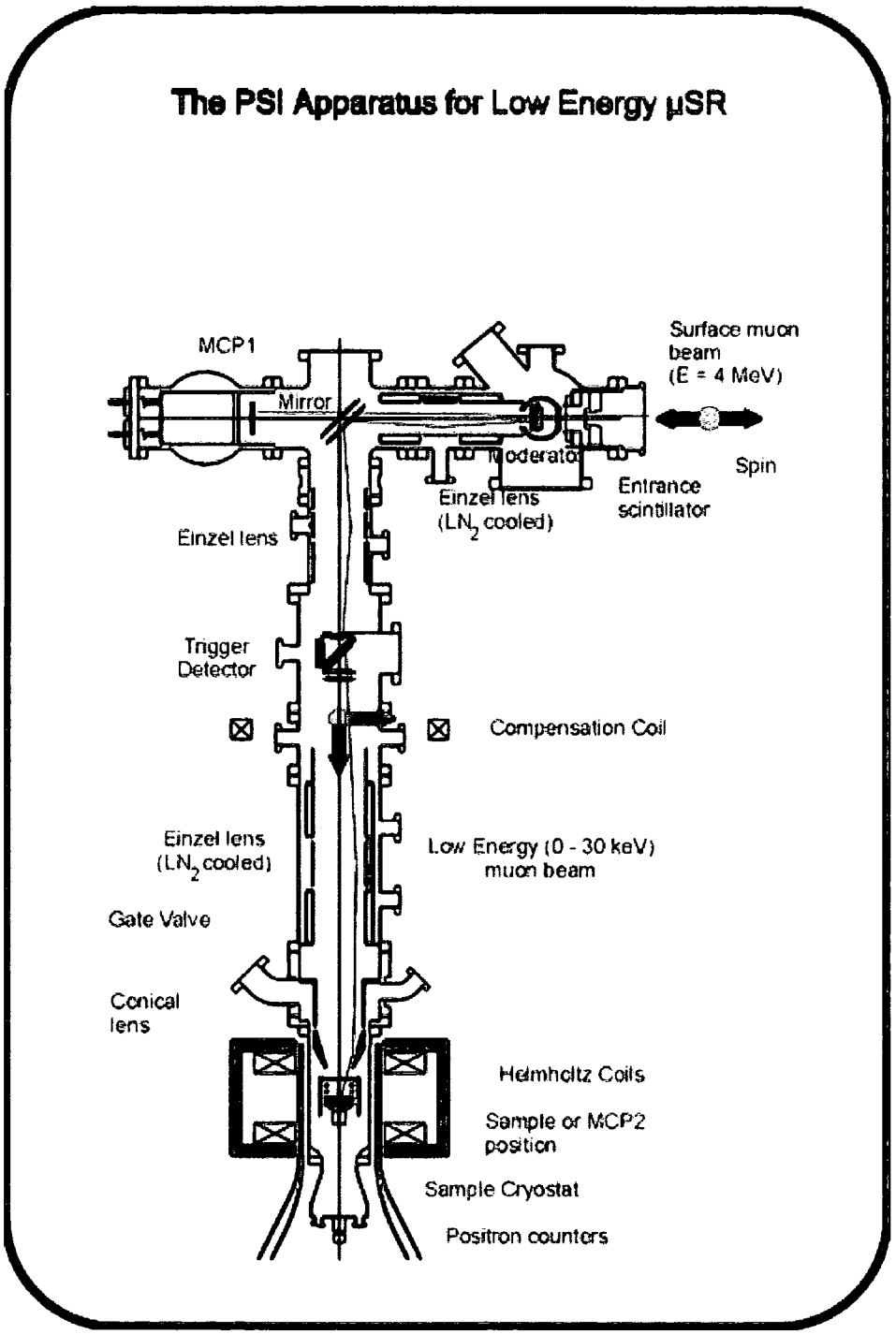

Figure 3.12: The LEM beamline at the PSI. The apparatus enables muons with an incoming energy of $\sim$ 4 Mev to be tuned to have energies between 0.5 and 30 keV[10].

down, this being done by passing the muons through solid Argon condensed (300nm thick) onto a silver substrate. The emerging muons, known as epithermal muons, have an energy of $\sim$ 15 eV and are still 100 % spin polarisied[9]. This is because the moderation process is much quicker than the depolarisation mechanism. The first Einzel lens focusses the muons onto an electrostatic mirror, which deviates the beam direction (but not the muon polarisation) by 90 degrees. The mirror is set so only low energy muons can be deviated into the sample space and high energy muons pass through into the beam dump. A scintillator detector starts the timing mechanism and there is a final lens to tune the energy of the incoming muons. The final tuning stage is carried out with an electric field close to the sample, electric field gradients across the sample are minimised by using thin samples. The implantation energies can be tuned to between 0.5 and 30 keV giving implantation depths between $\sim$ 20 nm and 160 nm, accurate implantation depths are calculated using TRIM:SP[11], a program which calculates ion solid interactions. The entire experiment is performed in ultra high vacuum to prevent scattering of the slow muons. The response of the muons to the sample and external fields is identical to a standard "bulk" muon probe.

References

[1] L. J. van der Pauw, Philips Res. Reports, **13**, 334 (1958)

[2] Quantum-Design, MPMS XL Users Manual (2004)

[3] D. E. Read, Ph. D thesis, University of Durham (2001)

[4] C. S. Roumenin, Handbook of Sensors and Actuators, Elsevier, Amsterdam (1994)

[5] Quantum-Design, SQUID Model 5000 Users Manual (2000)

[6] F. Pratt, Computer Program; Wimbda, Version 1.166: 11/04/05

[7] G. D. Morris, Ph. D thesis, University of British Columbia (1997)

[8] E. Morenzoni, H. Gluckler, T. Prokscha, R. Khasanov, H. Luetkens, M. Birke, E. M. Forgan, Ch. Niedermayer and M. Pleins, Nucl. Instr. and Meth. B, **192**, 254 (2002)

[9] E. Morenzoni, F. Kottmann, D. Maden, B. Matthias, M. Meyberg, T. Prokscha, T. Wutzke and U. Zimmermann, Phys. Rev. Lett. **72**, 2793 (1994)

[10] http://lmu.web.psi.ch/lem/overview.html, accessed 12/01/2005

[11] W. Eckstein, Computer Simulation of Ion-Solid Interactions, Springer, New York (1991)

Chapter 4

Observation of Magnetic Excitons in $LaCoO_3$

This chapter presents the results of extensive magnetic measurements obtained primarily from bulk magnetic susceptibility and muon spin spectroscopy investigations. Initially a brief introduction to the material will describe the progress of other researchers into understanding the fundamental physical properties of $LaCoO_3$, the conclusions of which provided the stimulus behind this particular study. The resulting work presented in this chapter will describe the first unambiguous observation of interacting magnetic excitons in $LaCoO_3$.

4.1 Introduction

Magnetic oxide materials have provided fascinating insights for physicists, producing interesting electrical and magnetic properties as a function of composition. Much work has concentrated upon perovskite manganites as they have produced properties such as giant magnetoresistance, Colossal MagnetoResistance (CMR) and co-incident metal-insulator transitions[1, 2, 3]. Although initial investigations after the discovery of perovskite cobaltites in the 1950s demonstrated interesting electrical and magnetic data[4, 5], comparatively little work has been performed. $LaCoO_3$ is unique among the $LaMO_3$ family (where M is a transition metal element) as it undergoes a thermally driven spin state transition, a detailed discussion of which will be given in section

4.1.1. The material has a distorted perovskite structure which is known to undergo a large thermal expansion[6], coincident with the observed spin state transition. Renewed interest in the material has been spurred on due to the recently discovered CMR effects[7, 8] and magneto-electrical phase separation[9] that occurs when hole doping the material with Sr ions. Specifically this study has been stimulated by the prediction of magneto-electrical phase separation occurring in $LaCoO_3$, because of defect induced magnetism from oxygen non-stoichiometry[10]. The rich phase diagram of $La_{1-x}Sr_xCoO_3$ is underpinned by the sensitivity of the magnetism to the possible spin states of the Co^{3+}/Co^{4+} ions respectively, as shown in Fig. 4.1.

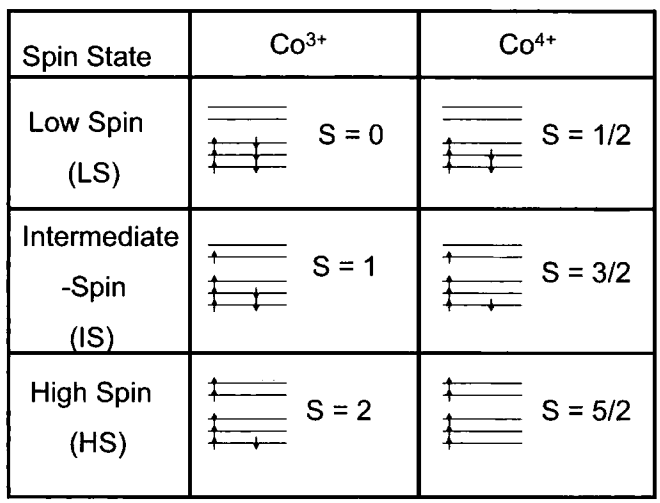

Figure 4.1: The possible spin states of the Co ions in $LaCoO_3$ (Co^{3+}) and $La_{1-x}Sr_xCoO_3$ (Co^{4+} and Co^{3+}).

4.1.1 Thermally Induced Spin Transition

The Co^{3+} excited spin state of $LaCoO_3$ is still a matter of some contention, 50 years after the initial investigation into the material. It is generally agreed that the ground state of the material is a low spin (LS) S = 0 state, $t_{2g}{}^6e_g{}^0$. Upon thermal agitation the material is excited into an intermediate spin (IS) S = 1 state, $t_{2g}{}^5e_g{}^1$, or a high spin (HS) S = 2 state, $t_{2g}{}^4e_g{}^2$; the three spin states can be seen schematically in Fig. 4.1. The excitation can occur because the crystal-field splitting of the *d* levels of the Co^{3+} ions is only slightly

greater than Hund's exchange energy, leading to a situation where a small input of thermal energy ($\sim$ 10 meV) can lead to the occupation of a higher spin state.

Initial work concentrated upon a LS - HS transition[11, 12, 13]. It was expected that if the excited state was in an IS state it would be Jahn-Teller (JT) distorted in a direct analogy to the manganties[1], which show a cooperative JT distortion when one electron of the Mn^{3+} ion occupies the e_g level. However no cooperative JT distortion has ever been observed in $LaCoO_3$. Initial neutron scattering data[14] provided evidence of a temperature dependent magnetic moment upon the Co ion that increases smoothly until 90 K where it saturates. This was inferred as evidence effectively for a LS - HS transition with a 50:50 ratio of LS to HS Co ions. This ratio was required as the net spin on each Co ion, inferred from mass susceptibility measurements, is 1. The excitation into an HS state was predicted along with a rich variation in the Density of States (DOS) around the transition[11]. However subsequent optical conductivity spectra showed no significant change in the DOS around the transition[15].

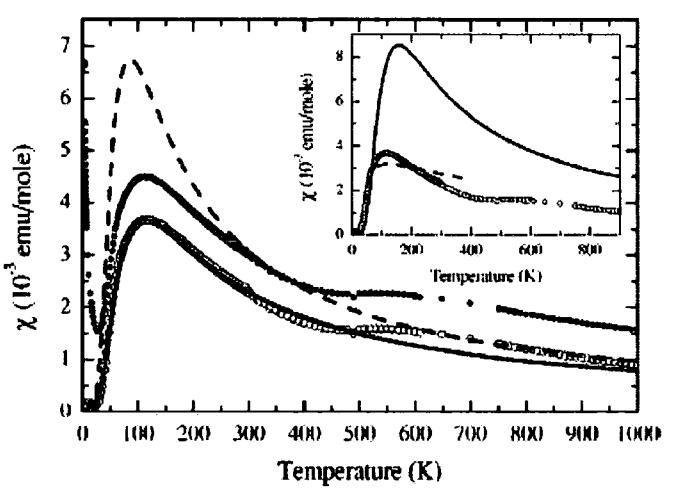

Figure 4.2: Temperature dependent mass susceptibility of $LaCoO_3$ as measured (solid circles) and the mass susceptibility with an impurity contribution removed (hollow circles). The dashed line is a fit to the data with an orbital degeneracy of 3 for a LS-IS transition whilst the solid curve represents an orbital degeneracy of 1. The inset shows the fit to a LS-HS transition. From [6].

The alternative description of the LS-IS transition was initially stimulated by Korotin *et al*[16], where results based upon Local Density Approximation + Hubbard (LDA + U) calculations propose a strong hybridisation between the Co - e_g levels and the O - 2_p levels, with the resulting ground state energy of the IS state lower than occupation into the HS state, leading to orbital ordering. This has lead to a variety of works supporting an LS-IS transition[15, 17, 18, 19]. Perhaps the clearest indication of a LS-IS transition is given by Zobel *et al*[6], who fit their magnetic susceptibility data, shown in Fig. 4.2, assuming a model nonmagnetic ground state and a thermally induced magnetic excited state. The theoretical form of the susceptibility is,

$$\chi(T) = \frac{N_A g^2 \mu_B}{3k_B T} \frac{\upsilon S(S+1)(2S+1)e^{\frac{-\Delta}{T}}}{1+\upsilon(2S+1)e^{\frac{-\Delta}{T}}} \tag{4.1}$$

where N_A is the Avogadro number, μ_B the Bohr magneton and k_B the Boltzmann constant. Δ represents the energy splitting of the LS and excited state, g is the gyromagnetic ratio and υ the orbital degeneracy of the excited state. The work also reports a large thermal expansion of the lattice at $\sim$ 50 K. No change in the specific heat capacity is observed at this transition[20]. The magnetic susceptibility data shown in Fig. 4.2 (filled circles), are typical of $LaCoO_3$ and all works reproduce the major features of this curve. Clearly visible is a cusp around 90 K indicative of the LS to excited spin state transition, along with an inflection at 500 K, believed to be the Insulator to Metal Transition (IMT). Importantly there is also a paramagnetic tail visible; following the Curie law at low temperatures ($<$ 35 K), this tail is visible in all work to date. Equation 4.1 was fitted to the temperature dependent susceptibility only after the paramagnetic tail had been removed from the raw data (hollow circles); the fitting of the data shown in Fig. 4.2 (solid line) allows S and Δ as fitting parameters. The parameter υ is fitted to 1, even though the expected orbital degeneracy of both the IS and HS state is three. The justification for setting the degeneracy to 1 was based upon the existence of a "local" JT distortion as inferred from the peak in the thermal expansion coefficient at 50 K. The comparison for the LS - IS state is shown in the main figure for both orbital degeneracy cases; υ = 1 clearly appears to fit supporting a local distortion around the LS-IS state. A major discrepancy in this fit occurs above the LS-IS transition, the fit un-

dershoots and then overshoots the data. The AntiFerromagnetic (AF) Co^{3+} - Co^{3+} interaction is ignored; the interpretation of the spin transition is still valid but the high temperature data has yet to be accurately fitted. No scenario explaining why the distortion is only local is offered. However HS regions in the bulk (not included in the Zobel fit) could prevent a cooperative effect. The inset shows the fit to an LS-HS transition and the data clearly do not fit when the degeneracy is set to 3. Similar conclusions have been inferred from other work, a local JT distortion being detected using infrared spectroscopy[21], Raman scattering[22] and inferred from orbital ordering using x-rays[23], although no cooperative effect is detected.

4.1.2 Low Temperature Magnetic Tail

The magnetic susceptibility measurements discussed so far have discounted any contribution to the magnetic properties of undoped $LaCoO_3$ from the Curie tail by claiming it is a consequence of either surface ferromagnetic defects, namely Co^{2+}[11, 24], or paramagnetic impurities within the bulk. Although attempts have been made to prove the importance of surface defects, the origin of the tail has not been unambiguously established. Yamaguchi *et al*[25] have fitted the tail to provide evidence for high spin (S=16) magnetic polarons, although no attempt to analyse the effect of the polaron on the high temperature (> 35 K) susceptibility was made. This work is important as it provides evidence for the possibility of HS regions (~3 % of the Co ions) whilst the majority of the Co ions are in an LS state at temperatures < 90 K. Specifically it would prevent any JT distortion being cooperative if the polarons exist up to the spin transition. Nagaev *et al* [10] have also proposed that the paramagnetic centres responsible for the Curie tail are magnetic polarons, although strictly they should be labelled "magnetic excitons", as discussed in chapter 2. In this model localised holes (electrons) bound to cobalt ions or oxygen interstitial (vacancy) sites induce LS to high spin (S=2) transitions in neighbouring Co^{3+} ions, leaving the remaining cobalt ions in the LS ground state. The radius of a magnetic exciton will extend over several unit cells, creating spin clusters of S = 10 - 15 which are dilute within the solid. The creation of the spin clusters is independent of the thermally excited LS-IS transition. Moreover, the

predicted magnetic exciton formation is the precursor for magneto-electronic phase separation at high hole (electron) densities. Tsutsui *et al*[26] predicted the possibility of coexisting Co_2O_{11} clusters intermixed with the LS $LaCoO_3$ matrix majority. Fig. 4.3, shows the possibility of two ferromagnetically coupled Co_2O_{11} clusters connected by one O ion, a doped hole induces a magnetic state not only in the "doped" site but also in neighbouring sites. A net spin of 5/2 is obtained for each cluster; aligning the sites around the doped state may result in a large spin moment of S = 25/2.

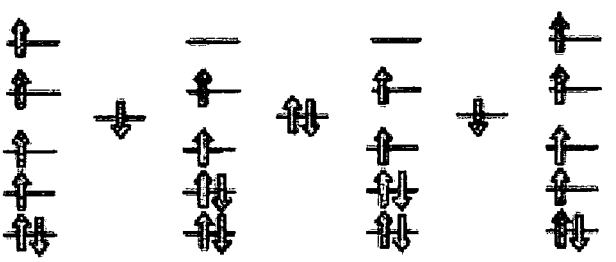

Figure 4.3: Ferromagnetic coupling of two Co_2O_{11} clusters connected by one O ion, from [26].

The predicted magnetic excited state due to oxygen vacancies, which will be known herein as a magnetic exciton, has never been conclusively observed. The aim of this study is to highlight the physical properties of the magnetic excitons and to observe any subsequent effect on the thermally induced spin transition. The nature of a magnetic exciton implies that it may be most easily observed in a system displaying a majority diamagnetic ground state (S = 0), making $LaCoO_3$ an ideal candidate to study such an defect-driven magnetic state.

4.2 Sample Fabrication and Characterisation

Three samples have been prepared for this study, two polycrystalline[27] and one single crystal[28], fabricated by a solid state reaction and floating zone furnace method respectively. Electron probe analysis[29] show that the polycrystalline samples were single phase with grains in the order of 10 μm in diameter. Polycrystalline samples were produced in order to compare and contrast the results

with the single crystal; because of the increased surface area of the grains they must act to emphasise any magnetic surface effect. The oxygen stoichiometry, obtained from titration experiments for each sample is shown in Table 4.1, showing the possibility of oxygen vacancies present in each sample. The typical concentration of paramagnetic impurities in the sample was obtained by inductively coupled plasma mass spectroscopy. The maximum concentration from a paramagnetic ion was 65 parts per million for Mg, corresponding to an impurity level of 0.0065 %. The corresponding defect induced magnetism from oxygen vacancies, which has a larger moment inferred from theoretical predictions[10, 26], has an impurity level of at least 0.7 %. Therefore it is likely that any extra contribution to the susceptibility of the LS state in $LaCoO_3$ is as a consequence of defect induced magnetism, or a ferromagnetic surface contribution[11].

Sample	Formula Unit
Polycrystal (*a*)	$LaCoO_{2.96\pm0.05}$
Polycrystal (*b*)	$LaCoO_{2.97\pm0.02}$
Single Crystal	$LaCoO_{2.98\pm0.02}$

Table 4.1: The formula unit of each sample studied is given; there is a clear indication of oxygen vacancies present in each sample.

4.2.1 Initial Magnetic Characterisation

As the study is primarily concerned with the Curie tail, and any subsequent effect of the tail on the bulk magnetism of $LaCoO_3$, it is essential to prove unambiguously that the data reported in the literature can be reproduced. Fig. 4.4 demonstrates the temperature dependent magnetic susceptibility, in a measuring field of 5 T for each sample. The diamagnetic susceptibility per unit mass (χ_{Dia}) has been subtracted from the data. Calculations reveal a value of - 3.8 x 10^{-8} m^3kg^{-1} using the Langevin result, which can be described by,

$$\chi_{Dia} = -\frac{\mu_0 N Z e^2}{6m} \left\langle r^2 \right\rangle \tag{4.2}$$

where N is the number of atoms per unit mass, Z is the number of electrons,

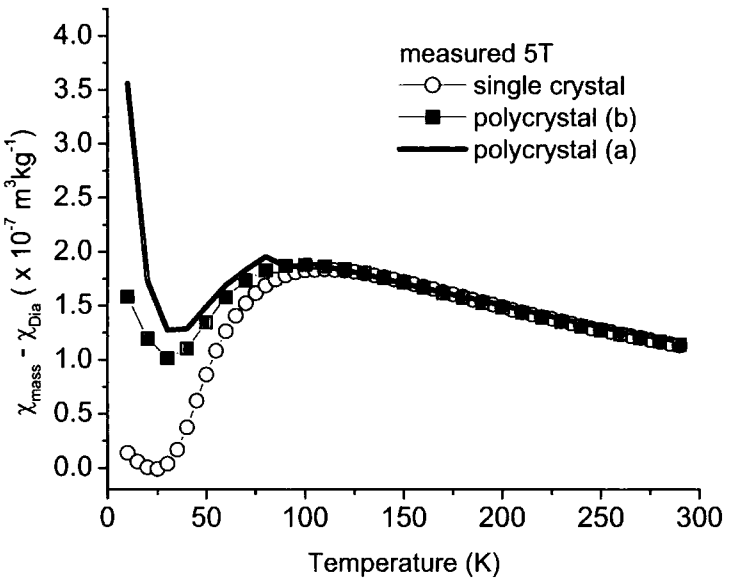

Figure 4.4: Temperature dependent magnetic susceptibility of each of the $LaCoO_3$ samples measured with an external field of 5T. The response of the Curie tail is clearly different for each sample.

μ_0 the permeability of free space, e and m the charge and mass of the electron respectively. The mean square radius of the electron orbit, $\langle r^2 \rangle$, has been calculated using the density functional theory and will be discussed further in section 4.3.3. The general shape of the curves are in agreement with published data. For a direct comparison refer to Fig. 4.2.

Fig. 4.4, shows an increase in the susceptibility in all samples examined at low temperatures, which is identified as the Curie tail. It is clear that the paramagnetic contribution increases as the composition deviates further from the ideal formula unit. The tail contribution, which has never been fully understood, leads to difficulty in comparing the data directly. To enable a fit to equation 4.1, a generic background subtraction will yield different data to fit to for each sample. This can clearly be seen in Fig. 4.4. There are two possible explanations for the increased susceptibility of the tail. Either there is a surface impurity contribution meaning that there is an increase in the susceptibility

with respect to the net surface area, or it is a bulk defect induced contribution from the predicted magnetic excitons[10]. It is unlikely that the surface contribution is the main cause of the Curie tail since the two polycrystalline samples used in this study have different susceptibilities, even though they have nominally the same grain size. Therefore the data can be inferred as evidence for exciton behaviour, as the tail becomes more dominant because the number of excitons increases in agreement with the change in formula unit. Although not conclusive it demonstrates the importance and sensitivity of the generally neglected paramagnetic tail.

4.3 Muon Spin Spectroscopy

Muon spectroscopy measurements were utilised due to their sensitivity as a local magnetic probe[30]. Specifically in cobaltite, implanted muons will be sensitive to dilute magnetic moments in an essentially diamagnetic matrix when the majority of the Co^{3+} ions are in a low spin state below $\sim$ 90 K. The results presented in this section are split into bulk μSR measurements and low energy μSR measurements as identified in chapter 3. Any magnetic contribution from the surface or the bulk can be differentiated. Measurements have been performed on both the single crystal sample and the polycrystalline sample *b*. To date the μSR technique has not been used to observe a pure LS (where S = 0) to IS transition, where the contribution to the muon relaxation is from one source, the valence electrons of the cobalt ions. Previous measurements have concentrated upon Spin-Peierls[31, 32] or Spin Crossover[33, 34] materials.

4.3.1 Muon Implantation Site

Due to the sensitivity of the muon to its local magnetic environment, knowledge of the stopping site is essential to allow full interpretation of the data. A muon *could* implant itself close to the nucleus and detect the magnetic response of the nuclear field, and only a weak contribution from the supposedly strongly magnetic valence electrons. Standard techniques of obtaining the muon implantation site have relied primarily upon electronic dipole calculations, however this will give no information upon the probability of site occupation, only

that a muon can sit in a certain position. Preliminary investigations have been performed using Density Functional Theory (DFT) in an attempt to resolve this problem. DFT can map out all possible implantation sites along with the respective ground state energy for each position and map out the perturbations of the electron density due to the implanted muons. This discussion will report on the initial results which suggest that DFT calculations are able accurately to predict the muon position. This is not a comprehensive review of muon implantation studies or theoretical DFT considerations, it is merely a proof of concept highlighting a new investigative tool.

In very simple terms, DFT allows an N-body Schrödinger equation to be written in terms of N 1-body Schrödinger equations, in terms of the charge density. Each operator can be expressed as single particle states, allowing modern computational techniques to solve many electron problems. Specifically the Schrödinger equation for each noninteracting particle moving under the influence of an effective potential ($V_{(r)}$) can be written in the form,

$$\left\{-\frac{\hbar}{2m}\nabla^2 + V(r)\right\}\psi_i(r) = \varepsilon_i\psi_i(r). \tag{4.3}$$

$V_{(r)}$ is chosen so that the equation can be solved. The charge density ($n(r)$) can be obtained and is of the form,

$$n(r) = \sum_{i=1}^{N} \psi_i^*(r)\psi_i(r). \tag{4.4}$$

The solution of the above equations leads directly to the energetic and electronic charge density of the ground state of the system. The commercial DFT package CASTEP[35] has been used to perform the calculations, with a muon being simulated by an electron with a mass of 200 x m_e and a positive charge.

4.3.2 Confirming the Capability of DFT to Predict the Muon Implantation Site

To confirm the accuracy of the muon implantation position in $LaCoO_3$ it is necessary to reproduce the results of known muon implantation sites in other materials. There are very few investigations comparing and contrasting various

muon sites in a specific sample; one result of relevance is the muon relaxation in Gd. Dension *et al*[36] performed zero field temperature dependent muon spin relaxation measurements on Gd, the results of which are shown in Fig. 4.5a. Once the moments on the Gd atoms order, the muons begin to precess. However below T_c the behaviour is somewhat complicated; the depolarisation rate and the initial asymmetry remain constant over the entire temperature range. From T_c until 230 K, the moments lie along the c axis, and as the temperature is lowered, the angle with respect to the c axis, gradually changes until it is at an angle of 30^o at 0 K as shown in Fig. 4.5b. This effect cannot explain the temperature dependence of the internal field.

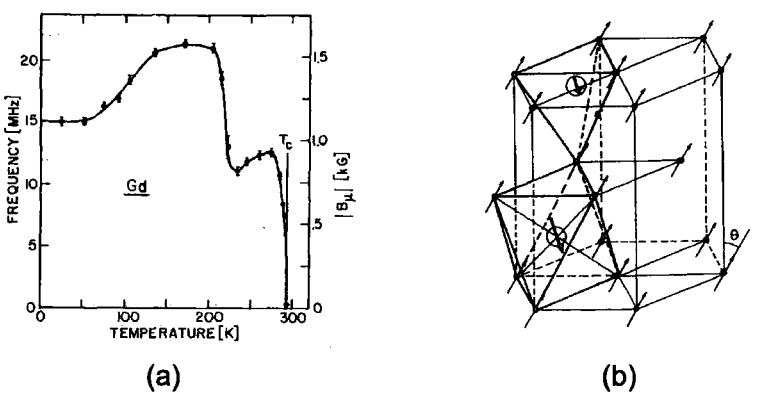

Figure 4.5: a. The temperature dependence of the local internal field in Gd. b. Gd moments at 0 K along with two possible muon implantation sites at a octahedral and tetrahedral site. From [36].

Fig. 4.5b demonstrates the possible position of two muon implantation sites, an octahedral and tetrahedral site. Denison *et al*[36] predicted the form of Fig. 4.5a by calculating that the muon will feel a contribution from the saturating moment, the magnetic dipolar contribution and a hyperfine field contribution, concluding that the only possible way to explain the data in Fig. 4.5a is to assume the muons occupy an octahedral site. CASTEP calculations reveal that the energy of an implanted muon is -18281.920 eV at the octahedral site and -18279.21 at the tetrahedral site, concluding in agreement, that an implanted muon has a lower energy if it occupies the octahedral site.

4.3.3 Calculating the Muon Implantation Site in $LaCoO_3$

Before considering the possible muon implantation sites it is necessary to study the structure of $LaCoO_3$. If DFT calculations cannot reproduce the crystal structure and electronic ground state then it will not be possible to calculate a muon site. The crystal structure of $LaCoO_3$ has been found to be a distorted perovskite structure, spacegroup $R\bar{3}c$, the lattice parameters as a function of temperature are shown in Table 4.2.

Temperature (K)	a (Å)	c (Å)
5	5.42625(5)	12.991(1)
50	5.427841(6)	12.999(1)
100	5.43317(5)	13.022(2)
300	5.44864(3)	13.1035(2)

Table 4.2: Temperature dependence of the lattice parameters for $LaCoO_3$. From[37].

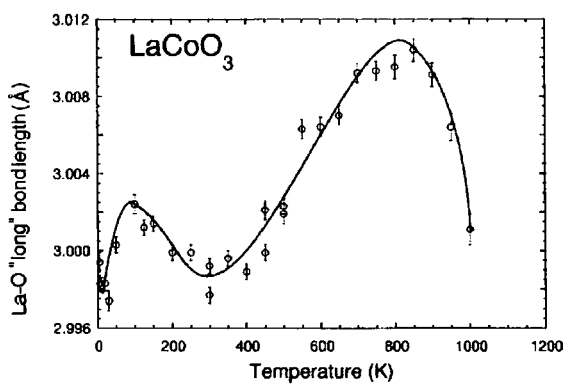

Figure 4.6: Temperature dependence of the "long" La-O bond length in $LaCoO_3$, obtained using neutron diffraction. From[37].

Radaelli *et al*[37] have measured the La-O "long" bond as a function of temperature with neutron diffraction. The results are shown in Fig. 4.6, which clearly indicates that the material is undergoing an expansion between $\sim$ 50 K - 100 K, in agreement with the thermal expansion work of Zobel *et al*[6]. The DFT calculations performed have assumed that the material is in an LS state at 0 K. Although it is possible to expand the work to investigate the relative ground states of the Co ion spin state, this is beyond the scope of this particular

calculation. Initial DFT calculations allow a minimisation of the energy when the lattice parameters from Table 4.2 are utilised, and thus calculations should be able to find the ground state once a muon has been implanted.

The results of the DFT calculations for the muon implantation are shown in Table 4.3, and correspond to a 1x1x2 "supercell" to enable an accurate minimisation of the energies. Thus the fractional co-ordinates are not for one unit cell. Ideally the energy of the implanted muon will minimise at an interstitial site. As can be seen in Table 4.3, two possible interstitial sites exist with similar energies. Fig. 4.7 shows the two possible interstitial sites. It is clear that these sites are symmetrical around an oxygen site. To ensure the implanted muon is at the true ground state various other starting positions of the implanted muon were considered; every calculation results in a finishing position at an interstitial site unless the muon is prevented from moving. This case is also considered in Table 4.3; a muon was pinned around an oxygen ion, the resulting energy is higher than the relative interstitial sites. Thus the muon implantation site can be determined to be an interstitial site, and as such will be susceptible to the magnetic contribution from the Co valence electrons.

Final fractional co-ords, (a b c)	site	minimised energy (eV)
0.405, 0.463, 0.530	interstitial	-19430.7
0.317, 0.343, 0.643	interstitial	-19431.1
0.317, 0.343, 0.643	oxygen atom	-19401.9

Table 4.3: Three possible muon implantation sites show their final ground state energy, the muon clearly resides at an interstitial site.

Figure 4.7: Two possible interstitial sites are shown in a $LaCoO_3$ "supercell". The Co ions are represented by the blue spheres, La by the turquoise spheres, O by the red spheres and muons by the white spheres.

4.3.4 Bulk μSR

Bulk Muon Spin Rotation and Relaxation (μSR) experiments were performed at the PSI in Switzerland upon the instrument Dolly. This is a surface decay channel, meaning the incoming muons (4 MeV) have a bulk implantation depth of approximately 0.5 mm[38]. Any measured relaxation will be sampling the bulk of the material. Initial investigations will concentrate upon the single crystal, as surface effects will be negligible due to the thickness of the sample (4 mm). The muon implantation site has been confirmed in section 4.3.3 to be at an interstitial site, corresponding to a neutral position away from the atoms, and meaning that any nuclear spin component will be dominated by the valence electron contribution from cobalt ions. Note that the muons will be influenced by the behaviour of more than one cobalt ion.

Initial experiments were performed in a transverse field (TF) of 10 mT. The

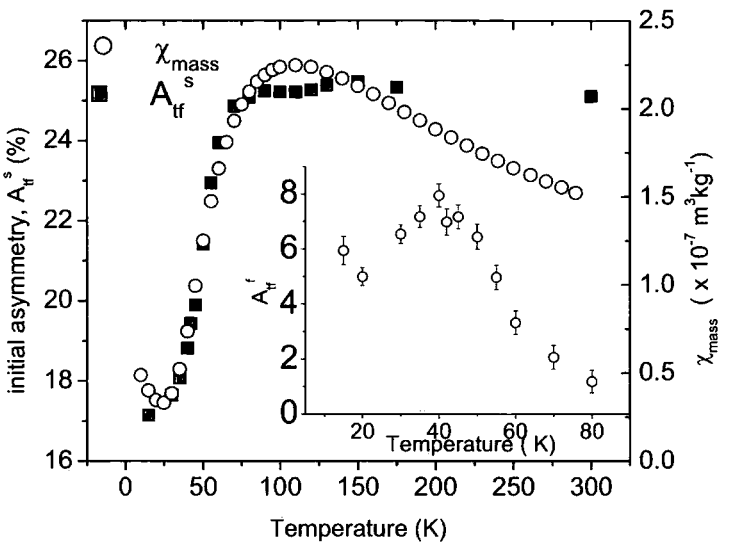

Figure 4.8: The temperature dependence of the initial asymmetry, A^s_{tf} of the TF μSR is shown, along with the mass susceptibility measured at 5 T of the single crystal. The LS-IS spin transition is clearly visible. The inset shows the temperature dependence of the initial asymmetry of the fast component, A^f_{tf}.

data were fitted over the entire temperature range using a relaxation function of the form:

$$G_x(t) = A^s_{tf} \exp(-[\lambda^s_{tf} t]^2) \cos(2\pi \upsilon_\mu t) + A^f_{tf} \exp(-[\sigma^f_{tf} t]^2) + A_{bg} \qquad (4.5)$$

where A^s_{tf}, A^f_{tf} and A_{bg} are the respective initial asymmetries of, the oscillatory, gaussian and background components, and s and f are for slow and fast relaxing components. λ^s_{tf} and σ^f_{tf} are the depolarisation rates for the two separate decays and υ_μ is the muon precession frequency, which is dependent upon the externally applied field; no other function was required to fit the TF data. The gaussian relaxation should have an oscillatory component. However, for this experiment no oscillating component was observed due to the very fast relaxation that does exist, and as such it is out of the muon time window. The temperature dependence of the fitting parameters A^s_{tf}, A^f_{tf}, λ^s_{tf} and σ^f_{tf} are shown in Figs. 4.8 and 4.9. Above 90 K, only the first term in equation 4.5 is required to fit the muon spin relaxation data; below 90 K both terms in equation 4.5 are required. The initial asymmetry (A^s_{tf}) of the oscillating decay shows evidence for a

strong dephasing upon reducing temperature (Fig. 4.8), coincident with the LS-IS transition as demonstrated by the 5 T Field Cooled (FC) and measured, mass susceptibility also shown in Fig. 4.8. Appendix A demonstrates the raw data of the TF experiments along with a comparison of the respective fits to obtain accurate fitting parameters.

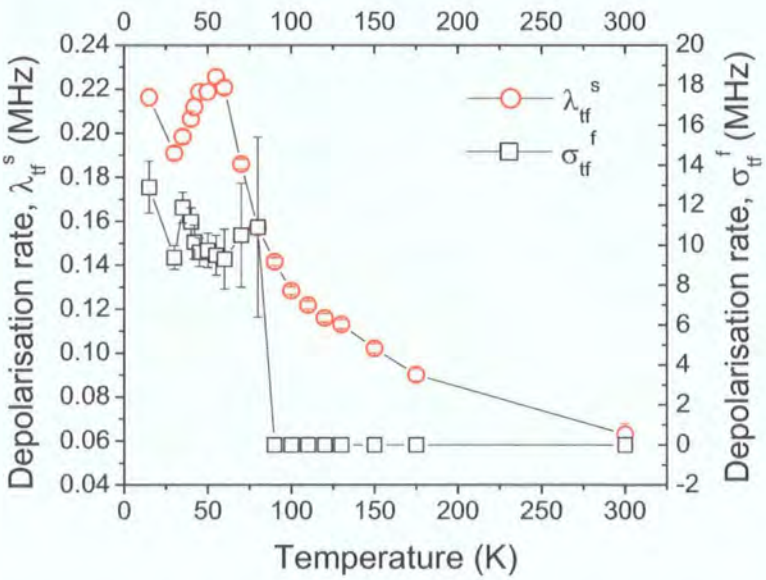

Figure 4.9: Temperature dependence of the depolarisation (λ_{tf}^{s}) rate of the TF data, showing clear evidence for a magnetic ordering at 50K in the LS state. A gaussian (σ_{tf}^{f}) contribution is apparent below 90K. The lines are a guide for the eye.

The drop in the initial asymmetry with decreasing temperature is accompanied by the appearance of the second gaussian component, σ_{tf}^{f} of the muon spin relaxation as illustrated in Fig. 4.9. This suggests that the LS-IS transition is observed in A_{tf}^{f} (inset of Fig. 4.8) because a fraction of the muons are now relaxing in a magnetic region of the material that only exists when the material enters the LS state. Also shown in Fig. 4.9 is the depolarisation rate λ_{tf}^{s} as a function of temperature. The peak in λ_{tf}^{s} indicates magnetic ordering at 50 K, below the LS-IS transition. Previous measurements have revealed that the thermal expansion coefficient increases dramatically around 50 K[6], although the heat capacity[20] does not show a similar evolution. The change in expansion

coefficient was interpreted as evidence for a thermally induced spin transition within the Co *d*-levels. This is an unlikely cause of the observed peak in λ_{tf}^{s} as any effect of thermal expansion would also be observed in σ_{tf}^{f}.

To clarify the origin of the observed magnetic ordering Zero Field (ZF) μSR, measurements were performed at temperatures representative of the three different magnetic regimes of this material; (*i*) above the 90 K spin state transition, (*ii*) near the magnetic ordering transition at 55 K and, (*iii*) in the "paramagnetic tail" at 35 K. The raw data are shown in Fig. 4.10 and a clear change in the initial asymmetry is seen to take place upon reducing temperature. The muon spin relaxation curves were fitted with a function of the form,

$$G_z(t) = A_{zf}^{s} \exp(-[\lambda_{zf}^{s} t]^{\beta}) + A_{zf}^{f} \exp(-[\sigma_{zf}^{f} t]^{2}) + A_{bg} \tag{4.6}$$

which represents a superposition of gaussian and stretched exponential relaxations. Here A represents the initial asymmetries of the relative relaxations, σ_{zf}^{f} is the depolarisation rate for the gaussian relaxation, and λ_{zf}^{s} represents the depolarisation for the stretched exponential, where β is the exponent. Appendix A again shows the comparison of the raw data with the respective fits for the ZF data; it also shows the temperature dependence of the initial asymmetry (A_{zf}^{s}) for the zero field experiment, reproducing the behaviour of Fig. 4.8.

When in the IS phase (*i*), where the majority of Co^{3+} ions have a spin state of 1, the relaxation is fitted best with the first term of equation 4.6, with $\beta = 2$, i.e. a gaussian relaxation. Around 55 K in the LS state (*ii*) the data is again best fitted with only the stretched exponential function, but now with $\beta = 0.5$, indicative of a dilute spin system with a single relaxation time τ[39]. A depolarization rate that tracks the TF data is also found, with a 50 K peak at 0.52 MHz, demonstrated later in the chapter. The inclusion of the extra gaussian component in $G_z(t)$ is only relevant when the first component indicates ordering and the paramagnetic tail in the magnetic susceptibility becomes dominant in the temperature region below 50 K (*iii*). This can clearly be seen in the inset of Fig. 4.10, where the temperature dependence of the depolarization rate of the muons, σ_{zf}^{f} (from the fast relaxation term in equation 4.6), shows a sharp

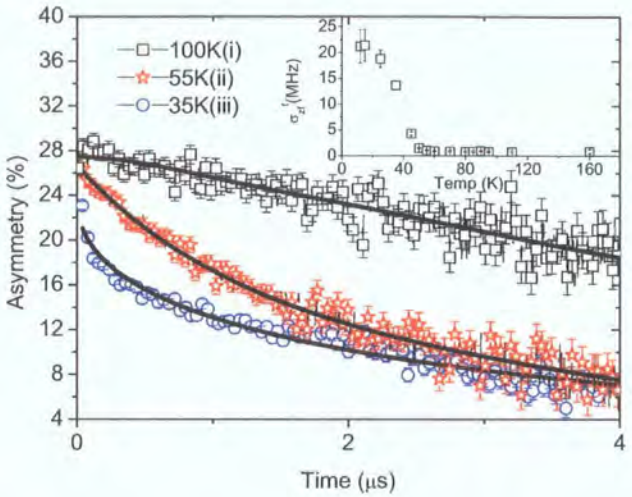

Figure 4.10: ZF μSR data is shown at 100K, 55K and 35K, representing the different magnetic regions, along with the fits to the the data. The inset shows the gaussian relaxation (σ_{zf}^{f}), which begins at 45K in the paramagnetic tail.

increase at 45 K. Longitudinal fields up to 0.5 T have been applied at 35 K and 55 K, and for both temperatures the relaxation was not fully decoupled, which is an indication of dynamic random local fields. Fig. 4.11 shows the relaxation at 35 K, 55 K and 100 K for the square root of the time scale; again the change in form is clear with only the 55 K rate decaying linearly against $\sqrt{t}$, although there is a slight deviation at low t. The fits to the data are also shown.

Oxygen non-stoichiometry is the dominant source of bulk defects in $LaCoO_3$, and are likely to effect the magnetism through the formation of magnetic excitons [10]. In this scenario, once the Co ions start relaxing into their LS state an exciton can form if an oxygen vacancy is contained in the unit cell and the neighbouring Co ions are also in a LS state, as the exciton formation will induce a HS state in these ions. The formation of excitons appears to occur under two distinct processes. The excitons can interact, either with other excitons or with the matrix in which it is imbedded, leading to high susceptibility large spin regions and possibly magnetic remanence. Such a model could explain the two separate relaxations observed by the TF μSR measurement (Fig. 4.9), showing an ordering approaching 50 K, a consequence of the excitons interacting

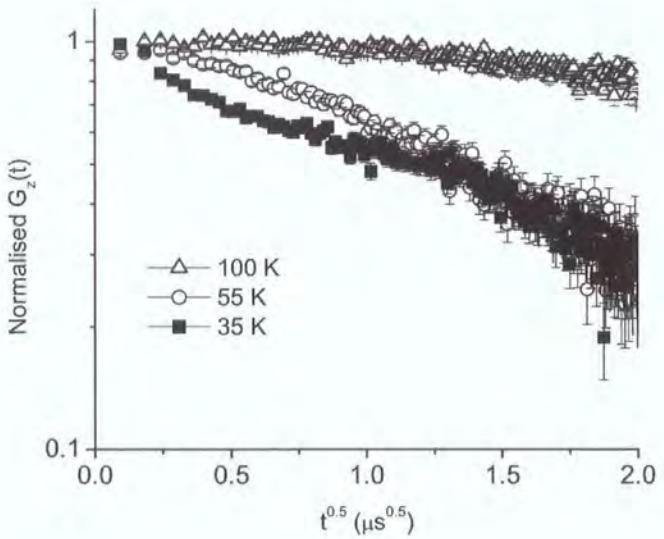

Figure 4.11: Normalized ZF μSR data is shown at 100K, 55K and 35K, representing the different magnetic regions. There is a clear indication of root exponential behaviour at 55K.

with the IS matrix, and another stable component indicative of exciton clusters that are polarised by the external field.

The ZF μSR experiment is able to distinguish between the two scenarios due to the difference in field distribution. It can be shown that[39],

$$\lambda = \pi c^2 \gamma_\mu < \Delta B^2 > \tau \tag{4.7}$$

where ΔB is the width of field distribution, τ the correlation time, γ_μ the gyromagnetic ratio of the muon and c is the fraction of the ions in a non-zero spin state for a dilute system. The stretched exponential function (slow component, λ_{zf}^{s}) has a maximum as the field distribution peaks due to the excitons interacting with the IS matrix. However, the exciton-exciton interacting species are expected to decouple as their fluctuation time becomes large with respect to the muon time window. This scenario can be given further credence when considering the relaxation of the fast component when a field is applied. The field distribution (depolarisation rate) decreases with increasing field for both the 10 mT and 25 mT (reduces to 6 MHz, see appendix A) data. These indepen-

dent relaxations are indistinguishable above 50 K in the ZF configuration. The observation of the possible exciton interactions are only possible because of the LS state of $LaCoO_3$ below 90 K. Moreover the separate relaxations suggest a temperature dependent relationship of the exciton formations and interactions.

4.3.5 The Effect of the Measuring Field on μSR

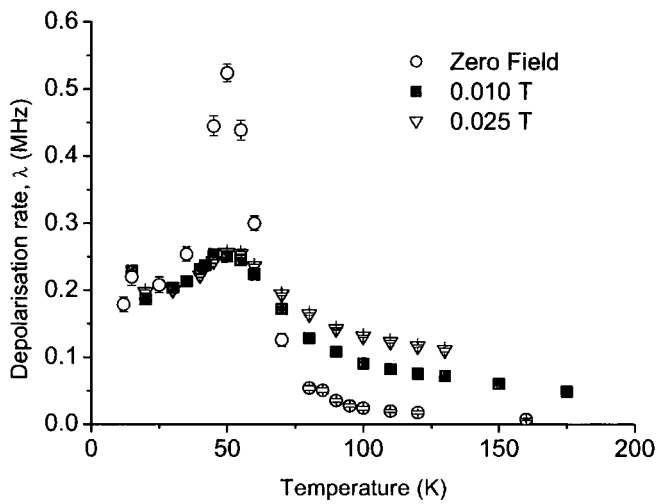

Figure 4.12: The temperature dependent depolarisation rates as a function of field. The applied fields were 0 T, 0.01 T and 0.025 T.

Discussions so far have concerned the identification of a defect driven impurity state in the LS region. According to Yamaguchi *et al*[25] the magnetic polarons (excitons) become the dominant susceptibility below 35 K. However no onset of remanence in the excitons is predicted and the effect of the exciton formation on the $LaCoO_3$ pure matrix background is neglected. Excitons have been shown to contribute to the μSR, there being two distinct apparent formations. Firstly there is a high temperature exciton - IS matrix interaction and secondly a high spin exciton - exciton interaction at low temperatures, which form because the majority of the matrix falls into a LS state, and thus the probability of exciton formation increases (inferred directly from equation 4.1).

It is difficult to differentiate between non interacting Co^{3+} ions in the IS state

and magnetic excitons, as both would contribute a paramagnetic component when the temperature is increased. However, if there is any interaction between the IS matrix and the excitons at high temperatures (> 50 K) then this interaction may be field dependent if there is a local frustrated component at the interface between the HS exciton and the IS matrix. Field dependent μSR measurements on the single crystal have been performed, at 0 T, 0.01 T and 0.025 T, the field being applied in the transverse field configuration. Fig. 4.12 demonstrates the temperature dependence of the depolarisation rates as a function of field, where the data were obtained from equations 4.5 and 4.6 depending upon whether or not a field was applied during the measurement. The zero field data show a temperature dependent depolarisation rate larger than that of the field dependent measurements. This appears to support the scenario that the 50 K peak is in fact simply the temperature at which the exciton - exciton interaction becomes dominant in the diamagnetic matrix, suggesting magnetic order as such has not been observed but simply that there is a temperature dependent contribution to the magnetism which begins to dominate the μSR below 100 K. No evidence of any glassy transition below 50 K is observed for the ZF data, since the expected Kubo-Toyabe relaxations in the data, as identified in chapter 2, were not observed[39].

Fig. 4.13 demonstrates that the field dependent depolarisation follows a simple Arrhenius thermal activation law of the form $\lambda = \lambda_0 \exp^{\frac{E_A}{k_b T}}$ above 50 K for all measured fields. Above 50 K any exciton formation is likely to be surrounded by IS matrix. Any interaction between a HS and IS Co ion is probably antiferromagnetic[11], leading to possible magnetic frustration on a "local" level. The high temperature tail of the field dependent depolarisation rates do not scale. This is unexpected as the paramagnetic IS Co ions should have a field distribution independent of applied field[40]. This directly implies that the effect of the excitons interacting with the IS matrix is field dependent. As the measuring field is increased so does the internal field distribution (λ_0), but the activation energy decreases. No Knight shift of the muons was observed, indicating that this is not the reason for the increase in depolarisation rate.

This exciton - IS matrix interaction appears to occur at temperatures well

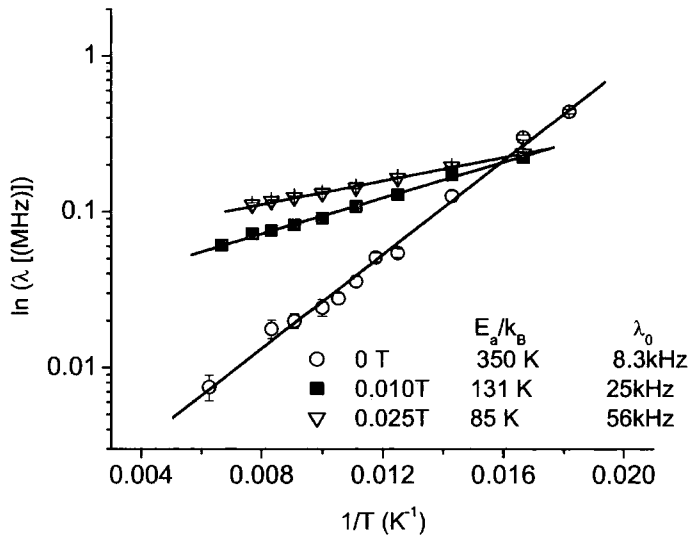

Figure 4.13: Natural log of the depolarisation rates as a function of reciprocal temperature. The activation energies of the depolarisation rates are shown; there is a decrease in the activation energy with increasing field.

above 90 K. Sadly the temperature dependence was examined in detail only below a maximum of 170 K for all experiments, therefore it is not possible to observe the actual temperature at which the excitons begin interacting with the matrix. However the Arrhenius behaviour is not applicable at 300 K. This temperature was used as a calibration test before cooling. This would suggest that the exciton - IS matrix interaction is temperature dependent. It is known (see section 4.4.4) that $LaCoO_3$ has a local antiferromagnetic interaction below 220 K. The field distribution may increase as the field increases because there is a competing interaction between the exciton and the surrounding IS matrix which is attempting to locally align itself antiferromagnetically. However the activation energy is reduced because of the local alignment of the exciton with the surrounding IS matrix. This scenario is shown schematically in Fig. 4.14.

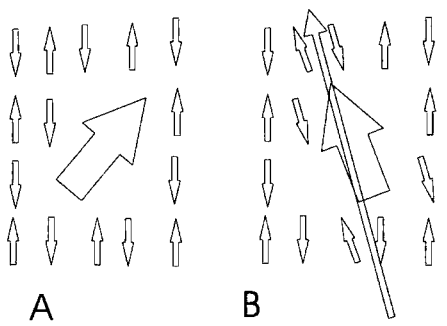

Figure 4.14: Schematic of the exciton (large arrow) IS matrix (small arrows) interface, with (B) and without (A) an applied field.

4.3.6 Low Energy Muon Results: A Depth Profile

The identity of the defects dominating the bulk implantation μSR may be the same as those responsible for the well known Curie tail, i.e. magnetic excitons. However it is necessary to rule out any possible surface contribution to the magnetism, as proposed by Goodenough *et al*[9]. To address this issue the muon spin depolarisation rates were investigated as a function of depth (20

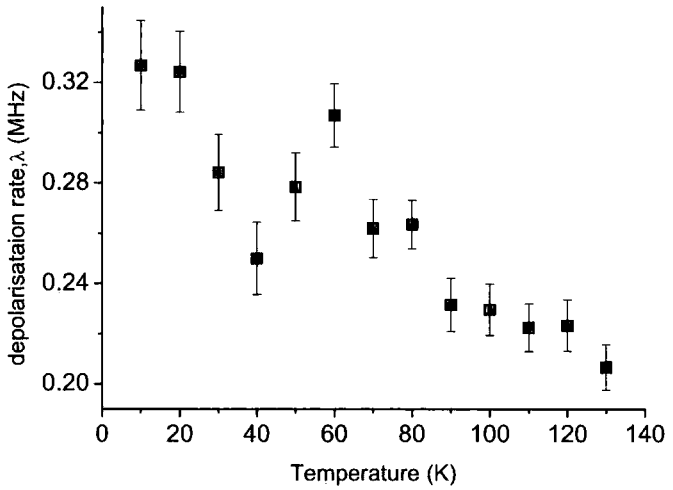

Figure 4.15: The depolarisation rate (λ) as a function of temperature at an implantation depth of 50 nm, for the TF measurement at 10 mT.

nm to 160 nm), with the LEM beamline at PSI (the beamline is described

in chapter 3). The object of this work was to distinguish between bulk and surface contributions to the μSR. A large diameter polycrystalline sample (*b*) was used because of the greatly reduced muon flux at the LEM beamline. The goal of the work was to reproduce the single crystal μSR results, where the implantation depth is 0.5 mm, in order to confirm that the observed magnetic ordering observed in section 4.3.4 is a property of the bulk and not a surface contribution. The 10 mT TF bulk μSR data was reproduced at a depth of 50 nm; the data could be fitted with the oscillatory term only in equation 4.5. Although the gaussian could be fitted to show the same trends as the single crystal, the extra gaussian terms contribution to the relaxation is marginal, due to the much reduced statistics on the LEM beamline.

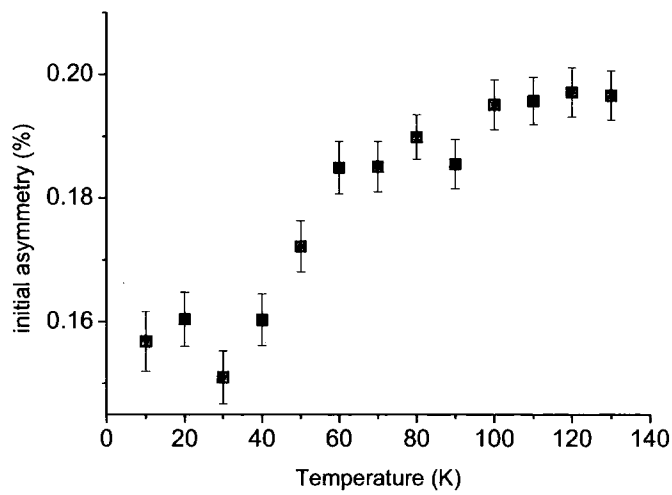

Figure 4.16: The temperature dependent initial asymmetry, at a penetration depth of 50 nm and in a TF of 10 mT.

A feature of the LEM beamline is the reduced flux. As time on such an experiment is at a premium it is often not possible to obtain the desired counting statistics. Appendix A gives an example of the raw LEM data compared to the bulk data. The depolarisation rate (λ) is shown in Fig. 4.15; again a peak in the depolarisation rate is observed at $\sim$ 50 K. The net increase of the depolarisation rate (compared to Fig. 4.12) is a consequence of the large electric field present around the sample, which is there to fine tune the muon energy, and a

general increase of $\sim$ 0.03 MHz is expected. The temperature dependence of the initial asymmetry is shown in Fig. 4.16. The gross change in asymmetry is smaller than the bulk behaviour seen in Fig. 4.8, though the net change in both cases is similar, with both the bulk and LEM asymmetries dropping by $\sim$ 30 %, coincident with the LS - IS transition.

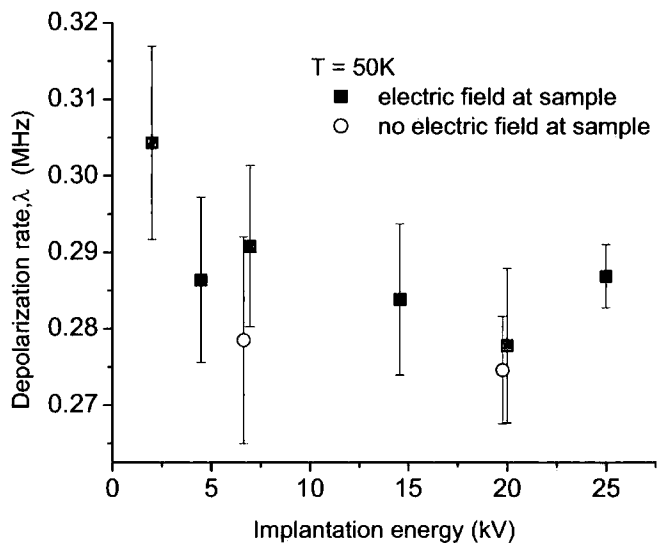

Figure 4.17: The depth profile (energy scan) of the depolarisation rate at 50 K, comparison of the rates with and without the "tuning" electric field is shown at the appropriate experimental energies for comparison.

Depth profiles were then performed at temperatures of 20 K, 50 K and 130 K. The results at 50 K are shown in Fig. 4.17. The figure shows that the depolarisation rate at various depths remains constant (within the error bars) over the entire depth range. The constant depolarisation rate is a feature of all the temperatures investigated, implying that the surface behaves in the same way as the bulk. Also shown is the effect of altering the energy of the incoming muons with the electric field at various points along the LEM apparatus as identified in chapter 3. The lowest muon energies are only available by applying a large electric field at the sample and the moderator. However the higher energies can be achieved by applying a field only at the moderator. There is an overlap region to examine the effect of the electric field at the sample plate, specifically

in this case at 7.5 and 20 kV. There is a small change as expected[41], but this will simply account for the difference between the bulk and LEM depolarisation rate as already mentioned. Thus the sample properties are not affected by applying a large electric field so close to the surface.

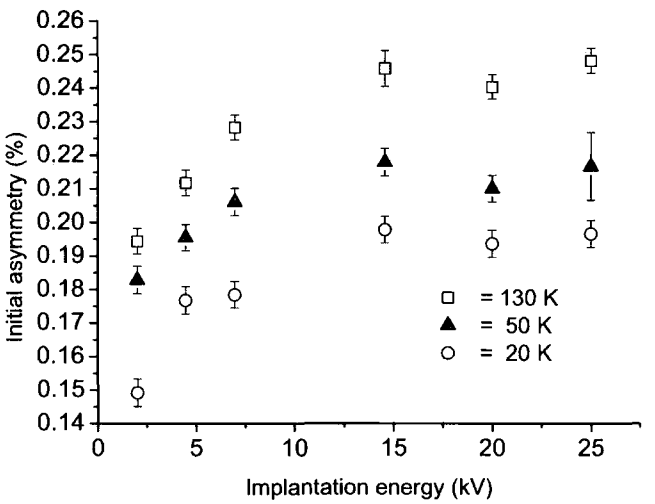

Figure 4.18: The energy dependent change in the initial asymmetry is shown for the three temperatures investigated.

Fig. 4.18 shows the initial asymmetries for the energy scans at 20 K, 50 K and 130 K. The difference between 15 kV and 2.5kV can be partially explained by the reflection probabilities at low energies[41]. Given the density of the material an asymmetry drop of approximately 10 percent is expected simply due to muon reflection, however, the drop at all temperatures is over 20 %. One possible explanation is that an increase in the reflection probability is due to some surface-related magnetic contribution although this appears to have no impact on the bulk magnetic properties of the material, as the asymmetry drop is temperature independent. The exact nature of the asymmetry drop requires further investigation. By directly comparing the absolute initial asymmetry values, the relative drop in asymmetry with temperature is in agreement with Figs. 4.16 and 4.8.

4.4 Bulk Magnetic Measurements

The field dependent μSR measurements described in section 4.3.5 suggest that the measuring field affects the local magnetic properties of the bulk $LaCoO_3$, specifically suggesting the occurrence of more than one possible magnetic species of magnetic exciton, leading to competing magnetic interactions. The discussion below will outline measurements primarily performed upon the single crystal sample, in an attempt to observe related properties with a magnetometer. Both the polycrystalline samples produce similar behaviour and examples will be given where necessary to outline that the same physical processes occur in all samples investigated.

4.4.1 High Temperature Magnetic Susceptibility Measurements

D.c magnetic susceptibility data of the single crystal have already been shown in Fig. 4.4. Those measurements, made at 5 T, reproduce earlier results reported in the literature [25, 29] and demonstrate both the LS-IS transition upon warming, and a Curie tail. This is reproduced in Fig. 4.19 (open squares). Also shown is a fit to the 5 T measured data by equation 4.1 as described by Zobel *et al*[6], confirming the existence of a LS-IS transition (as opposed to a LS-HS transition). Table 4.4 shows the comparison of the fitting parameters from the single crystal sample compared directly to that of Zobel *et al*[6]. The energy gap between the LS and the IS spin state is found to be about 15 meV.

Fitting Parameter	Zobel sample	Single crystal sample
g	2.1	2.2
S	1	1
v	1	1
Δ	180 K	180 K

Table 4.4: A comparison of the fitting parameters obtained from equation 4.1, for the single crystal sample and that of Zobel *et al*[6].

Thus by employing the same measurement protocol as others, the published data can be reproduced with the single crystal sample, and very similar fitting

parameters are obtained when considering both the polycrystalline samples (Δ changes to 175 K). A careful examination of the data shows that the high temperature data does not fit. No antiferromagnetic Co^{3+} interaction has been included in the fit parameters. Significantly, the published magnetic data have always been taken with a large measuring field, typically 1 T or 5 T, consequently any weak saturating component or magnetic defect related features have been swamped by the bulk response to this high measuring field. A much lower measuring field of 1 mT (Fig. 4.19) produces a dramatically different temperature dependent mass susceptibility. This initial measurement shows evidence for a saturating component around 50 K, with the large paramagnetic Curie-like dependence dominating below 35 K. Importantly once the IS spin transition has been achieved above 90 K the field dependent susceptibilities once again overlap. Taking these features to be related to exciton formation (see section 4.1.2) we suggest that the excitons become dominant once the majority of the Co ions are in the LS state. In the IS state the magnetic response of the excitons appears to be swamped. Specifically there appear to be two additional components to the magnetisation in agreement with the μSR work. The excitons have three possible interactions; (*i*) an exciton - exciton interaction, this will be labeled interaction 1. (*ii*) an exciton - IS matrix interaction, labeled interaction 2A and (*iii*) an exciton - IS matrix - exciton interaction, labeled interaction 2B.

A further investigation of the saturating component, observed in Fig. 4.19 below 90 K, has been made with a different measurement protocol, involving field cooling the samples to 50 K in various applied magnetic fields, and then cooling from 50 K to the base temperature in the remnant field, typically 100 μT. The resulting susceptibility was recorded upon warming in the remnant field. This cooling protocol was designed to align the saturating component of the susceptibility (i.e to align the excitons interacting with the IS matrix). The above assumes that the saturating component is a consequence of the exciton - IS matrix interactions (either interaction 2A or 2B), as indicated by the μSR measurements in section 4.3.5. The paramagnetic tail, which consists of high spin paramagnetic excitons and the Co ions in the $LaCoO_3$ matrix, will not contribute to any remnant component. The results are shown in Fig 4.20

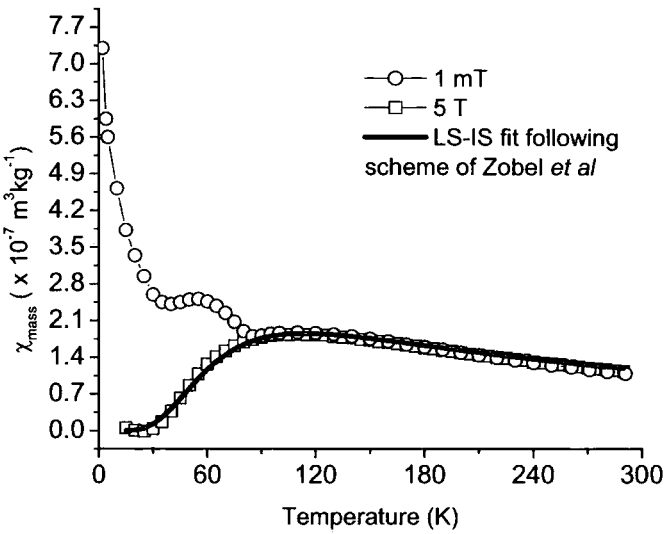

Figure 4.19: Temperature dependent magnetic susceptibility at the measuring fields 1 mT and 5 T along with a fit to the 5 T data as initially demonstrated by Zobel *et al*[6].

for cooling to 50 K in fields of 10 mT, 25 mT, 50 mT and 100 mT. Clearly the sample is showing remnant and saturating behaviour (with respect to both field and temperature), with no change in the magnetic moment being detected above a cooling field of 50 mT. Note that the mass magnetisation of this extra magnetic component is very small and is easily swamped by the paramagnetic Curie tail at modest measuring fields, this is inferred directly from Fig. 4.19. No previous results have ever observed a remnant component of the magnetisation. The thermally induced LS-IS transition cannot directly account for the remnant behaviour[6] and suggests that bulk defect-induced magnetism to be the cause.

Fig. 4.20 appears to provide evidence of remanence in the magnetic exciton - IS matrix interaction (2A or 2B); this will be discussed further in section 4.4.2. At high enough densities these may magnetically percolate in a direct analogy to the Sr hole doped cobaltites (see chapter 5) as predicted by Nagaev *et al*[10]. The fact there are at least two separate magnetic contributions from the magnetic excitons can be supported by looking for a magnetic cluster

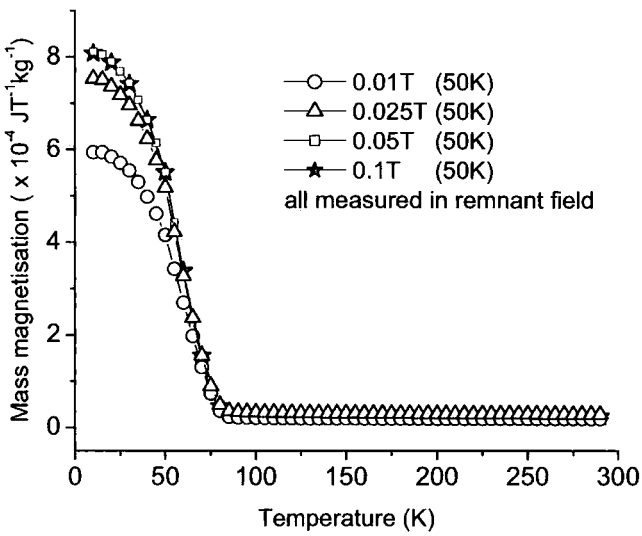

Figure 4.20: Remnant component of the mass magnetisation as a function of temperature. $LaCoO_3$ was cooled in various magnetic fields until 50K and then cooled and measured in the remnant field, with saturation occurring at 50 mT. A clear sign of remanence in the LS region is observed and provides evidence for saturating magnetic exciton behaviour.

type behaviour related to the exciton - exciton interaction (1). One simple procedure used to describe magnetic cluster behaviour is to examine the difference between 300 K Field Cooled (FC) and Zero Field Cooled (ZFC) experiments[42]. Fig. 4.21 shows the temperature dependent magnetic susceptibility as a function of field for FC (solid) and ZFC (hollow) data. There is a clear deviation below 85 K between the FC and ZFC data. As the field is increased the observed shoulder (also present in the 1 mT data) becomes suppressed. Although previously observed[24, 43] the origin of this shoulder has never been discussed. It appears that above 50 mT there is little difference between the FC and ZFC data, suggesting that at high fields one simply will not be able to view directly the magnetic exciton - exciton interactions in magnetic susceptibility measurements, as the exciton "clusters" will simply be saturated.

The bulk susceptibility supports the muon results depicted in section 4.3.4; a bulk defect induced magnetic component is detected. Moreover the observation

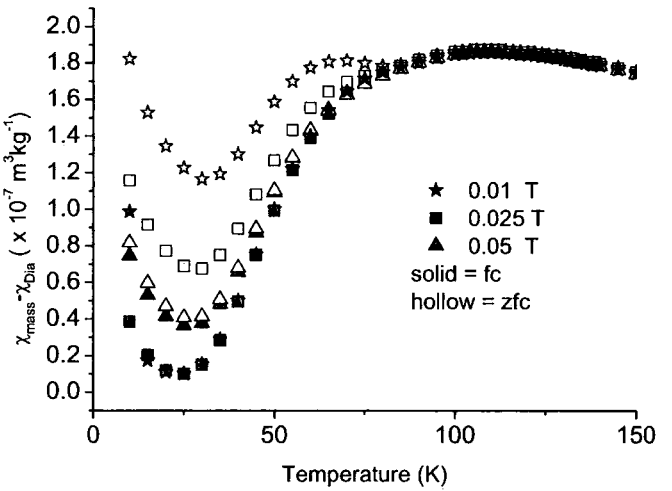

Figure 4.21: Temperature dependent magnetic susceptibility for FC and ZFC measurements. Data were taken at the field stated in the figure.

of the exciton is measuring field dependent and there appear to be at least two forms of the excitons, high spin interacting excitons that cluster and excitons that interact with the matrix.

4.4.2 How and Where do the Magnetic Excitons Form?

The existence of a remnant magnetic phase in an essentially non-magnetic region has clearly been established. The measurements infer that there are essentially two "species" of magnetic excitons; excitons that interact with the IS matrix, and those that interact directly with each other. These two distinct processes will yield different temperature dependent contributions to the magnetic susceptibility, however it is the origin of the remnant component that requires clarification. If the remnant component were due to an internal anisotropy of the excitons there would not be a paramagnetic tail associated with the low temperature measurements (as they too would saturate), therefore it would suggest the remnant component observed in Fig. 4.20, is from the exciton - IS matrix interactions, either 2A or 2B. However μSR indicates that the interaction exists above the 90 K spin transition, as the field dependent thermally activated behaviour exists up to 170 K (see Fig. 4.13).

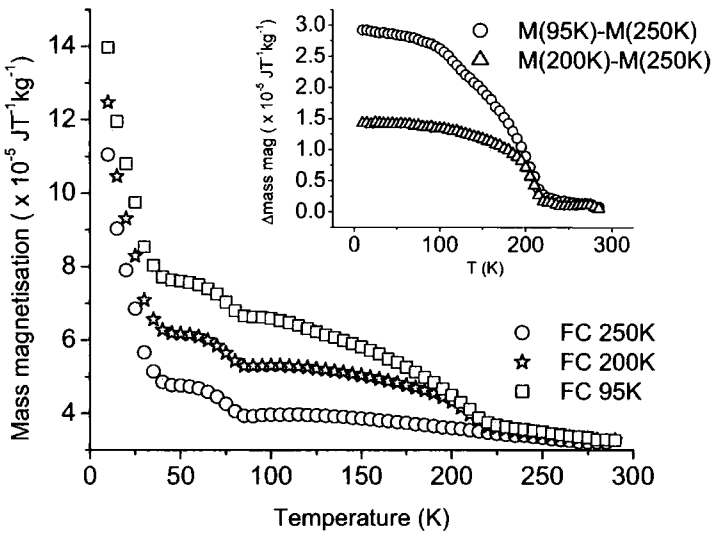

Figure 4.22: Temperature dependent mass magnetisation (M) after FC in 50 mT until just above and below θ (220 K). In all cases the sample was measured in the remnant field. The inset shows the temperature dependence subtraction between the mass magnetisations with and without remanence at high temperatures (220 K).

One simple conclusion is that the excitons can only exist if the total energy of the system is decreased by their presence. Specifically this can be easily envisaged when considering the exciton - IS matrix interaction, ie. those contributing to the remnant magnetic behaviour. $LaCoO_3$ is known to have strong Co^{3+} - Co^{3+} AF interactions with a $\theta \sim$ -220 K[29, 11], calculated from inverse magnetic susceptibility measurements; a detailed discussion of this result will occur in section 4.4.4. Essentially an exciton with remnant behaviour can only occur if it interacts with its local environment, this can also be inferred from the bulk μSR measurements in section 4.3.5. For an exciton to have magnetic anisotropy and therefore remanence, $LaCoO_3$ must be below 220 K, as the local AF interactions of the Co ions can then interact with the excitons. The energy of the system will then be lowered by the mixing of magnetic phases, an interaction between an exciton and the AF matrix. Fig. 4.20 indicates that no interacting excitons exist above the spin transition. However the sample was cooled until

50 K; at this temperature most of the matrix is in an LS state, therefore exciton formation is at its most abundant, but there are fewer IS Co ions. This reasoning suggests that remnant behaviour should exist to higher temperatures.

Fig. 4.22 shows the results of field cooling $LaCoO_3$ to just above θ and then cooling in the remnant field and measuring upon heating, along with when the sample was cooled to 200K and 95 K before the cooling field was switched off. There is a high temperature (90 K > T > 220 K) remnant component to the mass magnetisation when field cooled to below θ, indicating the importance of the local AF interactions. Fig. 4.22 also shows the temperature dependence of the difference between the remnant mass magnetisation and the non-remnant magnetisation. This demonstrates that the lower the temperature the sample is cooled to the more remanence there is up to 220 K. This suggests that the behaviour is linked to, the number of excitons and their local interaction with the AF matrix. Fig. 4.20 shows no such remanence up to 220 K after field cooling until 50 K, however it can been shown that if $LaCoO_3$ is cooled until 60 K and then cooled and measured in the remnant field remanence is shown up to 220 K (see Appendix A). There are two different remnant components (50 K and up to 220 K) that must originate from different magnetic species, otherwise their remanence would disappear at the same temperature. An exciton forms if there is an oxygen vacancy surrounded by LS Co ions[10]. In the high temperature region (T > 100 K) only a few excitons will exist because the vast majority of the matrix is in an IS state. This also implies that once the exciton forms it will interact with the IS matrix (interaction 2A). As the temperature is decreased the exciton formation will increase exponentially (from equation 4.1) and there is more chance of excitons having interactions mediated by the IS matrix (interaction 2B). The remanence observed in Fig. 4.20 occurs up to 75 K, as the probability of interaction 2B occurring begins as soon as the LS state is entered. Interaction 2A can still occur until 60 K, however 50 K is the limit because this is where the most excitons will form, interaction 2B will dominant. Note Fig. 4.22 still measures the paramagnetic tail and the 50 K remanence, this is because true zero field experiments cannot be performed. Experimental constraints dictate that magnetic excitons are only visible when they interact with the matrix below 220 K or when they become dominant because of the LS

state in $LaCoO_3$ below 50 K.

The excitons can therefore form when the surrounding Co ions are in a LS region, this can occur at any temperature! However they are only visible when they interact with the matrix below 220 K or become dominant because of the LS state in $LaCoO_3$ below 50 K.

4.4.3 Behaviour of the Polycrystalline Samples

The interpretation of results thus far has primarily been based upon data from the single crystal. μSR has identified similarities between the polycrystalline sample (*b*) and the single crystal sample, however as yet no bulk magnetic comparison has been made. The formula unit has already been discussed in section 4.2; this shows deviation away from oxygen stoichiometry for the polycrystalline samples. Further deviation from the formula unit would emphasise the contribution from the more abundant excitons, and this is clearly demonstrated in Fig. 4.4. However, the field dependence of the Curie tail (shown in Fig. 4.19) should be reproducible with both the polycrystalline samples. Fig. 4.23, shows the temperature dependent magnetic susceptibility of polycrystal *a* after FC from 300 K in 1 mT in an attempt to reproduce the single crystal behaviour. The tail shows an increase in susceptibility at low temperatures of a factor of $\sim$ 10, indicating the increased number of excitons present in the material due to the increased oxygen vacancy density. There is, however, a change in slope around the 50 K mark indicating the presence of remnant excitons.

To prevent repetition of section 4.4.1, representative data from each polycrystalline sample is shown. The data for polycrystal *b* is demonstrated to reproduce the remnant behaviour in $LaCoO_3$ in the LS region. The same field cooling protocol to 50 K is used as in Fig. 4.20, although a maximum field of only 50 mT is applied. Fig. 4.24 shows the temperature dependence of *b* after field cooling until 50 K and then cooling and measuring in the remnant field. There is clearly a remnant component to the magnetisation in the LS state. The remnant mass magnetisation is also larger due to the increased number of excitons.

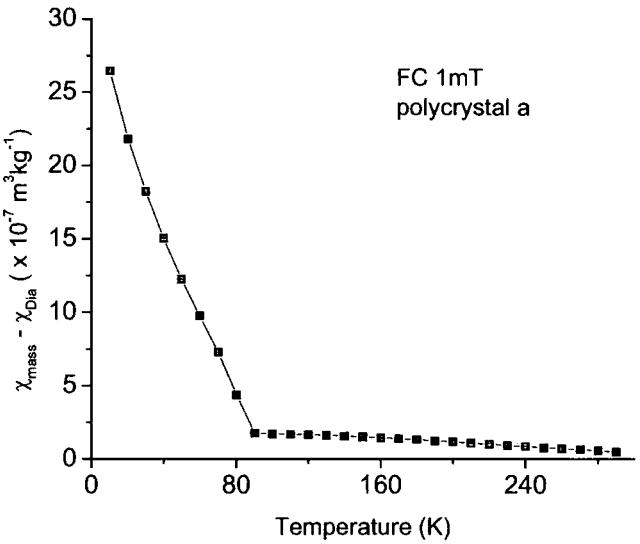

Figure 4.23: Temperature dependent magnetic susceptibility for polycrystal *a* measured in external field of 1 mT.

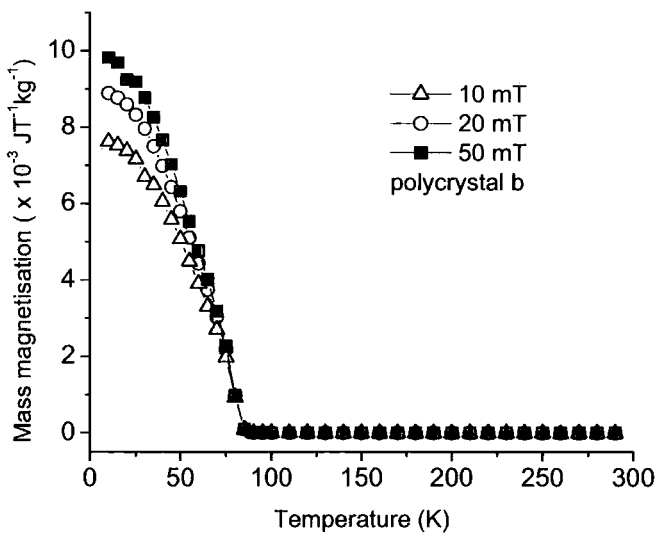

Figure 4.24: Temperature dependent magnetisation of polycrystal *b* measured in the remnant field of the magnet after FC in fields up to 50 mT until 50 K, as in Fig. 4.20.

In conclusion the major features of the single crystal work can be reproduced with both polycrystalline samples, although the deviation from the formula unit does make the interacting excitons harder to see because of the dominant paramagnetic excitons occurring at low temperatures.

4.4.4 Field Dependent Magnetisation Measurements

Temperature dependent field sweeps are now examined in an attempt to observe an ordering of the exciton - exciton interaction (1) at low temperatures (T < 50 K) due to their increased density, and to observe any effect of the exciton - IS matrix interaction (2A and 2B) that will only occur when the matrix attempts to order at $\sim$ - 220 K[11, 29, 25], as suggested by the Curie-Weiss temperature calculated from inverse susceptibility measurements (even though no work has observed AF ordering).

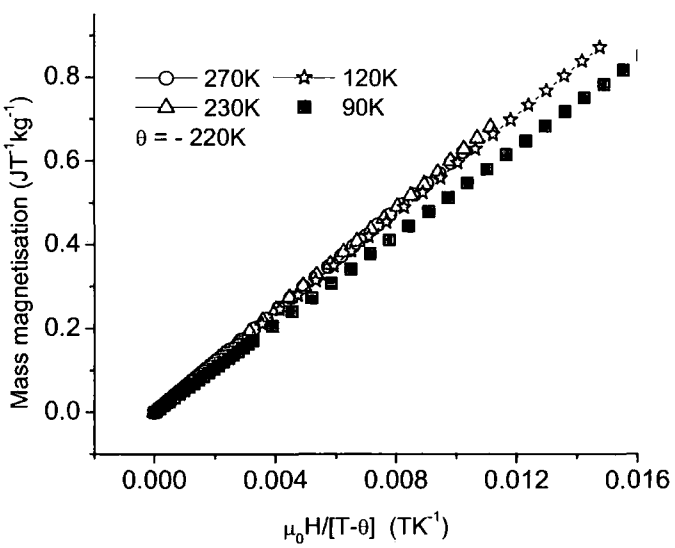

Figure 4.25: Mass magnetisation curves for $LaCoO_3$ up to 5 T, demonstrating scaling behavior from 120 K - 270 K.

Figs. 4.25 and 4.26 show the magnetic response of $LaCoO_3$ as a function of applied magnetic field for different temperatures. All measurements were performed up to a maximum field of 5 T in an attempt to observe behaviour

described by a Curie-Weiss function. Fig. 4.25 demonstrates the high temperature regime from 90 K (the spin state transition) up to 270 K. The data only scale if a Curie-Weiss (θ) temperature is included in the analysis; in this case a value of -220 K was required. The data scale even below θ, but it begins to deviate once the sample enters the LS region, which begins around 90 K. The continued fitting of the data below the θ parameter in Fig. 4.25 is no great surprise considering that three dimensional ordering may be somewhat difficult to achieve as some Co ions are relaxing into a LS state. Indeed it is not unknown for the magnitude of θ/T_N to be as large as 5[46], when next nearest neighbour interactions and possible sublattice arrangements are taken into account. Once below $\sim$ 90 K the data no longer scales as the proportion of Co ions in the LS state increases exponentially, inferred from equation 4.1.

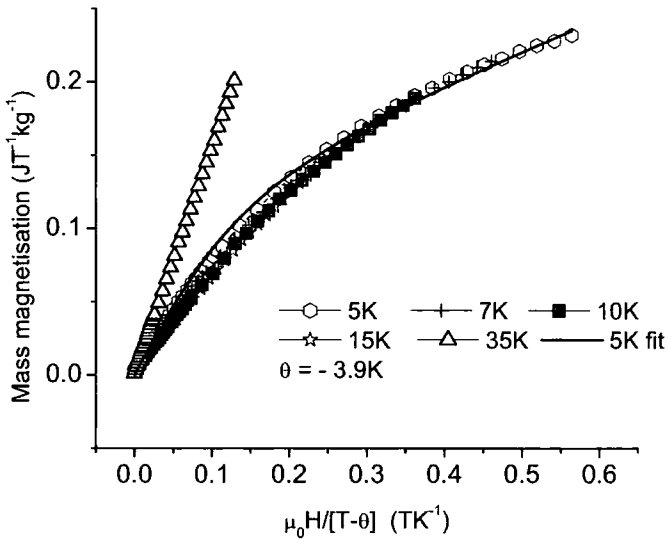

Figure 4.26: Mass magnetisation curves for $LaCoO_3$ up to 5 T, demonstrating scaling behaviour from 5 K - 15 K.

In the temperature window between 5 K and 15 K the data once again scale, shown in Fig. 4.26. However this time a θ value of -3.9 K is identified. The field dependence of the magnetisation measurements at low temperatures (< 50 K) in Fig. 4.26 can only be accounted for by magnetic excitons, as the $LaCoO_3$ matrix will be in a diamagnetic, S = 0 state. Fig. 4.26 is measuring

the effect of a direct exciton - exciton interaction (1) as at low temperatures there are no IS Co ions in the matrix. The data scale in the temperature region 5 K - 15 K with a θ value of - 3.9 K, and at 2 K the sample shows magnetic hysteresis. Note, this does not resemble superparamagnetic behaviour as a θ parameter is required to scale the field sweeps. To enable the magnetic response to be modelled, two magnetic components are required in the low temperature region. The Curie law and a susceptibility term containing the Brillouin function, as described in chapter 2, are required to fit the data. A fit for the 5 K data is shown in Fig. 4.26 and for both functions an S = 12.5 value is required to ensure accurate fitting. This is in agreement with Yamaguchi *et al*[25] who simply fitted the paramagnetic component of the magnetism. However, the data shown in Fig. 4.26 requires a magnetic species with an AF interacting component superimposed. The excitons appear to demonstrate a degree of clustering as two magnetic contributions are required to fit the data below 35 K. This behaviour is in a direct analogy with certain dilute magnetic semiconductors that show magnetic ion clustering, demonstrating spin glass behaviour below the nearest neighbour percolation limit[47].

4.4.5 Low Temperature Magnetic Susceptibility

To confirm the presence of an ordering temperature of the direct (overlapping) exciton - exciton interaction (1) in the system, the susceptibility was measured through the region 2 K - 5 K. The magnetic response of the excitons depends upon the matrix in which they are embedded. Evidence for magnetic exciton formation can only occur if the net susceptibility measurements can decouple the magnetic contribution from excitons and the matrix[45]. In this particular case for $LaCoO_3$ any attempt to gain information about the system upon the QD design MPMS SQUID yielded no apparent magnetic transition. This is because at the minimum measuring field obtainable upon the MPMS magnetometer (0.1 mT), the known paramagnetic contribution was found to dominate.

In an attempt to solve this problem, measurements have been performed upon the Durham low temperature d.c SQUID magnetometer, which has an effective

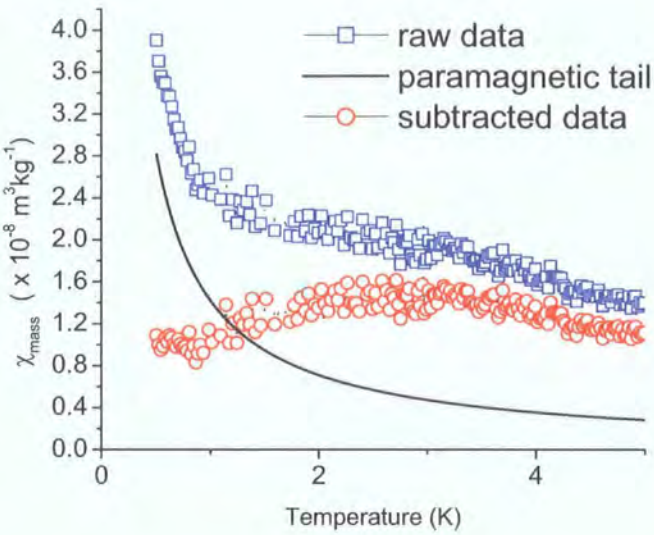

Figure 4.27: Temperature dependence of magnetic susceptibility for $LaCoO_3$ cooled and measured in a residual field of 10 μT. The raw data along with the subtraction of the paramagnetic fit are shown.

temperature range of 0.5 K to 4.5 K in a residual field of 10 μT as described in chapter 3. Fields of up to 0.01 T can be applied upon cooling, this is beneficial for $LaCoO_3$ as it allows the contribution from the excitons to saturate whereas the LS Co^{3+} background matrix and paramagnetic exciton contribution will not have a remnant component once the field has been switched off for measuring. The low temperature SQUID system only measures the absolute flux, and hence any attempt to calibrate the absolute moment requires the magnetic response to be compared to that obtained from the MPMS in the temperature overlap region between the two systems. The magnetic behaviour of the system can be modelled with an interacting and paramagnetic component, and then directly compared with the raw data, enabling an identification of the magnetic moment in the temperature overlap region.

The temperature dependent magnetic susceptibility is shown in Fig. 4.27 for $LaCoO_3$ in the temperature range 0.5 K to 4.5 K, measured in the low temperature SQUID system. Superimposed upon this is the Curie fit assuming a residual field of 10 μT, calculated from the magnetic response as in Fig. 4.26.

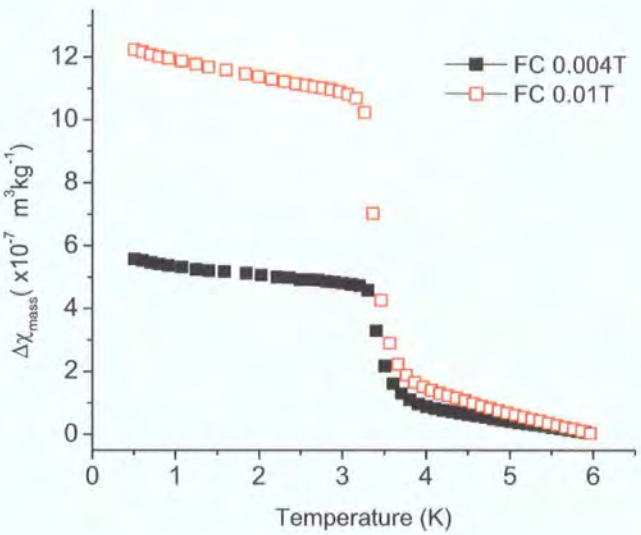

Figure 4.28: Temperature dependence of magnetic susceptibility for $LaCoO_3$ cooled in a field of 4 mT and 10 mT and measured in a residual field of 10 μT.

When this Curie type behaviour is removed there is a change in slope occurring at 3.5 K which is approximately the same as the θ value (-3.9 K) obtained from Fig. 4.26. The excitons in this particular case show an apparent interaction. Fig. 4.28. shows the temperature dependent change in susceptibility around the transition under different experimental conditions. For these experiments the cooling field was increased from 10 μT to 4 mT and 10 mT, and then warmed through the transition in the residual field of the experiment. In both scenarios the transition became much larger when increasing the cooling field strength. Any attempt to fit the transition with a ferromagnetic interaction failed[48].

Nagaev *et al*[10] did not predict the internal interaction of the exciton, concluding that it could be either AF or ferromagnetically coupled. However because the spin state of the Co ions in the excitons is likely to be the same it is more likely to be AF coupled[9, 44]. To produce an S value of 12.5 as identified in section 4.4.4 this would suggest the presence of a large cluster over several unit cells ($\sim$ 1 nm in diameter), with the high spin value resulting from uncompensated moments at the edge of the exciton. Any interaction between these large AF excitons will be field dependent and explain the remnant behaviour

observed in Fig. 4.28. There appears to be an exciton - exciton interaction (1) that is AF coupled, because of the large size of an AF exciton. The interaction is between the Co ions in the shell of the sphere. A large paramagnetic type tail exists when excitons do not overlap. Again internal magnetic anisotropy of the excitons cannot explain the remnant behaviour as there would be no paramagnetic tail.

4.5 Electrical Measurements

The electrical properties of $LaCoO_3$ are now described, the prime interest being to observe any temperature dependent features of the resistivity that can be related to magnetic excitons. The behaviour of the resistivity in $LaCoO_3$ is not fully explained; the actual carrier transport mechanism has never been resolved. Perhaps the clearest indication of the conduction mechanism has been provided by English *et al*[29], who observe a thermally excited spin disorder scattering contribution to the resistivity. However, at lower temperatures ($<$ 55 K), there is evidence for hopping conduction. The resistivity data reported in the literature appears to be sample specific. Table 4.5 shows the resistivity at 200 K and 250 K for selected publications along with the high temperature activation energy E_a, when calculated by the authors of the papers.

Author	Single Crystal	ρ - (250 K)	ρ - (200 K)	E_a
English[29]	No	10 Ωcm	14 Ωcm	146 meV
Senaris-Rodriguez[11]	No	-	-	150 meV
Yamaguchi[25]	Yes	4 Ωcm	10 Ωcm	110 meV
Asai[17]	Yes	2 Ωcm	5 Ωcm	-
Tokura[15]	Yes	10 Ωcm	19 Ωcm	-

Table 4.5: The general behaviour of the published resistivity data is shown with values given at specific temperature values. The activation energy E_a for the high temperature regime is also reproduced where applicable.

English *et al*[29] have performed their measurements upon the polycrystalline sample *a*. 250 K and 200 K have been chosen because at this temperature it is unlikely there are any Joule heating effects. The lowest temperature recorded for

resistivity is $\sim$ 50 K. Below this temperature the I-V characteristics identified in chapter 3 become non-Ohmic. Coincident with this "lowest" temperature value it is known that the Seebeck coefficient becomes zero[11], the carriers appearing to freeze out. There is a large range in resistivity values for each of the samples measured. Yamaguchi[25] and Tokura[2] work in the same group and for both references the sample was prepared in the same way, indicating the difficulty in reproducing resistivity data for lanthanum cobaltite. The E_a for each sample was calculated in the high temperature regime and clearly the polycrystalline data have a higher activation energy, although the region of activated behaviour reported is generally in a narrow temperature regime. Above 200 K all the reported data are non-linear. An example of the literature data is given in Fig. 4.29, from English *et al*[29].

4.5.1 Resistivity Measurements

The resistivity measurements were performed upon the single crystal sample, whose preparation is discussed in chapter 3. Great care was taken to ensure good Ohmic contacts and the measurements were performed in the van der Pauw configuration. Below 150 K a full I-V sweep was performed at each data point, specifically allowing for thermal equilibrium to be reached in the closed cycle refrigerator and to prevent sample heating. The results of the initial resistivity measurements are shown in Fig. 4.29, plotted as a $\ln(\rho)$ vs T^{-1}. There are clearly two activated behaviours above (E_0) and below (E_1) 64 K. The activation energies are extracted from a fit to $\rho = \rho_0 \exp\left(\frac{E_a}{k_B T}\right)$. The high temperature activation energy, E_0 is lower than any of those reported in Table 4.5, however the fit range is from 70 K to 300 K. In all reported literature the data are not linear above 200 K. The lowest temperature resistivity measurable was 50 K; below this the contact resistance increased dramatically. Note that even though the resistivity was a factor of 10 less than that of others[29], no data could be recorded below 50 K.

The data obtained for this study in Fig. 4.29 appear to follow the general form expected of a lightly doped semiconductor[49]. At high temperatures the conduction is intrinsic, with a temperature independent crossover regime to

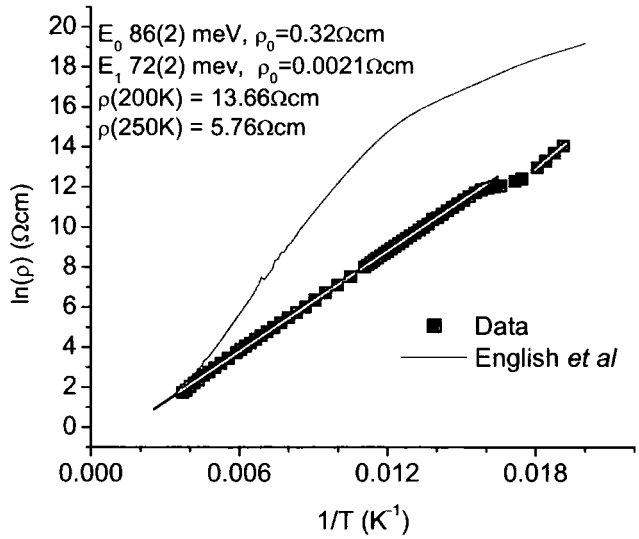

Figure 4.29: Temperature dependence of the zero field resistivity. The functional form of the data is clearly activated with a high temperature activation energy E_0 of 86 meV with a crossover to E_1 of 72 meV at 64 K. Also shown are the resistivity data from English *et al*[29].

extrinsic conduction which is once again activated. Eventually a hopping regime is also observed. This appears to be in contradiction to the data provided by English *et al*[29], no extrinsic conduction is observed as it passes straight into the hopping regime as shown in Fig. 4.29. One possible explanation is that their increased density of excitons means that is it acting as a heavily doped semiconductor, (The intrinsic and extrinsic regimes will not be differentiable.) and passes straight into the hopping regime. No hoping is observed in the data taken for this study due to the dilute nature of excitons in the single crystal sample compared to the sample used by English *et al.* The hopping regime will occur at lower temperatures. However it is difficult to measure below 50 K. Note that the energy difference between E_0 and E_1 (Intrinsic and Extrinsic behaviour) for the single crystal sample obtained from Fig. 4.29 is $\sim$ 10 meV. This corresponds to the spin state transition energy[29], possibly indicating the temperature regions over which the respective regimes dominate.

4.5.2 Evidence for a Magnetic Contribution to the Resistivity

Magneto-resistance in $LaCoO_3$ has only been observed when applying a field in excess of 1.5 T[29]. In the present work electrical measurements up to 1 T can be performed, and application of a magnetic field saw no magneto-resistance. The magnetoresistance is attributed to spin disorder scatter as briefly mentioned in section 4.5. However the possibility of a contribution from the excitons was not considered. Initial FC experiments have been performed, repeating the experimental procedure identified in section 4.4.1 of cooling in a field of 50 mT until 50 K and then carrying on the cooling, followed by the respective measurement in the remnant field (1 mT) of the magnet.

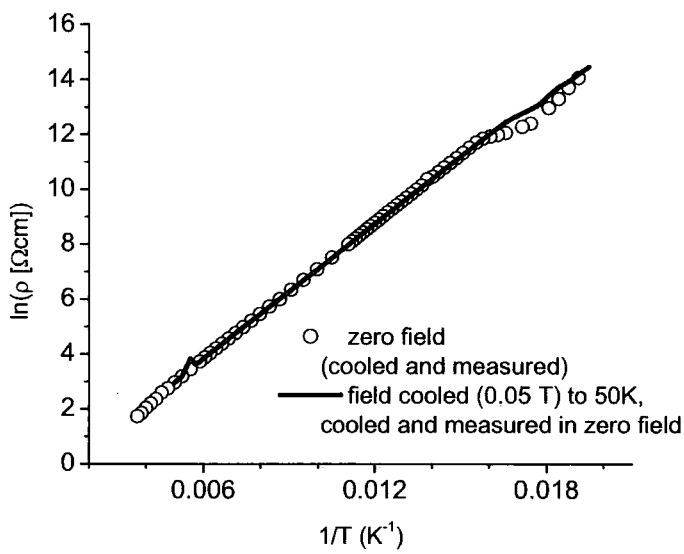

Figure 4.30: Temperature dependence of the zero field resistivity compared directly to when the sample is field cooled. The functional form of the FC data undergos a smaller change in activation energy at 64 K.

Fig. 4.30 directly compares and contrasts the results of the FC measurement with the ZFC measurement. At high temperatures the same activated behaviour is followed, however below 64 K the data no longer overlap. There is a clear increase in the resistance and the data no longer follows the qualitative behav-

iour of a lightly doped semiconductor. The similarity of the electrical response to the magnetic response, upon the application of a magnetic field on cooling, suggests that the effect of the magnetic exciton upon the resistivity is being observed. Indeed the FC data appear to turn over at low temperatures indicative of a semiconductor entering a hopping regime. If more oxygen vacancies are present and there is more disorder in the sample, it is reasonable to assume that the mobility edge in the conduction band has shifted. This situation is more likely in a polycrystalline sample and the data indicate that a hopping regime will be entered without the observation of spin disorder scattering. One conclusion that can be drawn is that the resistivity of the sample will be affected by the number of excitons and the quality of the material.

4.5.3 Temperature Dependence of the Anisotropy Ratio

As discussed in section 4.5.1 the electrical transport measurements have been made using a sample with contacts in the van der Pauw configuration. The anisotropy (κ) is the ratio of the two resistances and is not expected to change drastically as a function of temperature for good quality isotropic samples. Fig. 4.31 shows a comparison of the temperature dependent change in anisotropy for both the FC and ZFC experiment. The anisotropy is stable for high temperatures but begins to drop below 64 K, the temperature at which the impurity level becomes dominant, inferred from Fig. 4.29. Importantly the change in κ is present in both experimental conditions indicating that the electrical measurements may be sensitive to the magnetic excitons. The conduction process appears to be dependent on a remnant magnetic component.

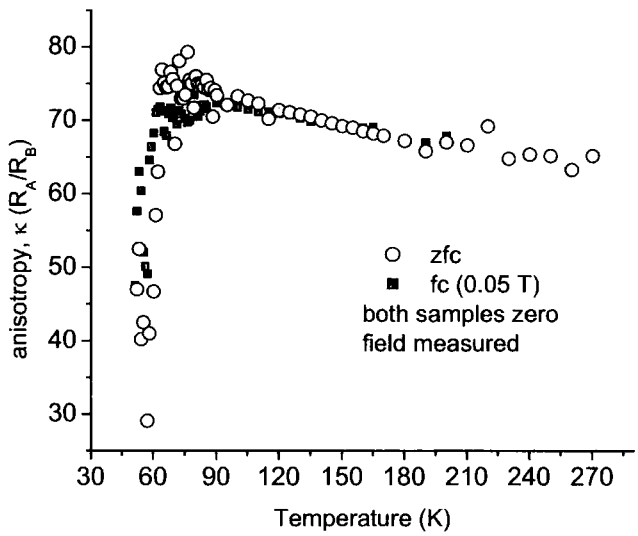

Figure 4.31: Temperature dependence of the anisotropy ratio (κ) for both the FC and ZFC data, a clear change in the anisotropy ratio is seen in both scenarios below 64 K.

4.6 Discussion of Results

μSR measurements have identified a bulk magnetic component in the LS temperature regime of $LaCoO_3$, which has been attributed to the formation of magnetic excitons. Moreover in section 4.3.4 an activated form of the depolarisation rate which is dependent upon the applied magnetic field was identified, suggesting that some magnetic excitons are interacting with the AF matrix at high temperatures (50 K > T > 220 K). If the remnant magnetic component at 50 K identified in section 4.4.1 is a consequence of this interaction then the remnant moment will be dependent upon the population level of the IS matrix surrounding the exciton. Therefore the remnant moment (μ) can be written in terms of the activation energy ($E_a(B)$) obtained from field dependent μSR measurements. The remnant moment can therefore be expressed in the form,

$$\mu \propto \exp\left(\frac{E_a(B)}{k_B T}\right). \tag{4.8}$$

Fig 4.32 shows the inverse field dependence of the natural logarithm of the remnant moment, suggesting that the remnant moment is indeed a consequence of

the IS matrix interacting with some excitons. The interaction is field dependent as determined by μSR measurements.

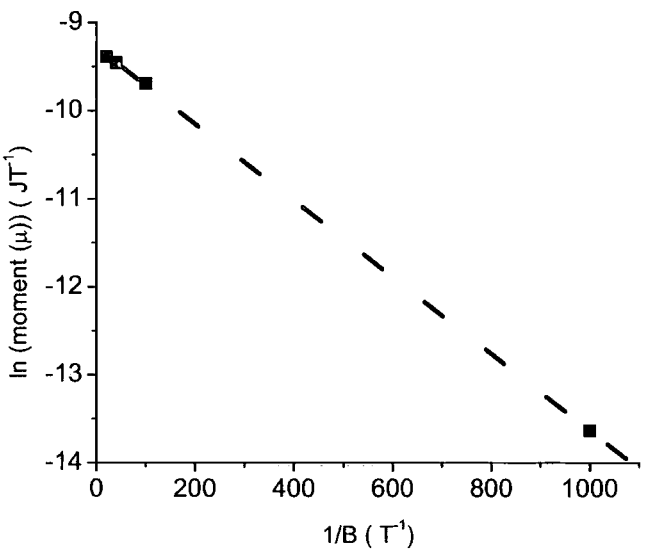

Figure 4.32: Field dependence of the remnant magnetisation obtained from Fig. 4.20 as an inverse function of magnetic field.

There is clear evidence for two high temperature remnant components in the magnetisation, one at 50 K (from interaction 2B) and one at 220 K (interaction 2A). This leads to the conclusion that the form of relaxation is different for the two regimes. μSR demonstrates that the internal field distribution fits a thermally activated law from 50 K to $\sim$ 170 K. This suggests that the exciton - IS matrix interaction is changing. Above 90 K there are few excitons but they couple to the surrounding IS matrix (2A) while below 90 K the IS matrix begins to relax into the ground state. If an oxygen vacancy is present an exciton will be created. Therefore the increased density of excitons leads to two distinct cases below 60 K, an exciton - IS matrix - exciton (2B) and an exciton - exciton interaction (1). The overlapping exciton leads to the low temperature order, whilst the exciton - IS matrix - exciton interaction (2B) leads to the remanence at 50 K. Note that it is also possible that paramagnetic excitons that do interact with anything also form. The possible types of exciton interactions are summarised in Table 4.6.

Temperature Range	Local Interactions	Matrix Spin State
T> 220 K	exciton and matrix are paramagnetic	IS
60 K < T < 220 K	exciton - IS matrix interaction(2A)	IS
35 K < T < 90 K	exciton - IS matrix-exciton(2B) and exciton-exciton	thermally excited LS-IS
T < 35 K	exciton - exciton interactions(1)	"truely" LS

Table 4.6: A list of the possible magnetic exciton interactions for specific temperature ranges, correlating all the results obtained from the experiments.

A simple cooling rate experiment can be utilised to further highlight the intimate form of the exciton matrix interaction. A ZFC temperature sweep of the

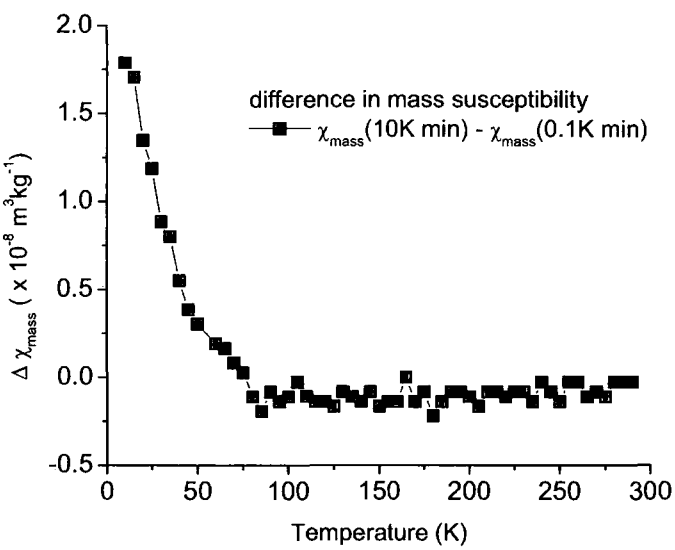

Figure 4.33: Temperature dependent difference in mass susceptibilities measured at two different cooling rates

magnetisation at different cooling rates has been performed; one experiment was cooled at 10 $Kmin^{-1}$ whilst the other was performed at 0.1 $Kmin^{-1}$. The difference in the magnetic susceptibilities obtained at the two cooling rates is shown in Fig. 4.33. The first thing to notice is that it strongly resembles the low temperature (< 90 K) FC 1 mT measured data described earlier in Fig. 4.19. This is to be expected when considering the consequences of magnetic exciton

formation that is dependent on the thermally induced IS-LS spin transition. No more excitons are formed when slow cooling, simply because of the activated form of the IS matrix obtained from equation 4.1. Note the remnant component at low temperatures (< 35 K), indicating that when excitons interact they no longer behave as true paramagnetic species.

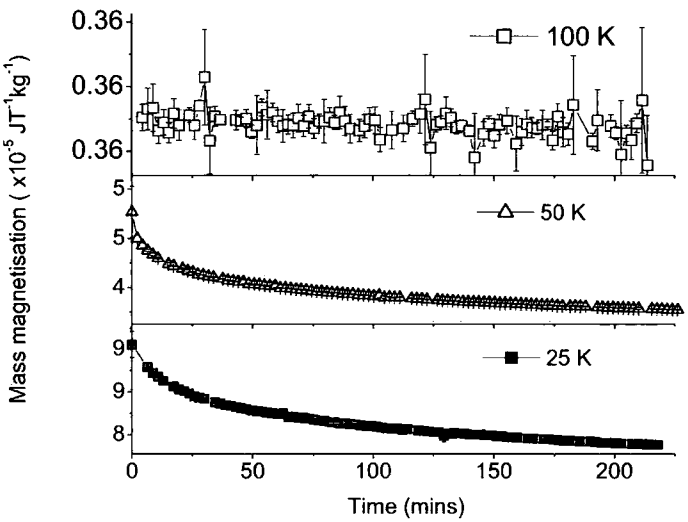

Figure 4.34: Temperature dependence of the magnetic relaxation rates at different temperatures, after cooling in a field of 1 mT.

The nature of the exciton is that it is "internally" AF coupled because all the Co ions will have the same spin state[10]. This requires a large exciton to get the net spin of 12.5 per exciton ($\sim$ 7 Co ions), obtained in section 4.4.4, however it is the question of remanence in the exciton that remains to be answered. If the moments that contribute to the net spin take hours to relax because of the interaction with the Co ions inside the exciton, this will explain the observed remanence. The spin "direction" of the exciton is controlled by the interaction of the exciton shell with its surrounding. This would require a very slow relaxation of the exciton as the excitons, remember upon cooling the direction of field cooling. This is shown in Fig. 4.34, which shows the time dependence of the mass magnetisation relaxation rates when cooled to specific temperatures in 10 mT. The measurements were performed in zero field

and clearly indicate that magnetic relaxation takes hours, much longer than any of the field cooling experiments performed. The remnant magnetisation observed in the 100 K is a factor of 3 greater than when the magnetisation is measured in the remnant field of the magnet, when no field has been applied on cooling. Note a stretched exponential is required to fit the moment relaxations, suggesting more than one barrier to relaxation.

This interpretation is supported by the application of large magnetic fields which swamp any of the transitions described in this work, indicating the subtle energy balance of the excitons. Without the LS ground state of $LaCoO_3$ the excitons would be extremely difficult to observe.

4.7 Conclusions

Experimental evidence of magnetic excitons in $LaCoO_3$, that are inherent to the bulk of the as-made samples has been obtained. The magnetic properties of the exciton clearly have an effect upon the intrinsic properties of pristine $LaCoO_3$ which has until now been unaccounted for. At high enough densities magneto electrical phase separation should occur although this is probably not possible to observe, as the material with not be single phase at high oxygen vacancy concentration[27]. Further electrical characterisation needs to be performed to intimately link the magnetic exciton with the intrinsic electrical properties of the material.

References

[1] M. Imada, A. Fujimori and Y. Tokura, Rev. Mod. Phys. **70**, 1039 (1998)

[2] Y. Tokura and Y. Tomioka, J. Magn. Magn. Mater **200**, 1 (1999)

[3] J. M. D. Coey, M . Viret and S. von Molnár, Adv. Phys. **48**, 167 (1999)

[4] W. C. Koehler and E. O. Wollan, J. Phys. Chem. Solids **2**, 100 (1957)

[5] R. R Heikes, R. C. Miller and R. Mazelsky, Physica (Amsterdam) **30**, 1600 (1964)

[6] C. Zobel, M. Kriener, D. Bruns, J. Baier, M. Gruninger, T. Lorenz, P. Reutler and A. Revcolevschi, Phys. Rev. B **66**, 020402 (2002)

[7] R. von Helmolt, J. Wecker, B. Holzapfel, L. Schultz and K. Samwer, Phys. Rev. Lett **71**, 2331 (1993)

[8] H. L. Ju, C. Kwon, Q. Li, R. L. Greene and T. Venkatesan, Appl. Phys. Lett **65**, 2108 (1994)

[9] M. A. Senaris-Rodriguez and J. B. Goodenough, J. Solid State Chem **118**, 323 (1995)

[10] E.L. Nagaev and A.I. Podelshchikov, J. Phys.: Cond. Matt **8**, 5611 (1996)

[11] M. A. Senaris-Rodriguez and J. B. Goodenough, J. Solid State Chem **116**, 224 (1995)

[12] M. Abbate, J. C. Fuggle, A. Fujimori, L. H. Tjeng, C. T. chen, R. Potze, G. A. Sawatzky, H. Eisaki and S. Uchida, Phys. Rev. B **47**, 16124 (1993)

[13] M. Zhuang, W. Zhang, C. Hu and N. Ming, Phys. Rev. B **57**, 10710 (1998)

[14] K. Asai, P. Gehring, H. Chou and G. Shirane, Phys. Rev. B **40**, 10982 (1989)

[15] Y. Tokura, Y. Okimoto, S. Yamaguchi, H. Taniguchi, T. Kimura and H. Takagi, Phys. Rev. B **58**, R1699 (1998)

[16] M. A. Korotin, S. Yu. Ezhov, I. V. Solovyev, V. I. Anisimov, D. I. Khomskii and G. A. Sawatzky, Phys. Rev. B **54**, 5309 (1996)

[17] K. Asai, A. Yoneda, O. Yokokura, J. M. Tranquada, G. Shirane and K. Kohn, J. Phys. Soc. Jap **67**, 290 (1998)

[18] Y. Kobayashi, N. Fujiwara, S. Murata, K. Asai and H. Yasuoka, Phys. Rev. B **62**, 410 (2000)

[19] S. Noguchi, S. Kawamata, K. Okuda, N. Nojiri and M. Motokawa, Phys. Rev. B **66**, 094404 (2002)

[20] S. Stølen, F. Grønvold, H. Brinks, T. Atake and H. Mori, Phys. Rev. B **55**, 14103 (1997)

[21] S. Yamaguchi, Y. Okimoto and Y. Tokura, Phys. Rev. B **55**, R8666 (1997)

[22] A. Ishikawa, J. Nohara and S. Sugai, Phys. Rev. Lett **93**, 136401 (2004)

[23] G. Maris, Y. Ren, V. Volotchaev, C. Zobel, T. Lorenz and T. T. M. Palstra, Phys. Rev. B **67**, 224423 (2003)

[24] J. Q. Yan, J. S. Zhou and J. B. Goodenough, Phys. Rev. B **70**, 014402 (2004)

[25] S. Yamaguchi, Y. Okimoto, H. Taniguchi and Y. Tokura, Phys. Rev. B **53**, R2926 (1996)

[26] K. Tsutsui, J. Inoue and S. Maekawa, Phys. Rev. B, **59**, 4549 (1999)

[27] Personal Comm, J. Wu, Department of Chemical Engineering and Materials Science, 421 Washington Ave SE, University of Minnesota, Minneapolis 55455, USA

[28] Personal Comm, D. Prabhakaran, Department of Physics, University of Oxford, Oxford, OX1 3PU, UK

[29] S. R. English, J. Wu and C. Leighton, Phys. Rev. B, **65**, 220407(R) (2002)

[30] S. F. J. Cox, J. Phys. C: Solid State Phys, **20**, 3187 (1987)

[31] K. Kojima, A. Keren, L. P. Le, M. Larkin, G. M. Luke, B. Nachumi, W. D. Wu, Y. J. Uemura, M. Azuma, M. Takano, K. Kiyono, S. Miyasaka, N. Motoyama, H. Takagi, S. Uchida, M. Hase, Y. Sasago, K. Uchinokura, M. Matsuda, K. Katsumata, A. Revcolevschi and R. Cava, Hyperfine Interact, **104**, 37 (1997)

[32] Th. Jestädt, R. I. Bewley, S. J. Blundell, W. Hayes, B. W. Lovett, F. L. Pratt and R. C. C. Ward, J. Phys.: Cond. Matt, **10**, L259 (1998)

[33] S. J. Campbell, V. Ksenofontov, Y. Garcia, J. S. Lord, Y. Boland and P. Gütlich, J. Phys. Chem. B **107**, 14289 (2003)

[34] S. J. Blundell, F. L. Pratt, C. A. Steer, I. M. Marshall and J-F. Létard, J. Phys. Chem. Solids **65**, 25 (2004)

[35] M. D. Segall, P. J. D. Lindan, M. J. Probert, C. J. Pickard, P. J. Hasnip, S. J. Clark and M. C. Payne, J. Phys.: Cond. Matt **14**, 2717 (2002)

[36] A. B. Denison, H. Graf, W. Kündig and P. F. Meier, Helvetica Physica Acta **52**, 460 (1979)

[37] P. G. Radaelli and S. W. Cheong, Phys. Rev. B **66**, 094408 (2002)

[38] http://lmu.web.psi.ch/facilities/dolly/dolly.html, accessed 03/03/05

[39] Y. Uemura, T. Yamazaki, D. R. Harshman, M.Senba and E. J. Ansaldo, Phys. Rev. B **31**, 546 (1985)

[40] S. A. Dodds, G. A. Gist, D. E. MacLaughlin, R. H. Heffner, M. Leon, M. E. Schillaci, G. J. Nieuwenhuys and J. A. Mydosh, Phys. Rev. B **28**, 6209 (1983)

[41] E. Morenzoni, H. Gluckler, T. Prokscha, R. Khasanov, H. Luetkens, M. Birke, E. M. Forgan, Ch. Niedermayer and M. Pleins, Nucl. Instr. and Meth. B, **192**, 254 (2002)

[42] D. N. H. Nam, K. Jonason, P. Nordblad, N. V. Khiem and N. X. Phuc, Phys. Rev. B **59**, 4189 (1999)

[43] J. Androulakis, N. Katsarakis and J. Giapintzakis, Phys. Rev. B. **64**, 174401 (2001)

[44] J. B. Goodenough, Magnetism and the Chemcial Bond, Wiley, New York (1963)

[45] S. von Molnár, A. Briggs, J. Flouquet and G. Remenyi, Phys. Rev. Lett. **51**, 706 (1983)

[46] C. Kittel, Introduction to Solid State Physics (seventh edition), Wiley, New York (1996)

[47] M. A. Novak, O. G. Symko, D. J. Zheng and S. Oseroff, J. Appl. Phys. **57**, 3418 (1985)

[48] A standard critical fit of the form $(1 - (T/T_c))^n$ would not fit.

[49] B. I. Shklovskii and A. L. Efros, Electronic Properties of Doped Semiconductors, Springer, New York (1984)

Chapter 5

Magnetic Phase Separation in $La_{1-x}Sr_xCoO_3$

This chapter examines in detail the results of magnetic susceptibility measurements and muon spin spectroscopy investigations into $La_{1-x}Sr_xCoO_3$. Of particular interest is the role of the $LaCoO_3$ matrix at low x concentrations. A brief introduction reporting the results reported to date will be given, followed by a detailed discussion of the results obtained in this study. Interpretation of the data obtained requires a direct comparison with the work performed on $LaCoO_3$ in chapter 4.

5.1 Introduction

The Sr doped cobaltite has received much attention due to the observation of CMR effects[1, 2], recent work has concluded that one specific key to CMR is the process of heterogeneity, where randomly doped materials exhibit spatial coherence of ferromagnetic metallic regions and non-ferromagnetic insulating regions[3]. Indeed, recent scanning tunneling microscopy investigations have imaged directly the metallic and insulating regimes in manganite materials which show CMR[4, 5]. $La_{1-x}Sr_xCoO_3$ has been shown to exhibit clearly spatially differentiable regions when investigated using electron microscopy[6] and Nuclear Magnetic Resonance[7] (NMR) techniques.

5.1.1 Phase Diagram of $La_{1-x}Sr_xCoO_3$

When hole doped with Sr ions, extra complexity is introduced into the $LaCoO_3$ system. The hole is accommodated by the formation of Co^{4+} ions which must have a magnetic ground state; the possible spin states of the Co^{4+} ions present are shown in chapter 4, Fig. 4.1. It is generally believed that Co^{3+} - Co^{4+} ions cluster, generating local ferromagnetic order, via the double exchange mechanism as described in chapter 2. Varying the composition of $La_{1-x}Sr_xCoO_3$ produces a fascinating phase diagram, including unexplained glassy ferromagnetism[8, 11, 13, 9, 24]. This rich magnetic behaviour is not limited to the material of interest, other materials such as $Y_{1-x}Ca_xMnO_3$[14] and $NdBa_2Cu_3O_{7-\delta}$[15] show mixed ferromagnetic and spin glass properties. However, $La_{1-x}Sr_xCoO_3$ has been chosen because of its "simpler" parent compound. Recent work has concluded that when $x < 0.18$, the material is in a spin glass

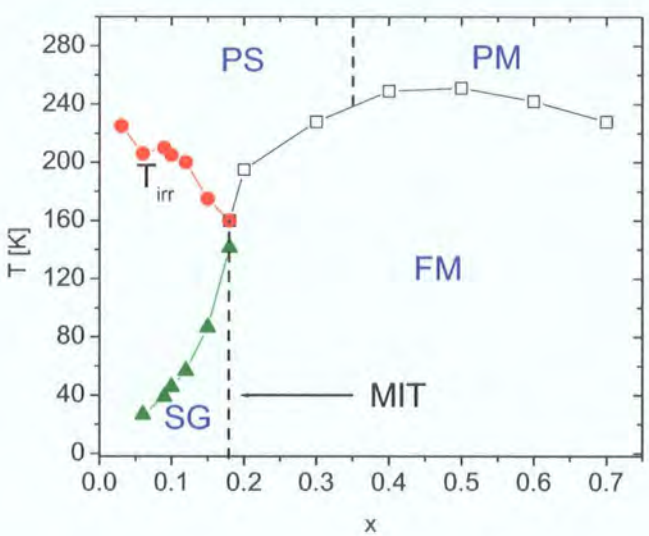

Figure 5.1: Magnetic phase diagram of $La_{1-x}Sr_xCoO_3$, PS/M = paramagnetic semiconductor/metal, FM = ferromagnetic metal, T_{irr} irreversibility temperature which marks the separation temperature of the FC and ZFC magnetic susceptibility curves and SG = spin glass. From [12].

phase at low temperature, and a Metal to Insulator Transition (MIT) occurs coincident with the onset of spin glass behaviour when decreasing the compo-

sition below $x = 0.18$[12, 13, 16]. Electrical resistivity measurements further support this interpretation by the presence of a percolation type transition[12] at $x = 0.18$. Fig. 5.1 shows the most recent phase diagram. The irreversibility temperature, T_{irr} identified in Fig. 5.1 will be discussed in depth later in this chapter. Low concentration $La_{1-x}Sr_xCoO_3$, where $x < 0.05$, has been considered by Yamaguchi *et al*[17]. Interestingly no contribution to the magnetic susceptibility from undoped $LaCoO_3$ is observed; and no LS-IS transition is observed at such low concentrations. A large Curie tail was interpreted as a doped hole contribution to the magnetism by Yamaguchi *et al*[17], whereby a doped hole can cause a LS-HS transition of Co sites around itself and interact via the double exchange mechanism[18, 19, 20]. The interactions of the hole induced high spin regions within the $LaCoO_3$ matrix may behave in a similar manner to the matrix-exciton interactions identified in chapter 4. The LS-IS transition may be occurring in the $LaCoO_3$ matrix. However, the measured susceptibility of this transition is orders of magnitude smaller that the magnetic susceptibility of the Sr rich clusters. As the origin of the magnetic interactions is still not well understood this work will concentrate upon the contribution to the magnetism from the majority cobaltite matrix, at low x concentration.

5.1.2 Clustering of Sr Rich Regions

There is strong evidence for the occurrence of ferromagnetic clusters throughout the compositional range from Small Angle Neutron Scattering (SANS). This is further vindication of the percolating insulator metal transition which is believed to arise from magneto-electronic phase separation. Such a conclusion can be interpreted from the work of Wu *et al*[21] who have performed SANS on $La_{1-x}Sr_xCoO_3$, where $x = 0.30$, 0.18 and 0.15. This compositional range was chosen due to the proximity of the MIT. Fig. 5.2 shows the temperature dependence of the SANS intensity as a function of the wavenumber q. The temperature dependence of the intensity of q suggests there are short range ferromagnetic interactions even below the percolation limit of $x = 0.15$, further confirming that the Sr ions do indeed cluster at all compositions studied and indicating that the interesting exchange mechanism is between the Sr rich clusters themselves. It is generally assumed that the Sr rich clusters interact to

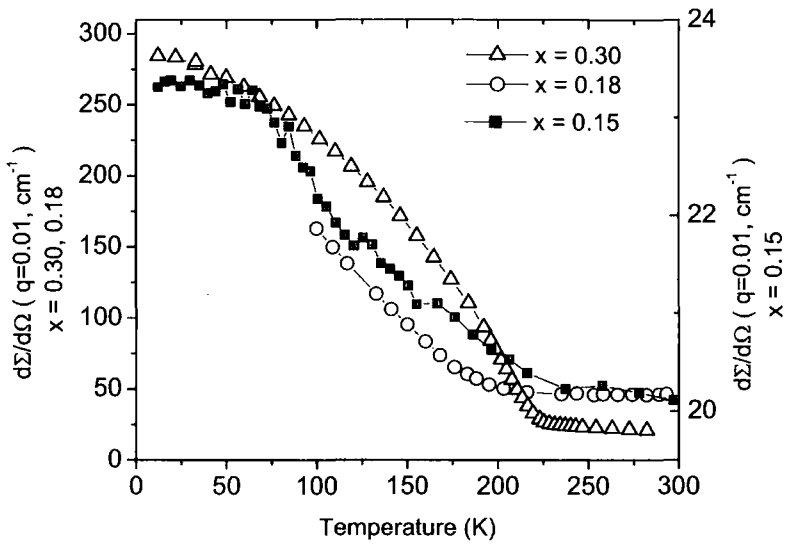

Figure 5.2: Temperature dependence of the SANS intensity for low q, the ferromagnetic interactions for $La_{1-x}Sr_xCoO_3$, where $x = 0.30$ (triangles), 0.18 (circles) and 0.15 (squares). From [21].

produce a cluster glass behaviour at high enough densities and that frustrated interactions between the clusters produce the spin glass behaviour at low x compositions. However the role of the $LaCoO_3$ background matrix remains largely unresolved. NMR[7] detects spatially differentiable magnetic regions although possible exchange interactions between the matrix and Sr clusters were neglected. The clusters were estimated to be approximately 10 nm in diameter via high resolution electron microscopy[6], the interpretation of this work being based upon the idea of superparamagnetic regions stabilised by the hole doping[16].

Fig. 5.2 clearly demonstrates that for all compositions studied short range ferromagnetic interactions occur, and this is in agreement with a cluster model. Here the ferromagnetic (Co^{3+} - Co^{4+} interactions) regions are separated by the $LaCoO_3$ undoped regions. Below the percolation limit the inter-cluster interaction is frustrated. However, below $x = 0.06$ no spin glass behaviour is observed. At this limit there is no exchange between the clusters. However a cluster matrix interaction has been neglected. When considering the spin state

of the Co ions in the $LaCoO_3$ matrix work has been confined to high concentration regions[16, 12] where $x > 0.2$, where a percolation of high spin clusters is known to occur. Therefore any contribution from the matrix is minimal. Indeed a recent theoretical paper has predicted that upon hole doping with Sr ions, all Co^{3+} ions obtain the same spin state for all compositions[22]. However this work "fixed" the spin to compare the ground state energies and did not directly compare Co^{3+} ions with different spin states. This conclusion can only be validated by a mapping of the observed Co^{3+} LS - IS/HS transition due to Sr doping of the $LaCoO_3$ matrix at low x compositions.

The purpose of this work is to examine for the first time the low doping regime of $La_{1-x}Sr_xCoO_3$ with a local magnetic probe, namely muon spectroscopy and to observe if any component of the $LaCoO_3$ background contributes to the magnetism. Specifically, any interaction with the $LaCoO_3$ matrix will unambiguously prove that the clusters are not superparamagnetic in nature[16]. Consequently if the induced moment of the Co^{3+} ions in the matrix can be modelled a plausible mechanism for the glassy behaviour shown in Fig. 5.1 may be possible.

5.2 Characterisation of the $La_{1-x}Sr_xCoO_3$ Samples

Polycrystalline samples were fabricated by the standard solid state reaction method from the starting materials La_2O_3, Co_3O_4 and $SrCO_3$ by J. Wu from Minnesota University[23]. X-ray characterisation of the samples used in this study[12] show that to within the sensitivity of x-ray diffraction the samples are single phase. Moreover titration experiments demonstrate that the formula unit is indeed $La_{1-x}Sr_xCoO_3$, and there are no oxygen vacancies present to within the error of the titration experiment[12]. The compositional range investigated using standard d.c magnetisation methods ranged from $x = 0.01$ - 0.50. For clarity, the majority of the discussion will concentrate upon the compositions $x = 0.03$, 0.15 and 0.20, as the μSR experiments have centred upon these samples. These particular compositions are of interest because of their proximity to different magnetic phases. $x = 0.03$ is of significance as this is in

the dilute limit of Sr clusters, and the majority of the material "exists" as the pure cobaltite matrix. Hence, any competing interactions between Sr clusters and the background matrix will be highlighted. The compositions $x = 0.15$ and 0.20 are of importance as these materials sit either side of the percolative MIT. Any contribution from the background matrix in these systems has yet to be identified.

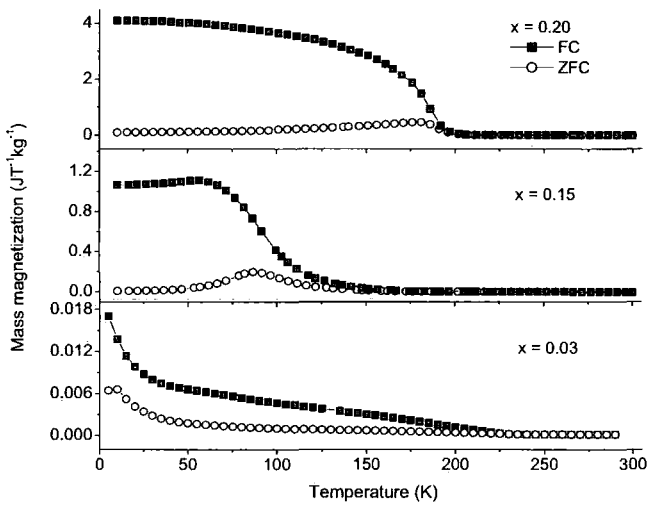

Figure 5.3: Temperature dependence of the dc magnetisation for $x = 0.20$, 0.15 and 0.03. ZFC curves are shown as open symbols and FC curves solid symbols.

The temperature dependence of the magnetisation for $x = 0.03$, 0.15 and 0.2 are shown in Fig. 5.3. Field Cooled (FC) and Zero Field Cooled (ZFC) data are shown; the measuring field applied for both cases was 1 mT. For $x < 0.18$, below the MIT, there is a separation of the FC and ZFC data (T_{irr}). This has been highlighted in the phase diagram (Fig. 5.1) and the value for $x = 0.15$ is in agreement with previous work[12]. The phase diagram shows an increase in T_{irr} as x continues to decrease. For the $x = 0.03$ composition the T_{irr} value has increased to 220 K. Interestingly this is the value of the local AF exchange between Co^{3+} ions present in $LaCoO_3$, as identified in chapter 4. Fitting of the FM region above the percolation with a Brillouin function as identified in chapter 2 does not provide an accurate S value of each cobalt spin.

Previous work has considered the Co^{3+} ions to have a uniform spin throughout the compositional range[12, 16, 22]. However no magnetic saturation has ever been observed in $La_{1-x}Sr_xCoO_3$.

The FC data show saturation like behaviour as T $\rightarrow$ 0except for the $x = 0.03$ sample. However, all the ZFC data show a peak which appears below T_{irr}, and this behaviour has previously been interpreted in terms of a short range ferromagnetic cluster model[8, 9, 11, 24], where the Sr clusters are dominated by ferromagnetic double exchange interactions between the HS Co^{3+} - Co^{4+} ions imbedded in a non-ferromagnetic matrix. After ZFC the clusters freeze into a random direction dictated by a local anisotropy field. This requires a competing magnetic interaction and thus the temperature dependence of the peak (T_a) will be dictated by two interactions governed by the strength of the applied field. Indeed, Nam *et al*[8] have shown empirically the ZFC cusp for $La_{0.50}Sr_{0.50}CoO_3$ (T_a) to be field dependent of the form,

$$T_a \propto T_c - CT_cH^{0.58} \tag{5.1}$$

where C is a constant and H is the external field. The standard spin glass exponent of the external field is 0.66[25] and is governed by the fluctuation rate dynamics determined by the frustrated interactions. The role of the Co^{3+} - Co^{3+} AF background matrix has never been examined and, referring back to chapter 4, it is easy to see why. When the oxygen vacancy level of $LaCoO_3$ was altered and the measuring field reduced, the LS-IS transition did not dominate the measured magnetic susceptibility. Hole doping with Sr ions would exaggerate the situation which will become far more severe with the FM Sr rich cluster interaction dominating net magnetic measurements such as susceptibility, swamping the contribution of the $LaCoO_3$ matrix and any interaction with the cluster.

5.3 Low Doping Region, $x < 0.05$

This section will examine the magnetic properties of lightly doped $La_{1-x}Sr_xCoO_3$, where $x = 0.01$ and 0.03, primarily it will concentrate upon $x = 0.03$ as this is the sample on which the vast majority of the work has been performed.

The compositions investigated have never shown any indication of spin glass behaviour[12], and by studying the sample with a local probe it may be possible to examine any interactions between the ferromagnetic clusters and the $LaCoO_3$ matrix at low Sr ion concentration.

5.3.1 Transverse Field μSR

Detailed TF measurements have been performed upon $La_{0.97}Sr_{0.03}CoO_3$ and preliminary investigations into $La_{0.99}Sr_{0.01}CoO_3$ have been initiated. For all muon investigations it is assumed that the muon implants at a interstitial site, directly inferred from the previous DFT results on $LaCoO_3$, as identified in chapter 4. No calculations were performed upon $La_{1-x}Sr_xCoO_3$ as the unit cell size required to perform minimisation calculations is too big for the computer cluster used in this work. TF μSR experiments were performed upon $La_{0.97}Sr_{0.03}CoO_3$ over the temperature range 5 K - 300 K. The polycrystal sample has a grain size of 10 μm[12] therefore the majority of the relaxation is expected to be from the bulk (minimal surface effects) of the sample. The TF data were fitted with a relaxation function of the form:

$$\begin{aligned} G_x(t) = A_{Osc}\cos(2\pi\upsilon_\mu t)\exp(-[\lambda_{tf}t]^2) \\ +A_{Gau}\exp(-[\sigma_{tf}t]^2) + A_{bg} \end{aligned} \tag{5.2}$$

where A_{Osc}, A_{Gau} and A_{bg} are the initial asymmetries of, respectively, the oscillatory and gaussian decays and the background. λ_{tf} and σ_{tf} are the depolarisation rates for the two separate decays and υ_μ is the muon precession frequency, which is dependent upon the externally applied field. The gaussian relaxation should have an oscillatory component. However, for this experiment no oscillating component was observed due to the very fast relaxation that does exist, as such it is out of the muon time window. There was a quick component at very short times that we were unable to fit with equation 5.2(see appendix B), this relaxation manifested itself as a single data point. When a third component was added it was found to be temperature independent below 50 K, this is the temperature at which it became apparent due to the dephasing of the muons as shown in Fig. 5.4. No useful information can be obtained from this extra

relaxation. Note that also the interesting physical interactions are determined from the oscillatory component in equation 5.2.

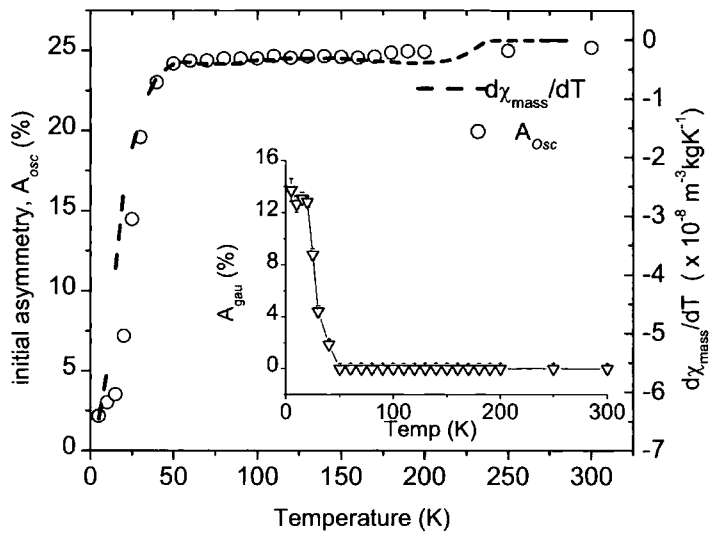

Figure 5.4: Temperature dependence of the initial asymmetry (A_{Osc}) of the oscillatory component for $La_{0.97}Sr_{0.03}CoO_3$ directly compared to the differential of the FC mass susceptibility with respect to temperature. The inset demonstrates the temperature dependence of the gaussian initial asymmetry (A_{gau}).

Fig. 5.4 shows the temperature dependence of the initial asymmetry of the oscillatory component (A_{Osc}) compared to the derivative of the FC magnetic susceptibility with respect to temperature, as this will highlight any subtle change in the magnetic response of the sample. There is a clear dephasing of the muons undergoing precession coincident with a change in the magnetic response below 50 K. A similar response was observed in $LaCoO_3$ as the system underwent the LS - IS transition and was inferred to be due to the presence of magnetic excitons which quickly dephase the muons, as described in chapter 4. In $La_{0.97}Sr_{0.03}CoO_3$ the situation is somewhat different as the material is essentially stoichiometric and the only doping occurs due to the presence of Sr ions. The inset shows the temperature dependence of the initial asymmetry of the gaussian component which clearly increases below 50 K. No change in A_{bg} is seen over the entire temperature range. Appendix B demonstrates the raw data along with the relative fitting parameters required to fit the data for the

relative temperature regions indicating the need for a quick relaxing term at short times below 45 K, when the dephasing occurs. As two terms are necessary to fit the data there are two possible conclusions, indicative of either two muon sites or two magnetic interactions causing the perturbations in the muon response from site to site. It is thought that the later is more likely because of the difference in the temperature dependence of the two depolarisation rates, which is demonstrated clearly later in this section.

Although a phase transition is not detected in the bulk magnetic susceptibility, Fig. 5.3, there is a clear change in the magnetic response below 50 K possibly indicating competing magnetic interactions. This topic will be returned to later in this discussion.

The depolarisation rates identified in equation 5.2 demonstrate fascinating properties. The second gaussian term in equation 5.2 only becomes relevant below 45 K when the muons begin to dephase due to a quickly relaxing component, causing the drop in A_{Osc} highlighted in Fig. 5.4. Below 50 K the depolarisation rate, σ_{tf} simply begins to rise and does not plateau in the temperature window investigated. This is demonstrated in the inset of Fig. 5.5. The depolarisation rate (λ_{tf}) of the oscillatory component demonstrates a rich temperature dependence, as is shown in Fig. 5.5. At low temperatures there is evidence for a previously unobserved magnetic ordering at 26 K, comparison with the FC d.c susceptibility shows no such evolution. However there is a peak in the ZFC data $\sim$ 20 K which is visible in Fig. 5.3. In $La_{0.97}Sr_{0.03}CoO_3$ the Co^{4+} ions in the Sr rich clusters are believed to remain in an S = 1.5 state over the temperature range 2 K - 300 K[12]. The $LaCoO_3$ matrix, is known to undergo a LS-IS transition in the undoped form as highlighted in chapter 4. However no transition is observed at low measuring fields. Chapter 4 clearly indicates that the LS-IS transition in $LaCoO_3$ can be swamped by high spin magnetic excitons, and it appears as though μSR could be sensitive to the $LaCoO_3$ matrix and Sr rich clusters interacting in $La_{1-x}Sr_xCoO_3$.

There are also two shoulders present in the depolarisation rate (λ_{tf}) shown in Fig. 5.5, at 100 K and 175 K. The 100 K shoulder is of general interest

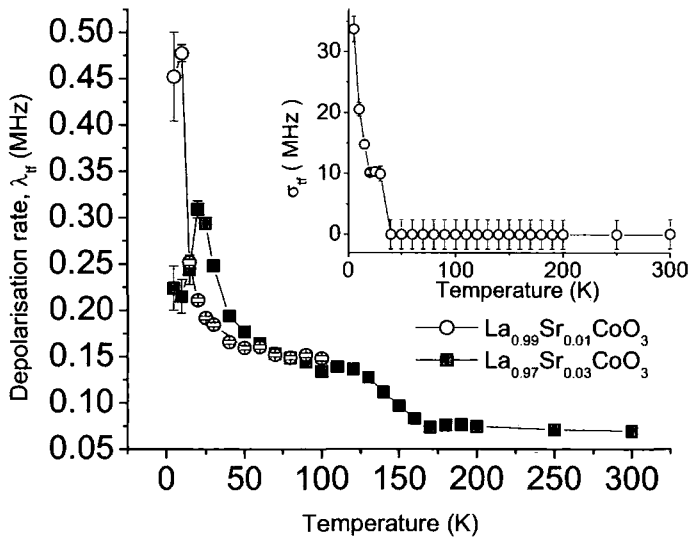

Figure 5.5: Temperature dependence of the depolarisation rates for $La_{0.97}Sr_{0.03}CoO_3$ and $La_{0.99}Sr_{0.01}CoO_3$ obtained from the oscillatory component in equation 5.2. The inset demonstrates the temperature dependent gaussian relaxation for $La_{0.97}Sr_{0.03}CoO_3$. The lines are a guide to the eye.

as this is the onset temperature of the IS-LS transition in pure $LaCoO_3$. The increase in the depolarisation rate is not accompanied by a change in the initial asymmetry or the background term; it simply shows that the internal field distribution of the muon is being affected. The 175 K shoulder is coincident with a subtle change in the initial asymmetry of the oscillatory component identified in equation 5.2. This is 45 K less than that at which the dc magnetic data undergoes a subtle change, i.e T_{irr}. The internal field distribution could be dependent upon the muon position and any Sr cluster-IS matrix interaction. The analogous interaction between the exciton and the IS matrix in $LaCoO_3$, is known to change upon application of magnetic field, as demonstrated in chapter 4. Also shown in Fig. 5.5, is the depolarisation rate for $La_{0.99}Sr_{0.01}CoO_3$ at low temperatures (higher temperatures were not obtained due to time restrictions). The data can be fitted with equation 5.2 and follows the same general behaviour as the $La_{0.97}Sr_{0.03}CoO_3$ sample. However the peak in the data occurs at 10 K, again suggesting the importance of the competing magnetic interactions. Assuming the matrix contributes to the magnetism, the peak will be at a lower

temperature for the $x = 0.01$ sample as the clusters are more dilute. The remaining fitting parameters and the magnetic susceptibility for $La_{0.99}Sr_{0.01}CoO_3$ are shown in appendix B.

5.3.2 Origins of the Sr Cluster and $LaCoO_3$ Matrix Interactions in $La_{1-x}Sr_xCoO_3$

The consensus of opinion is that spin glass behaviour is not seen in compositions below $x = 0.06$, however the interactions that give rise to the bulk spin glass behaviour at high enough densities may be present at lower x concentrations. Specifically a "local" exchange mechanism can be easily inferred from the following situation: each Sr rich cluster composed of competing HS Co^{3+} and Co^{4+} ions has internal ferromagnetic interactions. There are two possible causes of frustration between these isolated clusters. The exchange may be cluster to cluster or the frustration may be caused by coupling of clusters to the undoped $LaCoO_3$ regions of the matrix. Chapter 4 has already clearly demonstrated that the matrix of $LaCoO_3$ is attempting to undergo bulk AF ordering below 220 K. Such interactions in $La_{1-x}Sr_xCoO_3$ would create an individual local anisotropy field for each cluster to produce the cusp in the zero field dc magnetic data demonstrated in Fig. 5.3.1. μSR is extremely sensitive to spin glass behaviour as has already been discussed in chapter 2. However in section 5.3.3 it is shown that no freezing[26] is observed in the ZF μSR data below 26 K. Lappas *et al*[27] have demonstrated that if there is a range of freezing temperatures then it is possible for the depolarisation rate to follow a simple thermally activated behaviour above T_g. This behaviour is demonstrated for $La_{1-x}Sr_xCoO_3$ in Fig. 5.6, which shows the inverse temperature against the depolarisation rate for both the $x = 0.01$ and $x = 0.03$ sample. The deviation from the activation model for the $x = 0.03$ occurs around 135 K, this behaviour is similar to that shown in chapter 4.

$La_{1-x}Sr_xCoO_3$ is not a simple spin glass, and there would have to be a very large spread of spin glass freezing energies on a local scale to allow continued fitting up to 4 times the local spin glass temperature. The activation energy (E_a) for both compositions is calculated and stated in Fig. 5.6, the general behaviour is in agreement for a local T_g[27] as it identifies the peak in the depolarisation rate

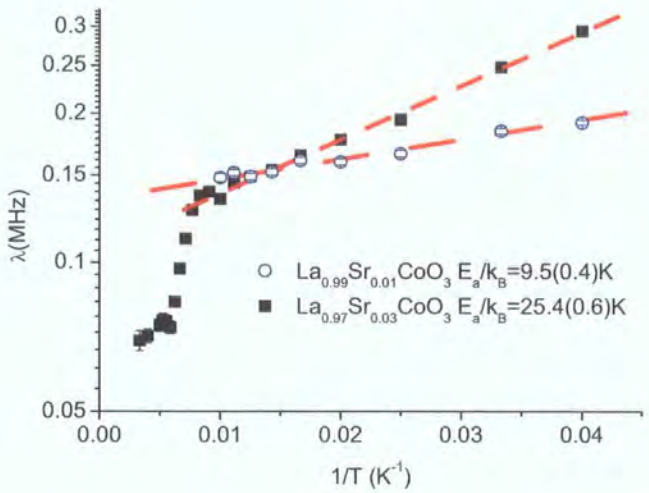

Figure 5.6: Inverse temperature dependence of the depolarisation rates for $La_{0.97}Sr_{0.03}CoO_3$ and $La_{0.99}Sr_{0.01}CoO_3$ obtained from the oscillatory component in equation 5.2.

and the cusp in the dc magnetic data from Fig. 5.3. However the temperature fitting range is far too large. The value of the E_a for the $x = 0.03$ sample is $\sim$ 26 K, for a pure activated form this makes little sense as the fitting range to obtain this energy is $\gg$ than 26 K, if the energy barrier is less than the temperature at which the data are fitted there may be more than one activated process involved. This can easily be envisaged when considering two competing activating energies E_1 and E_2, representing the competing magnetic interactions when a magnetic field is applied, of the form,

$$\frac{A\exp\left(\frac{E_2}{k_BT}\right)}{B\exp\left(\frac{E_1}{k_BT}\right)} = C\exp\left(\frac{E_2 - E_1}{k_BT}\right) \tag{5.3}$$

where A, B and C are constants. The activation energy of $LaCoO_3$ in the LS region when applying a TF field of 10 mT has already been calculated in chapter 4 to be 135 K, which is field dependent as the coupling between the magnetic excitons and $LaCoO_3$ matrix changes. Considering the $La_{0.97}Sr_{0.03}CoO_3$ sample only, as a full data set has been obtained, it is feasible to acknowledge the presence of pristine $LaCoO_3$ regions interacting with the induced HS Co^{3+} ions which form part of the clusters, leading to a situation where E_2/k_B described

by equation 5.3 can be assigned a value of 135 K. Assuming the resulting activation calculated in Fig. 5.6 is 26 K (from the Co^{4+} - Co^{3+} interaction), E_2/k_B obtains a value of the order 110 K, this is the shoulder identified in Fig. 5.5. This suggests that the muons appear to be sensitive to the pristine local $LaCoO_3$ and the exchange between thermally activated Co ions surrounding the Sr rich clusters, a LS-IS transition in $La_{0.97}Sr_{0.03}CoO_3$ is being observed. The $La_{0.99}Sr_{0.01}CoO_3$ shows similar behaviour. However not enough data have been collected and the only comment is that the activated behaviour follows the same pattern as the $La_{0.97}Sr_{0.03}CoO_3$ sample.

5.3.3 Zero Field and Longitudinal Field μSR

Evidence has been presented that demonstrates the possibility of competing exchange interactions at a local level using TF μSR, ideally ZF μSR experiments are preferential when dealing with dilute spin systems such as a spin glass. However due to time restrictions only a limited number of ZF experiments were performed. Specifically evidence for glassy behaviour in the form of a lorentzian Kubo-Toyabe (KT) below T_g is expected[28], as discussed in chapter 2. Three particular temperatures were examined, 10 K, 30 K and 60 K corresponding to temperatures below the observed transition in Fig. 5.5, around the transition and well above the peak at 60 K. Although somewhat limited, the results obtained show interesting behaviour.

Fig. 5.7, demonstrates the relaxation rate of $La_{0.97}Sr_{0.03}CoO_3$ in both the ZF (hollow circles) and LF (hollow squares) configuration at 60 K, with the latter in an external field of 0.5 T. The ZF data could be fitted with relaxation function $G_z(t)$ of the form;

$$G_z(t) = \left[1/3 + 2/3(1 + \Delta^2 t^2)\exp\left[-\left(\frac{\Delta^2 t^2}{2}\right)\right]\right] + A_{bg} \qquad (5.4)$$

where Δ is the distribution of the random fields. This is the KT relaxation discussed in chapter 2. The average local field Δ/γ_μ is found to be 0.3 mT. Application of a large external field fully decouples the relaxation and there is no observed relaxation in the muon time window. A more accurate determination

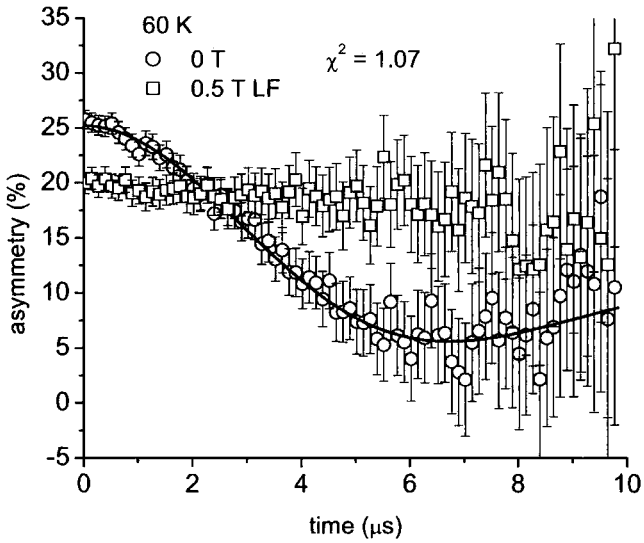

Figure 5.7: Asymmetry comparison of $La_{0.97}Sr_{0.03}CoO_3$ at 60 K in both the ZF configuration and in an external LF of 0.5 T.

of Δ can be obtained by applying small increments of the LF field. However time restrictions prevented this experiment. It is possible that the muons are detecting the local nuclear fields[29], it is expected that this nuclear component exists at lower temperatures but may become dominated by a valence electron contribution. The drop in initial asymmetry with applied field is most likely a consequence of the magnet shifting the beam with respect to the sample position. Hence there is a drop in the asymmetry as not all the muons will hit the sample at high temperatures.

Figs. 5.8 and 5.9, show the relaxation rate of $La_{0.97}Sr_{0.03}CoO_3$ in both the ZF and LF configuration at 30 K and 10 K respectively, both data sets can be fitted with a simple exponential $G_z(t)$ of the form;

$$G_z(t) = A \exp\left[-(\lambda t)\right] + A_{bg} \tag{5.5}$$

where A represents the respective initial asymmetries and λ the depolarisation rate. Clearly, as the transition is approached the muons begin to detect different magnetic interactions. However by comparison of the relaxation rates in Fig. 5.8 and 5.9 it is clear there is no change in the functional form of the relaxation,

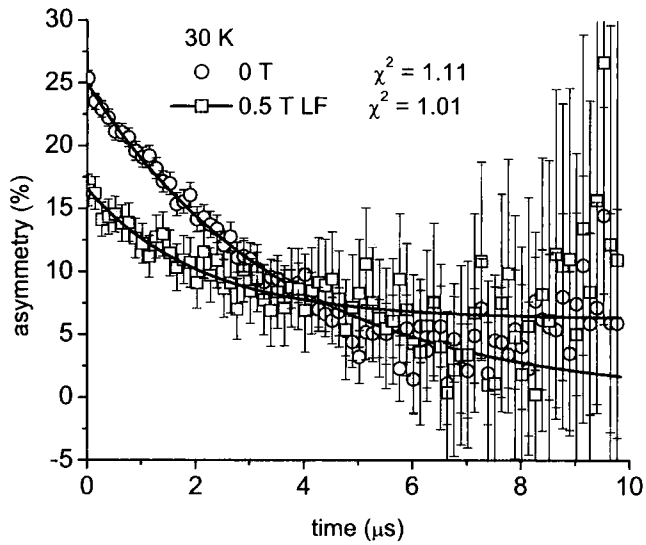

Figure 5.8: Asymmetry comparison of $La_{0.97}Sr_{0.03}CoO_3$ at 30 K in both the ZF configuration and in an external LF of 0.5 T.

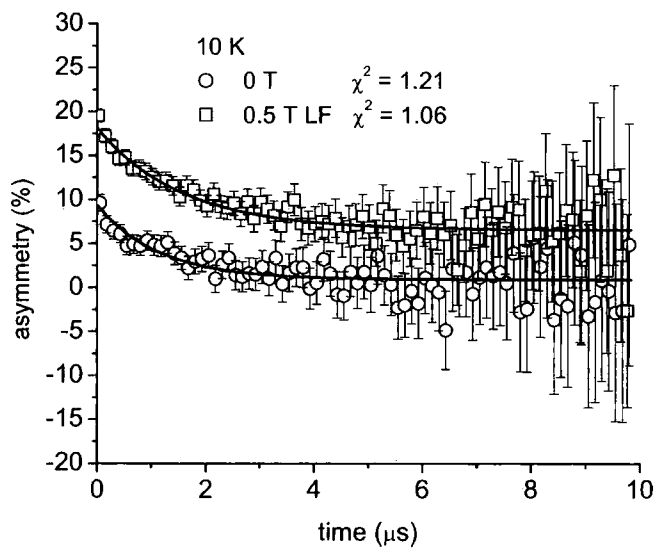

Figure 5.9: Asymmetry comparison of $La_{0.97}Sr_{0.03}CoO_3$ at 10 K in both the ZF configuration and in an external LF of 0.5 T.

which indicates spin glass behaviour. The application of a 0.5 T LF field in both scenarios shows somewhat different results, Fig. 5.8 shows evidence of a

coexisting static and dynamic field. However Fig. 5.9 demonstrates a repolarisation of the initial asymmetry, indicative of the LF orientating the Sr rich clusters, which are no longer affected by any matrix contribution. Although a limited data set, the plots highlight that around 26 K the internal exchange interactions in $La_{0.97}Sr_{0.03}CoO_3$ are undergoing fascinating changes that are unreported in the literature and may impact upon the high composition samples, thus demonstrating that the $LaCoO_3$ matrix at low x concentrations cannot be ignored.

5.3.4 High Temperature Bulk Magnetic Susceptibility Measurements

The evidence presented indicates the presence of magnetic interactions on a local level. However it should be possible to view the local interactions upon a global scale; if the magnetic interactions can be isolated it will be possible to tailor experiments to observe the exchange interactions. The work in this and the subsequent section will focus singularly upon $La_{0.97}Sr_{0.03}CoO_3$ due to the amount of data collected upon this sample.

It is necessary to reiterate the possible magnetic interactions so that the reader can easily visualise the behaviour of the sample. There are two possible magnetic "species" present in $La_{0.97}Sr_{0.03}CoO_3$, the undoped matrix and the Sr rich cluster. The magnetic properties of $LaCoO_3$ have been seen to be modified by the presence of magnetic excitons in the material; in $La_{0.97}Sr_{0.03}CoO_3$ Sr rich clusters exist, containing Co^{3+} and Co^{4+} ions. If there is an interaction between the cobaltite matrix and the cluster at low temperatures, through the LS-IS region, as the results of section 5.3.1 suggest, in the IS region at high temperatures this interaction should also be visible. Fig. 5.10, demonstrates the temperature dependence of the inverse magnetic susceptibility as a function of magnetic field applied during the measurement. The data measured at 5 T, 10 mT and 1 mT clearly superimpose above 225 K, and indeed the θ value for the high temperature Curie-Weiss fits produces a value of 3±4 K demonstrating that the material has essentially a paramagnetic temperature dependence. Below 225 K the data no longer scale and this has been inferred as evidence for a T_{irr} [12].

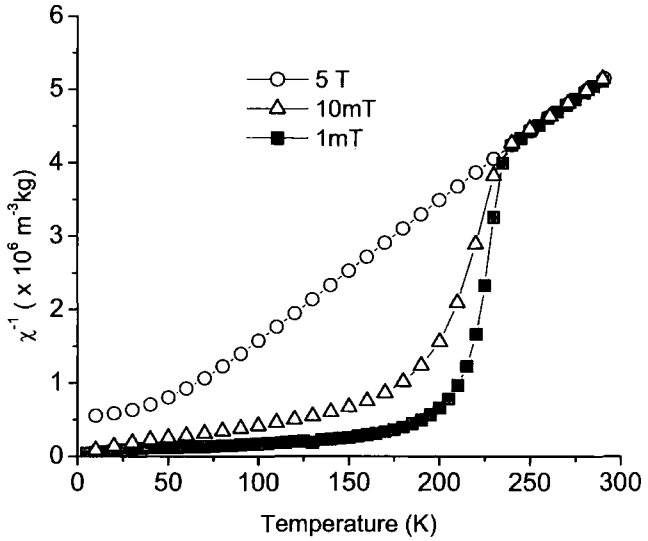

Figure 5.10: Temperature dependence of the inverse susceptibility for different applied magnetic fields.

The experiments performed were FC suggesting that the local anisotropy field is strongly field dependent highlighting the role of competing interactions. One simple origin of this behaviour stems from the local AF interactions in $LaCoO_3$ identified in chapter 4. If these "random" interactions are enveloping the Sr rich cluster a field dependent exchange mechanism can be envisaged where the Co^{3+} HS ions in the cluster are analogous to the magnetic excitons present in $LaCoO_3$ as shown in chapter 4. Note the ferromagnetic intra-cluster interaction (Co^{4+}-Co^{3+}) will be different to the AF interactions observed in the magnetic excitons in $LaCoO_3$.

From Fig. 5.10 it appears as though the $LaCoO_3$ matrix interacts with the clusters, and if this is true a magnetic response similar to that of magnetic excitons embedded $LaCoO_3$ can be expected. From Fig. 5.1, no magnetic remanence is expected in $La_{0.97}Sr_{0.03}CoO_3$. Therefore the cooling protocol identified in chapter 4 was reproduced to isolate the contribution of the clusters and the matrix. The sample was FC in various different fields until 50 K (solid symbols) and then cooled and measured in the remnant field of the magnet. The same procedure was repeated, except that the sample was cooled until 26 K (hollow symbols) as the magnetic response, if coupled by the matrix, will be different.

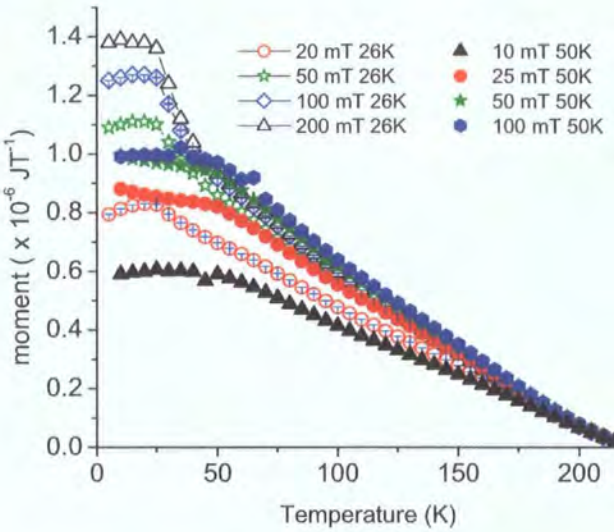

Figure 5.11: Temperature dependence of the remnant magnetic moment of $La_{0.97}Sr_{0.03}CoO_3$ when field cooled in various field until 26 K (hollow symbols) and 50 K (filled symbols).

(At 26 K the majority of the $LaCoO_3$ matrix will have relaxed into an S = 0 diamagnetic ground state.) The results for the cooling protocol comparison are shown in Fig. 5.11, which shows an increase in the remnant component of the moment upon increasing the cooling field as in $LaCoO_3$. The magnitude of the remnant moment also increases with decreasing temperature to which the sample was FC, so indicating a possible contribution from the $LaCoO_3$ matrix at higher temperatures. Note that when cooling fields > 0.2 T then there is a reduction in the remnant moment, presumably because one magnetic term becomes dominant.

The LS-IS transition in $LaCoO_3$ is thermally activated, therefore if the magnetic remanence shown in Fig.5.11 when FC to 50 K is related to the $LaCoO_3$ matrix then the logarithmic form of the remnant moment will be inversely proportional to the applied field on cooling, as described in chapter 4. This is because the internal field distribution will be susceptible to applied field when there are interactions with the matrix. Fig. 5.12 shows the inverse field dependence of the remnant moment with respect to the final cooling temperature. Clearly

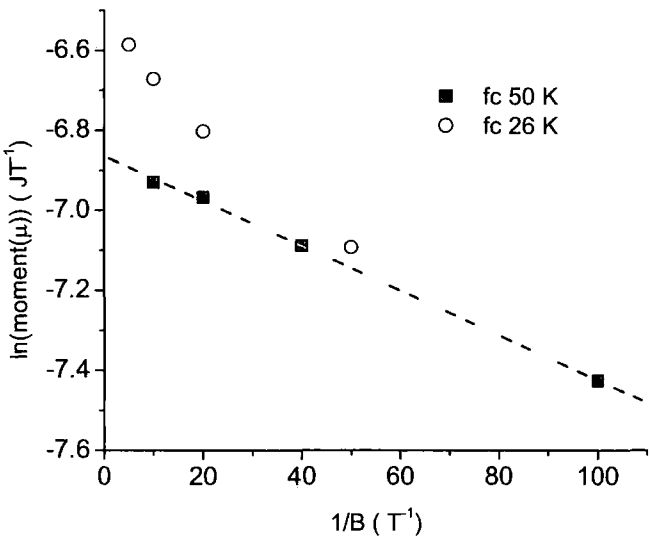

Figure 5.12: Reciprocal field dependence of the natural logarithm of the remnant magnetic moment obtained from Fig. 5.11, when the sample was field cooled to 50 K and 26 K.

the remnant moment is only inversely proportional to the applied cooling field when FC until 50 K; when FC to 26 K the remnant magnetisation no longer demonstrates such behaviour. Using the same interpretation as chapter 4 this would signify the importance of the $LaCoO_3$ matrix to the magnetic properties of $La_{0.97}Sr_{0.03}CoO_3$. Once the majority of the thermally activated Co ions are in a LS state, exchange between the Sr rich clusters can no longer be mediated by the $LaCoO_3$ matrix, leading to a situation where the only exchange between the Sr clusters below 26 K is due to overlapping or clustering regions.

5.3.5 Low Temperature Magnetic Susceptibility

The behaviour of $La_{0.97}Sr_{0.03}CoO_3$ is consistent with the pristine form when magnetic excitons are present, once the matrix has a spin state of zero it is possible that the Sr rich clusters will be exchange coupled. The possible exchange interactions are listed in Table. 5.1, the Sr rich clusters contain interacting Co^{3+}-Co^{4+} ions, and give a large ferromagnetic contribution to the magnetism.

Interaction	Mechanism
Co^{3+}-Co^{3+}	AF
Co^{4+}-Co^{4+}	AF
Co^{3+}-Co^{4+}	FM

Table 5.1: A list of the possible magnetic interactions in the Sr rich clusters[16].

Analogous to the magnetic exciton results in chapter 4, the ordering of the AF interactions may occur upon lowering the temperature. Application of a small measuring field will ensure that the ferromagnetic intra-cluster interactions will be dominant. Hence the low temperature susceptibility data can only be obtained from the Durham low temperature SQUID magnetometer, as identified in chapter 3, due to its small measuring field.

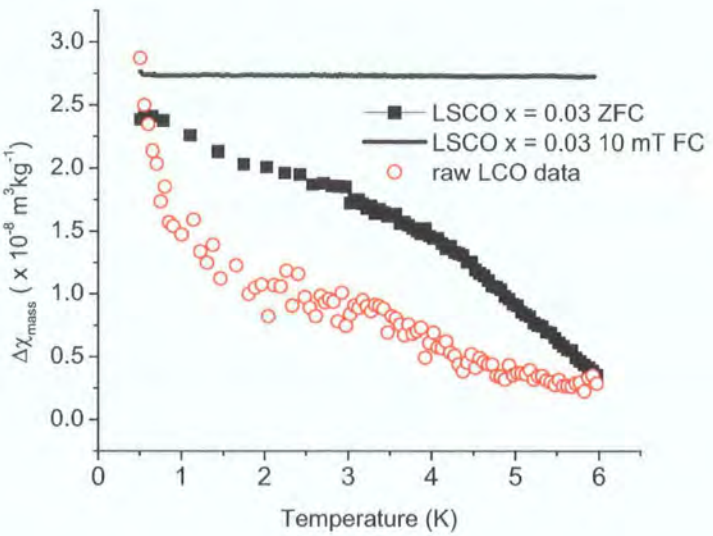

Figure 5.13: Temperature dependent change in magnetic susceptibility of $La_{0.97}Sr_{0.03}CoO_3$, for both FC and ZFC experiments, directly compared to the raw data of $LaCoO_3$, from chapter 4.

Fig. 5.13 shows the temperature dependent change in magnetic susceptibility of $La_{0.97}Sr_{0.03}CoO_3$ when ZFC and FC in 10 mT and subsequently measured in the remnant field of the magnet (10 μT), compared directly to the change in susceptibility for ZFC $LaCoO_3$ as identified in chapter 4. At low temperatures

no paramagnetic tail is present in the $La_{0.97}Sr_{0.03}CoO_3$ ZFC data, unlike in the $LaCoO_3$, suggesting the magnetic species contributing to the remanence is different. The ferromagnetic alignment of the intra-cluster exchange mechanism could be a plausible explanation for this. The ZFC data in $La_{0.97}Sr_{0.03}CoO_3$ also demonstrate a change in slope of the susceptibility at $\sim$ 4 K, in agreement with the $LaCoO_3$, however FC the $x = 0.03$ sample shows a starkly different result. Instead of the transition being amplified by the inter-cluster interaction it appears to be dominated by the intra-cluster ferromagnetic interaction and a flat essentially featureless line is the result. Thus the data appear different to those obtained from $LaCoO_3$, where evidence was obtained for the AF nature of the magnetic exciton.

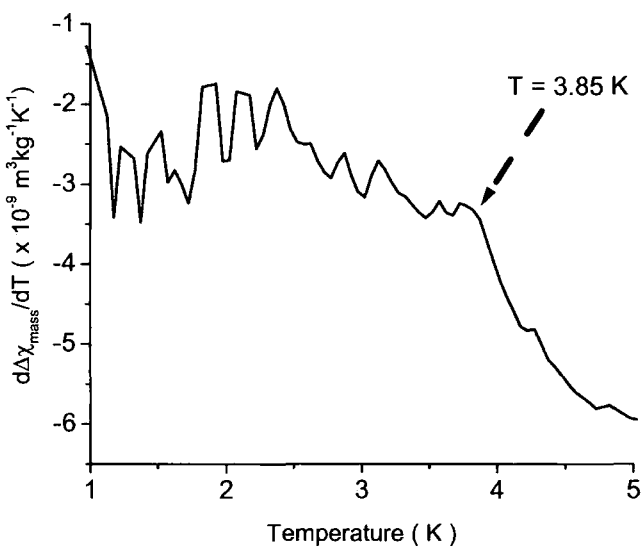

Figure 5.14: Temperature dependent change in derivative of the magnetic susceptibility (ZFC) with respect to temperature for $La_{0.97}Sr_{0.03}CoO_3$.

The derivative of the ZFC susceptibility data with respect to temperature for $La_{0.97}Sr_{0.03}CoO_3$ is shown in Fig. 5.14. A change in slope is identified at 3.85 K, and this is in agreement with the data obtained for the magnetically coupled excitons at low temperature in $LaCoO_3$. Fig. 5.14 suggests that the moment of the Sr-rich cluster can be weakly affected by inter-cluster AF type interactions, therefore once the matrix begins to dominate this exchange dominates and gives

rise to the remnant behaviour observed in Fig. 5.12.

5.3.6 Possible Interactions in Low Doped $La_{1-x}Sr_xCoO_3$

The interpretation of the data is based upon already published work, citing that the Sr rich clusters occur throughout the compositional range and give rise to the magneto-electronic phase separation observed in $La_{1-x}Sr_xCoO_3$[21, 16]. However previous work has constantly neglected any contribution to the magnetism from the $LaCoO_3$ matrix as it is difficult to observe with bulk magnetic measurements. Muon spectroscopy has the sensitivity to detect weak magnetic signals and appears to have detected two contributions to the magnetism. This has been confirmed by tailored bulk magnetic susceptibility measurements.

Temperature	cluster interactions	matrix interactions	matrix-cluster interactions
> 225 K	PM	PM	-
100 K < T < 225 K	Co^{3+}-Co^{4+}- FM	local AF ordering	Co^{3+}-Co^{3+}/Co^{4+}
26 K < T < 100 K	Co^{3+}-Co^{4+}- FM	local AF ordering	thermally activated response
< 26 K	cluster interaction	-	possible cluster overlap

Table 5.2: A list of the possible dominant magnetic interactions in $La_{1-x}Sr_xCoO_3$ suggested by the results of the magnetic measurements. PM = paramagnetic.

The resulting possible magnetic exchange interactions are highlighted in Table. 5.2, demonstrating the temperature regimes where different magnetic interactions are dominating. Above 225 K all the interactions are purely paramagnetic as highlighted in the high temperature region of Fig. 5.10. Below 225 K there are known local AF interactions in the $LaCoO_3$ matrix, inferred from chapter 4, these will interact with the Sr clusters producing a field dependent interaction. Below 100 K the $LaCoO_3$ will begin to undergo an exponential IS-LS transition. This is highlighted in Fig. 5.6, which suggests competing magnetic interactions are thermally activated. This is enhanced by considering the bulk magnetic data of Fig. 5.12 which show a remnant behaviour after FC to 50 K. Once the $LaCoO_3$ matrix is in a LS state the only exchange mechanisms present are inter-cluster interactions; in a direct analogy with magnetic excitons they have

approximately the same exchange energy.

5.4 High Doping Region, $x > 0.05$

Magnetic exchange has been highlighted between the $LaCoO_3$ matrix and the hole doped Sr rich clusters at low x compositions. As the insulator to metal transition is approached the clusters are believed to percolate, however any interaction with the $LaCoO_3$ matrix is always neglected as bulk ferromagnetism is assumed when $x > 0.18$. Preliminary μSR experiments have been performed upon two samples around the MIT, $x = 0.15$ and 0.20. Although recent work has investigated the transition using ZF μSR no direct conclusions were drawn from the relaxation data[30], and the depolarisation rates were not shown. Interpretation of the following data assumes that the muon implantation site is the same for both samples. Due to the large density of Sr clusters in both samples this is not unreasonable.

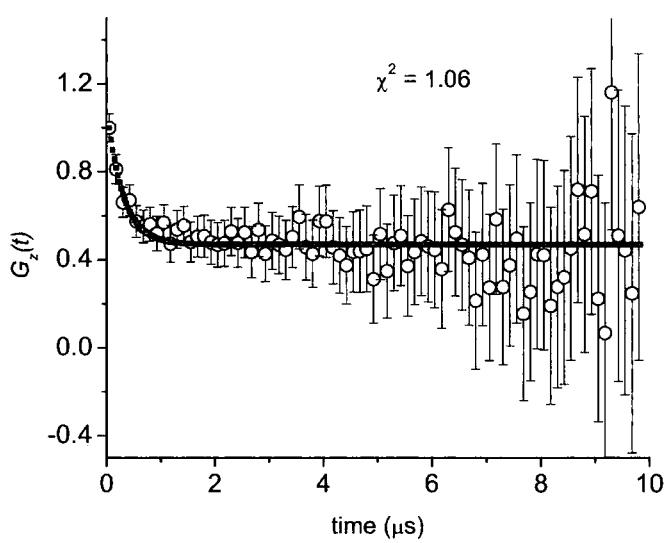

Figure 5.15: The variation of the relaxation function ($G_z(t)$) with time for $La_{0.85}Sr_{0.15}CoO_3$, at 90 K along with the relative fit.

$La_{0.85}Sr_{0.15}CoO_3$ is known to undergo a spin glass transition at 90 K[12] and

then the material becomes paramagnetic. Therefore both experiments were performed in the zero field configuration to enable a direct comparison. Both can be fitted with a relaxation function of the form,

$$G_z(t) = A_{lor} \exp(-\lambda t) + A_{bg}, \tag{5.6}$$

representing a exponential relaxation plus a background term. A_{lor} and A_{bg} represent the initial asymmetry of the exponential and the background term respectively. λ represents the muon spin depolarization rate which is proportional to the magnetic field distribution around the implanted muon and t represents time. Interestingly no spontaneous precession of the muon is observed indicating no long range magnetic ordering, and even above the percolation limit (x = 0.20) the muons are being quickly dephased, most probably by a inhomogeneous distribution of local magnetic moments. Fig. 5.15 demonstrates the relaxation of the muons at T_g which is inferred from Wu *et al*[12]. The data do not show standard spin glass freezing[29], as highlighted in chapter 2, and can be fitted well with a simple exponential relaxation. Furthermore no temperature dependent long time deviations of the relaxation tail are noted. Sadly time restrictions prevented LF measurements being performed.

The behaviour of the relaxation in both samples is not what is expected for a true ferromagnetic ordering of the bulk, suggesting that the clusters are undergoing local interactions. Section 5.3.1 has highlighted a contribution from the $LaCoO_3$ matrix that is strongly dephasing the muon depolarisation, Fig. 5.16 shows the temperature dependence of the initial asymmetry for both $La_{0.80}Sr_{0.20}CoO_3$ and $La_{0.85}Sr_{0.15}CoO_3$ compared directly to the FC d.c magnetic data of the samples. The gradual dephasing in the $x = 0.15$ sample is seen to occur clearly, beginning at 220K and finishing at T_{irr}. The drop in the initial asymmetry clearly tracks the increase in magnetic susceptibility, suggesting that below 220 K the muons are being dephased by local perturbations that induce local magnetic order. This behaviour has been previously observed in section 5.3.1 and chapter 4 and was attributed to the matrix interacting with the clusters/excitons. The muon data shown in Fig. 5.16 can be interpreted with this model assuming matrix-cluster interactions. Above the percolation limit the the muons still dephase indicating that the matrix still contributes to the magnetism even though there is contact between some clusters. The local

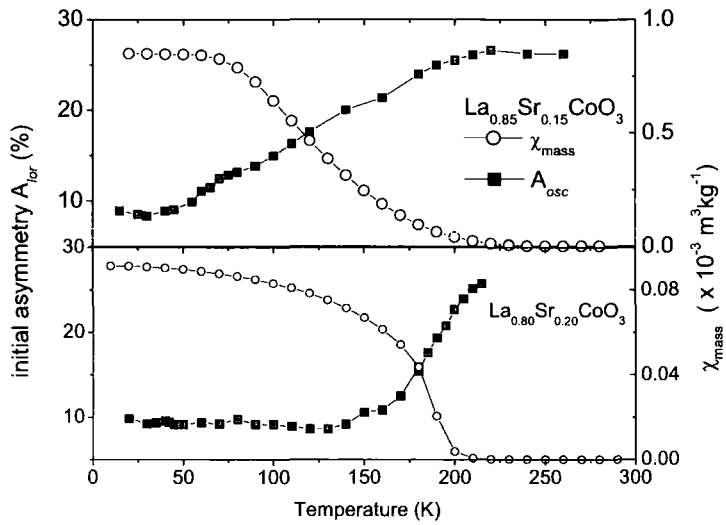

Figure 5.16: Temperature dependence of the initial asymmetry directly compared to the FC mass susceptibility of $La_{0.85}Sr_{0.15}CoO_3$ and $La_{0.80}Sr_{0.20}CoO_3$ respectively. The errors are smaller than the symbols.

matrix interactions moderate the cluster ordering, which explains why all the samples investigated dephase below 220 K, and a similar drop in the asymmetry is observed for the $x = 0.30$ composition[30].

Fig. 5.17 directly compares the temperature dependence of the depolarisation rates (λ) for $La_{0.80}Sr_{0.20}CoO_3$ and $La_{0.85}Sr_{0.15}CoO_3$, the depolarisation rate at the respective transitions are the same for both samples within the error bars, giving a clear indicating that the dephasing of the muons does not alter through the percolative metal insulator transition. This is an important result as it indicates the muons are sampling the Sr clusters (implied from the observed transition temperatures), and that the interaction between the clusters does not change through the MIT. Therefore it appears that the muons are picking up the known magnetic phase separation, however the matrix is moderating the magnetic response upon a local level. Both peaks are extremely broad with the $x = 0.15$ sample showing an increase in λ below 220 K, however the relaxation is not activated or representative of a spin glass transition[26].

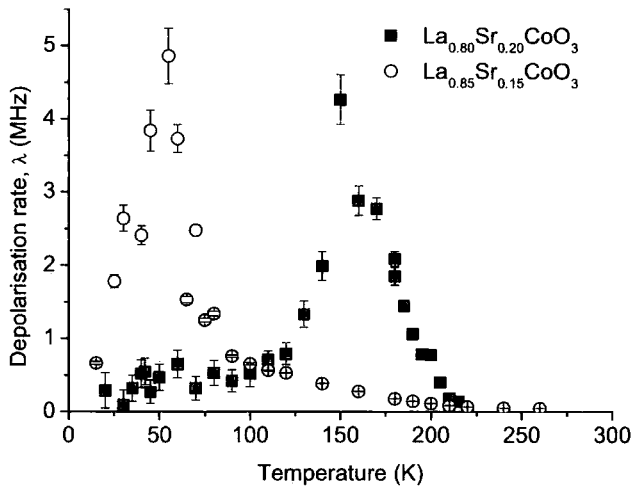

Figure 5.17: Temperature dependence of the depolarisation rates for $La_{0.85}Sr_{0.15}CoO_3$ and $La_{0.80}Sr_{0.20}CoO_3$.

These limited ZF measurements in a direct analogy with section 5.3.1 and chapter 4 indicate the importance of the matrix interaction with the ferromagnetic clusters. Indeed, these interactions allow a plausible explanation as to why the moment in $La_{1-x}Sr_xCoO_3$ cannot be saturated[12, 16].

5.5 Discussion

When Sr ions are used to dope $LaCoO_3$, evidence is presented for the first time of two competing magnetic interactions in $La_{1-x}Sr_xCoO_3$. This can be tentatively interpreted as evidence of interactions between the $LaCoO_3$ matrix regions and the Sr rich clusters, and the intra-cluster ferromagnetic interaction. This would allow for the glassy ferromagnetism which has been previously observed and explain the unmeasurable contribution of the pure $LaCoO_3$ matrix (LS - IS transition) at low doping levels. Bulk μSR evidence is also presented to support the concept of magneto - electrical phase separation around the MIT, along with data further suggesting two magnetic contributions to the muon dephasing. The processes described thus far in the chapter rely upon competing interactions induced by the Sr ions. This interpretation of the data can be further enhanced

by consideration of the Curie - Weiss θ parameter, identified in chapter 2, of $La_{1-x}Sr_xCoO_3$ inferred from high temperature susceptibility data. The change in θ is demonstrated in Table 5.3. There is a clear change in the dominant magnetic exchange interaction as the doping contribution increases. In agreement with previous work, the undoped sample has an AF interaction[31] and upon doping it changes by over 400 K to a ferromagnetic interaction[12] that remains constant above $x = 0.30$. The relatively large error is due to the generally small fitting region between 220 - 300 K, as is observed in section 5.3.4 for the $x = 0.10$ composition. No θ parameter is obtained from the $x = 0.01$ sample, over the temperature range investigated as no linear response to the field is observed.

$La_{1-x}Sr_xCoO_3$	θ
0	-220 ±3 K
0.01	-
0.03	3 ±5 K
0.10	124 ±5 K
0.15	165 ±5 K
0.18	180 ±5 K
0.20	220 ±5 K
0.30	240 ±5 K
0.40	240 ±5 K
0.50	240 ±5 K

Table 5.3: Curie - Weiss, θ parameter of $La_{1-x}Sr_xCoO_3$ as a function of x, calculated from high temperature magnetic susceptibility measurements.

The changing θ parameter indicates two possible scenarios, either the magnetic exchange is changing or it is a function of two contributing interactions of the form;

$$\frac{N_1C_1}{T-220} + \frac{N_2C_2}{T+220} = \chi \tag{5.7}$$

where N and C are the number of ions per unit mass and the Curie constant (without N) for each contributing term respectively. A simple interpretation is that the magnetic susceptibility measurements are in fact detecting magnetic phase separation as the ratio of the N parameter changes assuming C is a constant, i.e S remains constant the only difference is the density due to doping. However, equation 5.7 fails to fit the data for any sample below $x = 0.30$. The

poor fitting of the data could be explained by the clustering of Sr rich regions, but a simple phase separated material cannot be modelled by this scenario.

Assuming a simple Curie Weiss fit to the data the values of C can be tracked with composition. This is presented in Table 5.4 for compositions below the percolation limit. Doping with the Sr ions cannot increase the total number of cobalt ions contributing to the magnetism, as it can only vary the spin state. Therefore, mapping out the increase in C will give a relative increase of the spin state of the Co ions with respect to the doping concentration. A 3 % increase in doping levels produces a 28 % increase in the effective magnetic moment.

	$LaCoO_3$	LSCO x=0.03	LSCO x=0.10	LSCO x=0.15
C (Km^3kg^{-1})	4.4066 x 10^{-5}	5.65387 x 10^{-5}	7.256 x 10^{-5}	0.166
Increase of C	-	28 %	64 %	$\gg$ 99%

Table 5.4: The Curie constant of $La_{1-x}Sr_xCoO_3$ directly compared to that of $LaCoO_3$, along with the relative increase with doping.

Previous investigations of the spin state of the Co ions have considered only samples above the percolation limit[12, 16] and that the spin states of the Co^{3+} ions are the same throughout the material. This assumption is valid for high x values as the increase in the Curie constant is over 99 %. However for low x values, $x = 0.03$ and 0.10 the situation is somewhat complicated. For the $x = 0.03$ sample paramagnetic behaviour is assumed as the θ parameter is close to zero. This means that obtaining the spin state of the relative Co ions should be relatively easy, as C can be related to the spin state assuming the orbital angular momentum is quenched, by,

$$C \propto S(S+1) \tag{5.8}$$

Assuming that in pure $LaCoO_3$ all Co ions are in the IS state, a spin value $S(S+1) = 2$ is obtained. This is a conclusion of chapter 4. Upon Sr doping, 3 % of Co^{4+} ions are induced, and the relative increase of the magnetism can be obtained, The result is compared with the experimental increase in Table 5.4, assuming N remains constant. The first calculation is based upon the Co^{4+} ion being in the HS state, i.e the most magnetic state. Therefore at a composition

of 0.03, S(S+1) = 0.2625, whilst the contribution from the $LaCoO_3$ matrix at a composition of 0.97 is $S(S+1) = 1.94$. This leads to a net increase in the magnetism of only 10 %, which does not meet the obtained value of 28 % obtained from magnetic susceptibility experiments, as outlined in Table 5.4.

Doping must induce other Co ions into a higher spin state at low x concentrations. Table 5.5 directly compares the spin of the system after doping with Sr for the $x = 0.03$ composition. It also assumes the Co^{4+} ion induces a HS state in surrounding Co^{3+} ions, and shows the number of ions required to obtain the correct increase in C. All possible combinations have been calculated. However only the relevant spin states are shown.

Co^{4+} spin state	N° induced Co^{3+} HS ions	matrix S(S+1)	induced S(S+1)	net increase
HS	3	1.76	0.8025	28 %
HS	12.5	0	2.5625	28 %
IS	4	1.70	0.8325	26.6 %
IS	13.5	0	2.5625	28 %
LS	5	1.64	1.1025	28 %

Table 5.5: Contribution of the Sr ion induced spin, directly compared to the matrix contribution for $La_{0.97}Sr_{0.03}CoO_3$

If it is assumed that the matrix does not contribute to the magnetism and is in a LS state, over 12.5 Co ions have to be induced into a HS state. This seems an extremely large number and the muon data would appear to observe a LS-IS transition which is considered un-physical. If the Co^{4+} ion is in a HS state it must induce 3 Co^{3+} ions into a HS state assuming a contribution from the matrix. However the interaction will be AF, and it is known[16, 12] that upon a local scale the ferromagnetic interactions occur. If the Co^{4+} ion is in a LS state 5 Co^{3+} ions must be induced into a high spin state. However the final state of the Co^{4+} ion is thought to be in a IS state[12]. Therefore the conclusion is that the Co^{4+} ions are in a IS state and induces a HS state in 4 Co^{3+} ions.

Above $x = 0.03$ analysis becomes difficult as the θ parameter is undergoing rapid

change that is difficult to model. However it suggests that the rich magnetic and electrical properties are dominated by the Sr rich clusters, a conclusion that has been reached by many different works. However this work demonstrates the importance, although not fully understood, of the $LaCoO_3$ matrix. A similar analysis for $x = 0.10$ cannot be reliably performed because of the large θ parameter, but it is clear that doping with Sr ions has to induce a HS transition in some Co^{3+} ions and that it will interact with the matrix. The possibility of superparamagnetic behaviour of the clusters is ruled out by temperature dependent magnetisation measurements that show no scaling with temperature, see appendix B.

5.6 Conclusions

Evidence has been presented indicating the importance of the $LaCoO_3$ matrix in low doping concentrations of $La_{1-x}Sr_xCoO_3$. Specifically, exchange has been identified between the matrix and the Sr rich clusters. This indicates that at low compositions the $LaCoO_3$ matrix is interacting with HS Co^{3+} ions in the Sr cluster, which also interact with the Sr induced Co^{4+} ion, leading to the competing magnetic interactions detected. The number of HS Co^{3+} ions induced by Sr doping has been calculated. The Sr clusters above and below the MIT show similar behaviour demonstrating the sensitivity of the Sr cluster to its local environment.

References

[1] R. von Helmolt, J. Wecker, B. Holzapfel, L. Schultz and K. Samwer, Phys. Rev. Lett **71**, 2331 (1993)

[2] H. L. Ju, C. Kwon, Q. Li, R. L. Greene and T. Venkatesan, Appl. Phys. Lett **65**, 2108 (1994)

[3] E. Dagatto, T. Hotta and A. Moreo, Phys. Rep **344**, 1 (2001)

[4] M. Fäth, S. Freisem, A. A. Menovsky, Y. Tomioka, J. Aarts and J. A. Mydosh, Science **285**, 1540 (1999)

[5] Ch. Renner, G. Aeppli, B. G. Kim, Y. A. Soh and S. W. Cheong, Nature **416**, 518 (2002)

[6] R. Caciuffo, D. Rinaldi, G. Barucca, J. Mira, J. Rivas, M. A. Senaris-Rodriguez, P. G. Radaelli, D. Fiorani and J. B. Goodenough, Phys. Rev. B **59**, 1068 (1999)

[7] P. L. Kuhns, M. J. R. Hoch, W. G. Moulton, A. P. Reyes, J. Wu, and C. Leighton, Phys. Rev. Lett **91**, 127202 (2003)

[8] D. N. H. Nam, K. Jonason, P. Nordblad, N. V. Khiem and N. X. Phuc, Phys. Rev. B **59**, 4189 (1999)

[9] N. X. Phuc, N. V. Khiem and D. N. H. Nam, J. Magn. Magn. Mater **242**, 754 (2002)

[10] S. Mukherjee, R. Ranganathan, P. S. Anilkumar and P. A. Joy, Phys. Rev. B **54**, 9267 (1996)

[11] K. Asai *et al*, Phys. Rev. B **50**, 3025 (1994).

[12] J. Wu and C. Leighton, Phys. Rev. B **67**, 174408 (2003)

[13] M. Itoh, I. Natori, S. Kubota and K. Motoya, J. Magn. Magn. Mater. **140-144**, 1811 (1995)

[14] R. Mathieu, P. Nordblad, D. N. H. Nam, N. X. Phuc and N. V. Khiem, Phys. Rev. B **63**, 174405 (2001)

[15] A. K. Pradham, Y. Feng, S. Shibata, K. Nakao and N. Koshizuka, Europhys. Lett **56**, 105 (2001)

[16] M.A. Senaris-Rodriguez and J.B. Goodenough, J. Solid State Chem. **118**, 323 (1995)

[17] S. Yamaguchi, Y. Okimoto, H. Taniguchi and Y. Tokura, Phys. Rev. B **53**, R2926 (1996)

[18] G. H. Jonker and J. H. van Saten, Physica **19**, 120 (1953)

[19] C. Zener, Phys. Rev **82**, 403 (1951)

[20] P. W. Anderson and H. Hasegawa, Phys. Rev. B **118**, 141 (1960)

[21] J. Wu, J. W. Lynn, C. J. Glinka, J. burley, H. Zheng, J. F. Mitchell and C. Leighton, Phys. Rev. Lett **94**, 037201 (2005)

[22] P. Ravindran, H. Fjellvåg, A. Kjekshus, P. Blaha, K. Schwarz and J. Luitz, J. Appl. Phys **91**, 291 (2002)

[23] Private Commuincation, J. Wu, Department of Chemical Engineering and Materials Science, 421 Washington Ave SE, University of Minnesota, Minneapolis 55455, USA

[24] S. Mukherjee, R. Ranganathan, P. S. Anilkumar and P. A. Joy, Phys. Rev. B **54**, 9267 (1996)

[25] J. De Almedia and D. Thouless, J. Phys. A **11**, 983 (1978)

[26] Y. Uemura, T. Yamazaki, D. R. Harshman, M.Senba and E. J. Ansaldo, Phys. Rev. B **31**, 546 (1985)

[27] A. Lappas, K. Prassides, F. N. Gygax and A. Schenck, J. Solid. State. Chem **145**, 587 (1999)

[28] S. F. J. Cox, J. Phys. C: Solid State Phys, **20**, 3187 (1987)

[29] S. L. Lee, S. H. Kilcoyne and R. Cywinski, Muon Science, SUSSP, IOP, Bristol (1998)

[30] V. V. Sikolenko, A. P. Sazonov, I. O. Troyanchuk, D. Többens, U. Zimmermann, E. V. Pomjakushina and H Szymczak, J. Phys:condens. Matter. **16**, 7313, (2004)

[31] S. R. English, J. Wu and C. Leighton, Phys. Rev. B, **65**, 220407(R) (2002)

Chapter 6

Probing the Magnetic Ground State of the DX^- Centre in $Cd_{0.85}Mn_{0.15}Te$:In Using Muons

This chapter presents the results of detailed bulk magnetic susceptibility and μSR measurements on the II-VI materials $Cd_{1-x}Mn_xTe$:In and $Cd_{1-x}Mn_xTe$:Al. Primarily the magnetic ground state of the DX^- centre in $Cd_{1-x}Mn_xTe$:In will be investigated, along with the spin glass transition temperature (T_g) of both $Cd_{1-x}Mn_xTe$:In and $Cd_{1-x}Mn_xTe$:Al. The interpretation of the results obtained requires a basic knowledge of the fundamental electrical and magnetic properties of Dilute Magnetic Semiconductors (DMS) in general. Therefore a brief introduction to DMS will be discussed before the characterisation of the samples and the main body of results given. $Cd_{1-x}Mn_xTe$:In has previously been investigated by D. E. Read[1] as part of his Ph.D study at Durham, any magnetic measurements performed as part of that study will be attributed appropriately where necessary.

6.1 Dilute Magnetic Semiconductors

A dilute magnetic semiconductor is a non magnetic semiconducting host doped with magnetic ions. Semiconductors are of general interest because of their application to the microelectronics industry, and changing their physical prop-

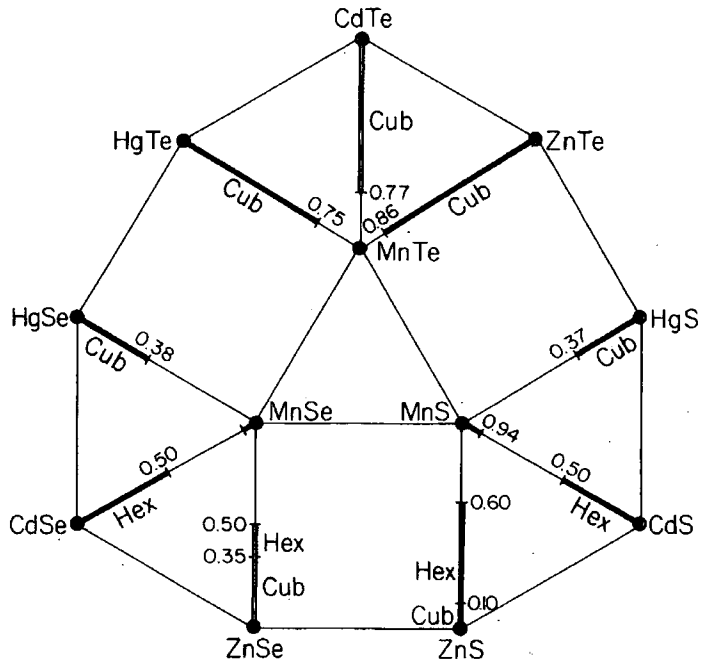

Figure 6.1: An overview of all the II-VI semiconducting materials that have been doped with magnetic Mn ions, "Hex" indicates a wurtzite crystal structure whilst "Cub" denotes a zincblende structure.

erties by doping with magnetic ions has provided a fertile research area for physicists in general over the last thirty years. Specifically, renewed attention in the area has concerned "spin-electronics" where the electron spin is utilised to provide new functionality. The advantage of using a semiconductor as a host material is based upon the reproducibility of well defined physical characteristics, such as carrier density and well defined doping characteristics. Mn ions have been substitutionally incorporated into many II-VI materials, an overview of all the possible bulk samples doped with Mn is shown in Fig. 6.1. The numerical values along the axis indicate the maximum concentration of Mn ions possible in the host material before mixed crystallographic phases occur.

The investigation is primarily concerned with $Cd_{1-x}Mn_xTe$, where CdTe is the non magnetic semiconducting host. The electronic structure of the Mn ion is essential to allow incorporation into the host. The outer valence electron configuration consists of a full s shell leaving the 5 remaining electrons in the

d shell, giving an S = 5/2 value. Hunds rule dictates that this is energetically stable; the addition of another spin would reduce the net moment of the ion. Therefore when doping with the Mn ions they act like a group II element and are readily incorporated into the host. The samples produced for this study were grown by P. Becla[2], and required a single crystal of both $Cd_{0.85}Mn_{0.15}Te$:In and $Cd_{0.85}Mn_{0.15}Te$:Al. Both samples were grown by the vertical Bridgman technique. The crystals were annealed in a cadmium atmosphere to reduce cadmium vacancies which act as compensating centres, thus the final materials produced are n-type.

6.2 Persistent PhotoConductivity

Persistent PhotoConductivity (PPC) is an effect shown by some DMS materials due to exposure to irradiation at a certain wavelength, below a temperature known as the quenching temperature, typically < 100 K in $Cd_{1-x}Mn_xTe$:In[3]. As the name PPC suggests, after the sample is exposed to light which is subsequently removed there is an increase in conductivity, and this persists until the quenching temperature has been exceeded and the material regains its original conductivity prior to illumination. PPC was discovered in $Al_xGa_{1-x}As$:Te[4], and Fig. 6.2, shows the temperature dependent carrier density for both darkness and after illumination[5]. The PPC state was discovered after a prolonged period of research into deep donor levels (induced by doping with impurity ions). Initial explanations by Lang and Logan[6, 7] linked the PPC with a large Stokes shift and a small capture cross section at low temperatures. This type of PPC model is somewhat different to a macroscopic model present in inhomogeneous semiconductors; here there are fluctuations in the conduction and valence band edge. The electron hole pair created by photoexcitation cannot recombine due to the spatial separation caused by fluctuations in the band edge. In the Lang and Logan model the capture of the electron into the deep state required the lattice to distort around the defect centre, this type of centre became known as the DX centre because it was thought to involve a deep state (D) and an unknown defect (X). PPC of the DX variety has been identified in many different materials including, GaAs:Si under hydrostatic pressure[8], $Al_xGa_{1-x}As$:Si[9], $Cd_{1-x}Mn_xTe$:In[3] or Ga[10] and $Cd_{1-x}Zn_xTe$:In[11]. The

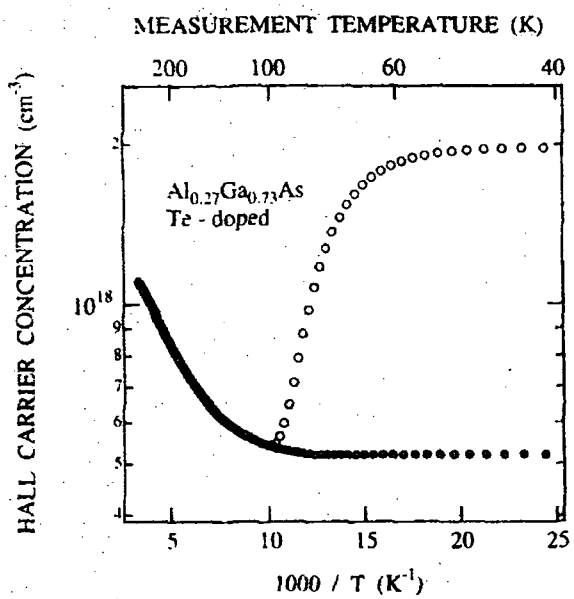

Figure 6.2: The temperature dependent carrier density in $Al_{0.27}Ga_{0.73}As$:Te is shown for both dark data (closed symbols) and illuminated data, reproduced from [5]

exact nature of the DX centre and PPC has generated much interest over the past twenty years.

6.2.1 Large Lattice Relaxation Negative 'U' Model

After the initial experiments it took several years before an accepted theoretical model to describe PPC and DX centres was devised. It is now generally accepted that the DX centres are an intrinsic property of the donor impurities in DMS which can be described by a "large lattice relaxation negative U model", this model was initially used to describe the results of $Al_xGa_{1-x}As$:Si by Chadi and Chang[12, 13]. The key to the model is the prediction of two different types of impurity states from the Si ion, a shallow donor (d^0) just below the conduction band and a second stable state that shifts the Si ion from a lattice site and acquires a second electron to become negatively charged, a so called DX^- state. The lattice distortion determined by pseudo-potential calculations shows an alteration of the Si-As bond. The atomic structure around a Si ion for both

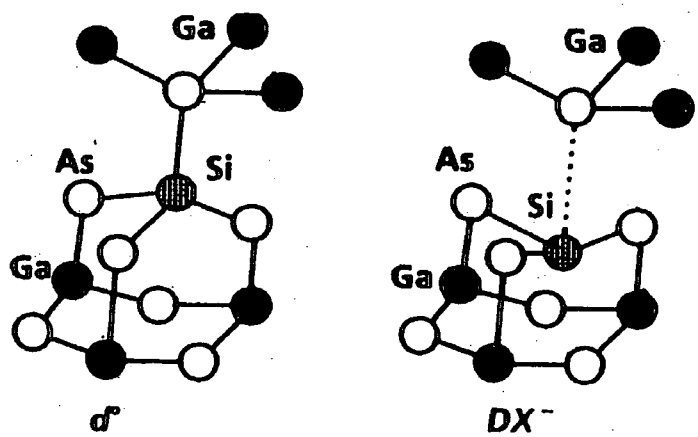

Figure 6.3: Atomic configuration of the shallow donor (d^0) and the deep DX^- level in $Al_xGa_{1-x}As$:Si, showing the distortion of the lattice around the donor atom Si[12, 13]

cases is shown in Fig. 6.3. Experimental evidence supporting this claim shows two separate activation energies as the molar concentration of $Al_{1-x}Ga_xAs$[14] is changed indicating the presence of two possible states. The DX^- centre was proposed to be the result of the following reactions,

$$d^0 \rightarrow d^+ + e^- \tag{6.1}$$

$$d^0 + e^- \rightarrow DX^- \tag{6.2}$$

adding to produce,

$$2d^0 \rightarrow d^+ + DX^- \tag{6.3}$$

where d^0 and d^+ represent the neutral and ionised shallow donor states respectively and e^- is simply an electron. As two electrons are captured by the DX^- centre the lattice distortion is required to overcome the Coulomb repulsion energy of the negatively charged electrons. The model is labeled the large lattice relaxation negative 'U' model because the electrons lead to a negative Hubbard correlation energy, U.

The above description can be described by a configuration coordinate diagram shown in Fig. 6.4, where E_s and E_d represent the the energy of the shallow and deep donor energy respectively. The conduction band is represented by

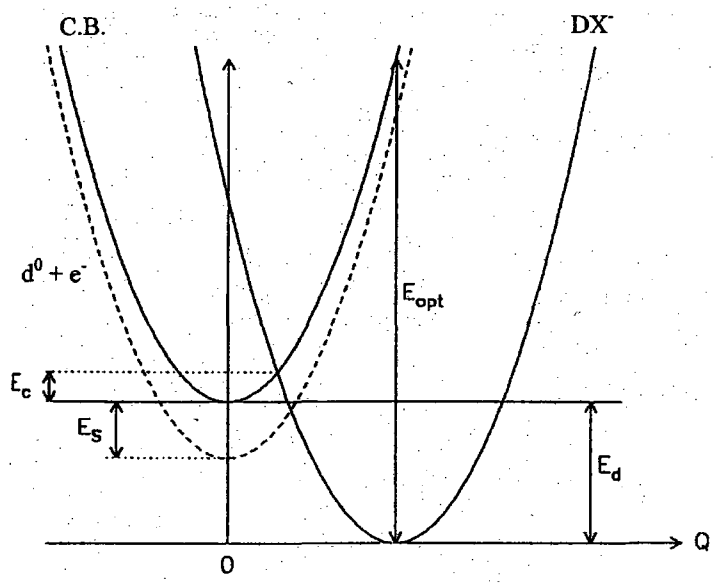

Figure 6.4: Configuration coordinate diagram illustrating the origins of PPC in $Al_xGa_{1-x}As$:Si[12, 13].

the higher energy curve, which also shows the shallow donor level, whilst the DX^- centre is shown using the lower energy curve. As the DX^- centre has the lowest energy when the sample is cooled in the dark all the electrons will fall into it. Therefore the electrons are frozen in the deep state and play no part in the conduction. Application of sub-bandgap radiation, with an energy greater than E_{opt} can be used to excite the electrons into the shallow state and the conductivity will therefore increase following the reaction,

$$DX^- \rightarrow h\nu \rightarrow d^+ + 2e^- \tag{6.4}$$

Once the DX^- centres have been excited, the deep state can only be repopulated once E_c has been surmounted, the so-called quenching temperature, as the material will return to the same value of resistivity as in the dark. This interpretation of the DX^- centre has been confirmed by electron paramagnetic resonance[15], in which the response was enhanced after illumination, as the electrons prior to illumination will be diamagnetic. The magnetic ground state of the DX^- centre has never been fully resolved. High sensitivity SQUID magnetometry measurements provide no convincing evidence for a moment change upon exciting the semiconductor into the persistent state[16, 17]. DC-SQUID measurements made on $Cd_{1-x}Mn_xTe_{1-y}Se_y$[18] were used to infer a singlet ground state of the

DX-like centre following the observation of bound magnetic polarons only after illuminating into the PPC state. However, such an observation cannot be taken as unambiguous proof of a singlet ground state of the DX-like centre; electrons bound to such an energetically "deep" state would be expected to be strongly localized and hence unlikely to form large magnetic polarons, even if in a doublet state. A local magnetic probe has never been used to observe directly the ground state of the DX$^-$ centre.

6.3 Magnetic Properties of Dilute Magnetic Semiconductors

Section 6.2.1 briefly discusses the fact that the magnetic ground state of the DX$^-$ centre is as yet unresolved, as the contribution from the DX$^-$ centre has to be separated from the magnetic ions present in the host material. This study aims to probe the magnetic state of the DX$^-$ centre directly for the first time. Therefore a discussion concerning the magnetic properties of the host DMS will take place, the addition of the impurity ions that cause the DX$^-$ relaxation will cause further complexity. Consideration will be paid primarily to $Cd_{1-x}Mn_xTe$ as this is the material of interest in this chapter.

High temperature magnetic susceptibility measurements show a paramagnetic Curie-Weiss behaviour consistent with an AF exchange interaction[20], and this is clearly demonstrated in Fig. 6.5. The behaviour is consistent with the S = 5/2 magnetic Mn ions being paramagnetic. Below $\sim$ 50 K the Curie-Weiss law is no longer applicable indicating the possible presence of interacting Mn ion clusters. The Curie-Weiss temperature θ can be given by[21],

$$\theta = \frac{2S(S+1)}{3k_B} x \sum_n z_n J_n \tag{6.5}$$

where x is the Mn fraction, z is the coordination number and J_n is the n^{th} nearest neighbour exchange constant. If nearest neighbour only exchange interactions (J_1) are considered and a coordination number of twelve, equation 6.5 simplifies to,

$$\theta = 70x\frac{J_1}{k_B} \tag{6.6}$$

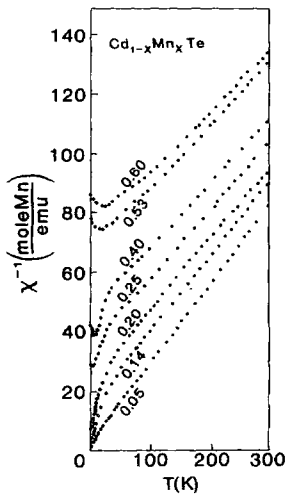

Figure 6.5: Temperature dependent inverse magnetic susceptibility of $Cd_{1-x}Mn_xTe$, for varying values of the composition x[20].

The next nearest neighbour interaction has been found to be a factor of 10 smaller[19] and can therefore be ignored, giving an exchange energy $J_1 \sim -6$ to -10 K. This particular result is of great importance as the interpretation of the data obtained in this study requires the direct experimental comparison of samples with the same Mn fraction, implying they must have similar bulk magnetic behaviour to that described in the literature.

6.3.1 Spin Glass Behaviour

A transition from the paramagnetic to a spin glass (SG) phase was first identified above the nearest neighbour percolation limit, $x \geq 0.17$ in $Cd_{1-x}Mn_xTe$[21]. Measurements were performed using a static magnetic field (d.c magnetisation as opposed to a.c). The standard Field Cooling (FC) and Zero Field Cooling (ZFC) protocols were utilised. Due to magnetic frustration between the antiferromagnetically aligned Mn ions the most energetically favourable states depend on whether the sample is cooled in a field or not. Fig. 6.6, shows the manifestation of these interactions; the temperature dependent magnetic susceptibility is shown for both FC and ZFC results clearing identifying a spin glass transition temperature, T_g, for various compositions of x above the percolation limit.

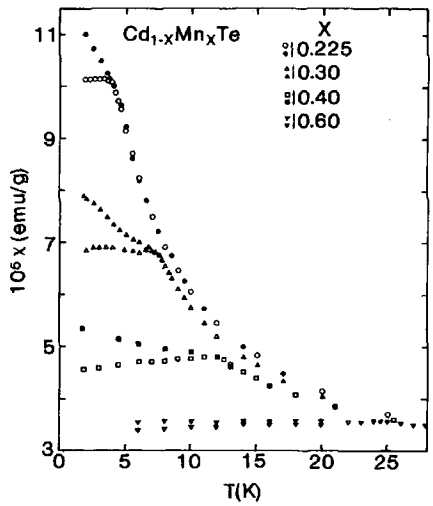

Figure 6.6: Temperature dependent magnetic susceptibility, for varying values of the composition x. Both FC (solid symbols) and ZFC (open symbols) are shown indicating a cusp in the susceptibility indicative of the SG transition. From [21].

Initially it was believed that only a paramagnetic phase existed below the percolation limit. This was disproved by Novak *et al*[22] who discovered spin glass transition temperatures at Mn ion fractions $x \geq 0.01$. The shape of the magnetic susceptibility is also different; as opposed to a cusp a discontinuity is observed. Due to the random nature of clustering one simple explanation is based upon the summation of susceptibility contributions from paramagnetic isolated clusters and a spin glass-like interacting cluster model[23]. As the doping decreases the clusters get smaller hence the lowered T_g.

6.3.2 Photoexcited Contribution to the Magnetic Susceptibility

Previously (section 6.2.1) the effect of the DX^- centre on the conductivity of doped $Cd_{1-x}Mn_xTe$ has been discussed, however the question of photoinduced magnetism has also generated much interest. The clearest indication of increases in magnetisation due to photoexcitation in DMS compounds involves $Cd_{1-x}Mn_xTe_{1-y}Se_y$:In[18], where persistent changes in the magnetisation are

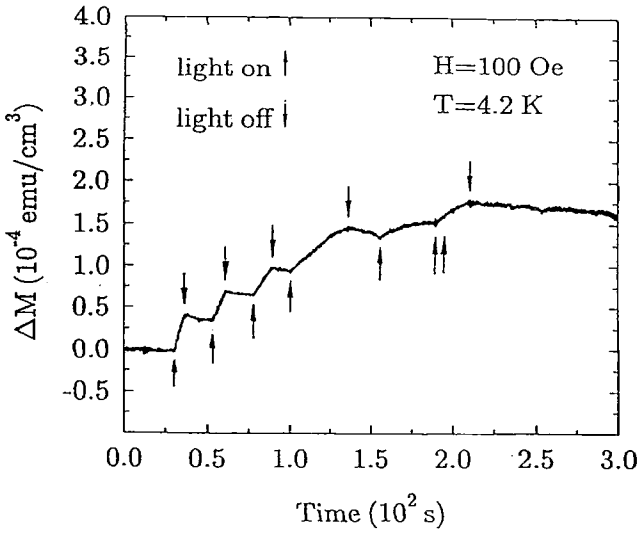

Figure 6.7: The time dependent photo-induced change in magnetisation after irradiation with light in $Cd_{1-x}Mn_xTe_{1-y}Se_y$:In[18].

observed after illumination, this is demonstrated in Fig. 6.7. When the DX^- centre is irradiated, electrons are excited into the shallow donor levels around the impurity ion. Bound Magnetic Polarons (BMPs) form through the ferromagnetic $s-d$ exchange interaction[24] between electrons in the Mn d orbitals and in the conduction band. The susceptibility of BMPs is high and a small external field will saturate their contribution to the magnetisation. Non-persistent photomagnetisation has also been observed in $Cd_{0.80}Mn_{0.20}Te$[25]. When pumped with circularly polarised light, the net magnetic moment was measured as a function of photon energy. Below the band gap energy (E_g) no change in magnetisation was observed. However at E_g a peak in the magnetisation is observed; because the light is circularly polarised any excited electron will be given a preferential spin direction. Hence the net magnetisation is increased. In this particular scenario there is also the possibility of recombination back into the ground state as the material does not exhibit PPC.

6.4 Characterisation of $Cd_{0.85}Mn_{0.15}Te$:In (I1) and $Cd_{0.86}Mn_{0.14}Te$:Al (A1)

The two specific samples, I1 and A1 were chosen for one simple reason. Both have approximately the same Mn concentration, the only difference being the dopant ion, this is important as only I1 will have DX^- centres because an Al ion is too small to distort the lattice to create a deep centre. The electrical transport data are shown in Fig. 6.8, for both samples, before and after illumination. Sample I1 was illuminated at 4.2 K until the PPC was saturated. The same illumination method was applied to A1 but no evidence of PPC was observed even after an extended period of irradiation. It is obvious under the given experimental conditions that only I1 was excited into a PPC state, indicating the presence of DX^- centres. Only one quenching temperature at 100 K is observed. However other investigations into $Cd_{1-x}Mn_xTe$:In[26] and $Cd_{1-x}Zn_xTe$:Cl[27] have recorded another higher quenching temperature indicating the existence of more than one possible deep centre, which have been theoretically predicted[28]. It is believed that heavy doping levels of the crystals could also contribute to multiple DX^- states[29]. Room temperature Hall measurements were performed, giving carrier densities of 1.1 x 10^{16} cm^{-3} and 2.3 x 10^{16} cm^{-3} for I1 and A1 respectively. Resistivity measurements indicate that the shallow donor binding energy for I1 is $\sim$ 220 K and $\sim$ 150 K for A1. Read[1] has recorded EDAX measurements for sample I1 giving a Mn concentration of $x = 0.15$, although no such measurements were performed for A1 the samples were grown under the same conditions and have similar spin glass freezing temperatures, as described in section 6.5.

High temperature d.c magnetic susceptibility measurements have been performed upon the QD MPMS magnetometer described in chapter 3. Measurements have been performed from 2 K - 300 K in fields up to 0.01 T for both samples A1 and I1. The magnetic susceptibility was also measured in lower fields to ensure the temperature dependent suscpetibility was dependent of measuring field, i.e paramagnetic at high temperatures. Fig. 6.9, shows the temperature dependent inverse mass susceptibility, for both samples. A temperature independent mass susceptibility from the diamagnetic background has

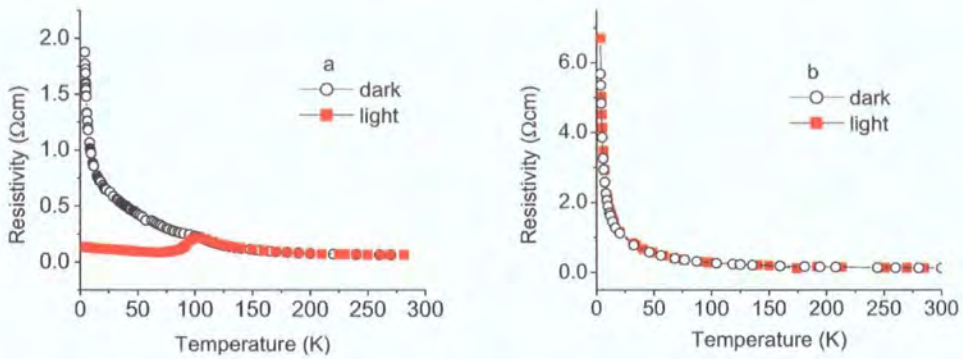

Figure 6.8: Temperature dependent electrical resistivity measurements of $Cd_{0.85}Mn_{0.15}Te$ doped with In (a) and Al (b) respectively, before and after illumination in an attempt to observe a PPC state.

been subtracted. In this case the diamagnetic contribution is from the host lattice, CdTe, and the susceptibility is χ_d = -3.9 x 10^{-9} m^3Kg^{-1}[30], this is applicable for low concentrations of x. At high temperatures the data can be fitted with a straight line, and for both samples an estimate for the Curie constant and the Curie-Weiss (θ) temperature can be obtained. From equation 6.6, assuming a Mn concentration of 0.15, the nearest neighbour exchange energy was determined to be $\sim$ 6 K for both samples, indicating that the bulk magnetic properties of both samples are very similar.

The deviations from simple Curie-Weiss behaviour are in agreement with previous measurements as identified in Fig. 6.5, for both samples A1 and I1 the deviation begins around 60 K. It must be stressed that this behaviour is consistent with other DMS materials such as $Hg_{1-x}Mn_xTe$[31], and is a property of doping the system with magnetic ions. Clustering of the Mn ions can be predicted through a purely statistical model[26], the results of which for each particular sample are described in section 6.6.3. However the basic idea relies on random doping of the Mn ions creating clusters containing up to three Mn ions. The resulting magnetisation is simply a summation of the susceptibility contribution of the different sized clusters. The value of S will be different between clusters of different size leading to a situation at low temperatures where Curie-Weiss behaviour no longer applies. For isolated spins the inverse temper-

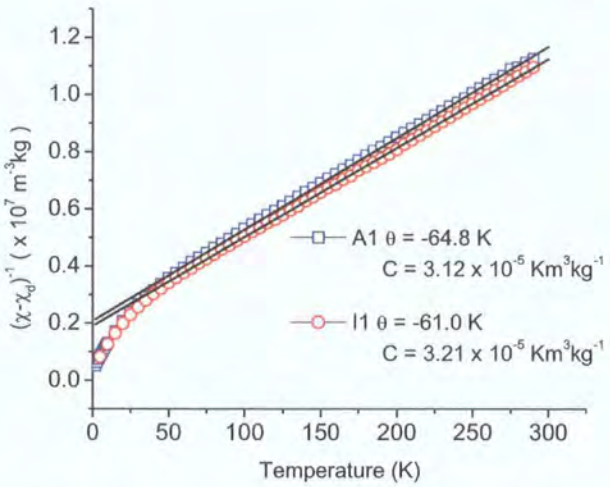

Figure 6.9: The temperature dependence of the inverse susceptibility for I1 and A1 along with the values obtained from a Curie-Weiss fit. The measured susceptibility has been corrected for the diamagnetic contribution of the host.

ature dependence of the susceptibility will be linear for all temperature ranges.

All subsequent measurements were performed upon samples cut from the same crystal ingots that have been used for electrical and magnetic characterisation.

6.5 Low Temperature Magnetic Measurements

In addition to a general characterisation of I1 and A1 described in section 6.4, a detailed report of the low temperature magnetic properties is required because of the low Mn fraction of the samples, denoting a spin glass temperature below 1.5 K[22]. Temperature dependent magnetic susceptibility measurements were performed upon the Durham low temperature SQUID magnetometer described in chapter 3. Both samples were studied using this SQUID system. Low temperature magnetic measurements performed upon $Cd_{0.85}Mn_{0.15}Te$:In (I1) described in this section were performed by Read[1]. The reason for the inclusion of these results in this chapter will become apparent when the muon studies of the spin glass transition region for sample A1 and I1 are discussed.

The temperature dependent magnetic susceptibility between 0.5 K and 1.5

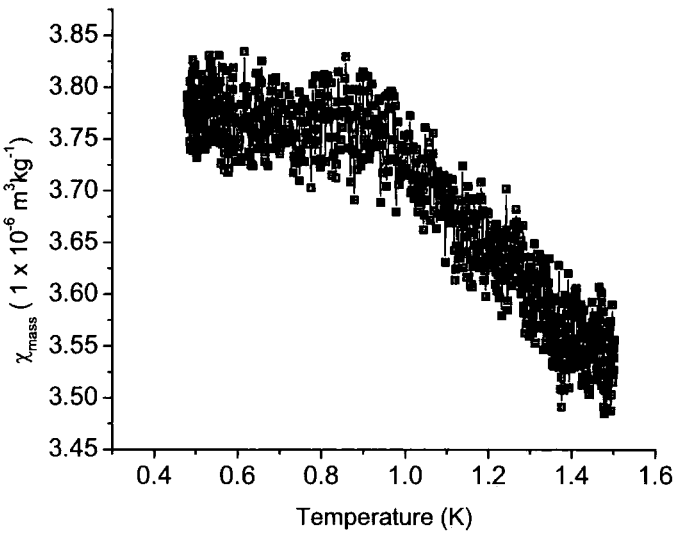

Figure 6.10: The temperature dependent magnetic susceptibility of $Cd_{0.86}Mn_{0.14}Te$:Al (A1), cooled and measured in a field of 10 μT.

K of A1 is demonstrated in Fig. 6.10. The sample was cooled and measured in the residual field of the system, which is 10 μT. The absolute moment was calibrated in the low field paramagnetic region at 2 K by direct comparison with the QD SQUID magnetometer. Although an expected cusp[32] is not apparent in the data it is clear there is a change in gradient at $\sim$ 0.95 K, the same feature at T_g was detected by Novak *et al*[22]. The actual shape of the χ_{mass} vs T curves has been the source of intense debate with evidence for Bloembergen-Rowland interactions[22] and a stronger superexchange interaction. The most plausible explanation is a competition between two interactions; a cluster glass component and a simple Curie-Weiss type behaviour will produce a cusp in the data as observed[23], along with a degree of randomness required for all frustrated systems. A fit to this form is difficult as the cluster glass is assumed to be large with respect to the sample size and there are no deviations in cluster size as expected (section 6.6.3) due to the random nature of the Mn ion doping.

T_g is somewhat difficult to identify directly from Fig. 6.10, and this problem arises from a combination of factors. The signal is very small and the relative

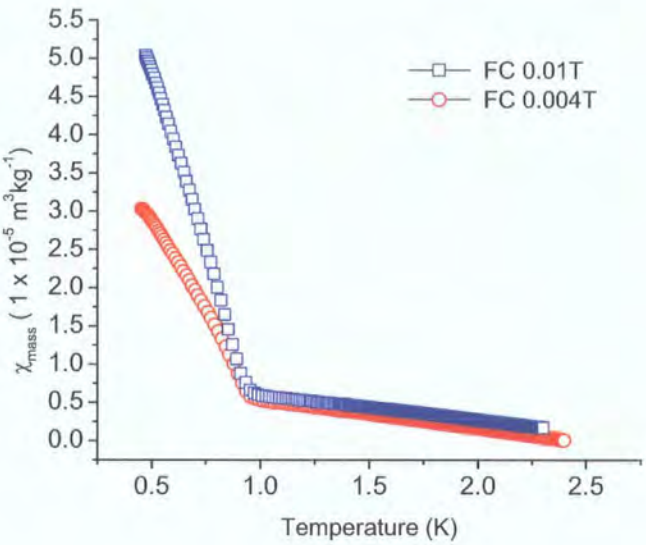

Figure 6.11: The temperature dependent magnetic susceptibility of $Cd_{0.86}Mn_{0.14}Te$:Al (A1), cooled in an external field of 0.01 T and 0.004T, then measured in a field of 10 μT.

change in moment is $\sim$ 4 x 10^{-12} JT^{-1}, therefore the noise base of the low temperature SQUID system is being approached. As the measurement has to occur in the residual field only a subtle change in the magnetisation can be identified. One possible solution involves exploiting the clustering of the Mn ions. If the sample is FC in various fields the response should be field dependent because of the competing interactions of the different sized Mn clusters. Fig. 6.11, demonstrates the temperature dependent mass susceptibility of sample A1 after field cooling in 0.01 T and 0.004 T. T_g is clearly identifiable in this graph giving an accurate value for this sample of 0.950 K $\pm$0.005 K. Clearly the magnetic response of the system is field dependent, and this can be interpreted as an increase in alignment of the clusters with field strength. The behaviour of A1 clearly cannot be described using spin glass theory appropriate to simpler canonical systems such as CuMn or AuFe as no cusp in the d.c magnetisation was seen. Due to the limitations of the measurements no time dependent measurements could be made because of the cooling and warming procedure of the cryostat. Both the cooling time and the warming times were found to be inconsistent over a time period of minutes meaning any relaxation experiments

required to further characterise spin glass behaviour are very difficult to perform.

The T_g of $Cd_{0.85}Mn_{0.15}Te$:In had to be identified in a different way to A1 because of experimental limitations at the time. Specifically the capability to cool in a field other than the remnant field (in this case 50 μT) was not present. Fig. 6.12 shows the results of bulk magnetic susceptibility measurements on sample I1. The main figure shows the derivative of the susceptibility with respect to the temperature before and after illumination into the PPC state. The inset demonstrates the mass susceptibility of the sample before illumination. There is clearly a change in slope around T_g. It was found that calculating the derivative of the magnetic susceptibility with respect to the temperature gives a clear, definitive value of T_g. In this particular case when the sample was measured in the dark the transition temperature was 1.06 $\pm$0.01 K, clearly identified in Fig. 6.12. As discussed in section 6.4, EDAX measured the concentration of Mn ions to be 0.15[1], this corresponds to a T_g of 1.06 K in agreement with previous work[21]. This is important because the Mn concentration of A1 can be inferred from its measured temperature and then compared to both the results I1 and those of Novak *et al*[22] to give a concentration of 0.14, indicating the only major difference between the two samples is the impurity ion.

Section 6.4 describes the effect of the DX^- centre on the resistivity after illumination. Such an observation prompted Read[1] to investigate the magnetic susceptibility of I1 when illuminated into a PPC. The effect of radiating the sample is compared directly to the dark data in Fig. 6.12, where there is an increase in T_g to 1.10 $\pm$0.01 K, this has been attributed to the formation of BMPs[33]. Previous measurements have indicated that photo-induced magnetism can make a significant contribution to the magnetic susceptibility in dilute magnetic semiconductors[18]. The enhancement has been attributed to an increase in the number of BMPs which are localised around donor atoms[1, 34]. For the case of I1 it is possible that the electrons can become localized at shallow donor impurity sites after they are photo excited from the deep DX^- centre. If the DX^- centre is near to Mn atoms which are part of the spin glass cluster it is feasible that these BMPs will have an effect upon the spin glass freezing temperature.

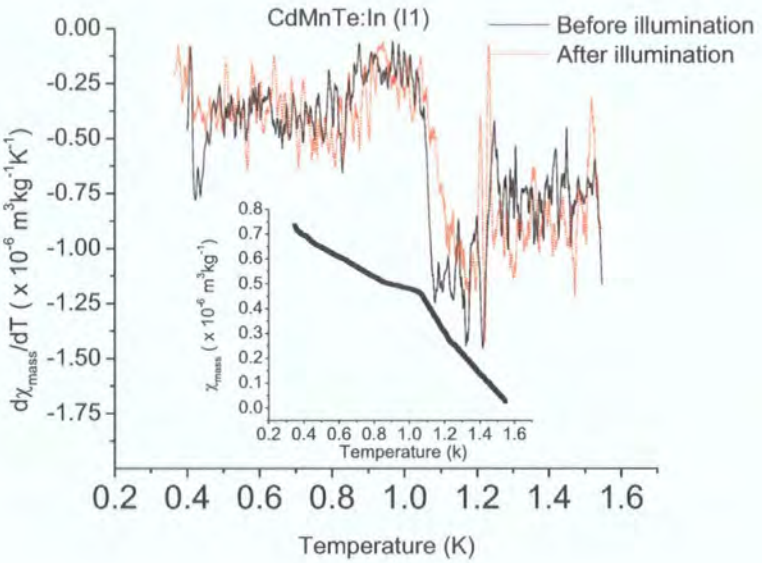

Figure 6.12: Magnetic susceptibility as a function of temperature for $Cd_{0.85}Mn_{0.15}Te$:In. The main figure shows the derivative of the moment with respect to the temperature before and after illumination. The inset shows the mass susceptibility before illumination.From [1].

6.6 Muon Spin Relaxation Measurements

Section 6.5 has already shown the effect of the DX^- centre on the spin glass transition, demonstrating that when electrons are excited out of the DX^- state they contribute towards T_g, and as such have a profound influence upon the magnetism. Previous work has concentrated upon bulk magnetic measurements (i.e electron paramagnetic resonance and SQUID measurements). The presence of BMPs has been determined, although the nature of the magnetic ground state in the DX^- centre as already discussed in section 6.2.1 has remained controversial. Muon Spin Relaxation (μSR) measurements have been made on $Cd_{0.85}Mn_{0.15}Te$:In (I1) and $Cd_{0.86}Mn_{0.14}Te$:Al (A1), and by a direct comparison of the μSR results, the magnetic ground state of the DX^- centre in I1 should be obtainable. This is the first use of a local probe of the magnetism. Section 6.5 indicates the Mn ion fraction and by inference the bulk magnetic properties of the I1 and A1 are similar, muons may be susceptible to the presence of DX^- centres.

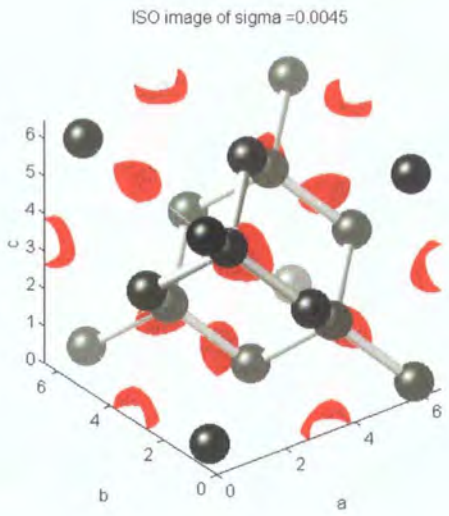

Figure 6.13: The muon implantation site probability distribution as a function of the unit cell ($\AA$), the implanted muons are predicted to sit at an interstitial site, an overlay of the crystal structure is shown for comparison.

Muons have been found to be a useful probe of SG behaviour in $Cd_{1-x}Mn_xTe$ with $x > 0.2$, where the expected muon behaviour, consistent with spin glass transitions is observed[35, 36]. However there is a depolarisation change well above the transition region that has yet remained unresolved. It is important to know the expected position of the muon at the point of decay after implantation, and assuming it to be a positive impurity atom of negligible size it is expected that the muon will sit in an interstitial site in $Cd_{1-x}Mn_xTe$. Electronic dipolar calculations have been performed which indicate the muons will indeed sit at an interstitial site[37]; the muon probability of implantation with respect to the crystal structure is shown in Fig. 6.13. This is in agreement with previous work that predicted interstitial occupation by the implanted muon[35]. Importantly, much work carried out on semiconductors indicates that the addition of donor impurity atoms has little effect upon muon implantation site[38].

6.6.1 Experimental Details

The original aim of the experiment was to reproduce the bulk experimental magnetic susceptibility data on samples I1 and A1 from section 6.5, and this required modifications to the standard ^{3}He sorption cryostat used upon the ISIS beamline, EMU. A bottom-loading OI Helium-3 cryostat with a silver sample holder was modified to enable direct illumination with an LED which has a peak output of 940nm. In particular, the LED was heat sunk to the 1 K pot to enable continuous illumination of the sample whilst at low temperatures. The LED was shielded from the muon beam by a silver plate. The experiment was performed in "fly-past" mode due to the relatively small sample sizes, this consists of two modifications to the overall beamline. A long aluminium tube is connected downstream from the sample so that any muons that miss the sample will decay away from the detectors and as such will minimise the background. Secondly at ISIS there are 4 banks of detectors as described in chapter 3, the 2 banks (one up and one down stream) furthest away from the sample space were disabled because of the large solid angle of the incoming muons, which could miss the small samples and only register in one detector bank and increase counting noise.

6.6.2 Experimental μSR Results

A typical decay rate for both samples, A1 and I1 is shown in Fig. 6.14 above T_g at 1.5 K, along with the respective fits for both samples, details of which will be described later in this section. The first observation is that the relaxation functions required to fit the data are different, immediately suggesting that the muon site is different in the two samples. Thus the nature of the donor impurity ion clearly has a major impact upon the muon relaxation. The specific form of relaxation for each sample did not change over the entire temperature range studied. Given the dilute nature of the donor impurities (10^{18} cm^{-3}) the muon implantation site was not expected to be affected by the donors. It is worth noting that there are $\sim$ 500 muons in the sample at any one time and the position of the muon in the lattice at the point of decay will be the most energetically stable point, normally determined by dipolar interactions. For both samples the application of a small longitudinal field (10 mT) decoupled the relaxation

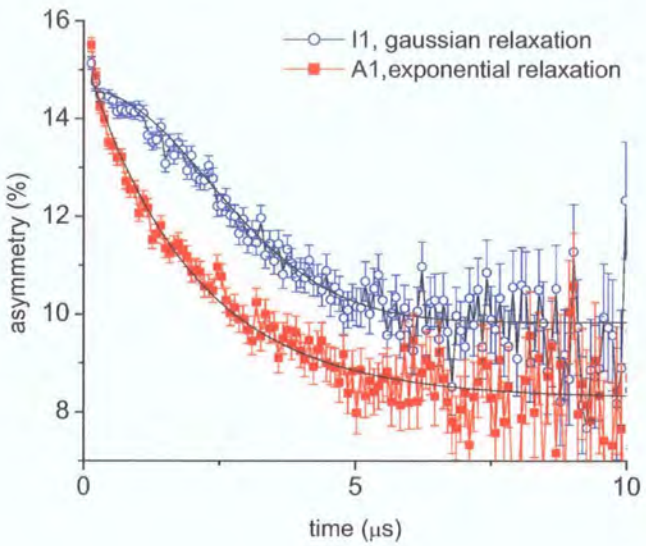

Figure 6.14: The μSR data is shown for both In and Al doped samples prior to illumination, along with their respective fits. The experiments were performed in the zero field configuration at 1.5 K.

below T_g. The signal is from muonium as TF measurements indicate an initial asymmetry of only 8 %. There is an initial point in Fig. 6.14 at short times for I1 that cannot be fitted with a simple gaussian. Although such a relaxation has been observed in previous studies[35], it is too quick for the ISIS time frame and as such it is interpreted as a zero time error in some of the detectors when the measurements were taken. Note the relaxation is much slower than when compared with undoped CMT[35]. The measurements described below were carried out in the zero field configuration.

For sample A1 the data were fitted over the entire temperature range with a relaxation function $G_z(t)$ of the form,

$$G_z(t) = A_{lor} \exp(-\lambda t) + A_{bg} \tag{6.7}$$

representing an exponential relaxation plus a background term. A_{lor} and A_{bg} represent the initial asymmetry of the exponential and the background term respectively. λ represents the muon spin depolarization rate which is proportional to the magnetic field distribution around the implanted muon, t represents time.

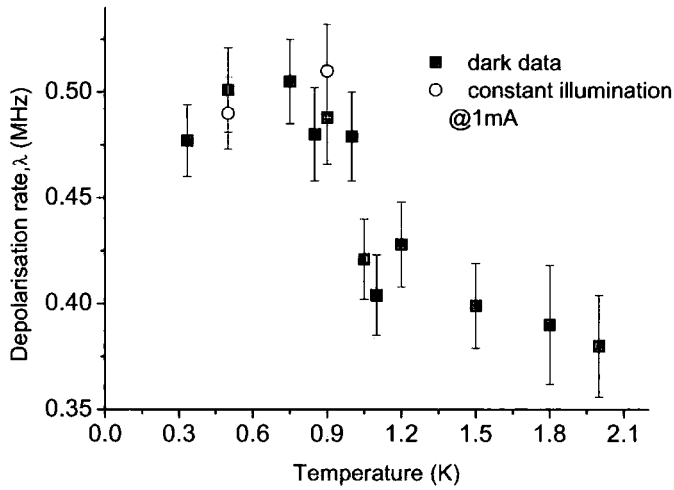

Figure 6.15: The temperature dependent depolarisation rate (λ) of CdMnTe:Al. A clear change in λ is observed at 0.95 K which is coincident with T_g obtained via bulk magnetic measurements (Fig. 6.11). Continually illuminating the sample did not change the depolarisation rate.

Fig. 6.15 shows the depolarization rate in sample (A1) with respect to temperature in the dark and it is clear from this that there is a subtle change in relaxation above 0.95 K, coincident with the observed T_g in the bulk magnetic susceptibility shown in Fig. 6.11 (solid squares). The temperature dependence of the depolarization rate shows no change within the experimental error from 2 K to 10 K. A_{lor} and A_{bg} remained constant through the transition region. Much work has been carried out using μSR to examine spin glass transitions, but the work has tended to concentrate upon canonical systems. Although the exponential relaxation tends to indicate dilute spin systems as described in chapter 2, none of the other expected properties were observed[39]. Measurements were also carried out under constant illumination at 0.5 K and 0.9 K, but no change in the relaxation was observed, as is also demonstrated in Fig. 6.15 (hollow circles). This measurement was essential to confirm the fact that A1 was not affected by sub-band gap radiation, as expected. It also doubled as a test to ensure that under constant illumination the temperature did not change. This is of particular importance around T_g and confirmed that the sample was not heated by the constant illumination.

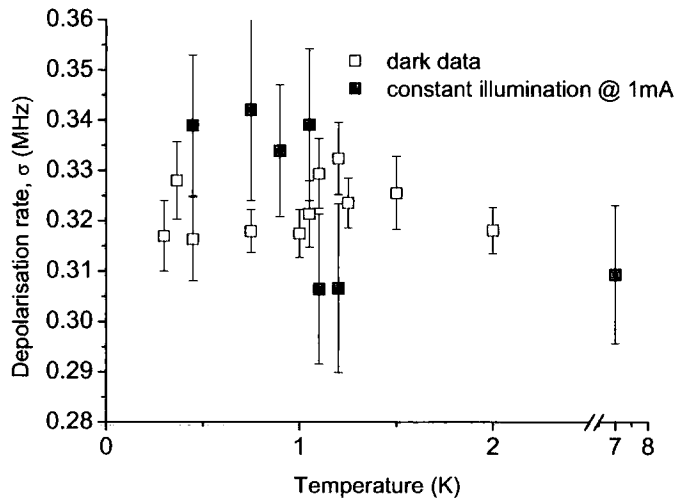

Figure 6.16: The depolarisation rate (σ) of CdMnTe:In is shown through the spin glass transition identified by bulk magnetic measurements, Fig. 6.12. Data prior to illumination and during constant illumination is shown with T_g only visible under constant illumination.

The ZF data of sample I1 was fitted with a relaxation function of the form:

$$G_z(t) = A_{gaus} \exp[-(\sigma t)^2] + A_{bg} \tag{6.8}$$

where A_{gaus} represents the initial asymmetry of the gaussian squared relaxation with σ representing the depolarization rate of the decay. Initial measurements were made without illumination and the results are presented in Fig. 6.16 (hollow squares). The results indicate that there is no change in the relaxation at T_g (1.05 K), and therefore suggest that the implanted muon is tightly bound and does not detect the magnetic Mn ions. Such a situation might be expected if the implanted muon is interacting with the DX^- centre, which appears to be diamagnetic and is only present in sample I1. Sample I1 has already been shown to undergo a subtle change in the bulk magnetization identified in Fig. 6.12 after illuminating until the PPC is saturated. Therefore this phenomena was investigated using μSR. The sample I1 was illuminated at 4 K and subsequently cooled to the base temperature in the dark. The ZF relaxation was measured in the dark. No change in the depolarization rate (σ) was detected

between 300 mK and 5 K, indicating the muons could still not observe the contribution to the magnetic susceptibility of the photo-induced carriers. Once again this suggests that the implanted muons are magnetically screened from the magnetic Mn ions even after illumination into the PPC state. This cannot be explained by the binding of the muon to a shallow state, as no evidence was detected upon the application of a transverse field[40]. Magnetic screening of the muon could occur if the implanted muon forms tightly bound muonium with a diamagnetic negative U centre which cannot be photo-excited under any conditions. However there is another possible explanation based on the premise that there is more than one type of DX^- centre, including a centre that does not contribute to the PPC state. For this particular scenario it is reasonable to assume that there is a relaxation back into the ground state after an initial excitation.

To elucidate the interaction mechanism between the muon and the DX^- centre the sample was continually illuminated from the base temperature through the spin glass transition. The results of this measurement are also shown in Fig. 6.16, (solid squares) where the relaxation rates were fitted with equation 6.8. The data show a major change in the depolarization rate between 1.05 K and 1.10 K, in agreement with T_g obtained from the bulk magnetic measurements as demonstrated in the inset of Fig. 6.12. No change in A_{gaus} and A_{bg} over the temperature range investigated (0.350 mK - 7 K) was seen. The experimental procedure of constant illumination from the LED that was heat sunk to the 1 K pot meant a much shorter stability time for the cryostat, leading to reduced statistics, hence the increase in the error bar size. However it is clear that there is a discernible difference above and below the T_g.

6.6.3 Discussion

The implantation site of the muon is clearly affected by the presence of the In/Al impurities, as has been clearly demonstrated and this can be attributed to the presence of DX^- centres in $Cd_{0.85}Mn_{0.15}Te$:In. A direct comparison of a material without a DX^- centre such as $Cd_{0.86}Mn_{0.14}Te$:Al with similar magnetic properties will allow for a direct comparison between the two systems.

It is clear from the measured relaxation rate (σ) in I1 that the muon position is intrinsic to the observation of the spin glass transition, suggesting that the positively charged muon is attracted to the DX$^-$ centre. This leads to the conclusion that both before and after excitation into the PPC state the muons are still relaxing close to a deep centre which does not detect the magnetic transition. Such a model indicates that not all the DX$^-$ centres are being photo-excited into the shallow donor state and only under continuous illumination are all electrons excited out of their deeply bound state and experience the host magnetism. The muon results also suggest that some electrons are recaptured, indicating there are some centres which do not contribute to the PPC state. This recombination rate is clearly of the order of micro-seconds as the muons can detect a subtle change in the local magnetic structure. Under constant illumination they are not bound to the deep state, but are quickly recaptured. The application of continuous illumination however only produces a small change in relaxation. The time dependent change in the muon relaxation for sample I1 in the dark and under constant illumination is shown in Fig. 6.17. The temperature is 0.9 K and the data shown are the fits to the raw data.

Park and Chadi[28] have predicted multiple DX$^-$ centres in CdTe, ZnTe and $Cd_{1-x}Zn_xTe$ when doped with group VII donors. However the same model predicts only one DX$^-$ centre when doped with a group III element such as In. Leighton *et al*[26] have noted that the very high quenching temperature (190 K) of the PPC they see for $Cd_{0.9}Mn_{0.1}Te$:In suggests the existence of another DX$^-$ centre. Indeed much work on $Al_{1-x}Ga_xAs$[41] has suggested that centres with different binding energies can arise because of the sensitivity of the impurity centre to its local atomic environment. The number of Mn ions surrounding a donor will affect the actual binding energy (E^i) of the DX$^-$ centre, which should be labeled according to the number of Mn (i) ions surrounding the impurity centre, where$i$ = 0, 1, 2, 3. Using a similar statistical argument as other work[26], and assuming no Mn clustering, this work finds that, for x = 0.14, the probability of obtaining a centre with i = 0, 1, 2 or 3 Mn atoms is 55 %, 37%, 5.7% and 2.3% respectively. So far the experimental evidence has only pointed to two possible deep centres. This has been explained by the low prob-

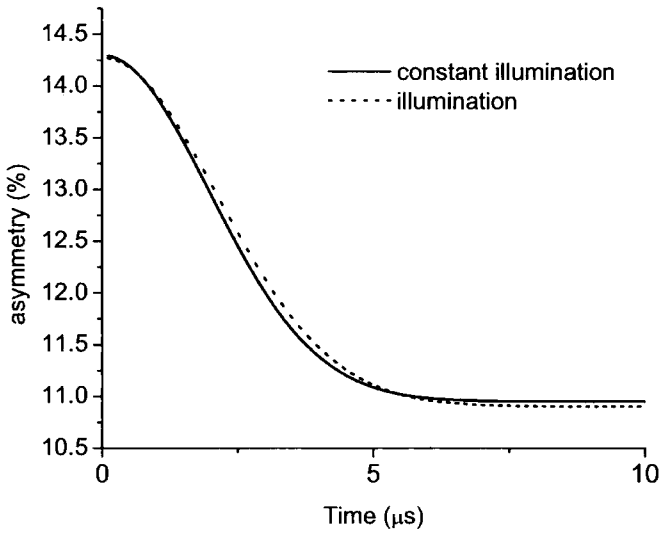

Figure 6.17: The time dependent change in the muon relaxation for $Cd_{0.85}Mn_{0.15}Te$:In in the dark and under constant illumination, the change in observed relaxation is very small at 0.9 K.

ability of finding the high Mn environment. However the results suggest that the muon is susceptible to any DX^- centre relaxation after excitation, leading to the situation where the implanted muon could be surrounded by 2 or 3 Mn ions. This could explain why the form of muon relaxation is different between A1 and I1. Muon decay in I1 would not be in a dilute environment and hence expalin the gaussian relaxation.

A recent theoretical study in CdTe[42], citing experimental work relating to a high In concentration (10^{21} cm^{-3}), has demonstrated that during illumination not all the DX^- centres can be transformed because the substitutional configuration becomes energetically unfavorable at a certain concentration of electrons in the conduction band. It has been predicted that only a concentration of 10^{18} cm^{-3} DX^- centres can be photo-excited. The results indicate that under illumination all the deep centres are excited into the conduction band. However a certain proportion of the electrons recombine to form a DX^- centre (in a time of approximately $10\mu s$), leading to a situation where constant illumination has to be applied to detect the spin glass transition. The electrons appear to re-

combine with previously unobserved DX^- centres.

The large negative U model also predicts that the DX^- centre is diamagnetic. This is a direct consequence of equation 6.3 as two electrons will pair with opposite spin. When the implanted muon is tightly bound to the DX^- centre no magnetic transition would is visible. However under photo - excitation a T_g is observed as the muons are no longer tightly bound. Previous work has concentrated on the influence of the deep centre on the bulk magnetic properties[43, 17, 15, 16]. However, here a local probe ($\sim$ 2nm) has been used, concentrated around the deep centre to probe its magnetic properties, and provide strong evidence for the diamagnetic nature of the DX^- centre ground state. Again it is essential to note that work has been performed on a sample (A1) without a DX^- centre with nominally the same Mn concentration, indicating importance of the deep centre upon the implantation site.

6.7 Conclusions

In conclusion the evidence suggests that muons are attracted to DX^- centres and the muon becomes a local magnetic probe of the deep centre. The first local magnetic measurements have been performed indicating the diamagnetic nature of the ground state of the DX^- centre. There is more than one possible DX^- centre, which has before been experimentally observed and theoretically predicted. However the previous measurements have only been able to distinguish centres which participate in PPC. From the measurements performed it has been possible to prove that there are more DX^- centres which do not participate in the PPC effect leading to the situation where this could possibly explain the lack of the expected photo induced carriers[1].

The sensitivity of the muon to weak magnetic behaviour in II-IV materials has clearly been demonstrated. One possible interesting experiment would be to observe the formation of BMPs using μSR. Obviously this would have to be performed upon a sample that does not contain DX^- centres and the relaxation of the polaron is within the muon time window, in effect reproducing the work

of Awschalom *et al*[25] with a local probe. The advantage of using muons is their sensitivity to ferromagnetic behaviour. Thus any coherent behaviour of the BMPs could be detected unambiguously for the first time.

References

[1] D. E. Read, Ph. D thesis, University of Durham (2001)

[2] P. Becla, Department of Materials Science and Engineering, MIT, Cambridge, MA 02139.

[3] I. Terry, T. Penney, S. von molnar, J. M. Rigotty and P. Becla, Solid. State. Comms **84**, 235 (1992)

[4] For a review see, P. M. Mooney, J. Appl. Phys **67**, 3 (1990)

[5] T. Laine, J. Makinen, K. Saarinen, P. Hautojarvi, C. Corbel, M. L. Fille and P. Gibart, Phys. Rev. B **53**, 11025 (1996)

[6] D. V. Lang and R. A. Logan, Phys. Rev. Lett. **39**, 635 (1977)

[7] D. V. Lang, R. A. Logan and M. Jaros, Phys. Rev. B **19**, 1015 (1979)

[8] G. W. Iseler, J. A. Kaflas, A. J. Strauss, H. F. MacMillan and R. H. Bube, Solid State Commun, **10**, 619 (1972)

[9] T. N. Theis, P. M. Mooney and B. D. Parker, J. Elec. Mat **20**, 35 (1991)

[10] N. G. Semaltianos, G. Karczewski, T. Wojtowicz and J. K. Furdyna, Phys. Rev. B **47**, 12540 (1993)

[11] K. Katchaturyan, M. Kaminska, E. R. Weber, P. Becla and R. A. Street, Phys. Rev. B **40**, 6304 (1989)

[12] D. J. Chadi and K. J. Chang, Phys. Rev. Lett **61**, 873 (1988)

[13] D. J. Chadi and K. J. Chang, Phys. Rev. B **39**, 10063 (1989)

[14] N. Chand, T. Henderson, J. Klem, W. E. Masselink, R. Fischer, Y. C. Chang and H. Morkoc, Phys. Rev. B **30**, 4481 (1984)

[15] P. M. Mooney, W. Wilkening, U. Kaufmann and T. F. Kuech, Phys. Rev. B **39**, 5554 (1989)

[16] K. A. Kachaturyan, D. D. Awschalom, J. R. Rozen and E. R. Weber, Phys. Rev. Lett **63**, 1311 (1989)

[17] S. Katsumoto, N. Matsunaga, N. Yoshida, Y. Sugiyama and S. Kobayashi, Jpn. J. Appl. Phys **63**, L1572 (1990)

[18] T. Wojtowicz, S. Kolesnik, I. Miotkowski and J. K. Furdyna, Phys. Rev. Lett **70**, 2317 (1993)

[19] J. K. Furdyna, J. Appl. Phys **64**, R29 (1988)

[20] S. B. Oseroff, Phys. Rev. B **25**, 6584 (1982)

[21] S. Oseroff and P. H. Keesom, Ch 3, (Volume*25*) Diluted Magnetic Semiconductors, Academic Press, Oxford (1988)

[22] M. A. Novak, O. G. Symko, D. J. Zheng and S. Oseroff, J. Appl. Phys. **57**, 3418 (1985)

[23] D. Karaoulanis, J. P. Xanthakis and C. Papatriantafillou, J. Magn. Magn. Mat **161**, 231 (1996)

[24] J. A. Gaj, R. Planel and G. Fishman, Solid State Comms **29**, 435 (1979)

[25] D. D. Awschalom, J. Warnock and S. von Molnar, Phys. Rev. Lett **58**, 812 (1987)

[26] C. Leighton and I. Terry, Phys. Rev. B **56**, 6689 (1997)

[27] T. Theio and J. W. Bennett, Phys. Rev. B **54**, 1754 (1996)

[28] C. H. Park and D. J. Chadi, Phys. Rev. B **52**, 11884 (1995)

[29] L. Dobaczewski, P. Kaczor, M. Missous, A. R. Peaker and Z. R. Zytkiewicz, J. Appl. Phys. **78**, 2468 (1995)

[30] R. M. Candea, S. J. Hudgens and M. Kastner, Phys. Rev. B **18**, 2733 (1978)

[31] S. Nagata, R. R. Galazka, D. P. Mullin, H. Akbarzadeh, G. D. Khattak, J. K. Furdyna, and P. H. Keesom, Phys. Rev. B **22**, 3331 (1980)

[32] J. A. Mydosh, Spin Glasses: An Experimental Introduction, Taylor and Francis, London (1993)

[33] A. L. Chudnovskiy, R. Oppermann, B. Rosenow, D. R. Yakovlev, U. Zehnder, and W. Ossau, Phys. Rev. B **55**, 10519 (1997)

[34] T. Dietl and J. Spalek, Phys. Rev. B **28**, 1548 (1983)

[35] E. J. Ansaldo, D. R. Noakes, J. H. Brewer, S. R. Kreitzman and J. K. Furdyna, Phys. Rev. B **38**, 1183 (1988)

[36] A. Golnik, A. Weidinger, Ch. Niedermayer, C. Bernhard and E. Recknagel, Phys. Rev. B **55**, 13002 (1997)

[37] Personal Comm, A. D. Hillier, ISIS Laboratory, Oxford, UK.

[38] S. F. J. Cox, J. Phys. C: Solid State Phys **20**, 3187 (1987)

[39] Y. Uemura, T. Yamazaki, D. R. Harshman, M.Senba and E. J. Ansaldo, Phys. Rev. B **31**, 546 (1985)

[40] J. M. Gil, H. V. Alberto, R. C. Vilao, J. Piroto Duarte, P. J. Mendes, L. P. Ferreira, N, Ayres de Campos, A. Weidinger, J. Krauser, Ch. Niedermayer and S. F. J. Cox, Phys. Rev. Lett **83**, 5294 (1999)

[41] E. Calleja, F. Garcia, A. Gomez, E. Munoz, P. M. Mooney, T. N. Morgan and S. L. Wright, Appl. Phys. Lett **56**, 934 (1990)

[42] S. Lany, H. Wolf and T. Wichert, Phys. Rev. Lett **92**, 225504 (2004)

[43] R. E. Peale, Y. Mochizuki, H. Sun and G. D. Watkins, Phys. Rev. B **45**, 5933 (1992)

Chapter 7

Characterisation of a Novel Organic Magnet

This chapter discusses the properties of the novel organic magnet PANiCNQ, and describes the preliminary characterisation of several samples of the material. Various investigative techniques conclude that the origin of the bulk magnetic order observed is organic in nature. The following study initially discusses the origin of magnetic exchange in organic based materials, along with selected examples specific to the material investigated and concludes with results obtained from several batches of PANiCNQ. This results presented in this chapter were the result of intensive and productive collaborations with various groups. This work would not have been possible if it was not for the generosity of Stephan von Molnár who allowed unlimited access to the facilities of the MARTECH laboratory at Florida State University. The work was primarily conducted in collaboration with Naveed Zaidi and Andy Monkman from the Organic and Electroactive Meterials group in Durham. The samples were fabricated by Naveed Zaidi, and the characterisation of the samples undertaken by the author of this thesis.

7.1 Introduction

Magnetic materials have been of great technical importance since their first application as a compass in approximately 300 BC, however, the phenomena

of ferromagnetism has generally been associated with metallic elements such as iron, nickel and cobalt to name a few. Rich magnetic phases have been detected in many materials and subsequently been utilised in technological advances, perhaps the most elegant being the discovery of giant magnetoresistance and its subsequent rapid deployment as a magnetic read head for computer hard drives. Despite all the advances, one of the greatest remaining challenges for solid state physicists is the search for ferro or ferrimagnetic ordering in organic materials at room temperature, where the magnetism is a consequence of lone electrons upon light elements such as carbon and hydrogen.

A brief introduction to the experimental and theoretical advances that allow a understanding of organic exchange will be given in section 7.2. To place the work in context, it is essential to list the main avenues of research attempting to develop bulk magnetic order in organic materials. There are many reviews that describe research prospects in detail, with Crayston *et al* producing the most useful report[1]. There is essentially a four pronged attack upon the problem. (*i*) Many researches are concentrating upon nitroxide based materials as this is the base of the first pure organic ferromagnet *p*-nitrophenyl nitronyl nitoxide (n-NPNN). However the Curie Temperature (T_c) is only 0.6 K[2]. T_c can be increased by reducing distances between the organic molecules and thus increasing the exchange energy. This has produced some success with crystalline forms of nitroxide radical material, rasing T_c to 1.38 K[3]. The highest T_c ever recorded for an organic molecular magnet is 36 K, for a sulphur-nitrogen dithiadiazolyl radical. This was inferred to be due to a spin canting transition[4]. (*ii*) Others have concentrated upon organo-metallic complexes in an attempt to understand the inter-chain magnetic exchange interactions. The behaviour of metallic orbitals is relatively well understood and as such the T_c has been gradually increased from an initial value of 1 K[5], to well above room temperature. For a full review, see the work by Miller *et al*[6]. (*iii*) The ground state of a carbon ion is a triplet, and as such there has been considerable effort to observe bulk ferromagnetism in pure carbon. The first evidence of a magnetically ordered phase in carbon was obtained serendipitously when attempting to polymerise carbon under high pressure, obtaining a T_c of over 500 K[7]. Indeed, a recent experiment upon extraterrestrial graphite (formed under high pres-

sure) has suggested a magnetic ordering temperature of 570 K[8]. (*iv*) The most relevant work to the present study is that performed in the drive for high spin polymeric materials. Large cross linked polymers have recently achieved ordering upon a bulk scale at 10 K, with each polymer unit having a spin, S $\sim$ 5000[9]. This particular work is of interest as it suggests high spin polymer repeat units can be fabricated that have a large intra-chain exchange energy in an amorphous material. It is the intra-chain coupling that is limiting T_c, if it is possible to increase the exchange strength the ordering temperature should subsequently increase.

7.2 Exchange Coupling

This section will highlight the possible exchange coupling present in organic materials. The actual mechanism is somewhat complicated and can be separated into two distinct components. The exchange can either be through space or through bond coupling, as bulk magnetic ordering has to occur in at least 2-D. Both mechanisms need to be well understood when describing organic magnetism. However, before such an in-depth discussion occurs it is essential to understand how to create lone electrons in primarily covalently bonded materials. The first organic radical was produced by Gomberg at the turn of the last century, the triarylmethyl radical as demonstrated in Fig. 7.1a, is made by reacting triarylmethyl chloride with silver in benzene[10]. This is not stable in air and as such forms bonds very easily.

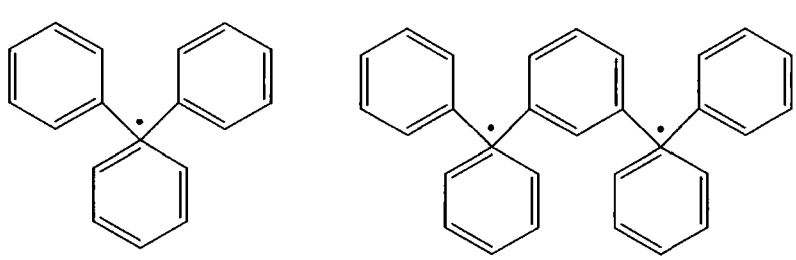

Figure 7.1: The original radical bearing materials, discovered by Gomberg (a) and Schlenk (b) respectively.

The initial prediction of a free radicals in organic systems was not confirmed until 1915 by Schlenk, see Fig. 7.1b, when the famous Schlenk biradical hydrocarbon was produced[11]. Again, the material is not stable in air. In essence the radicals were formed by using a strong electron acceptor. These initial experiments have stimulated work into creating organic magnets. Once a stable radical is formed, the exchange can be predicted (described in the following sections) and it is possible to design materials to have specific physical properties.

7.2.1 Intra-Chain Magnetic Coupling

Theoretical predictions of the magnetic coupling is based upon two distinct but complementary methods. The first is based upon molecular orbit theory which works by maximising bonding. If biradical systems contain non-bonding molecular orbitals (NBMOs) the effect of the spin state upon the Coulomb repulsion energy between the separated pair of electrons can be predicted. The valence bond approach is based upon electron repulsion minimisation, thus the Coulomb repulsion energy is ignored, however the results obtained (described below) are very similar.

Intra-chain coupling can be well predicted due to pioneering theoretical work in the latter half of the twentieth century by Longuet-Higgins[12]. The work is based upon molecular orbital theory of alternate non-Kekulé molecules. (A Kekulé molecule is one which can be described by alternate single-double bonds). Using Hunds rule of multiplicity, and the fact that the number of ground state unpaired electrons is at least as great as the number of NBMOs, it was predicted that the relative spins would be parallel and as such have a triplet ground state. The experimental clarification of this work was performed later by Dowd who obtained a triplet ground state for trimethylenemethane[13]. The inference of this early work is based upon the idea of connectivity, which implies that the spin state of the final molecule is determined by atoms connecting the lone electrons in a system. Fig. 7.2 shows the magnetic ground state of biradicals connected by an aromatic coupling unit.

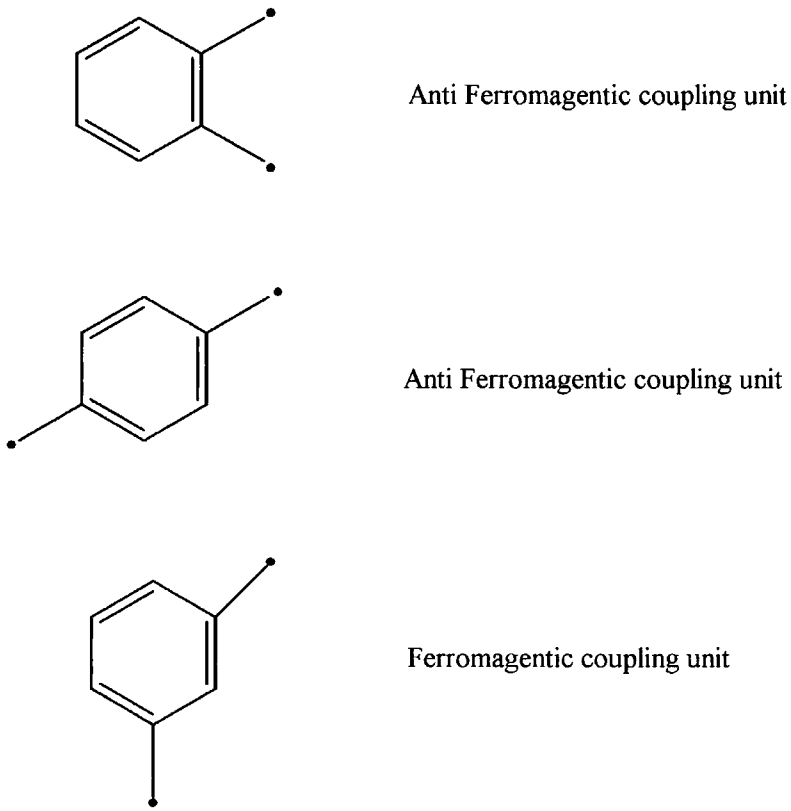

Figure 7.2: The aromatic coupling unit of connected biradicals.

This picture had been deduced by both molecular orbit and valence band theory, Bordon *et al* predicted the ground state of biradicals by considering Hückel's theory of aromatic systems[14]. A simple topological model is used to label a carbon atom starred and surrounded by unstarred carbon atoms. Borden argued that the sum of starred (+1) and unstarred (-1) may be zero for some biradicals and if the NBMOs share a common atom the biradicals are coupled ferromagnetically, the so-called coextensive or nondisjoint state. If the sum is nonzero it is known as a disjoint state with no NBMO overlap. Therefore the coupling is weak, and in Fig. 7.2 this has been labelled Anti Ferromagnetic.

Ovchinnikov used the valence band model to predict the ground state. The argument is relatively simple. The π-electrons are correlated so that one electron occupies the the p atomic orbital on each carbon. However a π bond can only form between adjacent atoms if their electrons have opposite spin. These

are traditionally labeled α and β or they can be called starred and unstarred. Therefore it was predicted that the spin state can be determined by,

$$S = \frac{N^* - N}{2}, \tag{7.1}$$

The ground state can be predicted by counting the number (N) of starred and unstarred atoms. Again this result holds for all the coupling units in Fig. 7.2. These initial considerations have been supported by the fact that aromatic units are observed to couple ferromagnetically if the biradicals are at *meta* sites, and are found to be singlets if coupled at *ortho* and *para* sites[16]. Recent calculations of superexchange coupling in the atomic orbitals has predicted perhaps the most simple rule to date; if the biradicals are separated by an odd number of atoms the ground state will be a triplet and if the number is even a singlet is expected[17].

Although not a complete theoretical description, the rules in designing high spin molecules are well defined. However the design of materials that meet these criteria must also guarantee that the ground state of the desired triplet is stable at temperatures approaching 300 K. Li *et al*[18] have performed calculations using the valence bond theory to predict the energy gap of the triplet ground state of aromatic molecules that meet all of the criteria for exchange outlined previously. Fig. 7.3 identifies the molecules examined theoretically. They are aromatic rings with (set a) and without (set b) spacer units, the topological distance can be increased by adding aromatic rings. The results of their calculations are demonstrated in Fig. 7.4 for both sets of molecules. From these results ferromagnetic intra-chain exchange can be expected well above room temperature for organic molecules.

7.2.2 Inter-Chain Magnetic Coupling

Although it is essential to obtain strong through-chain interactions the limiting factor in most organic materials is the through-space bond, as this tends to be weaker. If no exchange can be mediated between chains the best that can be expected is a superparamagnetic type behaviour. McConnell has provided two possible coupling mechanisms. The first is based upon the stacking of aromatic

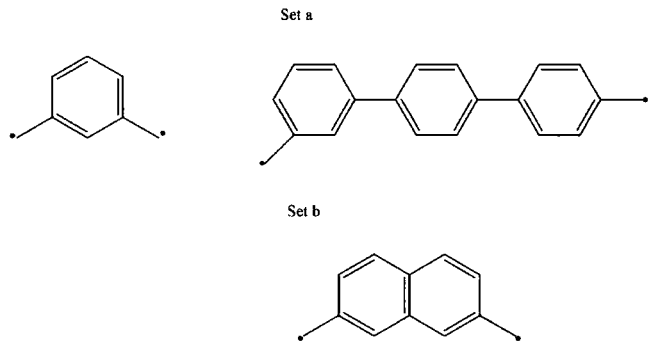

Figure 7.3: The aromatic coupling unit of connected biradicals upon which valence band calculations were performed. Set a contains a spacer between each aromatic ring whilst set b does not. From [18].

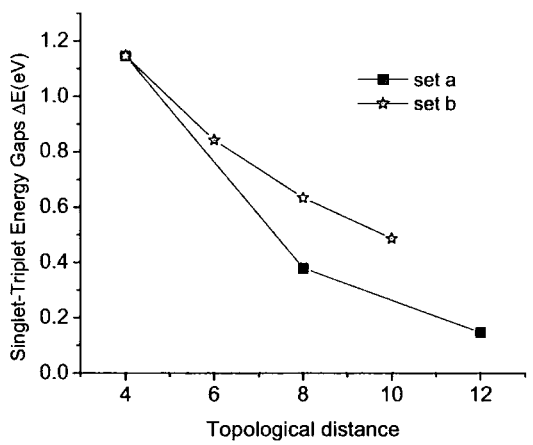

Figure 7.4: The singlet triplet energy gap for biradicals as a function of topological distance for set a and b. From [18].

radicals. The Heisenberg Hamiltonian as identified in chapter 2 can be written in the form,

$$H^{AB} = -S^A \cdot S^B \sum_{ij} J_{ij}^{AB} \rho_i^A \rho_j^B \tag{7.2}$$

where S^A and S^B are the spin operators for A and B, and ρ_i^A and ρ_j^B are the spin densities on atom i on molecule A. This is a many-centre problem and as such the exchange interaction J can become positive or negative depending upon the stacking[19]. A visualisation of these two possible scenarios is given in Fig. 7.5. If the spin density product is negative ferromagnetic overlap will occur between the two molecules, and such an exchange mechanism has been

ratified experimentally[20]. Moreover, molecular orbit calculations show that the exchange integral is negative (antiferromagnetic-like) for *ortho* and *para* stacking whilst it is positive for *meta* alignment of aromatic rings[21].

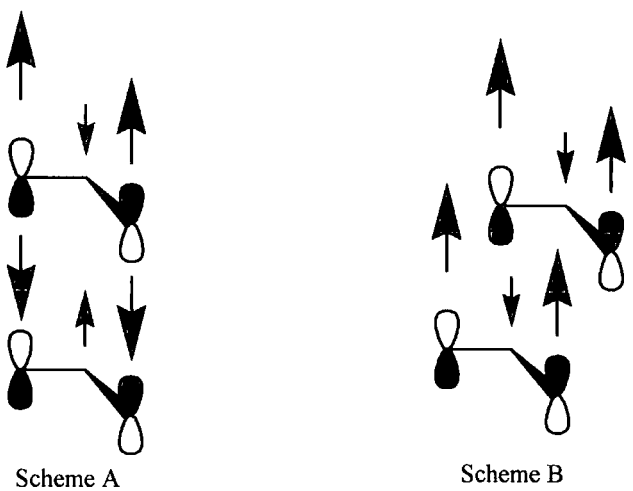

Figure 7.5: Schematic representation of alignment of ideal stacking density with scheme A being nonmagnetic whilst scheme B results in net magnetism.

The second model concerns charge transfer salts. This is of particular importance to organo-metallic complexes which are known to have large ordering temperatures. If a Donor (D) Acceptor (A) pair could be built whose ground state is a triplet (D^+A^-) then it is reasonable to predict that a large array of charge transfer complexes would show ferromagnetic interaction. Importantly, this interaction would extend in all directions to give true three dimensional ordering, however it requires strong acceptors and a compact crystal structure.

7.3 Designing PANiCNQ

From the discussion in section 7.2 it appears that the inter-chain coupling will be the most difficult to achieve, as stable radicals can be readily formed. The use of polymer chains containing π conjugated rings has long been expected to align unpaired electrons ferromagnetically. However the interchain coupling was expected to be weak as polymers tend to be amorphous. Two major

works have ensured that work has continued upon amorphous material, the first report of a magnetic polymer was derived from the oxidation of poly(1,3,5-triaminobenzene) which demonstrated magnetic ordering for one sample of 700 K, although the work has never been reproduced[24]. Cross linking of radicals has been demonstrated by Rajca *et al* to produce large spin polymer units that behave as if superparamagnetic[9], the advantage being that radicals can be missing and exchange will still be coupled. However the physical unit is large and unlikely to form ordered structures to mediate inter-chain coupling. These works have been based upon *meta* alignment of aromatic rings, as described in section 7.2. However it is clear from all the work contributed to this field so far that inhomogenous doping is still a major problem.

The design of PANiCNQ was made to take into account all of the criteria described in the previous discussions. The magnetic polymer fabricated is based upon emeraldine base polyaniline (PANi) as the starting material. Due to a π conjugated backbone, exchange interactions along the spine are expected to be strong once the radical have been stabilised. Indeed weak ferromagnetic behaviour has already been observed in oxidised *meta* PANi at low temperatures. However the resulting polymer is unstable[25]. Moreover with its *meta* and *para* sites PANi has been specifically identified as a building block for room temperature ferromagnetism[26]. One specific advantage of PANi is that it is known to form an air stable electrical conductor[27] that can be easily processed[28]. The possible spin states along the backbone were formed by reacting PANi with a well known stable radical forming molecule, tetracyanoquinodimethane (TCNQ)[29], as it is a strong acceptor. Fig. 7.6 shows the doping of PANi with TCNQ which eventually produces charge transfer complexes with electron donors, section 7.4 will emphasise the kinetic nature of this reaction which involves two stages before the final magnetic structure is achieved. TCNQ was chosen as it is known to form stacked layers when in Charge Transfer (CT) complexes[30]. This is important as it may help to achieve inter-chain coupling as previously identified in section 7.2. The actual mechanism proposed in Fig. 7.6 is ferrimagnetic. Using the design criteria identified in section 7.2 antiferromagnetic and ferromagnetic alignment of spins will form along the repeat unit backbone, producing a net of S = 1 spin per repeat unit.

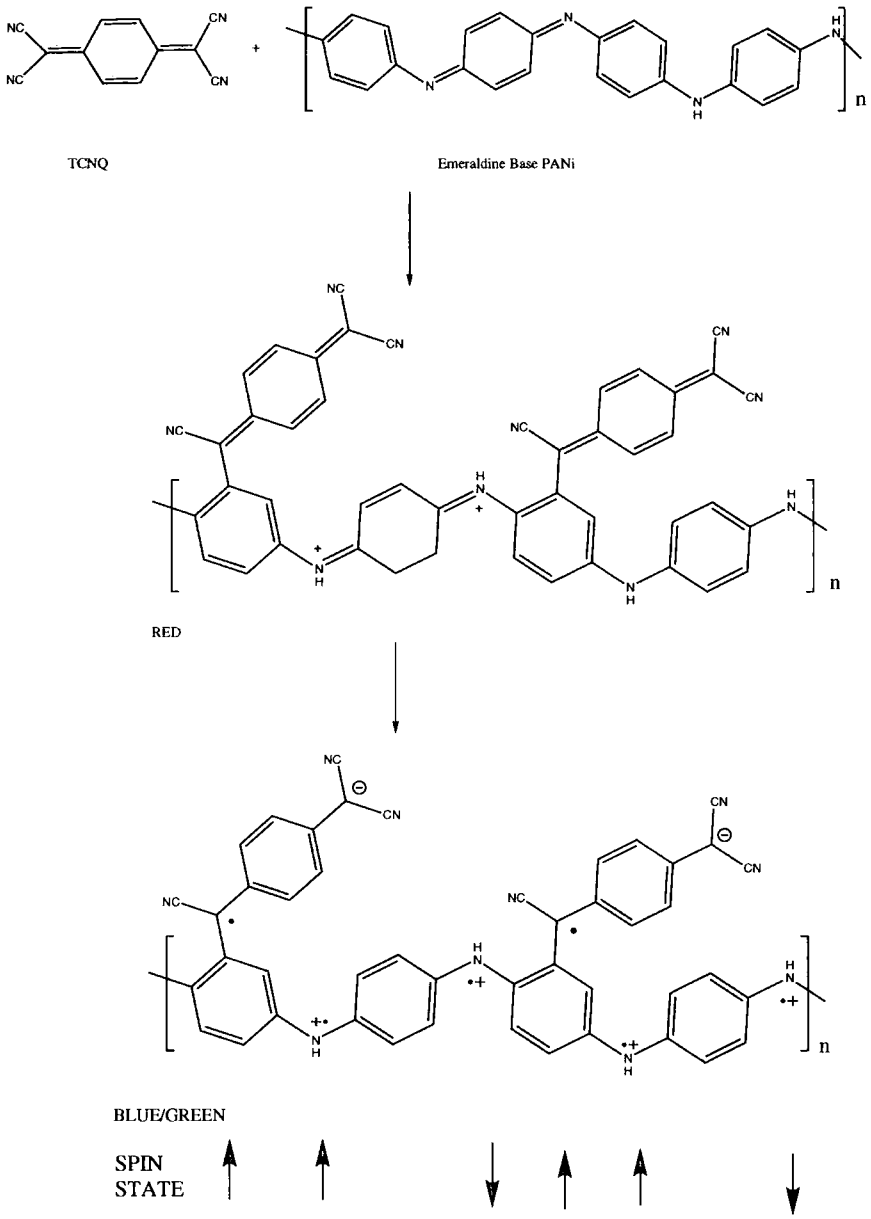

Figure 7.6: Chemical structure of PANi and TCNQ along with the most plausible form of the magnetically ordered polymer PANiCNQ, the two stages indicate a kinetic reaction.

7.3.1 Fabrication and Initial Characterisation of PANiCNQ

The synthesis of PANiCNQ involved taking Pani which is soluble in N-methyl-2-pyrollidinone (NMP) and simply adding TCNQ, the final solution was heated

at 450 K overnight in a vacuum oven. The resulting solution was filtered and the NMP removed in vacuum. The fabrication process allows two distinct samples to be obtained, a solid sample (a) above the filter and the filtrate itself (b). Several batches were produced and the resulting samples were labelled chronologically. For example the first sample produced above the filtrate is known as 1a, if two samples are drawn from this batch they will be labelled $1a_1$ and $1a_2$ respectively.

The two stage process identified in Fig. 7.6 to produce the final molecule can be given further credence by considering ultra-violet spectroscopy data. Fig. 7.7 shows the absorbance of the material initially produced and after drying, this behaviour is consistent for all samples produced. Specifically both the solid and the dried solution have a strong peak at 492 nm (yielding a red material). This is in agreement with other works when TCNQ has been reacted with aniline type molecules[31, 32]. After drying, the form of the absorbance changes as identified in Fig. 7.7. This green solution has a new absorption peaks at 625 and 661 nm, typical of conducting PANi. However PANiCNQ is not conducting and this can be inferred as evidence of protonated PANi, demonstrating a charge transfer complex between PANi and TCNQ producing zwitterions in PANiCNQ.

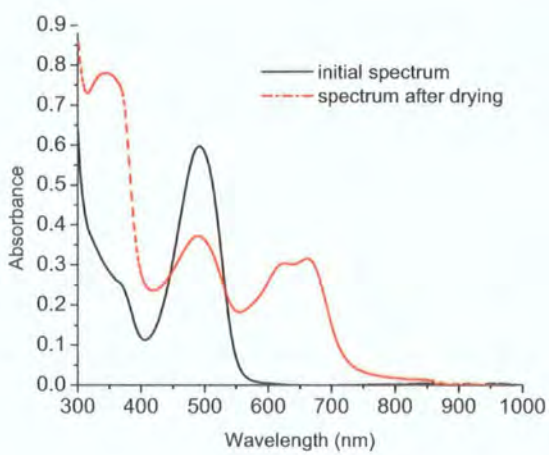

Figure 7.7: Optical absorption of PANiCNQ before and after drying, showing intremolecular charge transfer has occurred.

It appears that TCNQ is bonding to the PANi backbone. Supported by the solubility of PANiCNQ. Unlike normal PANi it will dissolve in acetone. Fast Fourier Transform Infrared Spectroscopy (FTIR) was carried out on the polymer and is in agreement with published work[33]. Most importantly there are new cyanides stretches at 2185 cm^{-1}. Fig. 7.8 clearly demonstrates this, for four samples of 3b. These samples are presented because of their contrasting magnetic properties described later in section 7.4. The absorption at 2185 cm^{-1} is evidence of the TCNQ molecule having covalently bonded to the PANi at the phenyl sites, along the polyaniline backbone. A strong, broad absorption between 2800 cm^{-1} and 3100 cm^{-1}, indicative of NH stretches, is also observed. This protonation could occur during synthesis, as hydrogen cyanide is produced during the reaction and could readily protonate imine sites. Gas permeation chromatography (GPC) and the elemental analysis indicate that the polymer has reduced in molecular weight and CHN content compared to PANi. From the FTIR data and previous known reactions of TCNQ a tentative structure for PANiCNQ was given in Fig. 7.6. One important observation is that the addition of the TCNQ will not affect the quinoid ring as it is electron deficient. However, it is also possible for the reaction not to have gone to completion and that there may be less than two TCNQ side groups per (four phenyl ring) repeat unit. The fabrication of PANiCNQ does not define the attachment point of the TCNQ on *meta* sites along the backbone; from steric considerations and the number of available electrons only a maximum of 2 TCNQ molecules can attach to the PANi backbone. Section 7.2 demonstrates that only one arrangement of TCNQ molecules on the backbone will result in a net ferrimagnetic spin (shown in Fig. 7.6), others will produce a net spin of zero. The yield will be less than 10 % without even considering doping efficiency.

7.4 Magnetic Characterisation of PANiCNQ

This section discusses the magnetic characterisation of various samples of PANiCNQ. It will describe a chronological investigation of the samples obtained. The work was performed before the SQUID magnetometer described in chapter 3 arrived in the laboratory, and as such, temperature dependent characterisation of the samples is somewhat limited. Room temperature measurements

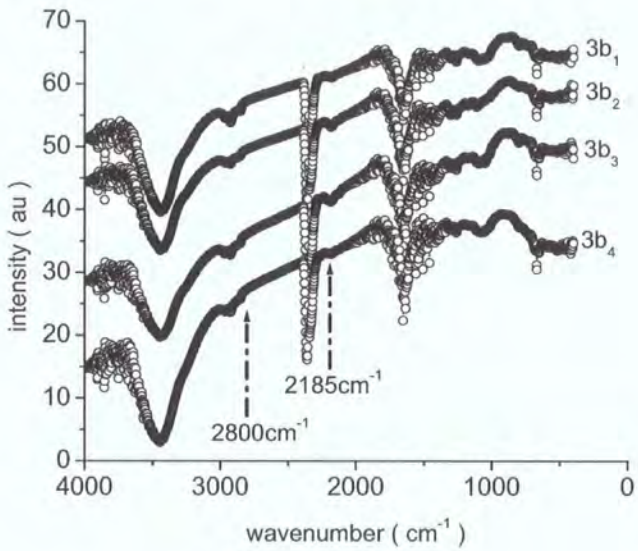

Figure 7.8: IR spectroscopy of batch 3 filtrate, demonstrating that the TCNQ molecule is bonded covalently to the backbone.

were carried out upon a Vibrating Sample Magnetometer (VSM). The limited SQUID data is because many samples were tested to destruction in order to account for possible magnetic impurities prior to the arrival of the magnetometer. All hysteresis loops are measured at room temperature unless otherwise stated.

7.4.1 Identifying Magnetic Impurities

Any work performed in the field of organic magnetism has to account for magnetic impurities present in the sample, indeed much work has not been independently reproduced as an impurity contribution is thought to contaminate the initial experiments. The work performed in this study has attempted to prove that the magnetic contribution cannot be from metallic impurities and, unlike previous studies, many different techniques have been used to provide evidence that the magnetic properties are inherent to the organic system.

Two methods have been used to identify magnetic impurities directly from inorganic atoms such as nickel (Ni), iron (Fe) and cobalt (Co). Inductively Coupled Plasma Mass Spectroscopy (ICPMS) has been performed upon those

samples showing bulk magnetic ordering and those that do not. This method can accurately determine impurity levels at a parts per million scale. However any Fe contribution must be compared to the presence of Ar and O as the sum of the atomic number of Ar and O is the same as Fe. Impurity concentrations will be given in section 7.4.2 and 7.4.3 for each sample measured. However it is essential to note that all the calculations are based upon a metallic ferromagnetic contribution to the magnetism, the worst case scenario. A typical impurity level is 10 ppm of Ni, assuming the distribution is homogenous throughout the material the transition metal ions will give a paramagnetic contribution, therefore an upper estimate of the mass susceptibility is $\sim 10^{-11}$ m^3kg^{-1}, generally the samples prepared had a susceptibility of $\sim 10^{-9}$ m^3kg^{-1} (shown later). To ensure the observations are consistent with organic magnetism all impurities are considered to be bulk, for example the mass magnetisation of bulk Ni is 55.4 $JT^{-1}kg^{-1}$. The second method is to assume that the transition metal impurities form ferrites. If present they will be detectable by Electron Spin Resonance (ESR).

7.4.2 Initial Bulk Magnetic Measurements

Initial magnetic measurements were performed upon two batches, 1 and 2. It is essential to stress that the chemistry at this point is not well understood and it is not possible to reproduce on demand the kinetic reaction identified in Fig. 7.6. The properties of the initial samples measured are shown in Table 7.1. They clearly show that the saturating behaviour can be accounted for if the Ni impurity contribution is taken into account (there is only a trace amount of Fe present) for sample 1b and 2a. The impurity contribution can only account for 85 % of the observed saturating component for 2b and sample 1a has a diamagnetic response even though the sample has the largest Ni impurity. This result would suggest that the impurities are not contributing to the magnetism. However as this is such a controversial topic it cannot be denoted as proof of organic magnetism. Note the PANi and TCNQ raw materials are diamagnetic and this is clearly indicated in appendix C.

The reaction is kinetic and the rate determining step is as yet not well understood[34].

Sample	1a	1b	2a	2b
mass	0.1193 g	0.1067 g	0.096 g	0.1554 g
saturation ($JT^{-1}kg^{-1}$)	diamagnetic	1.4 x 10^{-3}	0.85 x 10^{-3}	9.2 x 10^{-3}
measured moment (JT^{-1})	-	1.5 x 10^{-7}	9 x 10^{-8}	1.42 x 10^{-6}
Ni level (ppm)	376	39	30	148
impurity contribution	-	145%	125%	85%

Table 7.1: Initial magnetic characterisation of batches 1 and 2.

However this also means that the diamagnetic signal observed in sample 1a might not be the final magnetic phase. Therefore the sample was left in an air tight jar in its original gelatin measuring capsule. Approximately once every month the susceptibility of sample 1a was measured on a VSM. After 3 months a startling result was observed. The diamagnetic signal now displayed a saturating component upon a diamagnetic background, and this is demonstrated in the inset of Fig. 7.9. Although the mass magnetisation is weak it represents a significant change in the magnetic properties of the material. It is essential to note that the impurity contribution in the sample did not change.

It is unlikely that the reaction of PANi and TCNQ is 100 % efficient as already discussed. Therefore, to optimise the amount of magnetic polymer, sample 1a underwent magnetic separation. A 0.2 T permanent magnet was used to separate the magnetic component. Great care was taken to ensure no cross contamination occurred. The mass magnetisation of the magnetically separated sample subsequently increased to 0.1 $JT^{-1}kg^{-1}$, and while the susceptibility of the magnetically separated sample increased by two orders of magnitude, the impurity concentration remained constant, as confirmed by ICPMS. The temperature dependence of the magnetically separated sample is shown in Fig. 7.9, showing that the material is magnetically stable to over 350 K. Note that no impurity contributions to the magnetism can be observed, unlike in some previous studies[8] where the temperature dependent mass magnetisation clearly indicates an impurity transition. Also shown is the magnetisation of sample 1a after cooling from 350 K, indicating the thermal stability of PANiCNQ. Table 7.2 lists the magnetic properties of sample 1a once the magnetic order is observed and after the sample was magnetically separated. Importantly for the

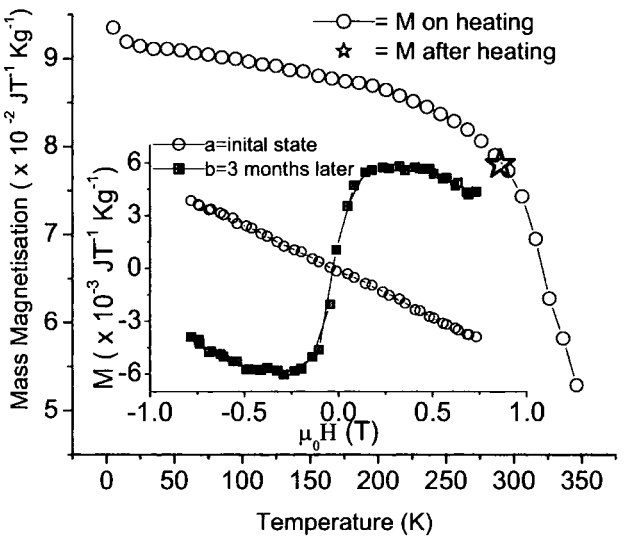

Figure 7.9: Temperature dependent mass magnetisation (M) of the magnetically separated sample 1a. The inset shows the initial change in susceptibility of 1a as a function of time.

magnetically separated sample the impurity contribution can only account for 20 % of the observed moment, indicating that the magnetism is organic in origin. Moreover the sample was placed in a ceramic dish in a conventional oven and heated until the polymer decomposed. The resulting dust has no magnetic component, whereas if the magnetic properties where due to bulk impurities such as Ni it is expected that the signal would not be lost.

Sample	1a, after transition	1a, magnetically separated
mass	0.1193 g	6 mg
saturation ($JT^{-1}kg^{-1}$)	5.6 x 10^{-3}	0.0996
measured moment (JT^{-1})	6.6 x 10^{-7}	5.98 x 10^{-7}
Ni level (ppm)	376	376
impurity contribution	100%	20%

Table 7.2: Magnetic characterisation of sample 1a after the observed magnetic ordering, and the magnetically separated sample.

7.4.3 Reproducing and Improving the Magnetic Properties of PANiCNQ

The material after the observed magnetic ordering is magnetically soft; there is no remnant magnetisation. Recent work has shown that after ultra violet irradiation the magnetic properties of metallic complexes changed due to the increased stacking of the lattice[35]. Ultra violet light was used to "cure" the magnetically extracted sample 1a and the dramatic result is shown in Fig. 7.10. The exact mechanism of the observed remanence will be discussed in section 7.4.4. A "wasp-waisted" hysteresis loop is present in Fig. 7.10. This is char-

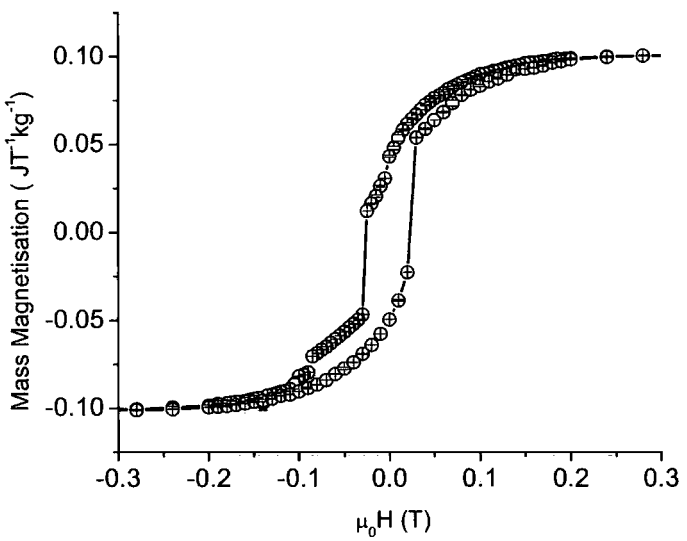

Figure 7.10: The field dependence of the magnetisation of the magnetically separated sample after uv irradiation. A remnant magnetic behaviour is observed.

acteristic of a mixture of soft and relatively hard magnetic components. Even in a magnetically separated sample there is clear evidence for inhomogeneous doping.

Clarification of the work discussed requires producing samples with a much lower Ni impurity, with hopefully improved doping. A similar fabrication process was followed as that described in section 7.3. However larger quantities of sample were used to increase the probability of TCNQ doping the correct backbone

sites to enable the net magnetic structure shown in Fig. 7.6. The filtrate of batch 3 was used. Four samples $3b_{1-4}$, were extracted and all initially showed diamagnetic behaviour, as can be observed in Fig. 7.11 immediately after fabrication (open circles).

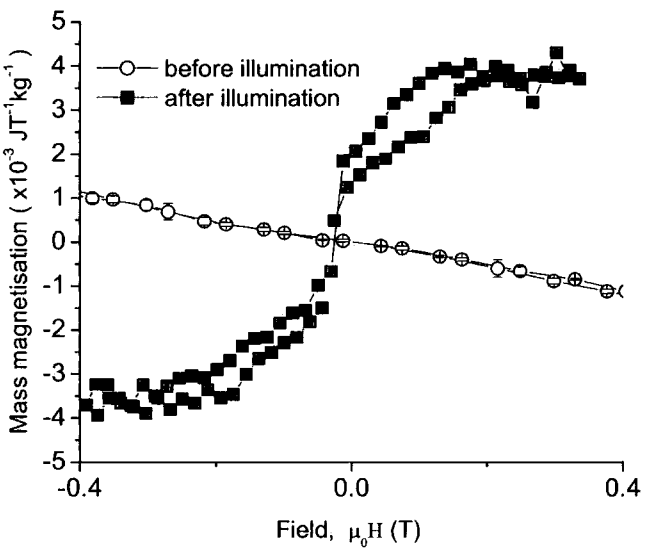

Figure 7.11: The field dependent magnetisation of sample $3b_1$ before and after irradiation with uv light.

However after illumination with a uv lamp, 2 samples drastically changed their magnetic properties. The absolute change compared to the diamagnetic signal is shown in Fig. 7.11 for sample $3b_1$. Clearly a small yet significant amount of remanence has been induced. Table 7.3 demonstrates the magnetic properties of batch 3b. It is important to stress that initially all the samples were diamagnetic. After illumination 2 samples underwent a magnetic transition. The magnetic component in both cases cannot be accounted for by transition metal elements. The behaviour of the "cleanest" sample produced is also shown in Table 7.3. The sample from batch 4 shows magnetic ordering at room temperature immediately after fabrication. There are no measurable contaminates detectable by ICPMS. Although the u.v light has affected the properties of 3 different sample its role in forming remnant magnetisation is not fully understood. Fig. 7.8 demonstrates that no change in the FTIR absorption can be detected

for $3b_{1-4}$, indicating the subtle changes associated with this large change in magnetic properties.

Sample	$3b_1$	$3b_2$	$3b_3$	$3b_4$	4a
mass	0.1618 g	0.141 g	0.1447 g	0.141 g	0.1180 g
photoinduced magnetism	Yes	Yes	No	No	N.A
saturation ($JT^{-1}kg^{-1}$)	4.0×10^{-3}	4.1×10^{-3}	diamagnetic	diamagnetic	3.2×10^{-3}
measured moment (JT^{-1})	6.4×10^{-7}	5.6×10^{-7}	-	-	3.8×10^{-7}
Ni level (ppm)	8	10	23	16	trace
impurity contribution	10%	14%	-	-	0%

Table 7.3: Magnetic characterisation of sample 3b and 4a.

7.4.4 Direct Imaging of the Magnetic Behaviour

Given the observation of remnant magnetisation in three samples of PANiCNQ induced from u.v irradiation, attempts were made to image the magnetisation directly. A Digital Instrument Dimension 5000 Atomic/Magnetic Force Microscope (A/MFM) was used in this investigation. The MFM tip had a remnant field of $\sim$ 25 mT, and if the magnetic behaviour associated with PANiCNQ has a surface component it will be visible. To interpret MFM data it is necessary to compare the data directly with the topological features of the surface. Atomic Force Microscopy (AFM) is first performed in tapping mode and then the same tip is lifted from the sample surface and an MFM image is taken in non contact mode. Because of the sensitivity of the MFM technique the phase component of the cantilever deflection is recorded as the cantilever is driven at a certain frequency (kHz range). The amplitude deflection can be affected by rough surfaces.

The magnetic nature of PANiCNQ is dramatically demonstrated by MFM images obtained from sample $3b_1$ after illumination with the uv lamp. Fig. 7.12 shows a sequence of AFM measurements (A, C, E) compared directly to appropriate phase contrast MFM images (B, D, F). The AFM measurements indicate regions of the polymer protruding from the surface of the material, whilst the MFM measurements indicate domain wall movement (dark/light striations) as the sequence of measurements progress. The magnetic domain is likely being driven by the magnetic tip used to image the sample, such behaviour has been noted previously for permalloy films[36]. Interestingly, the domain wall appears to be pinned around the protruding region, which suggests that the magnetic remanence is a result of domain wall trapping at defects within the material. The fact that the remanence is only observed after irradiating with uv light implies that the pinning defects are created by the radiation. The behaviour of domain wall motion is restricted to certain areas of the sample, indeed some parts of the sample show no magnetic images, again demonstrating the inhomogenous nature of the doping. Further measurements have been performed and are superfluous to the main discussion. However they are attached in appendix C, demonstrating that the behaviour is not a feature solely unique

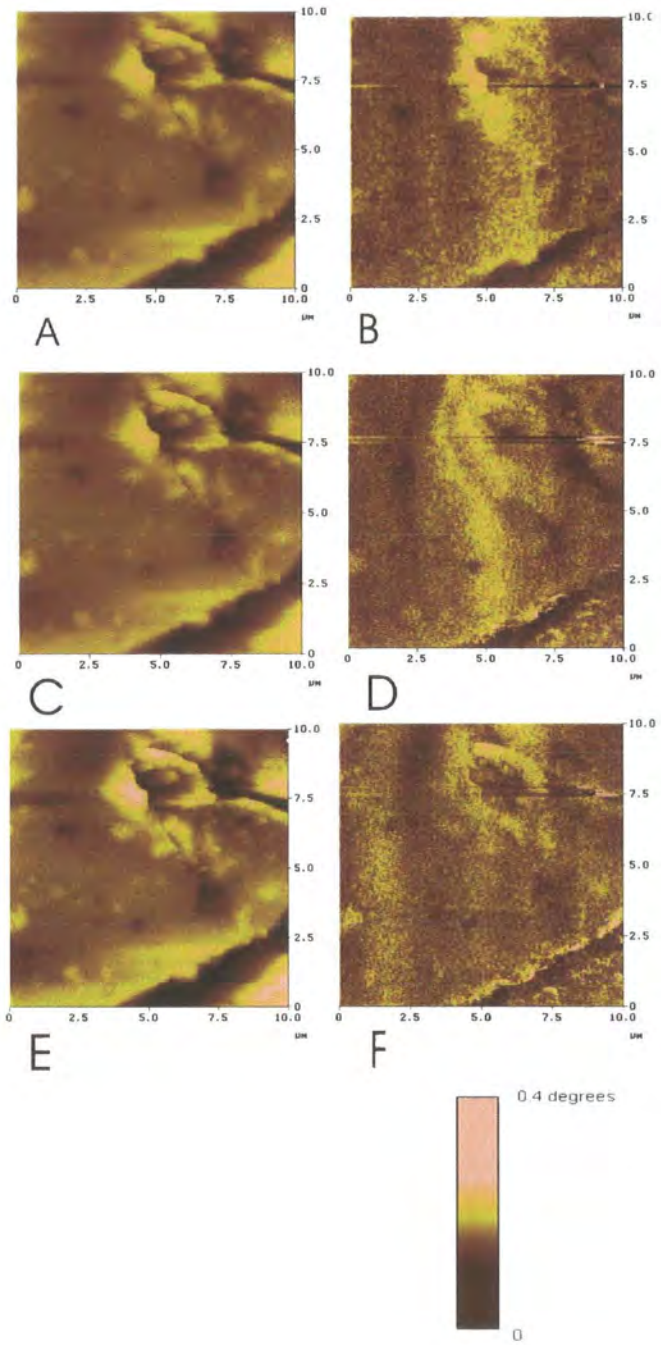

Figure 7.12: AFM images (A, C, E) and MFM (B, D, F) of PANiCNQ sample $3b_1$ after the uv induced magnetic transition.

to this section of sample. A sequence of MFM measurements performed upon sample 2b also indicate magnetic regions of the surface.

7.4.5 Further Characterisation of PANiCNQ

The MFM data described in section 7.4.4 appears to signify the importance of ordered regions within the polymer matrix upon the measured magnetic domains. Indeed the time dependent change of the magnetism in sample 1a is directly accompanied by a subtle change in the structure of PANiCNQ. Initially a broad peak is observed in the x-ray diffraction data. This is a characteristic of emeraldine base PANi[37]. However after the observed magnetic ordering of sample 1a there is a subtle change in the x-ray diffraction data as shown in Fig. 7.13. The position of the broad peak has moved by $\sim 6^o$ and a sharp peak appears at a d spacing of approximately 1.22nm. These changes are an indication that the polymer chains become more aligned, and that the material is becoming more structurally ordered with time. It is noted that polyaniline is known to become partially crystalline when doped, with a correlation existing between the protonation of the -N= in the emeraldine base and the crystalline form[37]. There are two well know mechanisms that could drive more order into the system. The residual NMP is known to act as a plasticizer in films of PANi[38]. However this alone cannot explain the change in structure of the material. Another possible explanation is that the TCNQ molecules are stacking, creating the structural ordering of the material with time. This work is limited to this one sample as the other magnetic samples identified were tested to destruction before the importance of the structure became apparent.

X-ray diffraction was not performed upon batch 3 as the magnetic samples were investigated by ESR. To ensure that the signal was not a consequence of impurities, all the measurements were repeated with the sample dissolved in acetone. Fig. 7.14 demonstrates a typical ESR response of a sample ($3b_1$) which showed ferrimagnetic behaviour, giving a single line at $g = 2.0045$ and a peak-to-peak width of 0.54 mT. Such a line is characteristic of the presence of free radicals, indeed an almost identical g value is obtained for p-NPNN[2]. By integrating the area under the ESR line and comparing with a DPPH reference signal an estimate of the spin density, 10^{21} spins kg^{-1} can be made. Such a number is about a factor of 7 greater than that determined from the saturation value of the magnetisation data, and this work tentatively concludes that the sample is

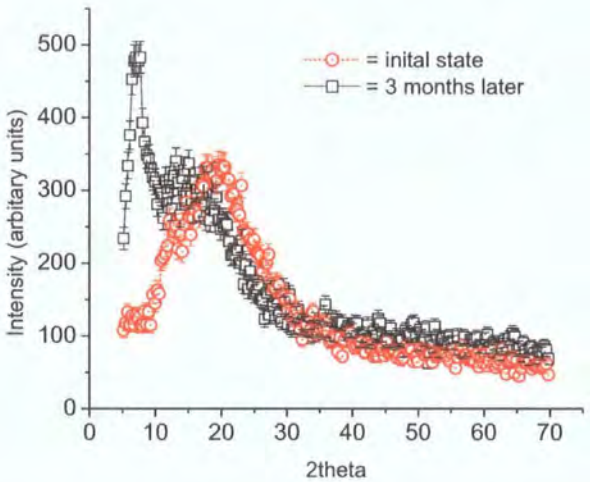

Figure 7.13: X-ray powder diffraction data, before and after the magnetic transition.

ferrimagnetic, with only 1 spin in 7 contributing to the saturation value of the magnetisation at the magnetic field strengths applied in the experiments. This conclusion supports the proposed spin structure shown in Fig. 7.6, where the intra-chain exchange is a combination of antiferromagnetic and ferromagnetic interactions along the backbone of the polymer structure. The inhomogeneous nature of the doping may also lead to paramagnetic and, perhaps, ferromagnetic areas within the material contributing to the magnetic properties of PANiCNQ. The ESR signal can be destroyed by simply dissolving the sample in acetone, this is also shown in Fig. 7.14, giving a clear indication that the origin of the spin is organic in nature. ESR is also very sensitive to ferrite impurities, which have a specific g values $\gg 2.1$. Such absorption was not observed in any samples demonstrating magnetic order, leading to the conclusion that impurities play no part in the observed magnetism.

Due to the nature of scientific investigations, hindsight gives an opportunity to further investigate the behaviour of PANiCNQ more quantitatively. However,the initial investigation clearly demonstrates the magnetic nature of the organic material PANiCNQ.

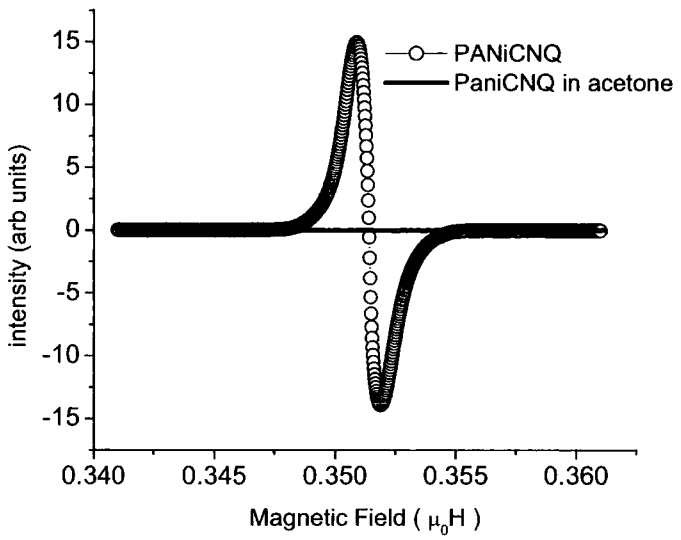

Figure 7.14: ESR signal of sample $3b_1$, before and after dissolving in acetone.

7.5 Discussion

The doping of PANi with TCNQ has been shown to be inhomogeneous, indeed several other batches have been prepared that show no sign of magnetism. Fig. 7.15 demonstrates the properties of two batches that show no bulk magnetic order, even at low temperatures. When contrasted to Fig 7.9, their mass susceptibilities are also very low even though they contain Ni impurities (a mass susceptibility three orders of magnitude greater is measured). Indeed the most efficient method of creating bulk magnetic order in PANiCNQ requires a bulk fabrication technique, i.e large quantities of the constituent materials, leading to an increased possibility of the TCNQ molecules attaching "correctly" to enable bulk magnetic order. There are several further scenarios that could lead to only the 1 % efficiency that is observed. (*i*) The NMP is not fully dissolving PANi, meaning that not all chains are susceptible to doping with TCNQ molecules. (*ii*) The TCNQ can only dope the surface. This is a similar problem associated with oxidation techniques and the MFM would seem to support regions of surface magnetism. However, this problem is surmountable as it is possible to produce oligomer repeat units of PANi. If these could be reacted with TCNQ, true bulk magnetism could be observed.

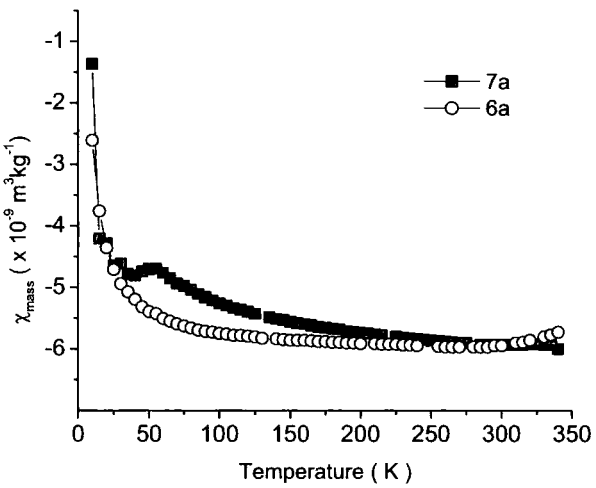

Figure 7.15: Temperature dependence of the mass susceptibility for two samples showing no magnetic order, measured in an external field of 10 mT.

Other acceptor molecules have reacted with PANi ($TCNQBr_2$ and TCNE). Initial expectations were that any strong acceptor would create radicals with strong intra-chain coupling. However in all cases no bulk magnetic order is observed. This signifies the importance of the TCNQ molecule. Indeed recent work in charge transfer salts has noted that TCNQ forms dimers[39]. Previously in the drive for organic exchange dimers have been avoided because although 2 radicals couple together they antiferromagnetically coupled. (Note that dimers will be ESR silent). Due to the nature of the exchange of a dimer the net moment per polymer unit would be zero. However inhomogeneous doping or twisting of the polymer repeat unit will result in a net moment. A recent study has predicted a Curie constant of -741 K for such dimers[40], indicating a possible mechanism for the coupling at high temperatures. In PANiCNQ the interactions will not be as simple as charge transfer salts because the PANiCNQ is exchange coupled to the backbone. Investigations into the possible intra-chain coupling have begun, although not concluded as yet. No magnetic order has been observed when PANi is doped with $TCNQF_4$, although this is a stronger acceptor has not been observed to form dimers in other organic systems. The stacking of the polymer will be affected. Nevertheless the exact mechanism of inter-chain

exchange coupling is one that requires some consideration to determine whether it is dimer driven or a simple stacking model as proposed by McConnell[19].

7.6 Conclusions

Evidence has been provided demonstrating that bulk magnet ordering associated with PANiCNQ can be attributed to organic magnetic exchange. Although not well characterised, and the mechanism for magnetic order not yet understood, it gives justification for further work on this compound as already the saturation magnetisation has been improved to give a value of 0.1 $JT^{-1}kg^{-1}$. Importantly the results of this chapter have been subsequently reproduced. Specifically more characterisation of the chemistry needs to be performed, so the reaction can become well defined and more predictable, and theories for the inter-chain interactions can then be tested. Indeed further work upon PANi doped with an acceptor that does not produce bulk magnetic ordering will be useful in determining the exact nature of the intra-chain interaction. Finally, and perhaps most essentially, the yield of the material needs to be drastically improved if any technological applications are to be sought.

References

[1] J. A. Crayston, J. N. Devine and J. C. Walton, Tetrahedron **56**, 7829 (2000)

[2] M. Tamura, Y. Nakazawa, D. Shiomi, K. Nozawa, Y. Hosokoshi, M. Ishikawa, M. Takahashi and M. Kinoshita, Chem. Phys. Lett **186**, 401 (1991)

[3] R. Chiarelli, M. A. Novak, A. Rassat and J. L. Tholence, Nature **253**, 201 (1993)

[4] A. J. Banister, N. Bricklebank, I. Lavender, J. M. Rawson, C. I. Gregory, B. K. Tanner, W. Clegg, M. R. J. Elsegood and F. Palcaio, Angew. Chem. Ed. Engl **35**, 2533 (1996)

[5] J. S. Miller, J. H. Zhang and W. M. Reiff, J. Am. Chem. Soc **109**, 769 (1987)

[6] J. S. Miller and A. J. Epstein, Angew. Chem. Int. Edut **33**, 385 (1994)

[7] T. L. Makarova, B. Sundqvist, R. Hhne, P. Esquinazi, Y. Kopelevich, P. Scharff, V. A. Davydov, L. S. Kashevarova and A. V. Rakhmanina, Nature **413**, 716 (2001)

[8] J. M. D. Coey, M. Venkatesan, C. B. Fitzgerald, A. P. Douvalis and I. S. Saunders, Nature **420**, 156 (2002)

[9] A. Rajca, J. Wongsriratanakul and S. Rajca, Science **294**, 1503 (2001)

[10] M. Gomberg, J. Am. Soc. **22**, 757 (1900)

[11] W. Schlenk and M. Brauns, Chem. Ber **48**, 661 (1915)

[12] H. C. Longuet-Higgins. J. Chem. Phys **18**, 265 (1950)

[13] P. Dowd, J. Am. Chem. Soc **88**, 2587 (1966)

[14] W. T. Borden and E. R. Davidson, J. Am. Chem. Soc **99**, 4587 (1977)

[15] A. A. Ovchinnikov, Theor. Chem. Acta **47**, 279 (1978)

[16] D. A. Dougherty, Acc. Chem. Res **24**, 88 (1991)

[17] T. P. Radhakrishnan, Tetrahedron Lett **32**, 4601 (1993)

[18] S. Li, J. Ma, Y. Jiang, J. Phys. Chem. A **101**, 5567 (1997)

[19] H. M. McConnell, J. Chem. Phys **39**, 1910 (1963)

[20] A. Isuoka, S. Murata, T. Sugawara and H. Iwamura, J. Am. Chem. Soc **107**, 1786 (1985)

[21] K. Yamaguchi, Y. Toyoda and T. Fueno, Chem. Phys. Lett **159**, 459 (1989)

[22] H. M. McConnell, Proc. Robert A. Welch Found. Conf. Chem. Res **11**, 144 (1967)

[23] N. Mataga, Theor. Chim. Acta **10**, 372 (1968)

[24] J. B. Torrance, P. S. Bagus, I. Johannsen, A. I. Nazzal, S. S. P. Parkin and P. Batail, J. Appl. Phys **63**, 2962 (1988)

[25] A. Ito, K. Ota, K. Tanaka, T. Yamabe and K. Yoshizawa, Macromolecules **28**, 5618 (2000)

[26] M. M. Wienk and R. A. J. Janssen, J. Am. Chem. Soc **119**, 4492 (1997)

[27] P. N. Adams, P. J. Laughlin, A. P. Monkman and A. M. Kenwright, Polymer **37**, 34117 (1996)

[28] S. J. Pomfret, P. N. Adams, N. P. Comfort and A. P. Monkman, Adv. Mat **10**, 1351 (1998)

[29] L. R. Melby, R. J. Harder, W. R. Hertler, W. Mahler, R. E. Benson and W. E. Mochel, J. Am. Chem. Soc **84**, 3374 (1962)

[30] J. Y. Becker, J. Bernstien, S. Bittner, N. Levi and S. S. Shaik, J. Am. Chem. Soc **105**, 4468 (1983)

[31] B. P. Bespalov, V. V. Titov and A. A. Pankrato, Zhurnal. Org. Khimii **8**, 1662 (1972)

[32] O. P. Dimitriev and N. V. Lavrik, Synth. Met **90**, (1990)

[33] N. A. Zaidi, M. R. Bryce and G. H. Cross, Tetrahedron Lett **41**, 4645 (2000)

[34] J. March, Advanced Organic Chemistry, 3rd ed. New York, Wiley, p183 (1985)

[35] D. A. Pejakovic C. Kitamura, J. S. Miller and A. J. Epstein, Phys. Rev. Lett, **88**, 057202 (2002)

[36] H. J. Mamin, D. Rugar, J. E. Stern, R. E. Fontana, Jr., and P. Kasiraj, Appl. Phys. Lett **55**, 318 (1999)

[37] J. P. Pouget, M. E. Jozefowicz, A. J. Epstein, X. Tang and A. G. MacDiarmid, Macromolecules **24**, 779 (1991)

[38] C. Chen and H. Lee, Macromolecules **26**, 3254 (1993)

[39] A. M. Madalan, V. Voronkova, R. Galeev, L. Korobchenko, J. Magull, H. W. Roesky and M. Andruh, Eur. J. Inorg. Chem, 1995 (2003)

[40] K. Mukai, S. Jinno, Y. Shimobe, N. Azuma, Y. Hosokoshi, K. Inoue, M. Taniguchi, Y. Misaki and K. Tanaka, Polyhedron **20**, 1573 (2001)

Chapter 8

Summary and Further Work

This section will summarise the work performed in this thesis, and suggest further work as a consequence of the results obtained. Each results chapter will be considered individually in the relevant sections outlined below.

8.1 Observation of Magnetic Excitons in $LaCoO_3$

Chapter 4 shows several significant results demonstrating fascinating new magnetic behaviour, inherent to as fabricated $LaCoO_3$. Specifically, magnetic excitons have been observed for the first time. Moreover they have been identified by two different experimental methods, μSR and tailored bulk magnetic susceptibility measurements. The exciton formation is specifically linked to the LS-IS transition and the resulting excitons have been shown to have two specific forms of magnetic exchange between them. They either interact directly (possibly due to overlap) or via the IS matrix which is thermally activated. Hence at low temperatures (< 30 K) only the former interaction occurs. The excitons have AF internal interactions and the exciton has been deduced to be large (1 nm).

It is the inter-exciton exchange that requires further clarification. The nature of the results presented in chapter 4 suggest that the exciton exchange is frustrated. Specifically, this can be observed by measuring the remnant magnetisation as a function of time. Initial measurements suggest there is a large

time dependence of relaxation. However to obtain a full model more in-depth measurements need to be performed. Note this will have to be performed using d.c relaxation measurement techniques, as a.c susceptibility measurements will perturb the exciton interaction due to the required applied field. The absolute sensitivity of this method is also much lower (2 orders of magnitude). Magnetostriction experiments would also benefit the understanding of this material as it may be possible to observe the effect of the exciton matrix interaction.

The resistivity of $LaCoO_3$ has been dramatically demonstrated to be affected by a cooling field of 50 mT, even though magnetoresistive effects are not normally observed until an external field of 1.5 T has been applied. Further clarification of the work performed is required. If the excitons are linked to the features of resistivity, a.c measurements should be performed in an attempt to highlight any frequency dependent component of the resistivity.

The physical characteristics of the magnetic excitons need to be determined to complement this initial investigation, possibly by using optical excitation The effect of the magnetic excitons upon the pristine $LaCoO_3$ is clear, and could have consequences for other magnetic oxide families.

8.2 Magnetic Phase Separation in $La_{1-x}Sr_xCoO_3$

The occurrence of Sr rich clusters has been determined in $La_{0.97}Sr_{0.03}CoO_3$. Moreover, the Sr ions appear to induce surrounding Co^{3+} ions into excited spin states, giving rise to two specific interactions. These are a local ferromagnetic interaction within the cluster and an AF interaction between the HS Co^{3+} ions and the IS Co^{3+} ions that make up the vast majority of the matrix. Moreover the LS-IS state transition can be observed in the matrix. However this has only been performed for one low concentration sample. The MIT has been probed and again the clusters are visible. However the behaviour of the clusters and the matrix have always previously been ignored. The work in this thesis suggests that this is not an accurate model of the possible interaction. This work would benefit from further work examining the behaviour of the cluster matrix

interaction on increasing the composition, using μSR as the probe. Specifically the muon work performed indicates two magnetic contributions to the depolarisation, from the cluster and the matrix, and should be investigated upon increasing composition.

The behaviour of the Sr rich cluster interaction needs to be examined in detail at low temperatures, in a direct analogy to the magnetic exciton - exciton interactions in $LaCoO_3$. As such, in addition to the mapping of the matrix contribution, magnetic relaxation measurements need to be performed to examine any frustrated behaviour between the clusters, and the effect of the matrix upon this frustration.

8.3 The Magnetic Ground State of the DX^- Centre in $Cd_{0.85}Mn_{0.15}Te$:In

The magnetic ground state of the DX^- centre has been unambiguously identified for the first time using a local magnetic probe, namely μSR. This result is also of interest because it highlights the sensitivity of the muon to its implantation site, demonstrating that in the absence of a DX^- centre the muon obtains a different implantation site that manifests itself in different relaxation properties. μSR has clearly been shown to be sensitive to very small changes in the local magnetic environment in a DMS.

The implantation site of the muon can be modelled in order to check further the validity of the DFT calculations performed in chapter 4. Time constraints prevented this work being performed for this particular study. μSR experiments should be performed that detect other magnetic properties inherent to semiconductors. Specifically muons could be utilised to look for magnetic polarons in the appropriate material (such as $Cd_{1-x}Mn_{Mn}Te$) so that the dynamics of the polarons in the semiconductor can be studied. Specifically polarised light could be used to excite spin polarised electrons that will contribute to the magnetic properties which can subsequently be studied using muon spectroscopy. This is a major investigation and will be of interest as it will allow magnetic polarons

to be studied for the first time using a local magnetic probe.

8.4 Characterisation of a Novel Organic Magnet

The magnetic properties of PANiCNQ suggest that the observed magnetic order at room temperature is organic in nature. This is a fascinating property, however there are several features of this work which suggest the material is as yet not fully understood. The yield of the material is very low, and in general only 1 % of the PANi has been doped to produce PANiCNQ. Moreover the physical process of attaching the side group is not yet understood, as other side groups produce diamagnetic materials. Much work needs to be performed, including improving and understanding the chemical reaction and understanding the importance of the observed structural order. It will be necessary to explain why this unique system creates room temperature magnetic order compared to other more "established" organic magnets with a much lower T_c.

Appendix A

The fitting functions of the μSR data described in chapter 4 for $LaCoO_3$ are briefly discussed. The interpretation of the data is based upon the depolarisation rates inferred from the fits. Therefore when a different function is required a comparison will be made with the previous function that no longer fits, along with the respective error analysis.

A.1 10 mT Transverse Field Measurements

The bulk transverse field experiments were all fitted with a fitting function of the form,

$$G_x(t) = A^s_{tf} \exp(-\lambda^s_{tf} t)^2 \cos(2\pi\nu_\mu t) + A^f_{tf} \exp(-\sigma^f_{tf} t)^2 \qquad \text{(A.1)}$$

The parameters are defined in chapter 4. Essentially, the first term is required when considering temperatures above the spin transition. However both terms are required below the the spin transition as a quick relaxation is detected. Fig. A.1 demonstrates the time dependence of the fitting function and the data for the TF data at 100 K. With the oscillatory term only of equation A.1 an accurate fit is obtained. When the temperature is reduced the second gaussian term is required, a comparison of the data fitted with the oscillatory term only and both terms is demonstrated in Fig. A.2 and Fig. A.3 respectively. Quite clearly the muons detect a quickly dephasing component of relaxation and both terms are required to fit the data.

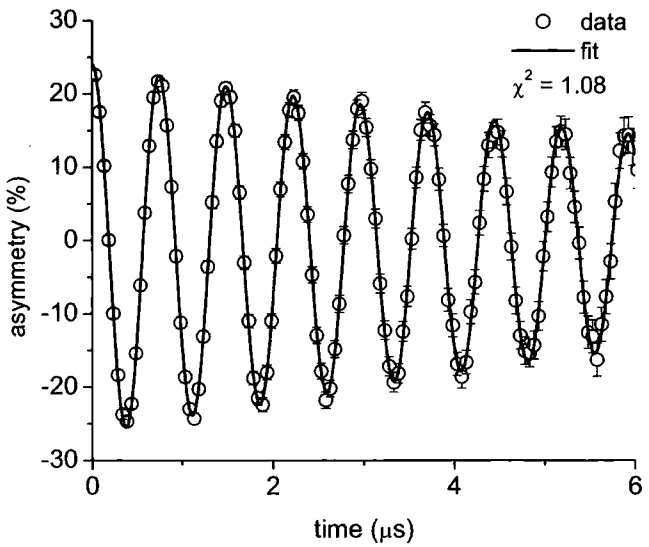

Figure A.1: Time dependence of the fitting function and the data for the TF data at 100 K, with the oscillatory term of equation A.1

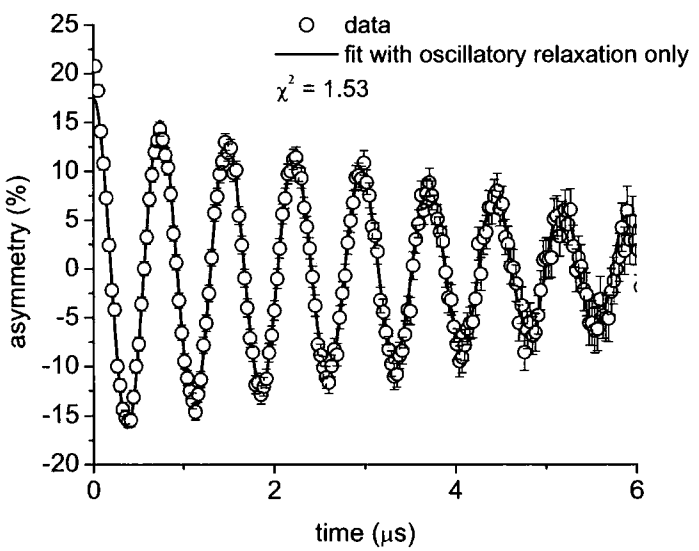

Figure A.2: Time dependence of the fitting function and the data for the TF data at 30 K, with the oscillatory term of equation A.1

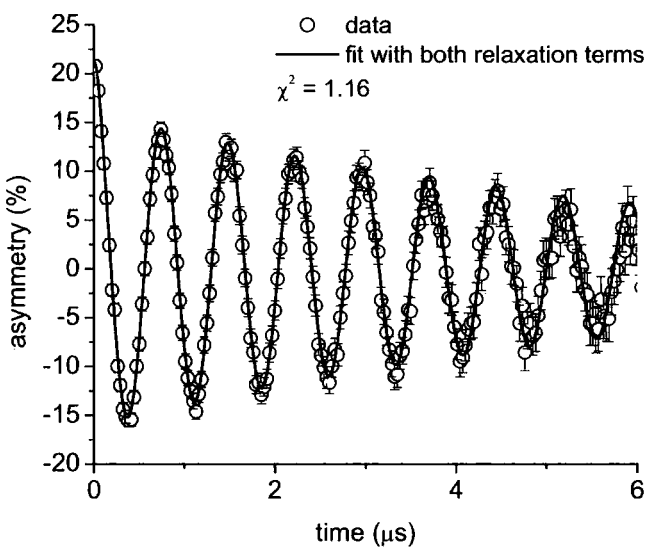

Figure A.3: Time dependence of the fitting function and the data for the TF data at 30 K, with both terms of equation A.1

A.2 25mT Transverse Field Measurements

The 25 mT data is somewhat more complicated than the 10 mT data, this is because to obtain the 25 mT data a spin rotator is required. However only $\sim$ 90% of the muons are polarised perpendicular to the applied field, and the relaxation rate is somewhat more complicated as the larmour precession of the muons around the applied field is not uniform. The general form of the quick relaxation can be fitted with a simple gaussian and is shown in Fig. A.4, the temperature dependence shows a maximum at 6 MHz. The absolute value can be trusted although the temperature dependence is complicated because of the muon precession, note the relaxation of the oscillatory component is not affected.

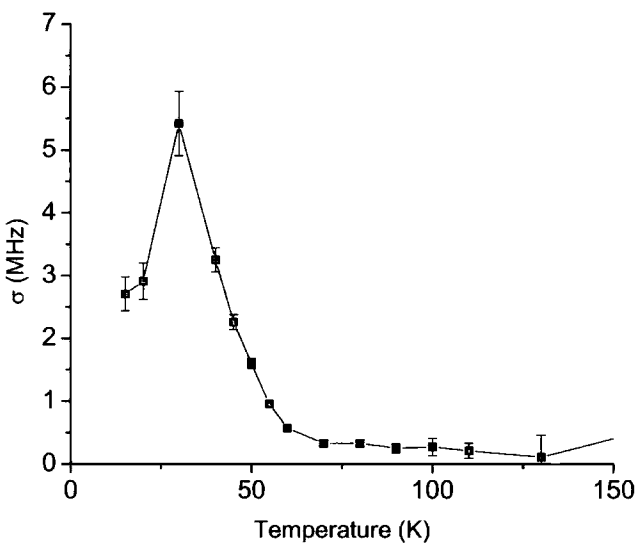

Figure A.4: Temperature dependence of the depolarisation rate of the quick relaxation in the 25 mT TF data.

A.3 Low Energy Muon Measurements

A direct comparison of the LEM data is shown to indicate that the quick dephasing of the gaussian relaxation in equation A.1 cannot be detected due to

the reduced statistics. The χ^2 for the fitting oscillatory function is 1.10 at 30 K. The fit to this data is shown in Fig. A.5, the gaussian can be included but due to the large error bars at short time it is not possible to isolate its contribution to the decay.

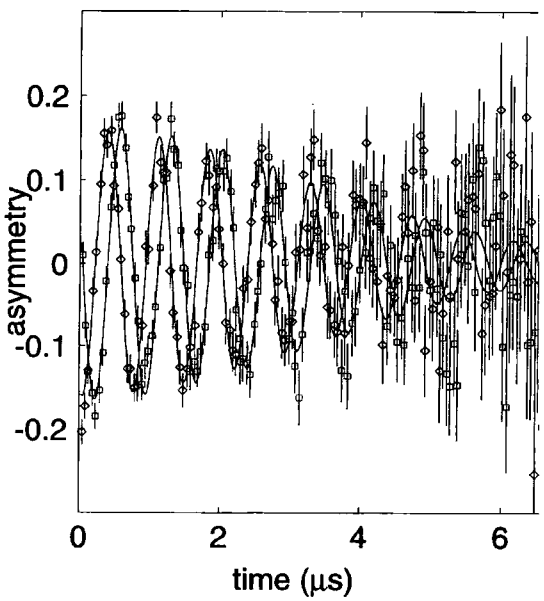

Figure A.5: Time dependence of the fitting function and the data for the TF data at 30 K, with both terms of equation A.1

A.4 Zero Field Measurements

The bulk zero field experiments were all fitted with a fitting function of the form,

$$G_z(t) = A^s_{zf} \exp(-\lambda^s_{zf} t)^\beta + A^f_{zf} \exp(-\sigma^f_{zf} t)^2 \quad \text{(A.2)}$$

The comparison of the fitting parameters supports the interpretation in chapter 4. Above 90 K the data is fitted with a simple exponential as, the first term in equation A.2, the fitting is demonstrated in Fig. A.7. At 55 K the gaussian relaxation no longer fits the data and changes to root exponential as shown in Figs. A.8 and A.9 respectively. At 35 K the data is no longer fitted with a root exponential (Fig. A.9) and an extra gaussian component is required as shown in Fig. A.10.

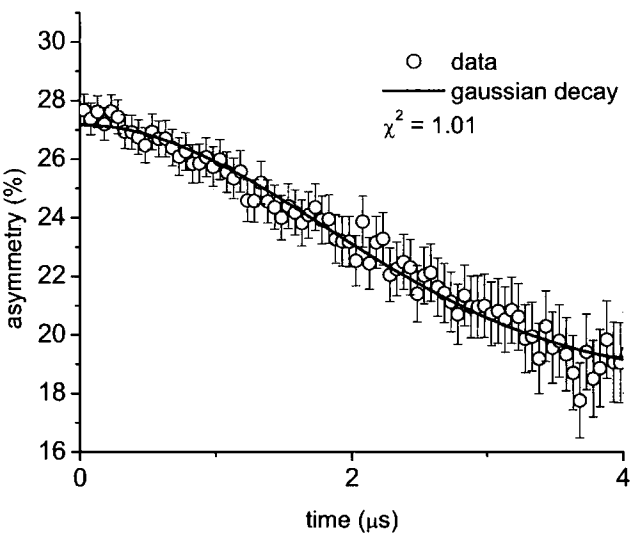

Figure A.6: Time dependence of the fitting function and the data for the ZF data at 100 K, with the gaussian term of equation A.2

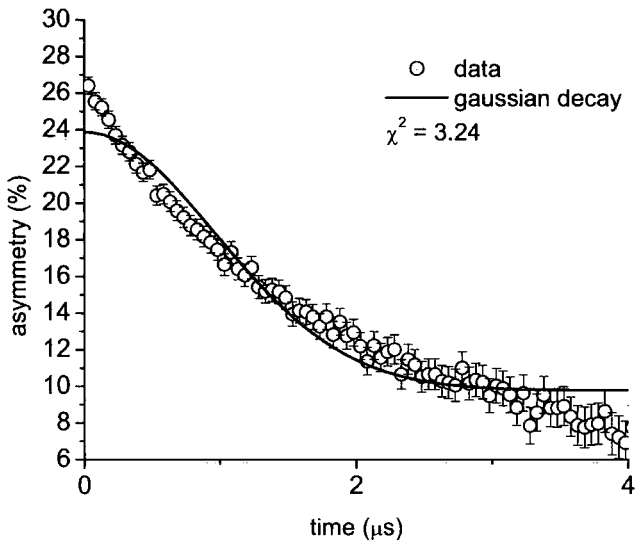

Figure A.7: Time dependence of the fitting function and the data for the ZF data at 55K K, with the gaussian term of equation A.2

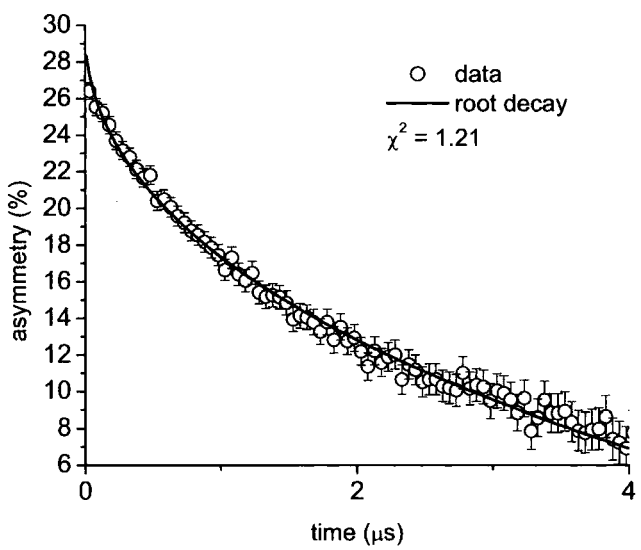

Figure A.8: Time dependence of the fitting function and the data for the ZF data at 55 K, with the root exponential term of equation A.2

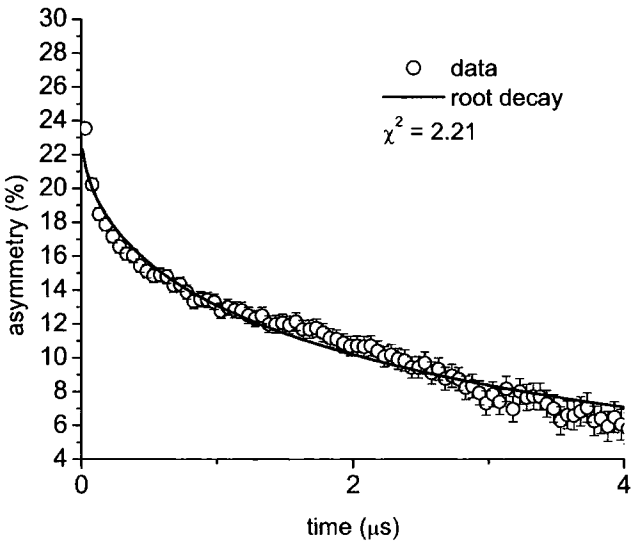

Figure A.9: Time dependence of the fitting function and the data for the ZF data at 55 K, with the root exponential term of equation A.2

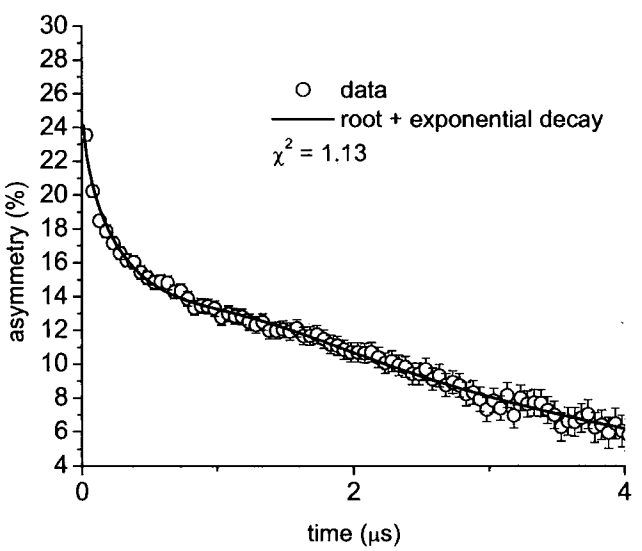

Figure A.10: Time dependence of the fitting function and the data for the ZF data at 35 K, with the root exponential term and the extra gaussian component of equation A.2

A.5 Initial Asymmetry of the ZF and 25 mT TF data

Fig. A.11 confirms the initial asymmetry behaviour as observed in the 10 mT TF data for both the ZF and 25 mT TF experiments. In both cases the muons are dephased below 90 K, the thermally induced spin transition, in agreement with the main body of results.

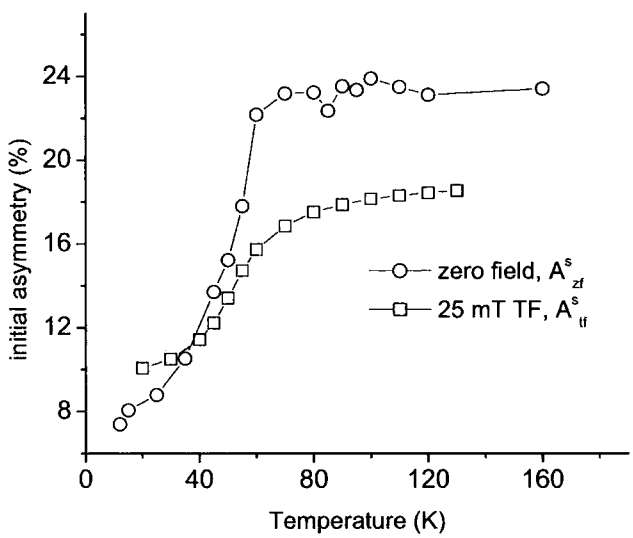

Figure A.11: Temperature dependence of the initial asymmetry parameters for the ZF and 25 mT TF data as defined in A.2 and A.1.

A.6 Further Magnetic Characterisation of $LaCoO_3$

This section shows the temperature dependence of the remnant mass magnetisation of $LaCoO_3$ when the sample was field cooled until 60 K and then cooled and measured in the remnant field of the magnet. Clearly visible is a remnant component of magnetisation at 50 K and 220 K, indicating the significance of the temperature to which the sample is field cooled. Moreover it signifies the importance of 50 K as the temperature at which the maximum number of excitons form.

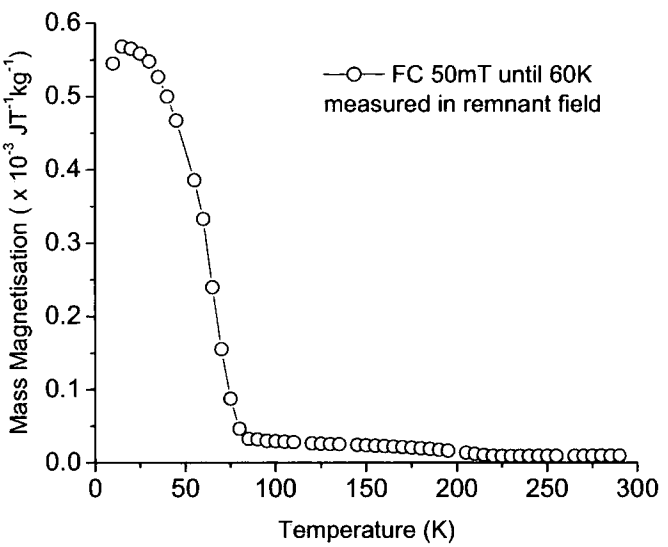

Figure A.12: The temperature dependence of the remnant mass magnetisation of $LaCoO_3$ when field cooled until 60 K and then measured in the remnant field.

Appendix B

B.1 Transverse Field μSR Measurements

The bulk transverse field experiments were all fitted with a function of the form,

$$G_x(t) = A_{Osc}\cos(2\pi\upsilon_\mu t)\exp(-[\lambda_{tf}t]^2) + A_{Gau}\exp(-[\sigma_{tf}t]^2) + A_{bg} \tag{B.1}$$

The parameters are defined in chapter 5, essentially the first term is required when considering temperatures above 50 K however both terms are required below, when a fast relaxation component is detected. Fig. B.1 demonstrates the time dependence of the fitting function and the data for the TF data at 50 K, with the oscillatory term only of equation B.1, quite clearly an accurate fit is obtained. When the temperature is reduced (20 K) the second gaussian term is required, a comparison of the data fitted with the oscillatory term only and both terms is demonstrated in Fig. B.2 and Fig. B.3 respectively. Clearly the muons detect a quickly dephasing component of relaxation and both terms are required to fit the data.

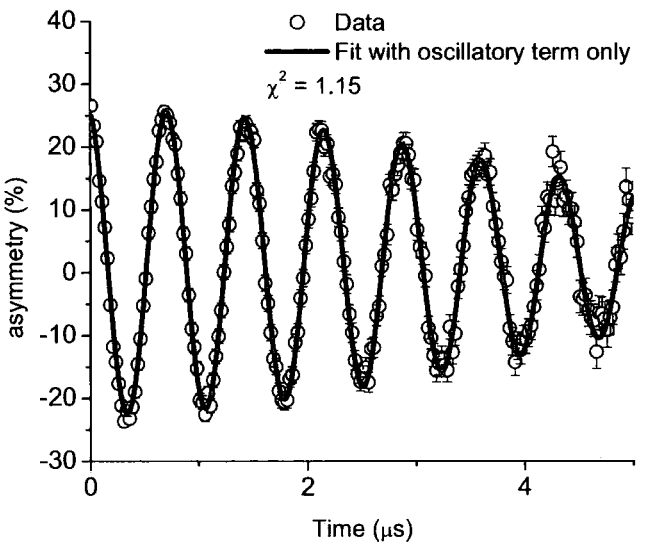

Figure B.1: Time dependence of the fitting function and the data for the TF data at 50 K, with the oscillatory term of equation B.1

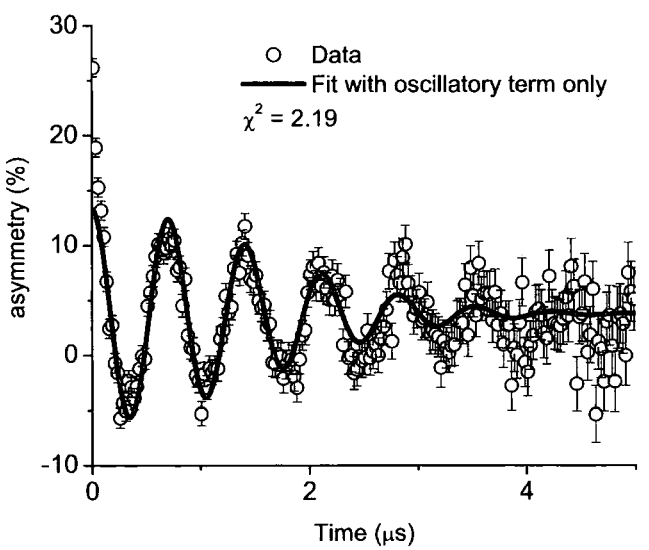

Figure B.2: Time dependence of the fitting function and the data for the TF data at 20 K, with the oscillatory term of equation B.1

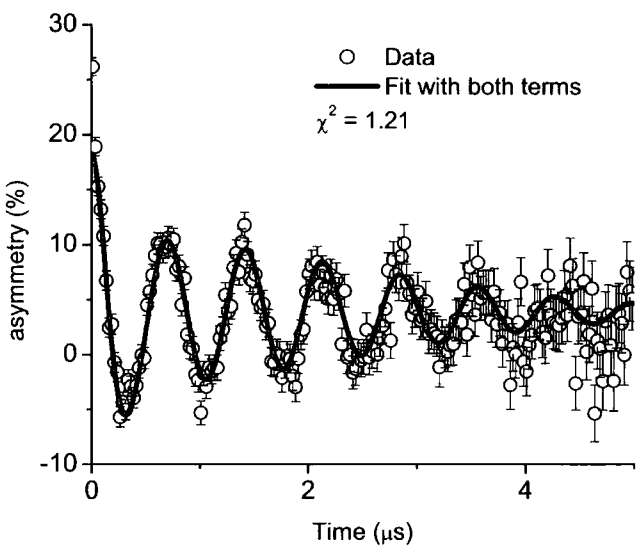

Figure B.3: Time dependence of the fitting function and the data for the TF data at 20 K, with both terms of equation B.1

B.2 Field Dependent Magnetisation Measurements

The field dependent magnetisation measurements of the $La_{0.97}Sr_{0.03}CoO_3$ below 50 K are shown in Fig. B.4. The mass magnetisation only scales when the a θ parameter of 55 K is used, indicating that the Sr rich clusters themselves are not superparamagnetic, i.e there may be interactions between each Sr rich cluster as described in chapter 5. Note the data only scale below the observed magnetic transition described in chapter 5.

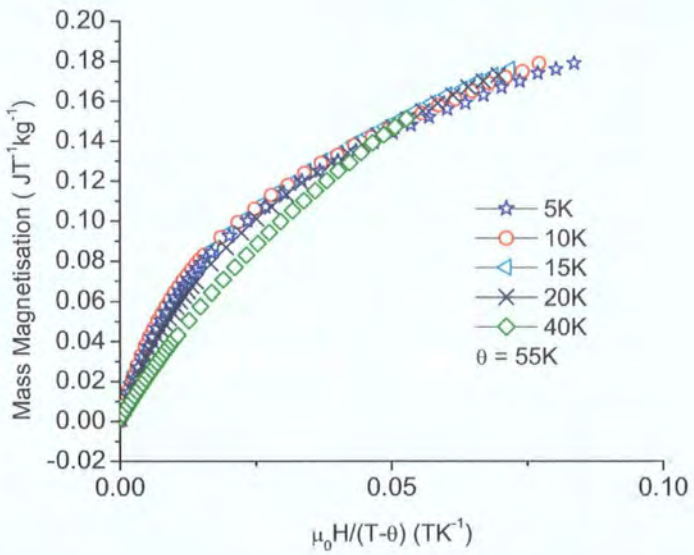

Figure B.4: Mass magnetisation curves for $La_{0.97}Sr_{0.03}CoO_3$ up to 5 T, demonstrating scaling behavior from 5 K - 20 K.

B.3 $La_{0.99}Sr_{0.01}CoO_3$ μSR and Magnetic Measurements

The remaining data for $La_{0.99}Sr_{0.01}CoO_3$ is shown for completeness, both the muon parameters not shown in the main text and the magnetic data are shown in Fig. B.5. The muon fitting parameters are obtained from equation B.1, and the mass magnetisation is differentiated with respect to temperature and also

shows a change in moment coincident with the dephasing of A_{Osc}. Note there is no difference between the FC and ZFC magnetic data.

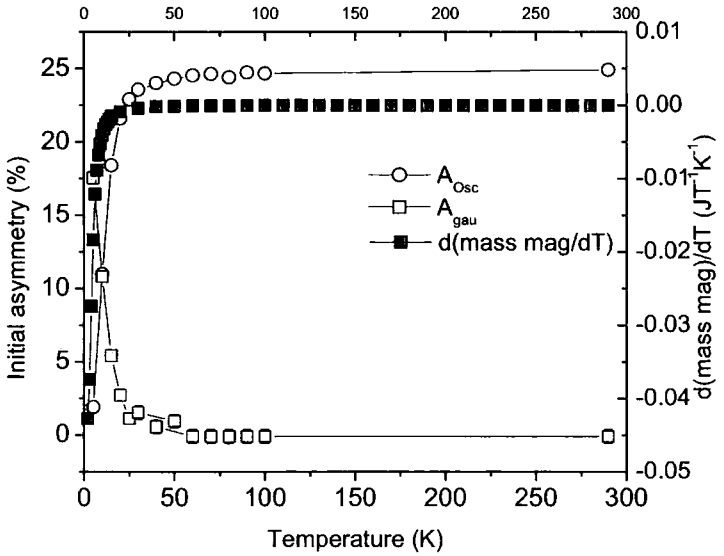

Figure B.5: Temperature dependence of the initial asymmetry of the fitting parameters identified in equation B.1 A_{Osc} and A_{gau} and the derivative of the mass magnetisation with respect to temperature.

Appendix C

C.1 Room Temperature Characterisation of the Raw Materials

The background materials have been tested for any magnetic impurities before fabrication of PANiCNQ was produced. The results of the mass magnetisation hysteresis loops at 290 K, for both PANi and TCNQ are shown in Fig. C.1, clearly indicating that the materials are diamagnetic.

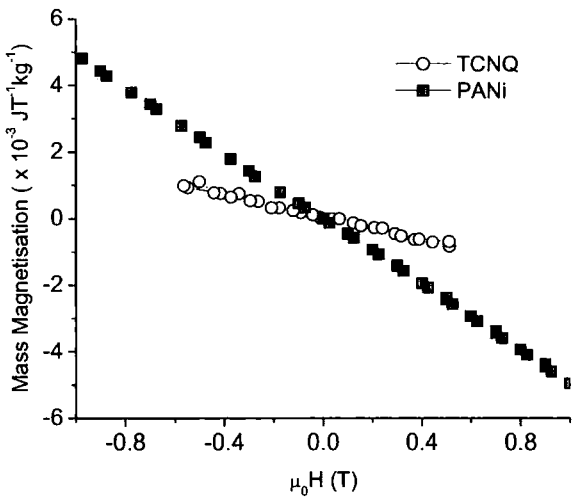

Figure C.1: Mass Magnetisation of the background materials, PANi and TCNQ.

C.2 Complimentary AFM and MFM Measurements

The following are images from extra AFM (on the left) and MFM (on the right) images, again the domain wall is being driven across the sample by the tip.

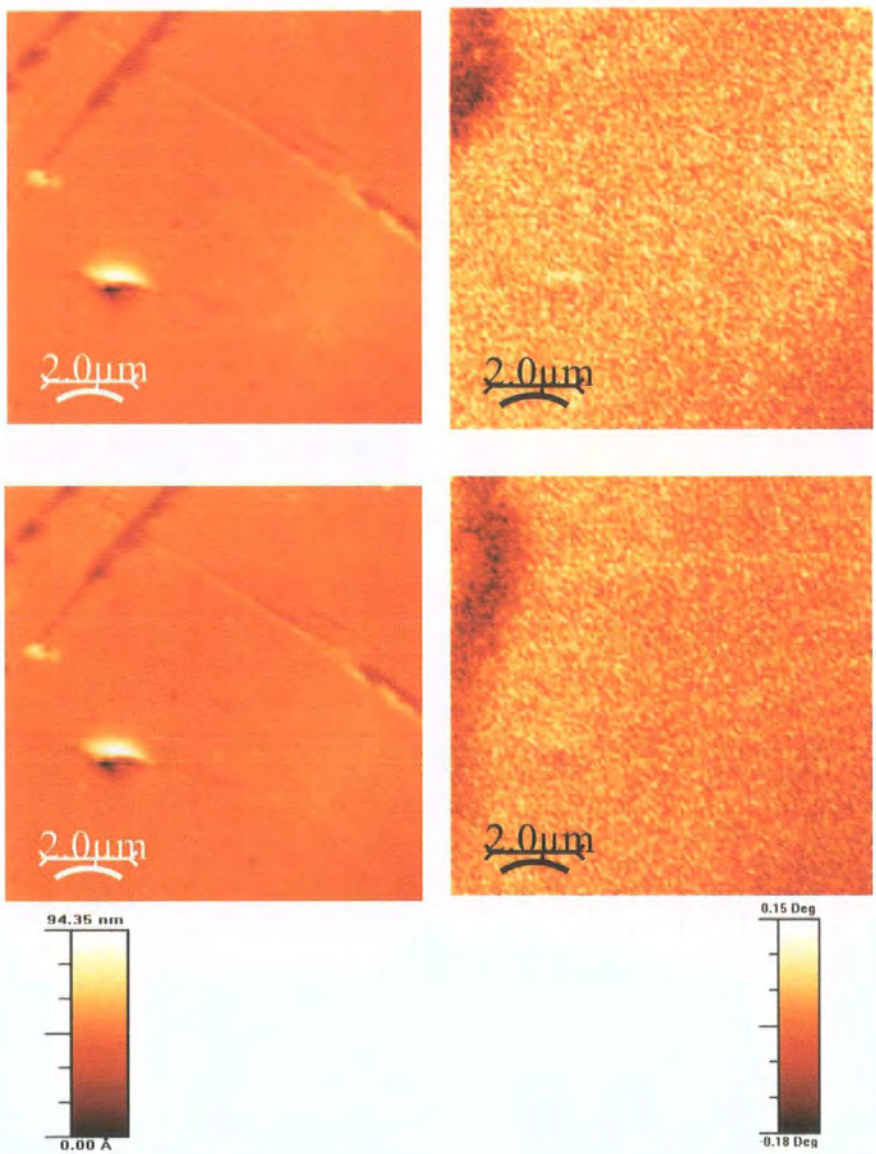

Figure C.2: AFM (on the left) and MFM (on the right) images of a sample of PANiCNQ.

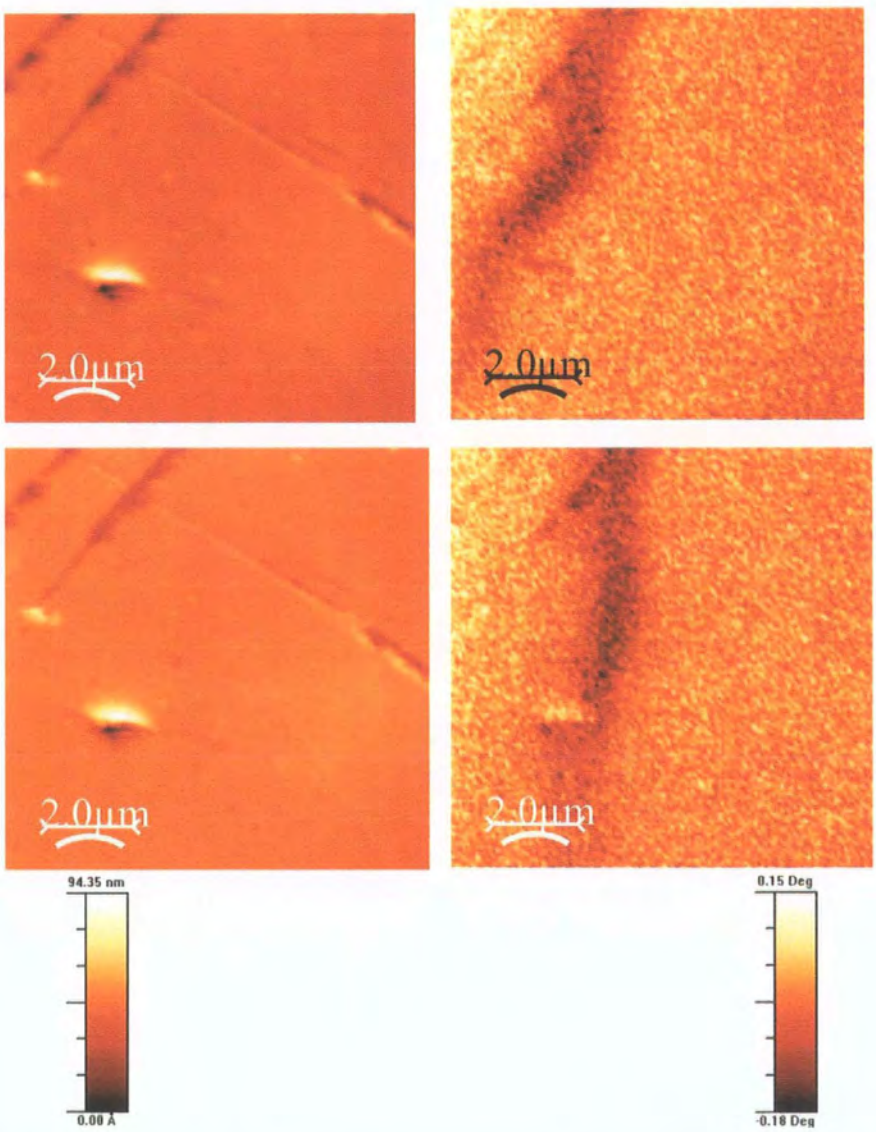

Figure C.3: AFM (on the left) and MFM (on the right) images of a sample of PANiCNQ.

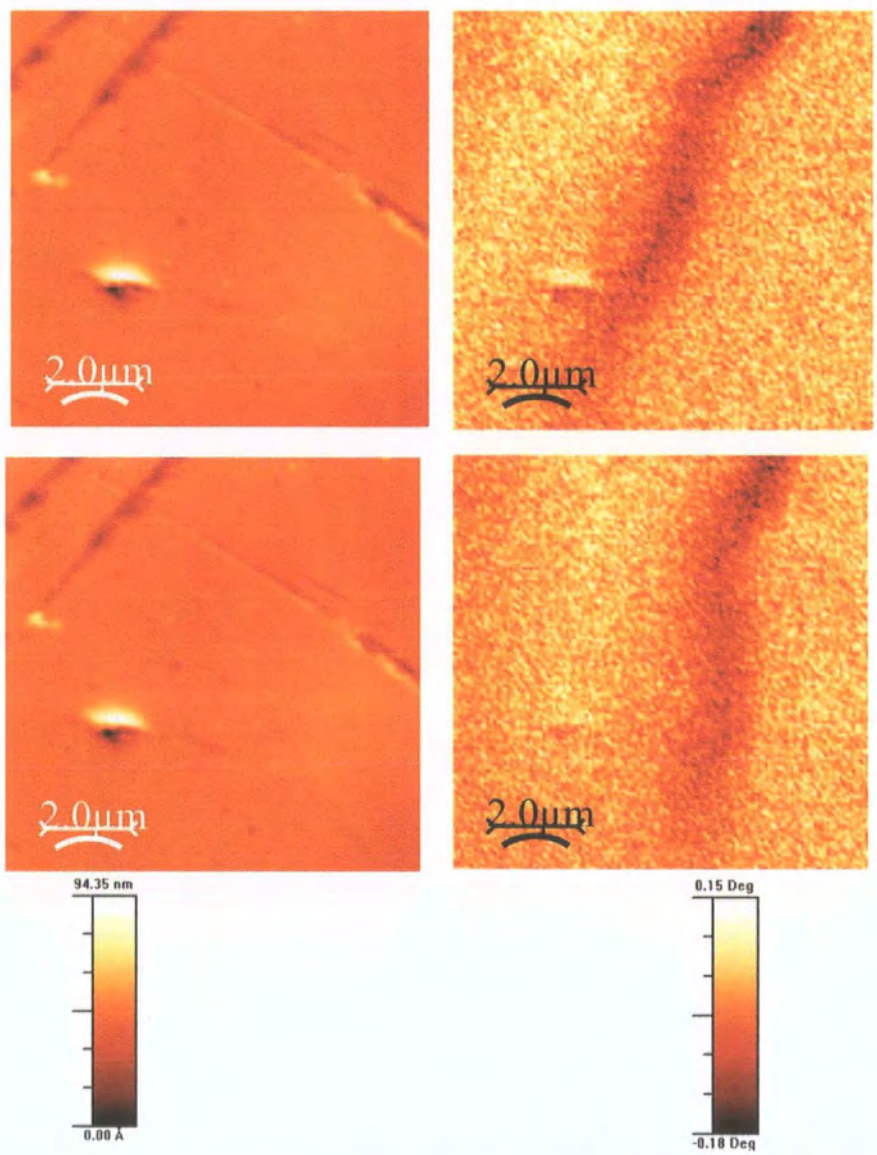

Figure C.4: AFM (on the left) and MFM (on the right) images of a sample of PANiCNQ.

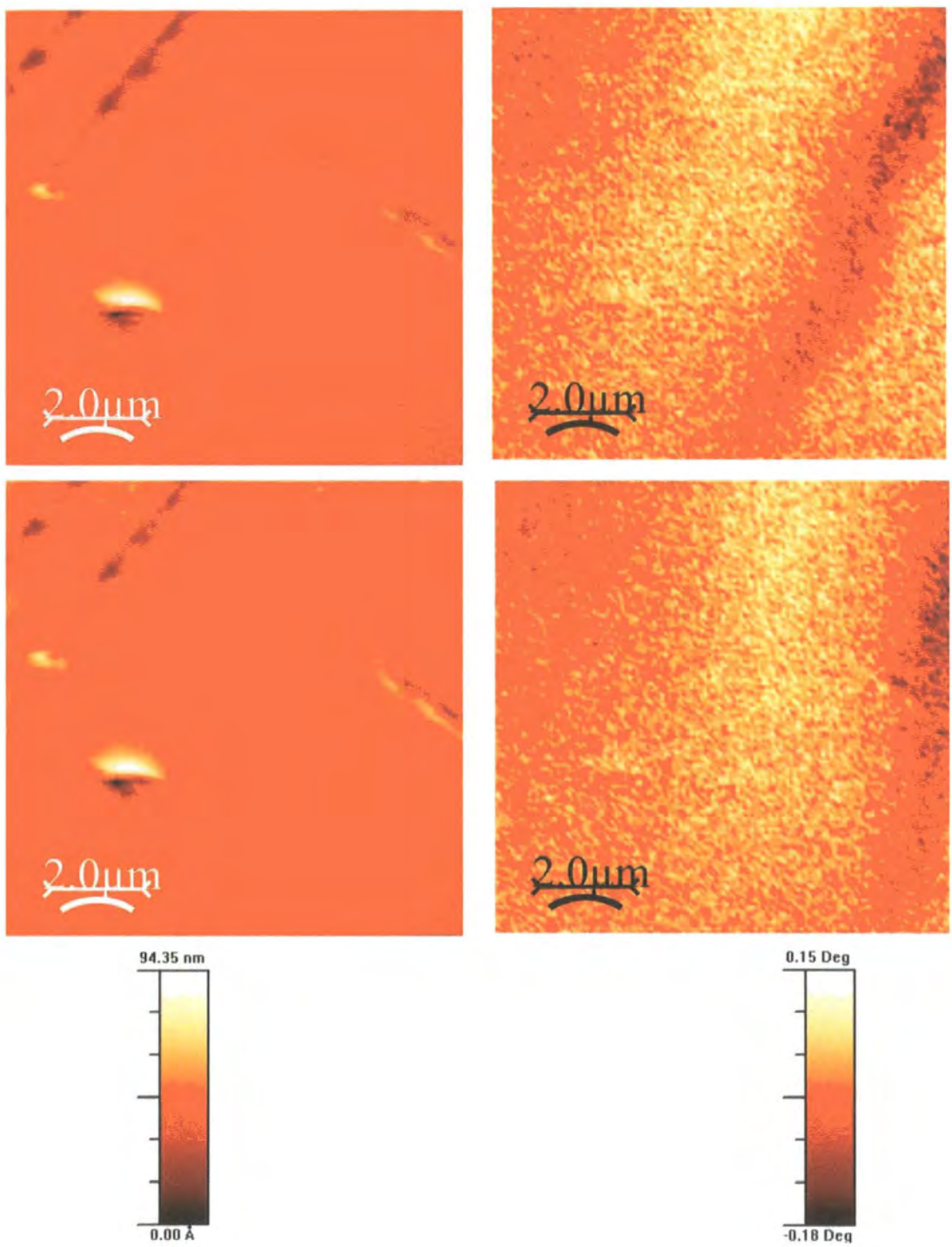

Figure C.5: AFM (on the left) and MFM (on the right) images of a sample of PANiCNQ.